Simulation of patient-specific glioma models for therapy planning

Erin Stretton

To cite this version:

Erin Stretton. Simulation of patient-specific glioma models for therapy planning. Modeling and Simulation. Ecole Nationale Supérieure des Mines de Paris, 2014. English. NNT : 2014ENMP0064 . tel-01144425

HAL Id: tel-01144425
https://pastel.hal.science/tel-01144425
Submitted on 21 Apr 2015

École doctorale n° 84 :

Sciences et technologies de l’information et de la communication

Doctorat ParisTech

THÈSE

pour obtenir le grade de docteur délivré par

l’École nationale supérieure des mines de Paris

Spécialité “ Contrôle, Optimisation, Prospective ”

présentée et soutenue publiquement par

Erin STRETTON
14-11-2014

Simulation of patient-specific glioma models for therapy planning

Simulation de modèles personnalisés de gliomes pour la planification de thérapies

Directeur de thèse : **Nicholas AYACHE**
Co-encadrement de thèse: **Hervé DELINGETTE**

Thèse préparée à l’INRIA Sophia Antipolis, projet Asclepios

Jury

Christian BARILLOT, CNRS / INRIA Research Unit	Président
Elsa ANGELINI, Computer Science: Image & Signal Processing ,Telecom ParisTech	Rapporteur
Emmanuel MANDONNET, Hôpital Lariboisiere, Neurosurgery Department, Paris	Examinateur
Bjoern MENZE, ETH Zurich	Examinateur
Nicholas AYACHE, Asclepios Research Project, INRIA Sophia Antipolis	Directeur
Hervé DELINGETTE, Asclepios Research Project, INRIA Sophia Antipolis	Co-Directeur

THÈSE

MINES ParisTech
Centre de Mathématiques Appliquées
1, Rue Claude Daunesse, CS 10207, 06904 Sophia Antipolis Cedex, France

To my husband,
Rafael Quintanilla Escalante

and my father,
Michael Stephen Stretton II

This thesis was prepared in ASCLEPIOS Research Project, Sophia Antipolis, FRANCE. This research was partially funded by the Care4ME project (ITEA 2 - ip08004) and the ERC Advanced Grant MedYMA (number 2011-291080).

Acknowledgements

I would like to thank Dr. Nicholas Ayache and Dr. Hervé Delingette for their support during my graduate studies. It has been a great honor to work with them. I wish to acknowledge my committee members Dr. Elsa Angelini and Dr. Christian Barillot for their constructive comments and suggestions on my research. I would like to express my very great appreciation to Dr. Emmanuel Mandonnet for all of his valuable clinical insights, comments, time, and most of all his interest and collaboration in my research. I would also like to offer my special thanks to Dr. Aymeric Amelot and Dr. Lars Gerigk for their clinical collaboration that was crucial for my work. I am particularly grateful to my mentors Dr. Bjoern Menze and Dr. Ezequiel Geremia for their invaluable recommendations and encouragement. In addition, I would like to thank Dr. Grégoire Malandain for advising me on registration algorithms, Dr. Maxime Sermesant on modeling, Dr. Xavier Pennec on non-linear registration algorithms, and Dr. Ender Konukoglu on his personalization algorithm. Finally, I would like to offer my special thanks to Isabelle Strobant for all of her administrative help and friendship. It was a great pleasure working with all of you! I also want to thank Jatin Ralhan, Rocio Cabrera Lozoya, Islem Rekik, Sonia Zaidenberg, Julien Gueytat, Alejandro Mottini, Emma Fulton, James Maclaurin, Christian Föcker, everyone in the Asclepios lab and all of my friends at Inria that helped me in one way or another in the realization of this thesis. Finally, I would like to thank my family for all these years of support and encouragement, especially Michael Stretton II, Philip Stretton, Claudette Aiken, and Rafael Quintanilla Escalante.

Contents

Chapter 1

Introduction

Contexte

Le cancer peut se définir comme une croissance irrégulière de cellules qui se divisent et croissent tout en formant de manière non contrôlée des tumeurs malignes, rendant invalides certaines parties du corps avoisinantes. Le cancer du cerveau est rare en comparaison avec d'autres maladies mortelles ou qui déclinent la santé. Ceci dit, aux états-Unis seuls, plus de 18000 personnes se voient diagnostiquées chaque année une tumeur cérébrale. Deux tiers d'entre eux décéderont et les autres survivront avec de sévères restrictions fonctionnelles [Buzdar and Freedman, 2007]. Ces statistiques s'appliquent pour le reste du monde, et c'est pourquoi une abondance de recherches et développements a été menée sur ce sujet. Cependant, la cure continue nous échapper. Dans cette thèse, nous utilisons la modélisation mathématique combinée avec de l'imagerie médicale pour décrire la progression de tumeurs cérébrales. Ce chapitre décrit la motivation de ce travail de thèse et présente un plan de ce manuscrit.

Motivation

Les modèles de croissance de tumeurs basés sur l'équation de réaction-diffusion de Fisher Kolmogorov (FK) ont montré des résultats convaincants dans la réplication et la prédiction des motifs d'invasion des tumeurs cérébrales du type gliome. La motivation principale de cette thèse était de proposer de nouveaux outils de traitement et d'évaluation utilisant les formulations du modèle FK en combinaison avec de l'imagerie médicale afin d'améliorer l'élaboration de stratégies thérapeutiques. Cette thèse apporte la contribution de quatre chapitres destinés aborder cette problématique. Dans cette étude doctorale, les questions suivantes ont été posées

:

- *Chapitre 2:* Quels modèles de croissance de gliomes ont été proposés dans le passé ?
- *Chapitre 3:* Pour produire des prédictions de croissance de tumeurs réalistes en formulant le modèle par l'équation FK, est-il important d'utiliser un ITD spécifique au patient, un ITD Atlas, ou bien pas de ITD du tout ?
- *Chapitre 4:* Est-il possible d'utiliser une formulation du modèle FK pour estimer si un gliome est volumineux ou bien diffus après une résection cérébrale pour améliorer l'élaboration de la stratégie thérapeutique ?
- *Chapter 5:* Est-il possible de faire un lien entre les métriques radiologiques basées sur la taille avec la vitesse de croissance d'une tumeur estimée en utilisant une formulation du modèle FK afin de déterminer si la maladie est en progression ?

Organisation du manuscit

Chaque chapitre de cette thèse a répondu une question et contribue quantifier la croissance des gliomes. Dans le chapitre 2, nous décrivons la maladie du gliome et présentons une revue de l'état de l'art des modèles de simulation de croissance de gliomes. Dans le chapitre 3, nous discutons l'importance du DTI du patient dans la modélisation précise de la croissance du gliome en utilisant un modèle de formulation FK. Dans le chapitre 4, nous proposons une méthode d'estimation de l'infiltration du gliome après une résection cérébrale en utilisant un modèle de formulation FK et l'ITD du patient. Dans le chapitre 5, nous évaluons la maladie progressive du gliome mal différencié en utilisant les estimations de la vitesse de croissance d'un modèle de formulation FK. Enfin, dans le chapitre 6, nous décrivons notre principale contribution, ainsi que les perspectives.

Introduction

⋆ English translation

Context

Cancer can be defined as unregulated cell growth where cells divide and grow uncontrollably forming malignant tumors and invade nearby parts of the body. Brain cancer is rare in comparison with other life-declining and fatal diseases. With this said, more than 18,000 persons are diagnosed with brain tumors in the United States alone each year. Two thirds of them will die and the others will survive with grave functional restrictions [Buzdar and Freedman, 2007]. These statistics are similar for the rest of the world, which is why there has been an abundance of research and development on this topic. However, the cure remains elusive. In this thesis, we use mathematical modeling combined with medical images to describe brain tumor progression. This chapter describes what motivated this thesis work and provides an outline to this manuscript.

Thesis Motivation

Tumor growth models based on the reaction-diffusion Fisher Kolmogorov (FK) equation have shown convincing results in reproducing and predicting the invasion patterns of glioma brain tumors. The main motivation behind this thesis was to propose novel processing and evaluation tools, using FK model formulations in combination with medical images, to aid in therapy planning. This thesis contributes four chapters aimed to address this motivation. In this PhD research, the following questions were asked:

- *Chapter 2:* What glioma growth models have been proposed in the past?
- *Chapter 3:* To produce realistic tumor growth predictions using a FK model formulation, does it matter if one uses a patient specific DTI, an Atlas DTI, or no DTI?
- *Chapter 4:* Is it possible to use a FK model formulation to estimate if a glioma is bulky or diffuse after a brain resection to aid in therapy planning?
- *Chapter 5:* Is it possible to link size-based radiological metrics with a tumor's growth speed estimated using a FK model formulation to determine progressive disease?

Manuscript Organization

Each chapter in this thesis answered a question and contributes to quantifying glioma growth. In Chapter 2, we describe the glioma disease and review the state-of-the-art models to simulate glioma growth. In Chapter 3, we discuss the importance of patient DTIs to accurately model glioma growth using a FK model formulation. In Chapter 4, we propose a method, using a FK model formulation and patient DTIs to estimate glioma infiltration after a brain resection. In Chapter 5, we assess LGG progressive disease using tumor growth speed estimates from a FK model formulation. Finally, in Chapter 6, we describe our main contributions and perspectives.

Chapter 2

Background and Tumor Growth Modeling Review

Contents

Based on a coauthored paper published in Optimal Control in Image Processing [Menze et al., 2011a], which gives a good literature overview of tumor growth modeling.

2.1 Context

In this thesis, we use mathematical modeling coupled with medical imaging to define brain tumor progression and its implications. To understand how to model brain tumors, it is necessary that we give some biological background first.

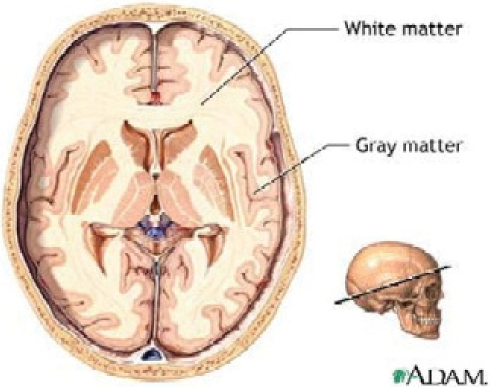

Figure 2.1: Axial cartoon view of the two brain tissue types.[1]

2.2 Background

The brain is the center of the nervous system and the most complex organ in the body. The brain is essentially composed of two types of tissue: gray and white matter as depicted in Figure 2.1. Gray matter consisting of neuronal cell bodies, neuropil, capillaries, and glial cells (astroglia and oligodendrocytes) that are responsible for controlling the brain's activity. The brain uses 20% of all oxygen taken in by the body and 95% of that goes specifically into the gray matter [Miller et al., 1980]. The gray matter color, gray-brown, comes from capillary blood vessels and neuronal cell bodies. White matter consists mostly of glial cells and myelinated axons. It is the tissue that passes signals between different areas of gray matter within the nervous system. An analogy of the relationship between gray and white matter could be a computer network, where gray matter can be thought of as the computers, and the white matter represents the network cables connecting the computers together. The white matter gets its color (pinkish white) from the fatty substance (myelin) that surrounds the nerve fibers (axons). This myelin can be found in almost all long nerve fibers. It acts as an electrical insulation and allows the signals to pass quickly from place to place.

Glial cells, which are found in both white and gray matter, are among the few neural cells capable of division and are the supporting cells of the nervous system functioning to insulate, support, and maintain the neurons [Campbell, 1996]. The three types of glial cells are: astrocytes, oligodendrocytes, and microglia. Astrocytes provide physical support and regulate the chemical environment for neurons. They also encircle the capillaries contributing to the blood brain bar-

---

[1] ADAM. (2010). Gray and white matter of the brain. [Online; accessed 4-July-2013]. `http://health.allrefer.com/pictures-images/gray-and-white-matter-of-the-brain.html`

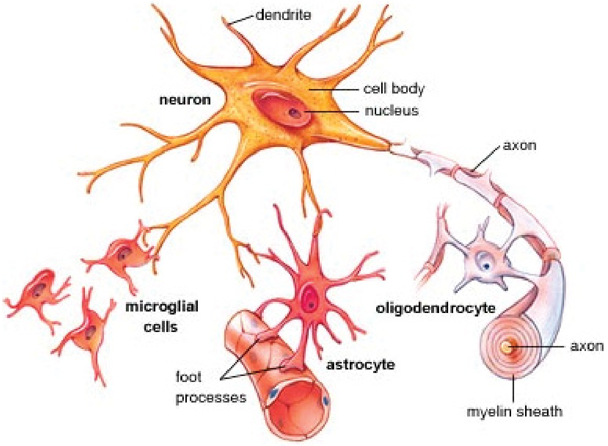

Figure 2.2: Types of glial cells: astrocytes, oligodendrocytes, and microglia[2].

rier. Oligodendrocytes form the insulating myelin sheath surrounding the axon of the neurons. Microglia contributes as the main immuno-surveillance component of the central nervous system. A cartoon depiction of these cells is shown in Figure 2.2.

Brain tissue can be further divided into lobes as can be seen in Figure 2.3. The cerebral cortex is nearly symmetrical, where the left and right hemispheres are approximate mirror images. Anatomists conventionally divide each hemisphere into four lobes: the frontal lobe, parietal lobe, occipital lobe, and temporal lobe. It is important to note that, in general, cancer tumor cells cannot travel from one lobe to another. A brain segmentation (delineation of the brain), in glioma modeling, must reflect these lobe separations for realistic simulations.

2.2.1 Glioma

Gliomas are a type of brain tumor that are diffuse and invade fastest along white matter fiber tracks [Giese et al., 1996]. They make up 30% of all brain and central nervous system tumors and 80% of all malignant brain tumors [Goodenberger and Jenkins, 2012]. Gliomas get their name because they arise from glial cells. They start in the spine, or most commonly in the brain [Mamelak and Jacoby, 2007]. Gliomas are histologically classified by grade according to the World Health Organization (WHO) grading system. Table 2.1 explains this classification.

Low-Grade Gliomas: Low-grade gliomas (LGG) are slow proliferating tumors, which are classified as grade I or II in the WHO grading system. LGGs

---

[2] Sajben, N. (2013). Rsd advisory- where chronic pain and depression collide. [Online; accessed 4-July-2013]. `http://rsdadvisory.com/category/glial-cell-activation/`

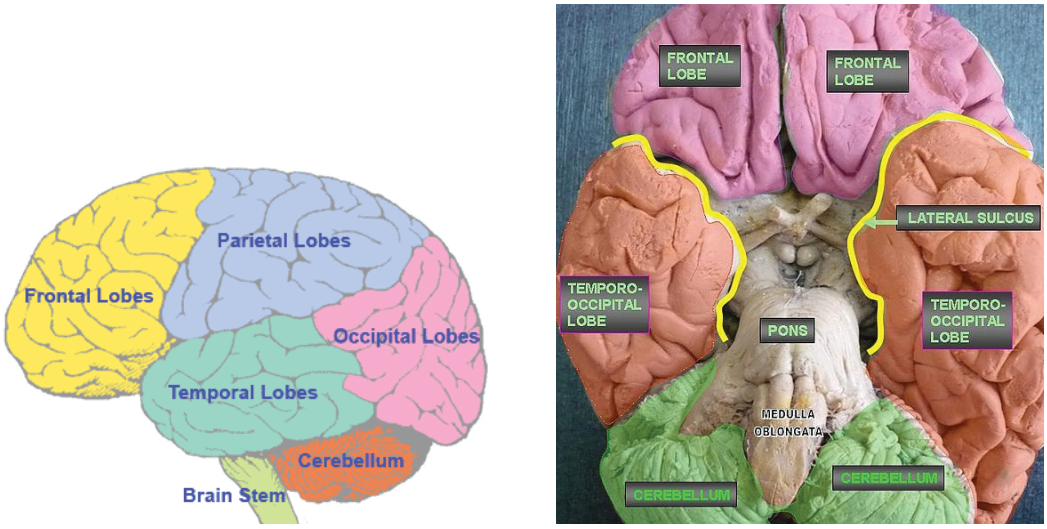

Figure 2.3: Sagittal cartoon view of the brain with the lobes labeled (left)[3]. Axial view of the labeled lobes (right)[4]. Note that these images are color coded differently.

can further be categorized into two groups: "astroglial variants" (grade I) and diffusely infiltrating LGGs (grade II). In this thesis, we will only focus on the diffusely infiltrating LGGs since astroglial variants can be benign whereas diffusely infiltrating LGGs are cancerous. All diffuse LGG are considered grade II in the WHO classification system because of their mild to moderate nuclear pleomorphism without evidence of mitotic activity, vascular hyperplasia, or necrosis. There are three different types of these diffusively infiltrating LGG: astrocytomas, oligodendrogliomas, and mixed gliomas. These tumors characteristically spread widely throughout the brain and typically progress to higher-graded glial tumors and must invariably be treated with multiple modalities of therapy.

High-Grade Gliomas: High-grade gliomas (HGG) are tumors that proliferate rapidly. They are classified as grade III or IV in the WHO grading system. Anaplastic astrocytomas and glioblastoma multiforme grow rapidly and quickly invade the brain in tentacles penetrating into the brain parenchyma. Most often these gliomas are surrounded by edema. Grade IV gliomas are characterized by creating extensive networks of blood vessels and having a necrotic core. Since these tumors grow rapidly and the edema exerts pressure on the brain tissue, often

---

[3] Wikipedia (2011). Lobes of the brain. [Online; accessed 4-July-2013]. http://en.wikipedia.org/wiki/File:Lobes_of_the_brain.jpg

[4] Norman, P. (2013). Healthy brain for life. [Online; accessed 4-July-2013]. http://www.healthybrainforlife.com/images/brain/brain-lobes-color.gif/view

Grade	*Characteristics*
Low-Grade ($I\&II$)	- Slow proliferation - Cells look almost normal - Infiltrative into normal brain parenchyma - Progression to a high-grade glioma is almost inevitable
High-Grade ($III\&IV$)	- Rapid proliferation - Cells look abnormal - Infiltrative into large areas of normal brain parenchyma - Might have a necrotic core - Forms new vascularization to support growth

Table 2.1: World Health Organization (WHO) Glioma Grade Characteristics

these tumors exhibit local mass effect (effect of a growing tumor that results in secondary pathological consequences by pushing on surrounding tissue) [Wilson and Berger., 1999; Deangelis, 2001].

2.2.2 Medical Imaging of Gliomas

Imaging plays a crucial role in the patient care of intracranial tumors. Magnetic Resonance Imaging (MRI) has been the principal modality used to assess brain tumors (grading and biology), make differential diagnoses, identify targeted biopsy sites, assist in treatment planning, and evaluate treatment response without exposing patients to ionizing radiation. MRI is a medical imaging technique used in radiology to analyze the anatomy and function of the body in both health and disease. MRI scanners use powerful magnetic fields and radio waves to construct images of the body. MRI is more sensitive than Computed Tomography (CT) for small tumors and offers better visualization of the posterior fossa. Additionally, MRI provides good contrast between gray and white brain matter.

Imaging is used to evaluate changes in glioma size and enhancement pattern, where advanced imaging techniques incorporate hemodynamic, cellular, metabolic, and functional information [Bangiyev et al., 2014]. Advanced imaging techniques include: diffusion-weighted imaging (DWI), positron emission tomography (PET), functional magnetic resonance imaging (fMRI), MR spectroscopy (MRS), dynamic susceptibility-contrast (DSC) imaging, and dynamic contrast-enhanced imaging (DCE) to name a few. In this section, we will first describe several MRI sequences, and then touch on the image-based indices (imaging biomarkers), along with glioma treatment planning challenges. Following, we will introduce population atlases for specific image types and segmentations of certain brain areas.

MRI Sequences: The three main MRI protocols are anatomical, diffusion, and functional.

Individual anatomical structures or pathologies can be shown by both T1 and T2 weighted MRIs. T1 and T2 weighted images (also referred to as T1WI and T2WI) are basic pulse sequences in MRI and demonstrate the differences in the T1 and T2 relaxation times of tissues. The T1 weighting depends on the longitudinal relaxation of the net magnetization vector (NMV). T1 weighting has a tendency to have short echo time (TE) and repetition time (TR) times. In contrast, the T2 weighted relies upon the transverse relaxation of the NMV. T2 weighting often has long TE and TR times. A scan is created by allowing each tissue to return to its equilibrium state after proton excitation by the separate relaxation techniques. T1 MRI image weighting is practical for assessing the cerebral cortex, distinguishing fatty tissue, and for post-contrast imaging. T2 MRI weighting is useful for recognizing edema, and exhibiting white matter lesions. There are two sub-types of anatomical MRIs that are frequently used in glioma imaging: Fluid Attenuated Inversion Recovery (FLAIR) and T1-gadolinium. FLAIR, which is a type of T2, is an inversion-recovery pulse sequence utilized to nullify the signal from fluids and is exploited in brain imaging to repress cerebrospinal fluid (CSF) so as to display periventricular hyper-intense lesions. T1-gadolinium, which is a type of T1, is used to show a tumor's necrotic core using a common contrast agent (gadolinium).

The diffusion process of molecules (mainly water) in vivo can be mapped non-invasively using DWIs. In DWI, the intensity of each image voxel shows the optimal estimate of the rate of water diffusion at that location. The hypothesis supporting DWI is that findings may indicate early pathological change since the mobility of water is powered by thermal agitation and extremely dependent on its cellular environment. Diffusion tensor images (DTIs) can be created from DWIs. Wu et al. [2007] showed that DTI-based functional neuronavigation (maps of fractional anisotropy) in surgery contributes to maximal safe resection of cerebral gliomas with pyramidal tract involvement with more than seven months of additional survival for high-grade glioma patients. Thereby decreasing post-operative motor deficits for both HGGs and low-grade gliomas while increasing high-quality survival for HGGs. In Chapters 3 and 4 we use DTIs within computational models to simulate how tumors diffuse in white matter.

Functional MRIs (fMRI) are employed to appreciate how different parts of the brain react to external stimuli. 3D parametric maps of the brain are constructed using statistical methods indicating the regions of the cortex that demonstrates notable changes in activity in response to a task. FMRI is used in behavioral and cognitive research and in planning neurosurgery in eloquent areas of the brain.

Image-based Indices of MRI Sequences: There have been various image-based indices established in FLAIR, T2-weighted MRI, T1-gadolinium, and DWI for the quantification of brain tumor longitudinal growth and treatment response.

In practice, glioma progression is evaluated with combined clinical and radiological assessment [Van den Bent et al., 2011]. In this thesis, we will focus on the radiological assessment. Commonly, imaging is used to establish the diagnosis of tumor progression in LGG phase 3 clinical trials and the outcome to treatment of phase 2 trials [Van den Bent et al., 2011]. FLAIR MRIs produce the clearest and most reproducible definition of WHO grade II glioma (LGG) margins of all of the imaging modalities, where the precise relationship between these sequences and the histological tumor margin has not been established [Bynevelt et al., 2001; Pallud et al., 2010]. For HGGs, both FLAIR MRIs and T1-gadolinium are used.

Focusing on LGGs, FLAIR and T2-weighted images are used for measuring tumor extent or response to therapy. However, FLAIR and T2-weighted have limited sensitivity in noticing both response and progression in LGG [Van den Bent et al., 2011]. An increase of about 2-5 mm in diameter per year [Mandonnet et al., 2003] (see Figure 2.4) and a mean volume increase of about 15% per year [Rees et al., 2009], which was studied in different cohorts, has been recorded using FLAIR and T2-weighted images for LGG. In Chapter 5 four types of criteria, which help oncologists determine the progression status of gliomas and decide when therapy should be given, are compared in terms of progressive disease: the Response Evaluation Criteria in Solid Tumors (RECIST) [Eisenhauer et al., 2009], the Macdonald [Henson et al., 2008], the Response Assessment in Neuro-Oncology (RANO) [Wen et al., 2010], and a volumetric-based criterion [Galanis et al., 2006]. It should be noted that LGG are often irregularly shaped and grow anisotropically, which results in poor reproducibility of area or volume estimation based on linear measurements [Van den Bent et al., 2011]. The RECIST, Macdonald, and RANO criteria are based on measuring diameters and as a result have the down side to not taking into account i) irregularities in tumor shape, ii) differences in growth speed in white and gray matter, iii) inter-observer variability, and iv) tumor volume. The volumetric criterion has only the first three weaknesses. It is foreseen, in the near future by the RANO Working Group that volumetric measures, new physiologic imaging techniques (perfusion imaging, permeability imaging, diffusion imaging, magnetic resonance spectroscopy), metabolic imaging, and other end points such as quality-of-life measures will be further developed, validated, and incorporated into the RANO response criterion.

MRI interpretation can be subjective; a number of LGG clinical trials reported low to no radiographic response despite significant clinical benefit, particularly

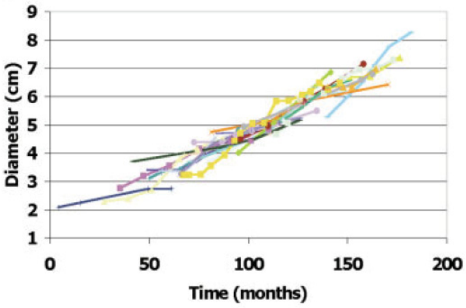

Figure 2.4: Modeling of LGG growth rate. The mean linear tumor growth rates of twenty-seven patients were $4mm/year^5$.

seizure reduction and prolonged disease control [Soffietti et al., 2010]. This brings up the point that even after a patient has gone through a successful treatment, there might be a residual T2-weighted abnormality that cannot be distinguished from the tumor due to difficulties in MRI interpretation. This limitation has lead to minor response classifications between stable disease and partial response for LGG [Van den Bent et al., 2011]. In addition, there can also be local white matter changes that are radiotherapy-induced (leukoencephalopathy or microangiopathy) that also can be seen in T2-weighted or FLAIR images as increasing areas of abnormal signal intensity. These white matter lesions increase the difficultly for deciphering what hyper-intense FLAIR or T2-weighted voxels are malignant glioma and which are non-malignant white matter lesions. In a future chapter we will encounter this challenge during the segmentation of a glioma that has a microangiopathy lesion touching it.

Regarding LGGs transformation to HGGs, conventional imaging with contrast-enhanced CT or MRI is often insensitive to the earliest phases of malignant transformation [Danchaivijitr et al., 2008]. Therefore, reliable discrimination between patients who have already undergone malignant transformation with T1-weighted MR images and so-called true LGG is poor [Van den Bent et al., 2011].

Image-based indices can also be found in DWIs. Quantitative DWI has been suggested as an early indicator of early treatment response in high-grade gliomas and transformed LGG, which usually contain regions of low apparent diffusion coefficient [Moffat et al., 2006]. LGG apparent diffusion coefficient is often higher than that of normal brain, yet there is sizable overlap in values [Van den Bent et al., 2011].

Glioma Treatment Planning Challenges: Gliomas can be highly diffuse, which makes them very difficult to treat. Experimental results suggest that

---

[5] Figure was published in [Mandonnet et al., 2003].

glioma cells can be identified throughout the central nervous system (CNS) within seven days of a tumor being implanted in a rat brain [Silbergeld and Chicoine, 1997]. Although there are solitary tumor cells throughout the CNS [Chicoine and Silbergeld, 1995; Silbergeld and Chicoine, 1997], the locally dense solid tumor rests where the cancerous tissue was originally implanted. This demonstrates a potential shortcoming of therapy since most glioma treatments are targeted locally to the bulk mass when the action of the glioma growth is elsewhere. An additional challenge is that not all of a glioma can be seen in MRIs. There have been many assumptions made in research on this front and will be discussed later in this thesis. Since gliomas are usually quite diffuse, it is even hard to decipher the visible tumor boundary in MRIs. Angelini et al. [2007] points out that this ambiguity is due to two factors. First, the enhancement appearance of the tumor on MRIs depends on the degree of vascularization. Second, manual tracing of tumors bears high variability.

It is because of these reasons that there is a controversy over the optimal treatment strategy and clinical management for LGG gliomas. Early detection is critical and today possible because of the routine use of MRIs. Patients have MRIs taken even when having few or no symptoms and when have normal neurologic function. Currently, physicians follow two different schools of thought on this: i) the early intervention approach for possibly curing diffuse LGG since they have slow growth and low histologic grade, ii) the “watchful waiting” approach for favoring patient quality of life instead of time. This thesis highlights both approaches. Chapter 4 features a method to aid physicians in follow-up treatment planning after an early intervention (brain resection) and Chapter 5 presents the growth speeds of nine patients who are undergoing the approach of “watchful waiting”, where only two of the patients received any prior therapy before their tumors were monitored without receiving additional therapy.

In regards to HGG patients, they are usually treated immediately or not treated at all to preserve the patent’s quality of life.

Brain Atlases: Brain atlases are collections of reference information that have been constructed to represent the brain’s i) structural, ii) functional, and iii) diffusion organization. One use of these atlases is to be used in tumor growth modeling. These brain atlases create a standardized reference coordinate system in which individual brain maps can be transformed into one coordinate system (registered) and contrasted. Talairach proposed one of the pioneering reference systems, which later became the standard reference in brain mapping [Talairach and Tournoux, 1988]. However, this atlas was created from one subject and varied in slice thickness. In the nighties, the Surgical Planning Laboratory and Montreal Neurological Institute (MNI) created one-subject atlases of improved

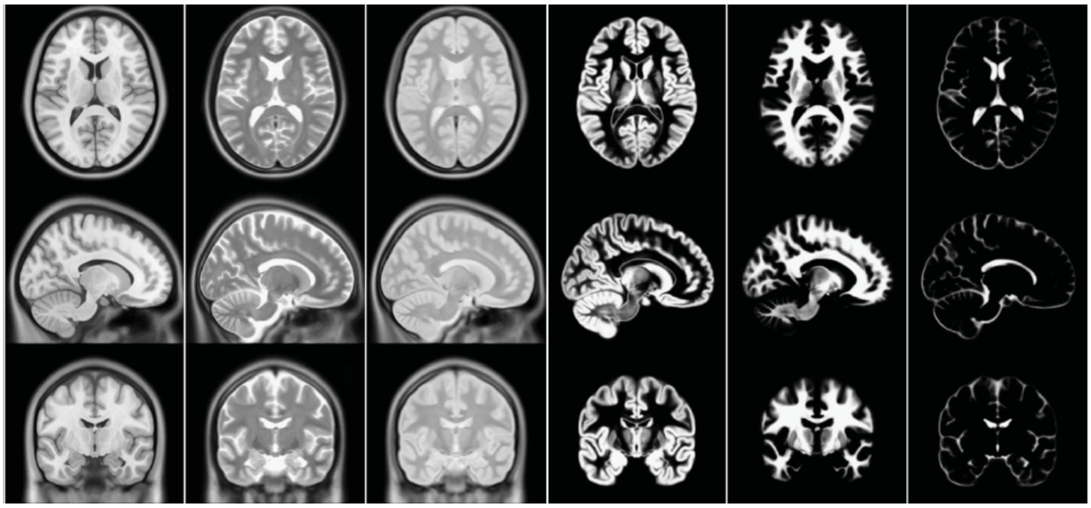

Figure 2.5: MNI-ICBM-152 probabilistic atlas. Images from left to right: T1, T2, and Proton Density weighted images; Gray Matter, White Matter and CSF probability maps[6].

resolution [Kikinis et al., 1996; Holmes et al., 1998].

Since one subject structural atlases were not representative of the population and might introduce bias, population structural atlases were developed from a group of scans that were registered and averaged. MNI and the Laboratory of Neuro Imaging of UCLA created a structural atlas of 305 subjects (both male and female around the age of 23 years old) [Collins et al., 1994]. All subject images were registered to the Talairach space, image intensities normalized, and then a voxel-wise averaging of intensities over all volumes was performed. Then, an improved structural averaged atlases of 152 [Fonov et al., 2009, 2011] (depicted in Figure 2.5) and 452 [Mazziotta et al., 2001] subjects were created. These atlases had probabilistic versions that were created by segmenting the white matter, gray matter, and CSF of the different subject's tissues after registration. These probabilistic atlases describe the spatial distribution of the tissue classes and were created by averaging the labels across all the subjects. These probabilistic population atlases can be thresholded into i) white matter, ii) gray matter, iii) CSF regions that can be used in tumor growth modeling. The advantage to using these segmentations over patient segmentations is it is difficult to segment the white matter in the presence of a lesion and brain parenchyma (keeping the sulci patterns and lobes separated) for individual patients, which is necessary for simulating tumor growth. In this thesis, we use methods for registering white matter and brain parenchyma atlas segmentations.

---

[6] Figure was published in [Fonov et al., 2011].

For functional atlases, Lancaster et al. [2000] generated a 3D database of labels for the 1988 Talairach atlas, which compared well with functional activation foci.

For diffusion atlases, Prastawa et al. [2009] averaged 75 subjects and Rohlfing et al. [2010] 24 subjects to create population DTI atlases. Since patient DTIs are not widely ordered in clinical practice and gliomas are hypothesized to grow anisotropically fastest along white matter fiber tracts, the availability of a DTI atlas is crucial. In this thesis, we show (in Chapter 3) that using a registered DTI atlas is in many cases almost as good as using a patient DTI in simulating tumor growth for an individual patient.

2.3 Tumor Modeling

Mathematical tumor growth models try to explain the complex dynamics of cancer progression as a function of biological processes, which are assumed or known from prior experiments. Examples of such processes are the dynamics of individual tumor cells, their interactions with each other, their interactions with the surrounding tissue through mechanical or biochemical mechanisms or the generation, transport and allocation of substances relevant to specific biochemical processes. There are three strategies that have been used to study tumor growth:

In vivo: Latin for “within the living,” is experimentation using a whole, living organism in their normal intact state. In vivo is standardly used in animal testing and clinical trials to observe the complete effects of an experiment on a living subject.

In vitro: Latin for “in glass,” i.e., in a test tube or petri dish, refers to biological experiments that are conducted using isolated components of an organism to permit a more detailed or more convenient investigation than is possible with whole organisms. In vitro allows an enormous level of simplification of the system that is being studied, which allows the investigator to focus on a small number of components. However, it can also be very difficult to extrapolate in vitro experimental results back into the biology of the whole organism.

In silico modeling: Refers to experiments performed via computer simulation, where one of the prime benefits is to be able to simulate a phenomena of interest faster than can be observed in real time. In silico models, which use concepts from systems biology, also address the ever-increasing volume of molecular data in biomedicine and the availability of similarly inexpensive computational power required to run larger and clinically applicable simulations. In addition, in silico models have required strong interdisciplinary collaborations, which has brought computer scientists and biological scientists together to jointly examine biological phenomena. Drawbacks include being able to inject a complete understanding of molecular dynamics and cell biology into the in silico models, and available computer processing power, which forces scientists to make large simplifying assumptions to their models.

2.3.1 In Silico Tumor Modeling

In silico models have been used to address a multitude of questions such as studying volumetric tumor growth dynamics, vascularization patterns, investigating genetic instability, mutagenesis, and complexity of tumor-immune system interactions using applications of game theory, scaling laws, fractals, and graph theory [Deisboeck et al., 2008]. These in silico models can be classified as:

Continuous Models: These models describe variation as involving gradual quantitative transitions without sudden changes or discontinuities. Examples of these models aim at explaining the change in tumor cell density, chemo-attractant diffusion, and kinetic molecular pathway networks with a set of differential equations [Deisboeck et al., 2008].

Discrete Models: These models use individual formulae that are fit to data and are used to model events. Discrete cell population models describe processes that happen on the single cell scale and initiate cell-cell interaction using cellular automatatype computational machinery. A set of local integration rules among neighboring nodes described the cellular automaton dynamics, where transition and communication among grid points are decisions [Roose et al., 2007; Deisboeck et al., 2008].

Hybrid Models: These models use both continuum and discrete techniques combined where individual cells are treated discretely yet interact with other continuum fields. In exclusively discrete models it is complicated to build in interactions with diffusible chemicals. These are much simpler to deal with as continuous models. An example of a hybrid model would be one that combines phenomena at the single cell level with continuous equations for macro-molecular transport and comprising coupled discrete and continuous equations. For instance Ferreira Jr et al. [1998, 1999] used a two-dimensional hybrid cellular automaton to model a population of cancer and normal cells.

Agent-based Models (ABM): These models are used for simulating the actions and interactions of independent decision-making entities (both individual

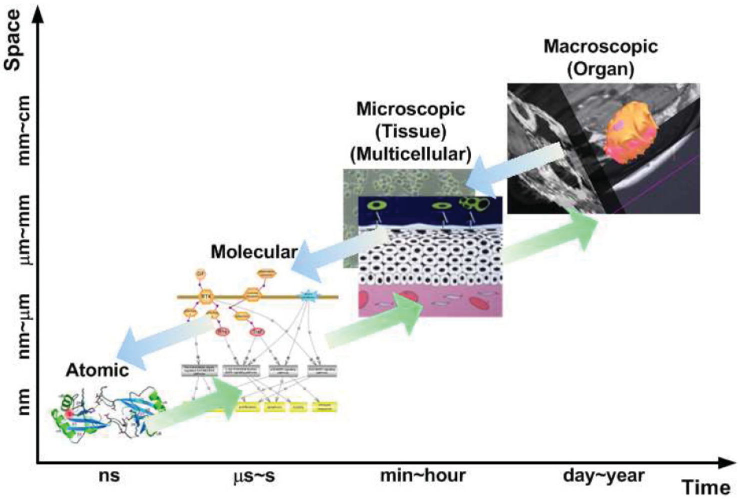

Figure 2.6: Schematic illustration of the significantly relevant biological scales for cancer modeling. Each scale represents a different spatial and temporal range, and the methods for modeling these specific scales also differ. Multi-scale cancer modeling necessitates a linkage between these distinct scales.[7]

or collective) called agents. Examples of agents would be clusters of cells, single cells, protein(s), or gene(s). These agents follow a set of predetermined rules where each agent can independently carry out a series of actions and make choices. The purpose of ABM is to analyze the effects of actions and interactions of agents on the whole system. These in silico models are used to solve specific questions on one scale of interest. There has also been effort in the scientific community to understand biological phenomena on many scales, with key pieces of information transferring between the several scales. In the future, large multiscale models are likely to be used by many researchers since researchers will venture to integrate detailed subcellular information to make predictions on the tumor scale (see Figure 2.6).

2.3.2 Multi-Scale Tumor Modeling

Tumor evolution complexities arise at different spatial-temporal scales including processes at the sub-cellular, cellular, and tissue levels. To date, a majority of cancer research has centered around the identification and characterization of the genetic and molecular properties of cancer cells. This is because cancer initiation seems to depend on a series of genetic mutations that influence the intrinsic cellular programs of the cancer cells. Additionally, tumors are heterogeneous

---

[7] This figure was copied from [Deisboeck et al., 2011]

cellular entities whose growth depends on constantly changing microenvironments and dynamical interactions among cancer cells. Therefore, a complete model would include both micro- and macro-scales to study these phenomena. Since the time and space scales of observation for biological experiments are often restricted by experimental complexity, some scientists have proposed in silico multi-scale tumor models. These researchers study cancer as a system disease to examine how individual components interact to create a function and behavior of the cancerous system as a whole. The different spatial-temporal scales of multi-scale models include:

Atomic: Models at this scale are used to study the structure and dynamics of proteins, peptides, and lipids.

Molecular: This scale is used to model protein population properties. Cell signaling mechanisms are typically investigated at this scale. At this scale, ordinary differential equations (ODEs) are commonly used to portray biochemical reactions to explore the potential for new therapeutic targets to combat cancer.

Microscopic: This scale includes tissues, multicellular, and cellular levels. Examples of microscopic phenomena are malignant transformations of normal cells, associated alterations of cell-cell and cell-matrix dynamics, the heterogeneous tumor environment, the element of tumor heterogeneity, and other factors such as acidity or cell-specific promoter substances. These processes and factors are usually modeled using partial differential equations (PDEs) or ABM. Simulation run time can increase substantially if individual cell interactions are investigated in detail.

Macroscopic: At this scale the focus is on whole tumor dynamics such as morphology, shape, extent of vascularization, and invasion with different environmental conditions. PDEs are often used to consider cell responses to gradient fields of various origins. Examples include the concentration of gradients of diffusible or non-diffusible molecules as well as strain and stress gradients caused by the growing of a tumor mass. In clinical applications, the primary source of information comes from medical images. Image based tumor modeling describes the average behavior of tumor cells, macroscopic effects, and general features at an organ level, such as tumor invasion in white and gray matter, or the deformation of the brain due to the mass effect of a tumor. The theoretical approach of multi-scale models has increasingly been recognized to be able to simulate experimental procedures, as well as optimize, and predict clinical therapies and their outcomes. Additionally, multi-scale tumor modeling can be used to test and refine medical or biological hypotheses, such as was done by Jiang et al. [2005] and Benjamin et al. [2006].

Jiang et al. [2005] used a multi-scale approach to model avascular tumor growth spanning three distinct scales. At the cellular level, a lattice Monte Carlo model described cellular dynamics, such as proliferation, adhesion, and viability. At a subcellular level, the expression of proteins, which control the cell cycle, were modeled using a Boolean network. At a extracellular level, the chemical dynamics, such as nutrient, waste, growth promoter, and inhibitor concentrations, were modeled by reaction-diffusion equations. The model parameters were derived from spheroids using the mouse mammary tumor cells, EMT6/Ro. The model compared well with experimental data (i.e., a spheroid with 0.08 mM O_2 and 5.5 mM glucose in the medium).

Benjamin et al. [2006] also used a multi-scale approach. The 2-D framework included a Boolean description of a relevant colorectal cancer genetic network, a discrete model of the cell cycle, and a continuous macroscopic model of the tumor growth and invasion. The cell cycle kinetic parameters used in this model were taken from flow cytometric analysis of human colon cancer cells. The model's basis is that the sensitivity to irradiation depends on the cell cycle phase and that DNA damage is proportional to the radiation dose. Hypoxia and overpopulation (anti-growth regulation signals) activate the SMAD/RAS and adenomatous polyposis coli (APC) genes and hindered the proliferation through cell cycle regulation.

The idea of in silico multi-scale tumor models is very innovative. It solves spacial and temporal problems that are encountered with lab experiments. However, this modeling technique is still in an elementary stage in development since most scientists have to use literature parameter values, which would not be specific to a patient. Image-based tumor modeling, which is on the macro scale only, relies on often routine images, and these models are able to be patient specific (personalization).

2.3.3 Image-based Tumor Modeling

Image-based tumor mathematical models have been proposed in biological-cancer research since the 1950's. Murray [2002] elaborates on the early models proposed that studied solid tumor growth and later diffusive tumor growth [Tracqui et al., 1995b; Cruywagen et al., 1995; Woodward et al., 1996; Swanson et al., 2000]. Extensions of these models considered effects of treatments [Swanson et al., 2002, 2007]. In this section, we summarize recent works in imaged-based tumor modeling.

In the diagnosis of brain tumors, extensive imaging protocols are routinely used to evaluate therapeutic options or to monitor the state of the disease. This

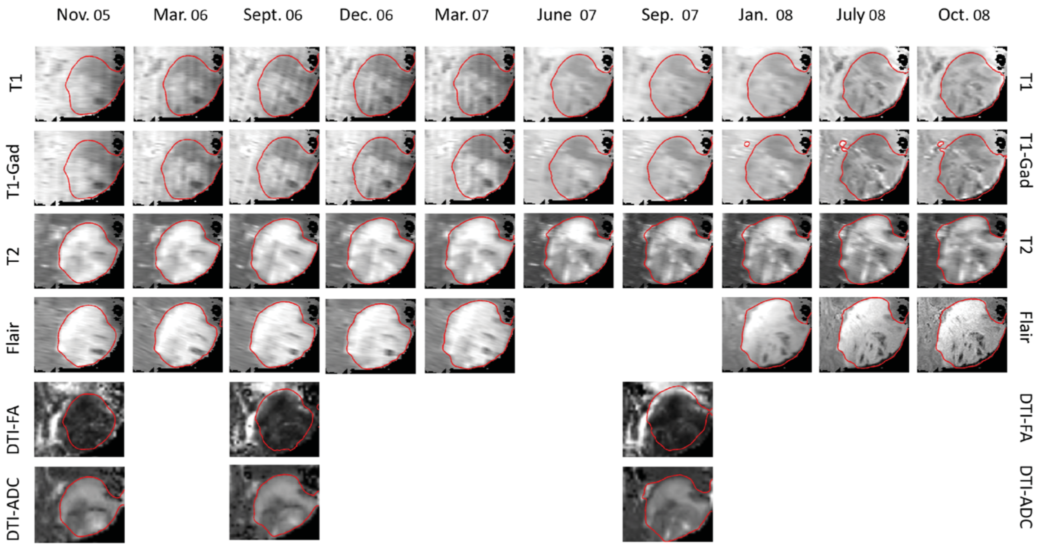

Figure 2.7: Segmentation of the 44 MR volumes of a glioma patient using lesion-specific atlases for ten time points of a multimodal image volume. Notice that some modalities are missing for certain time points – which is a common problem in longitudinal studies. The tumor outlines are obtained using the latent atlas approach by Riklin-Raviv et al. [2009, 2010].

gives rise to large numbers of multi-modal and multi-temporal image volumes even in standard clinical settings (Figure 2.7), requiring new approaches for comprehensively integrating information of different image sources and different time points. As all observations in these data sets arise from one underlying physiological process – the tumor-induced change of the tissue – a patient-specific model of tumor growth may provide new means for analyzing the acquired images and evaluating patient's options. The information available from an image observation, such as computed tomography scans, or magnetic resonance imaging, is at a macroscopic scale – with typical spatial resolutions at the millimeter level. Among the tumor-induced processes visible at this scale, two effects are most prominent: changes in tissue properties resulting from the invasion of healthy tissue by tumor cells, and the displacement of tissue resulting from tumor growth. As a consequence, image-based tumor models can be grouped into two classes: models that concentrate on the migration of tumor cells and their invasive processes, and models that consider the mechanical mass effect of the lesion and their imprint on surrounding tissues.

2.3.3.1 Reaction-diffusion Models of Cell Invasion

The majority of all macroscopic tumor models use the reaction-diffusion formalism [Murray, 2002], describing very generally the dynamics of tumor growth:

$$\frac{\partial u}{\partial t} = \underbrace{\nabla \cdot (D \nabla u)}_{\text{Diffusion Term}} + \underbrace{R(u,t)}_{\text{Reaction Term}} , \tag{2.1}$$

where u is the tumor cell density, $\partial u / \partial t$ is the differentiation operator with respect to time, D is the diffusion tensor for tumor cells, which can be a function of location x, and $R(u,t)$ is the reaction term. This partial differential equation model changes the continuous tumor cell density u by two individual processes: cell migration and cell proliferation. The first term on the right-hand side, $\nabla \cdot (D \nabla u)$, describes the invasion of tumor cells as a diffusive flux along the concentration gradient (Fick's diffusion). This process is characterized by the diffusion tensor D. The second term in the equation, $R(u,t)$, describes the cell proliferation, of tumor cells as a function of the current cell concentration. Common population growth equations for this reaction term are exponential, logistic, and Gompertzian. Exponential growth models use $R(u,t) = \rho \cdot u$ and are valid for low tumor cell concentrations, with ρ being the proliferation rate that determines cell doubling. Logistic and Gompertian reaction terms represent self-limiting growth, with $R(u,t) = \rho \cdot u \cdot (1-u)$ and $R(u,t) = \rho \cdot u \ln(1/u)$, respectively. In addition to the functional description on tumor cell evolution governed by Equation 2.1, there are no-flux boundary conditions such as

$$\eta \cdot (D \nabla u) = 0 \tag{2.2}$$

that introduces additional structural information on the patient-specific shape and geometry of the brain. These boundary conditions consider that tumor cells will only migrate within white and gray matter tissues along normal directions η of boundaries to other tissues. Tissue boundaries are derived from a preceding tissue segmentation in a patient-specific manner.

An early study proposing to use a reaction-diffusion framework for modeling tumor growth in patients with gliomas was Cruywagen et al. [1995]. They included the effect of treatment as another, negative reaction term $R(u,t)$ in Equation 2.1. In this model the invasion of tumor cells was assumed to be isotropic, following a homogeneous diffusion, i.e., with D being a global tensor value. In a subsequent study, and motivated by the experimental results of Giese et al. [1996], Swanson et al. [2000] proposed to improve on this model by assuming nonhomogeneous diffusion. To consider the differential motility of tumor cells in gray and white matter, they replaced the diffusivity constant D by an isotropic but nonhomogeneous diffusion coefficient $D(x)$ that took different values depending the location of x. For x in white matter $D(x) = d_w I$ and for x in gray matter

$D(x) = d_g I$. I is a 3x3 identity matrix, and d_w and d_g are scalar coefficients, where $d_w > d_g$ acknowledges the observation that tumor cells move faster in white matter. Extending the idea of Swanson et al. [2000], and refining on the differential motility of tumor cells in different tissues, Clatz et al. [2005] and later Jbabdi et al. [2005] proposed to use anisotropy to model the invasion mechanism of tumor cells. They modeled the diffusivity of tumor cells through an anisotropic-nonhomogeneous diffusion. The assumption they made is that tumor cells not only move faster in white matter, but also follow the white matter fiber tracts in the brain. This idea followed the observation that tumor cells tend to follow the preferred directions of water diffusion, which can be measured using magnetic resonance diffusion tensor imaging (MR-DTI). These models were able to consider the resulting anisotropy in white matter diffusion and to capture the "spiky" and fingering patterns of tumors observed in the images. Both authors evaluate their models qualitatively by comparing visible tumors in the magnetic resonance images with the ones simulated with the model.

The Fisher Kolmogorov (FK) Model: The Fisher Kolmogorov (FK) equation is a type of reaction-diffusion model, which has been used extensively in tumor growth modeling [Tracqui et al., 1995a; Murray, 2002; Swanson et al., 2007; Clatz et al., 2005; Jbabdi et al., 2005; Konukoglu et al., 2009; Menze et al., 2011a; Gooya et al., 2011a; Hogea et al., 2008; Stretton et al., 2013, 2012]. In this thesis, we use the following formulation:

$$\frac{\partial u}{\partial t} = \underbrace{\nabla \cdot (D(\mathbf{x})\nabla u)}_{\text{Diffusion Term}} + \underbrace{\rho \cdot u \cdot (1-u)}_{\text{Logistic Reaction Term}} \quad ; \quad \underbrace{\eta_{\partial\omega} \cdot (D\nabla u) = 0}_{\text{Boundary Condition}}, \tag{2.3}$$

where u is the tumor cell density, D is the diffusion tensor, ρ is the proliferation rate, and $\eta_{\partial\omega}$ are the normal directions to the boundaries of the brain surface. We used the tensor construction method, proposed by Clatz et al. [Clatz et al., 2005], which uses global scaling on the DTI,

$$D(\mathbf{x}) = \begin{cases} d_g I & \text{if } \mathbf{x} \text{ is in gray matter} \\ d_w D_{water} & \text{if } \mathbf{x} \text{ is in white matter,} \end{cases} \tag{2.4}$$

where $D(\mathbf{x})$ is the inhomogeneous diffusion term, which takes into account that tumor cells move faster along anisotropic white matter fiber tracts, estimated by $d_w D_{water}$, than in isotropic gray matter $d_g I$. D_{water} is the normalized water diffusion tensor in the brain measured by the DTI. D_{water} is normalized so that the largest eigenvalue in white matter is one. In Figure 2.8, we show how different values of d_w significantly change the diffusion tensor (depicted as ellipsoids) in

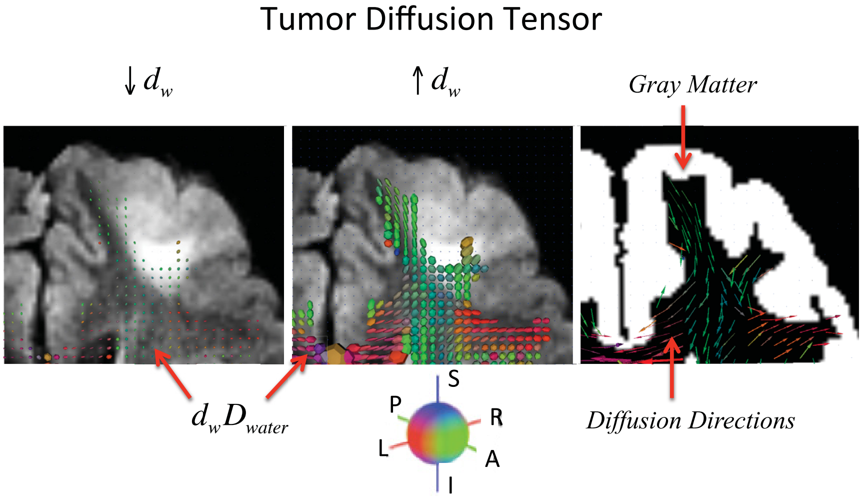

Figure 2.8: Tumor Diffusion Tensor. The first two images depict using ellipsoids the diffusivity tensor $d_w D_{water}$ for two different values of d_w overlaid on a FLAIR MRI. The third image shows with arrows the diffusion directions in white matter.

white matter. The use of a different tensor construction method would have an impact on the shape of the DTI tensors that the model uses to define the direction of tumor diffusion. Therefore, the predicted tumor shape would be slightly different if another tensor construction method is used.

The Eikonal Approximation of the FK Model: Even though the FK model in Equation 2.3 is well suited in predicting tumor cell density concentrations in the brain, it is computationally very expensive for 3D simulations. Then, we show an approximation of this reaction-diffusion model by a traveling time formulation [Konukoglu, 2009] which we use to estimate the proliferation and diffusivity parameters of the model by minimizing the mismatch between a simulated tumor and a real one extracted from MRIs. As presented in [Konukoglu, 2009] we can approximate the reaction-diffusion model in Equation 2.3 by considering that for large times the FK model with constant coefficients admits a traveling wave solution in the infinite cylinder. In other words, when the change of u occurs in only one direction, $\mathbf{n}$, for extremely large times the solution of Equation 2.3 can be formulated as

$$u(x,t) = u(\mathbf{n}\cdot x - vt) = u(\zeta) \quad as \quad t \to \infty, \tag{2.5}$$

where v is the asymptotic speed of the wave front and $\zeta = (\mathbf{n}\cdot x - vt)$ is the moving frame of the traveling wave. Then, by substituting Equation 2.5 into Equation 2.3 and considering a constant diffusion tensor we get

$$\mathbf{n}'D\mathbf{n}\frac{d^2u}{d\zeta^2} + v\frac{du}{d\zeta} + \rho u(1-u) = 0, \tag{2.6}$$

which is a non-linear ordinary differential equation. In order to have admissible solutions, the asymptotic speed v should depend on the diffusion tensor D, ρ, and on the shape of the initial condition $u(x,0)$. When the initial condition has a compact support the asymptotic speed of the traveling wave can be given as, [Murray, 2002],

$$v = 2\sqrt{\rho\mathbf{n}'D\mathbf{n}}. \tag{2.7}$$

However, there exist a transient behavior for the traveling wave speed while it converges to the asymptotic speed in Equation 2.7. Ebert et al. studied this convergence behavior and derived in [Ebert and van Saarloos, 2000] the following analytical time-dependent representation of the traveling wave speed:

$$v(t) = \sqrt{\mathbf{n}'D\mathbf{n}}\frac{4t\rho - 3}{2t\sqrt{\rho}}. \tag{2.8}$$

Now we can formulate the traveling time formulation for the tumor delineation. Based on the concepts described in [Sethian, 1999], $v(t)$ can be characterized as

$$|\nabla T| = \frac{1}{v(t)} = \left(2\sqrt{\rho\mathbf{n}'D\mathbf{n}} - \frac{3}{2T}\sqrt{\frac{\mathbf{n}'D\mathbf{n}}{\rho}}\right)^{-1}, \tag{2.9}$$

where T is an implicit time function such that it embeds the locations of the tumor delineation as iso-time surfaces ($T(x)$ is the function described as the time when the tumor delineation passes over the point x). Thus, $\mathbf{n}$ can be written as $\nabla T/|\nabla T|$ resulting in the traveling wave formulation as

$$\sqrt{\nabla T^T D \nabla T} = \frac{2\sqrt{\rho}T}{4\rho T - 3}, \tag{2.10}$$

where the equation has the Eikonal form ($F\sqrt{\nabla T^T D\nabla T} = 1$ with F being a general speed function). This equation by itself solely gives the relation of consecutive iso-time surfaces of T. In order to construct the solution everywhere in the domain we require a Dirichlet type boundary condition, i.e., an initial surface for which we know the T value. For the tumor growth modeling case, this surface is given by the tumor delineation in the first image, i.e.,

$$T(x) = T_1 \quad \forall x \in \Gamma_1, \tag{2.11}$$

where Γ_1 is the tumor delineation established in the first image and T_1 is the time from the origination of the tumor to the acquisition of the first image. For the asymptotic case, the traveling time formulation is given by

$$2\sqrt{\nabla T^T \rho D \nabla T} = 1. \tag{2.12}$$

Notice from Equation 2.12 that T_1 is not needed for the asymptotic case and that ρ and D appear in the product form and cannot be separated. The formulation given in equations 2.10, and 2.11 is valid in the infinite cylinder where the evolution is in one direction (in this situation, the traveling wave is a plane). In the case of tumor growth, the delineation is curved and consequently its evolution is not analogous to an evolution in the infinite cylinder. We can still implement the formulation obtained in the infinite cylinder to more general cases in 3D by assuming that within a voxel, the tumor delineation is planar and the model coefficients are constant. Then by starting from the initial tumor delineation and sweeping the domain outwards we can construct the solution. Still, such a generalization does not consider the effect of curvature in the more general evolutions. Following the derivations of Keener and Sneyd [1998], Konukoglu [2009] proposed the following Eikonal equation to describe the evolution of a tumor delineation in 3D:

$$\left(\frac{4\rho T - 3}{2\sqrt{\rho T}} - \nabla \cdot \frac{D\nabla T}{\sqrt{\nabla T^T D \nabla T}}\right)\sqrt{\nabla T^T D \nabla T} = 1, \tag{2.13}$$

where $\nabla \cdot (D\nabla T / \sqrt{\nabla T^T D \nabla T})$ is the effect of the curvature. In the derivation of Equation 2.13 it is assumed that the surface is slightly curved, which requires the effect of the curvature to be of a lower order than the term $2\sqrt{\rho}$. However, the value of the curvature might be higher in the general case due to the presence of anisotropy in the diffusion process. Therefore, one needs to saturate the effect of curvature to satisfy this assumption. Thus, adding saturation to the curvature effect in Equation 2.13 we obtain the final formulation, which describes the evolution of the tumor delineation in 3D based on the reaction-diffusion formalism:

$$\left(\frac{4\rho T - 3}{2\sqrt{\rho T}} - 0.3\sqrt{\rho}(1 - e^{-|K_{eff}|/0.3\sqrt{\rho}})\right)\sqrt{\nabla T^T D \nabla T} = 1, \tag{2.14}$$

$$K_{eff} = \nabla \cdot \frac{D\nabla T}{\sqrt{\nabla T^T D \nabla T}}, \tag{2.15}$$

$$T(x) = T_1 \quad \forall x \in \Gamma_1, \tag{2.16}$$

Notice that Equation 2.14 can become negative for low values of T due to the fact that the approximation for the time convergence and curvature effects get worse for lower T values [Ebert and van Saarloos, 2000]. In order to overcome this approximation error, Konukoglu [2009] prevented the speed function in Equation 2.14 to drop lower than $0.1\sqrt{\rho}$, i.e.,

$$\frac{4\rho T - 3}{2\sqrt{\rho}T} - 0.3\sqrt{\rho}(1 - e^{-1|K_{eff}|/0.3\sqrt{\rho}}) \geq 0.1\sqrt{\rho}, \tag{2.17}$$

which serves as the minimum threshold for the speed of the tumor. In terms of the speed of progression of the tumor deliniation, this limit can be written as

$$v_{min} = 0.1\sqrt{\rho \mathbf{n}^T D \mathbf{n}}, \tag{2.18}$$

where $\mathbf{n}$ in the direction of the vector ∇T. As a result of this constraint we have a growing tumor delineation at all times, consistent with the reaction-diffusion model.

The Parameter Estimation Problem for the FK Model: For estimating the parameters of the FK model for a given patient Konukoglu [2009] proposed to use the Eikonal approximation in equations 2.14, 2.15, and 2.16 together with two MRIs with tumor delineations at two different time points, a DTI, and a white matter segmentation. Consider T_1 and T_2 to be the times from the origin of the tumor to the acquisition of the first and second MRIs respectively, $\Delta T = T_2 - T_1$ to be the time between the MRIs, and Γ_1 and Γ_2 to be the real tumor delineations extracted from these MRIs at times T_1 and T_2 respectively. Thus, the parameter estimation problem was defined by Konukoglu [2009] as follows:

$$\arg \min_{d_w, d_g, \rho, T_1} C = \text{dist}(\Gamma_2, \overline{\Gamma_2})^2 + (v_{min}|T_{min} - T_1|)^2, \tag{2.19}$$

where $\overline{\Gamma_2} = \{x | T(x) = T_1 + \Delta T\}$ is the simulated tumor delineation at T_2 using equations 2.14, 2.15, and 2.16. dist() is the symmetric distance between two surfaces normalized by the surface area. The second term of Equation 2.19 penalizes $|T_{min} - T_1|$, where T_{min} is calculated by running the traveling time formulation backwards in time with Γ_1 as an initial condition until the simulated delineation collapses to a single point, which coincides with time zero (origin of the tumor). As a result of this, in the minimization problem above, T_{min} shall be equal to T_1 in order for the estimated parameters to be consistent with the size of Γ_1. v_{min} (the minimum allowable speed) is used to have consistent units in the cost function of Equation 2.19 and defined by

$$v_{min} = 0.1\sqrt{\rho \mathbf{n}'_{max} D(x_{min}) \mathbf{n}_{max}}, \tag{2.20}$$

at point x_{min}, where 0.1 is the limiting factor (minimum threshold for the speed of the tumor) and $\mathbf{n}_{max}$ is the principal eigenvector of $D(x_{min})$ yielding the maximum diffusion rate.

Konukoglu [2009] chose to use the unconstrained optimization method proposed by Powell [2002] to solve Equation 2.19 and the Fast Marching method for Eikonal equations in [Sethian, 1999] modified for anisotropy to solve equations 2.14, 2.15, and 2.16.

Infiltration Map Calculation: To perform simulations with the FK model in Equation 2.3 we need the tumor cell density distribution in the brain. However, MR images can only visualize tumors where cancerous cells are dense enough, masking the low density infiltration. A common approach to overcome this problem is to take a constant margin around the visible boundary of a tumor. This approach does not consider differential motility of tumor cells in white and gray matter. Konukoglu [2009] proposed a new formulation based on the reaction-diffusion FK model in Equation 2.3 to estimate tumor cell density distribution beyond the visible part in an image. For this formulation, Konukoglu considered the traveling wave approximation of the reaction-diffusion equation given by Equation 2.6 and assumed that at a moving frame point ζ^* the value of the tumor cell density $u = u^*$ is known (this corresponds to having the delineation of a tumor and assuming it corresponds to an iso-density surface). Then, by linearizing Equation 2.6 around ζ^* and u^* we get the following linear ODE:

$$\mathbf{n}'D\mathbf{n}\frac{d^2u}{d\zeta^2} + 2\sqrt{\rho\mathbf{n}'D\mathbf{n}}\frac{du}{d\zeta} + \rho(1-2u^*)u = 0, \tag{2.21}$$

which has the following analytical solution:

$$u(\zeta) = Ae^{-\sqrt{\frac{\rho}{\mathbf{n}'D\mathbf{n}}}(1-\sqrt{2u^*})\zeta} + Be^{-\sqrt{\frac{\rho}{\mathbf{n}'D\mathbf{n}}}(1+\sqrt{2u^*})\zeta}. \tag{2.22}$$

Notice from Equation 2.22 that the slope of the tumor cell density distribution depends on the ratio between the proliferation and the diffusion rate ($\sqrt{\frac{\rho}{\mathbf{n}'D\mathbf{n}}}$). Konukoglu et al. [2010a] extended the solution in Equation 2.22 to 3D obtaining a static Hamilton-Jacobi equation, which constructs an approximation of the low density infiltration of a tumor. Figure 2.9 shows the tail infiltration extents. This method produces tumor tail estimation values outside the segmentation of a tumor range from zero to tumor threshold of visibility (0.2 in this thesis). Konukoglu et al. [2010a] proposed a constant cell density threshold of visibility inside the contours of the tumor in order to not over estimate the size of a tumor. Notice that as d_w/ρ gets larger, the tumor becomes more infiltrative.

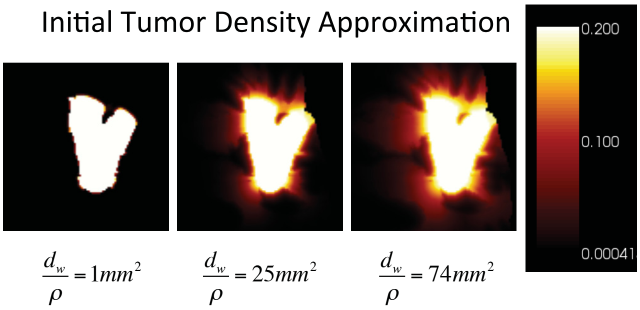

Figure 2.9: The tail extrapolation estimates the invisible tumor tail based on FK model parameters d_w and ρ. The simulated tumor has maximum tumor cell density value 1 and the model depicts the tumor cell density out to 0.001. One can see the differences in tumor infiltration based on the ratio d_w/ρ.

Joint Invasion and Displacement Models: Few approaches consider the invasion of tumor cells or tissue water ("edema"), and the displacement of the tissue resulting from the mass effect at the same time.

When introducing anisotropic nonhomogeneous diffusion for modeling tumor cell invasion in [Clatz et al., 2005], Clatz et al. also considered tissue deformation due to bulk tumor growth. In their model, brain tissue is modeled as a linear viscoelastic material in a static equilibrium. Local pressure is caused by the mass effect both from tumor growth and the invasive process. With this model, they were able to simulate invasion and mass effect simultaneously.

Hogea et al. [2008] used an optimal control framework to model the brain tissue as a piecewise linearly elastic material. The mass effect of tumor bulk and its infiltration are captured by a reaction-diffusion-advection model. Diffusion is isotropic as in [Cruywagen et al., 1995]. The mechanical coupling is via the pressure field, which is a parameterized function of the tumor cell density. The displacement is considered by complementing Equation 2.1 with an advection term:

$$\frac{\partial u}{\partial t} = \nabla \cdot (D \nabla u) + \nabla (u\mathbf{v}) + \mathbf{R}(\mathbf{u}, \mathbf{t}), \tag{2.23}$$

with tumor cell drift $\mathbf{v}$. They also propose an adjoint-based, PDE-constrained optimization formulation for estimating model parameters from displacements visible in standard magnetic resonance images. They put forward two different objective functionals, matching the spatiotemporal evolution of the normalized tumor density $u(x,t)$ and landmark registration. Hogea conducted 1D experiments to show, for solving the optimization problem, the advantages of estimating the gradient of the objective functional in terms of the adjoints. The advantages are that there is only one solution required of the adjoint system (per optimization iteration) despite the number of inversion variables, and good scalability with regards to the number of control variables.

Liu et al. [2014] also proposed a reaction-diffusion-advection model, which used multimodal imaging data including dual-phase CT and FDG-PET. Their proposed model is capable of integrating cancerous cell proliferation, infiltration, metabolic rate, and extracellular matrix biomechanical response. They formalized their inverse problem as a constrained optimization problem, using coupled PDEs, to estimate the patient specific model parameters by fitting the model to the observation. Finally, the optimal system is derived and solved by the Finite Difference Method.

Modeling the Response to Therapy: A practical application to in silico modeling is modeling glioma response to therapy, such as resection, chemotherapy, drug delivery, and radiotherapy.

Generally, shortly after diagnosis, HGG are resected. LGG may or may not be resected as a first order of treatment depending on the aggressiveness of the approach of the treating physician. Woodward et al. [1996] was among the first to model various extents of surgical resection regrowth on a virtual human brain. Later, in a post mortem study, Swanson et al. [2007] investigated the effectiveness of using different types of brain resections. However, their model was limited to personalization using patient T1-gadolinium and T2 MRIs, without taking into account the anisotropy in white matter fiber tracts visible in DTIs. In addition, they ran their simulations on virtual controls instead of on patient data. Primarily, their model did not estimate the tumors infiltration after the resection. Estimating tumor infiltration is important since gliomas often reoccur and it is important for a clinician to be able to assess if a tumor is bulky or diffuse. If a tumor is bulky, a second resection or radiotherapy would be recommended, but if a tumor is diffuse, chemotherapy would be the optimal treatment.

Tracqui et al. [1995b] and Swanson et al. [2002] proposed simple approaches not for considering when to administer therapy, but for considering the effects of therapy by using an additional reaction term in Equation 2.1. The extra term of Tracqui in the 2D model was c(x,t), at location x and time t, which characterized a tumor's sensitivity to various chemotherapy regimes. The patient had five cycles of six drugs for treatments that were given over 15 days and repeated every 6-8 weeks (6-thioguanine, procarbazine, dibromodulcitol, CCNN, 5-fluorouracil, and hydroxyurea), and two cycles of cisplatin and neutron beam irradiation. Tracqui et al. used a optimization algorithm which minimized the error between simulated tumor area and glioma area on CT to establish the best fit of the model's six unknown parameters (two of them being cell-diffusion coefficients and proliferation rate). Good agreement with clinical data was shown and Tracqui et al. showed that the emergence of a chemo-resistant tumor subpopulation was capable of causing treatment failure, which could appear at a later stage during chemotherapy.

Swanson et al. [2002] included the effect of chemotherapy by using a negative reaction term $R(u, t, x)$ in Equation 2.1, which is a function of both time and space, considering the time of drug delivery and the possible spatial heterogeneity of the drug efficacy. Notice that by using this model they considered the different growth speeds in white and gray matter. They hypothesized that this heterogeneity may have an effect on chemotherapy delivery, affecting the efficiency of treatment. They considered that glioma cell motility is higher in white matter and that gray matter is more vascularized than white matter. This lead to their assumption that glioma cells would stay in gray matter areas for longer times, consequently being exposed to higher levels of chemotherapy for longer. Swanson et al. tested this model using images of a high-grade glioma patient, whose tumor was located in the fronto-parietal region of the brain. This work showed that for this patient, who was treated with the receptor tyrosine kinase inhibitor imatinib mesylate, the gray matter part of the tumor was most likely more reachable by chemotherapy than the white matter areas. More importantly, Swanson et al. showed that even though the total number of glioma cells had decreased, the extent of invasion was not affected due to the mobility of tumor cells within the white matter.

Ribba et al. [2012] developed a model of tumor growth inhibition that successfully describes the time course of tumor size, which was measured as mean tumor diameter (MTD), in patients with LGGs treated with chemotherapy or radiotherapy. Their model does not use PDEs (no diffusion), but instead uses ODEs and is able to predict the time of recurrence of tumors of patients under chemotherapy. They used the longitudinal MTD data from 21 patients treated with first-line procarbazine, 1-(2-chloroethyl)-3-cyclohexyl-l-nitrosourea, and vincristine (PCV) chemotherapy to develop a model that incorporated tumor-specific and treatment-related parameters that reflected the response of proliferative and quiescent tumor tissue to treatment. The model was then employed to analyze the longitudinal tumor size data in 24 patients treated with first-line temozolomide (TMZ) chemotherapy and in 25 patients treated with first-line radiotherapy. The model successfully described the MTD dynamics of LGG before, during, and after PCV chemotherapy as well as successfully described the MTD dynamics in LGG patients treated with TMZ chemotherapy or radiotherapy. These preliminary results indicate that their proposed model can predict treatment response on the basis of pretreatment tumor size data.

Chakrabarty and Hanson [2005] proposed an approach of optimizing drug delivery to brain tumors through an optimal control framed problem by estimating distributed parameters. Chakrabarty's goal was to minimize these tumor functionals with respect to the drug input rate, also considering physical restriction on the amount and costs of drugs that can be administered. This results in a coupled system of equations with a forward state equation and a backward co-state equation that are solved using a modified double-shot, forward-backward method. They proposed an algorithm to decide the optimal drug delivery using an optimal distribution of the drug about the initial tumor location, and they tested their model in 1D.

Unkelbach et al. [2014] also used a reaction-diffusion type model for the improvement and automation of target volume delineation for glioblastoma. The motivation of this work was that in current clinical practice a uniform margin of about two centimetres is usually applied to account for tumor cell infiltration that cannot be seen in imaging. Their model takes into account spatial growth patterns of gliomas (heterogeneous tissue and anisotropic in white matter growth) and anatomical barriers. They present a case study of a HGG located close to the falx. The authors conclude that this approach is useful for tumors located close to the falx and the corpus callosum. Also, that the key input to the model was an accurate segmentation of the brain parenchyma, in particular the anatomical barriers falx cerebri and tentorium cerebelli. In a later chapter, we propose a method to register a neurosurgeon segmented brain segmentation that accounts for all of the brain anatomical barriers, which was highlighted as critical in the work of Unkelbach et al. [2014].

2.3.3.2 Coupled Bio-mechanical Models of Tissue Displacement

The reaction-diffusion formalism, equations 2.1 and 2.2, models tumor growth as a reactive flow into a porous medium – with reactive tumor cells migrating into the surrounding, sponge-like tissues. In this model, tumor cells replace or transform healthy tissue, and the "mass effect" of newly generated cells are neglected. Bio-mechanical models explicitly consider this mass effect by modeling the interaction between a tumor and its surroundings, and the displacement of the healthy tissue resulting from it. These models consist of two formal components: the tumor growth and the mechanical characteristics of the whole brain. Approaches have to make strong assumptions on the bio-mechanical properties of the brain, in particular on the elasticity and viscosity of the tissue, and the character of the mechanical coupling. A particular difficulty is in estimating parameters of the model from image information.

Wasserman and Acharya [1996] modeled brain tissue as a linear elastic material. The stress-strain relations are modeled by the generalized Hooke's law, and the amount of strain imposed on the tissue is proportional to the density of the tissue. For tumor growth, they assume an exponential growth rate, i.e., a constant cell doubling increase. They couple tumor and tissue model by assuming that pressure will be proportional to the volume of the neoplastic tissue.

Kyriacou et al. [1999] improved on this by modeling brain tissue as an incompressible, hyper-elastic neo-Hookean material. Tumor growth is also modeled as an exponential process imposing the same strain as in [Wasserman and Acharya, 1996]. They consider complex boundary conditions, and use their model to register patients with tumor-induced deformation to standard tissue atlases.

Mohamed and Davatzikos [Mohamed and Davatzikos, 2005] propose to model the brain tissue as an isotropic and homogeneous hyper-elastic material. They assume an exponential tumor growth, considering the mass effect caused by the edema surrounding the tumor. Pressure induced on the tissue by the tumor and edema is proportional to the added volume. In [Hogea et al., 2006], Hogea et al. reformulated the model with a level-set-based approach for the evolving tumor aiming at a more efficient method. They point out the use of patient-specific models with parameters estimated by solving an inverse problem.

Gevertz et al. [2008] incorporated the impact that organ-imposed physical confinement and heterogeneity have on the tumor into their computational model. They show that models need to have organ geometry and topology in order to draw correct conclusions about tumor spread, shape, and size. They also show that the impact that confinement has on the tumor growth is greater when the tumor is growing close to the confining boundary. They conclude that tumor models must consider shape, structure of the organ, and location of tumor within the organ to accurately predict the tumors growth dynamics.

2.3.4 Registration and Segmentation in Tumor Modeling

A major field in medical image processing is three-dimensional segmentation for localizing and quantitatively measuring anatomical structures of particular interest. The accurate segmentation of normal and tumorous tissues is also of crucial importance in personalizing tumor growth models. Here, generative models for both physiology and image appearance of tumors may serve the purpose of providing realistic, “ground truth” data sets to evaluate segmentation approaches.

Many tools for image segmentation have evolved around registration methods. Consequently, tumor models have been used repeatedly to address problems such as atlas-to-patient registration and segmentation in the presence of a lesion. In these cases pathological changes require standard atlases to use non-linear registration (see Section 2.2.2 Brain atlases), and using an appropriate tumor modeling framework allows one to adapt generative image models with respect to tissue displacements resulting from tumor growth. This increases the accuracy of image registration in the presence of extensive lesions.

Generative Tumor Models in Image Segmentation: Manual tumor segmentations show a high variability between raters. Different approaches may be used to infer a single, accurate segmentation from multiple tumor outlines [Kaster et al., 2010]. This problem multiplies when multi-modal imaging sequences are used and different tumor-induced changes become visible in the different modalities, demanding for robust automated segmentation approaches. Examples for such approaches are the level set-based segmentation by Riklin-Raviv et al. [2009, 2010] using a latent atlas prior for modeling the lesion (Figure 2.7), or the generative probabilistic model of both brain tissues and tumor segments by Menze et al., amending the standard EM segmentation with a similar prior to obtain tissue segmentations of both the healthy brain and the tumor outlines for every modality at the same time [Menze et al., 2010]. Accurately segmenting tumors in different modalities, however, remains a difficult task due to the high variability of tumor location, shape, and image texture. Tumor growth modeling can be used to synthetically generate both realistic tumor images, for different tumor types, tumor locations, in different modalities, and to provide quantitative "ground truth" segmentations for evaluating different tumor segmentation strategies, as in Kaster et al. [2010]. Warfield et al. [2004] also proposed a method to assess the performance of automated image segmentation algorithm by a direct comparison of human rater and algorithm performance.

Generating realistic appearing images has two components: it requires a model of the tumor growth process, and an image appearance model describing the effect of tumor growth on the image appearance, i.e., if and how tumor cells infiltrate the surrounding tissues, and if and how actively proliferating areas, edema, and necrosis change the observed MR signal intensities.

Rexilius et al. [2004] reports one of the first approaches for such a synthetic image data generation. They use a basic tumor model with three compartments: the active tumor, the necrotic tumor core, and the edema in the surrounding tissue. The active tumor is manually drawn on the MR image of a healthy subject. A radial displacement model is adapted to fit its size and model the resulting displacement of the surrounding tissue, assuming linear elastic material properties for gray and white matter. The image intensities in the active and necrotic regions are modeled as Gaussian mixtures with predefined average and variance. Edema is modeled in the white matter with the intensity fading with increasing distance to the active tumor.

An approach for realistic MR images using a more sophisticated tumor growth model and an improved image appearance model has been developed by Prastawa et al. [2005]. It is based on the tumor growth model by Clatz et al. [2005] with extensions considering the displacement and destruction of white matter fibers in DTI-MRI, motivated by observations of Lu et al. [2003]. They also model the dynamics of the contrast agent, its high-contrast accumulation in the cerebrospinal fluid, and in the active tumor regions. For edema and active tumor regions, the image appearance is modified using characteristic image textures.

Geremia et al. [2013] proposed a new image generation method, where they propose to use a detailed tumor growth model to synthesize labeled images that can then be used to train an efficient data-driven machine learning tumor predictor. Their MR image synthesis step produces images with both healthy tissues and various tumoral tissue types. Their method used a large synthetic dataset of 740 simulated cases for training and evaluation. In addition, they performed a quantitative evaluation on 14 clinical cases diagnosed with LGGs, where the method demonstrated tissue class accuracy comparable with the state-of-the-art, is computationally more efficient, and has the ability to estimate tumor cell density as a latent variable underlying the multimodal image observations.

It should also be mentioned that there is a public database of tumor images and a MICCAI challenge that used this database. Menze et al. [2014] reports the set-up and results of the Multimodal Brain Tumor Image Segmentation (BRATS) benchmark that was arranged together with the MICCAI 2012 and 2013 conferences. Twenty state-of-the-art tumor segmentation algorithms were applied to a set of 65 multi-contrast MR scans of low- and high-grade glioma patients, which were manually annotated by up to four raters, and to 65 similar scans created using tumor simulation software. This study showed a considerable disagreement between the human raters in segmenting various tumor sub-regions (Dice scores in the range 74-85%), demonstrating the difficulty of this task. Menze et al. [2014] found that different algorithms worked best for different sub-regions (reaching performance comparable to human inter-rater variability), but that no single algorithm ranked in the top for all sub-regions concurrently.

Despite the effort to create automatic tumor segmentations, these segmentations are not satisfactory enough to be used in a clinical setting yet, or in tumor growth modeling. Over the next decade, tumor segmentation algorithms will improve and open doors to new ways of working for both clinicians, but also medical image processors.

Generative Tumor Models in Image Registration: The registration of a patient's MRI with a large lesion to an anatomical atlas is a difficult task. An essential idea in this process, essential for example in the task of tissue segmentation, is to separate standard inter-subject variation of brain anatomy – captured in anatomical atlases, i.e., priors on the spatial distribution of the brain tissues – from the patient-specific, tumor-induced deformations.

Kyriacou et al. [1999] proposed a pipeline for correcting tumor-induced modifications of the normal anatomy. They simulate the resection of the tumor allowing images to be registered to a standard atlas and obtain a "tumor-free" image of the patient in a first step. Using these tumor-free images together with the real observations, they estimate parameters of a simple tumor growth model in a second step. The mass effect of the optimal tumor model is then used to modify the standard atlas, and to perform the final atlas-to-patient registration with subsequent segmentation.

Bach Cuadra et al. [2004] proposed an approach requiring manual user interaction for identifying landmarks in the atlas and patient images. The tumor is modeled as a radial displacement on surrounding structures. The resulting displacement field is considered in a non-linear registration using the “demons” registration algorithm.

Mohamed et al. [2006] took a statistical approach jointly modeling normal and tumor-induced variation. They extend the idea of using atlases for variability between healthy subjects. They suggest decomposing the deformation field from a non-linear registration into the natural variability between healthy subjects and the tissue displacements resulting from tumor growth. The formation fields of the normal brain are estimated from healthy subjects. Tumor growth is simulated by generating a space of displacement fields that results in tumor variation. The simulated tumor varies over different growth parameters, location and observed extent of tumor and edema. Once the deformation field linking the atlas to the subject and tumor growth parameters is found, the atlas is registered and the tumor is grown in it. An extension has been proposed by Zacharaki et al. [2008].

Gooya et al. [2011a] proposed an approach to the problem of atlas registration of brain images with gliomas. They used multi-parametric imaging modalities for segmentations of various tissues, and then using supervised learning to compute the posterior probability map of membership to each tissue class. By modeling the tumor growth using the reaction-diffusion equation, similar maps were generated in the initially normal atlas. Deformable registration using a demons-like algorithm was used to register the patient images with the atlas having the tumor. Joint estimation of the simulated tumor parameters such as location, mass effect and degree of infiltration, and the spatial transformation was achieved by maximization of the log-likelihood of observation. An Expectation-Maximization (EM) algorithm was used in a registration procedure to approximate the spatial transformation and other parameters related to tumor simulation were optimized through Asynchronous Parallel Pattern Search.

Gooya et al. [2012] also proposed a generative approach for simultaneously registering a probabilistic atlas of a healthy population to brain MR scans showing glioma and segmenting the acquisition scans into tumor and healthy tissue labels. However, for this work, the method proposed does not require segmentations of both brain images to initialize the registration process and accounts for edema. The proposed method was based on the EM algorithm that incorporates a glioma growth model for atlas seeding, a process which modifies the original atlas into one with tumor and edema adjusted to optimally match a given set of patient images. The adjusted atlas is registered into the patient space and utilized for estimating the posterior probabilities of different tissue labels. EM iteratively improves the estimates of the posterior probabilities of tissue labels, the deformation field and the tumor growth model parameters.

Bauer et al. [2011] presented an automatic method to segment brain tissues from volumetric MRI brain tumor images. The method was based on non-rigid registration of an average atlas in combination with a biomechanically justified tumor growth model to simulate tumor induced soft-tissue deformations. The tumor growth model, which is formulated as a mesh-free Markov Random Field energy minimization problem, guarantees agreement between the atlas and the patient image, prior to the registration step. Their method was non-parametric, straightforward, and fast compared to other approaches with similar accuracy.

2.4 Perspectives and Further Directions

In this chapter we presented a general background on gliomas and on the state-of-the-art in tumor modeling. We pointed out studies of specific relevance in the design of these models. Most of the image-based approaches integrate image information into basic reaction-diffusion models, with or without coupling the tumor model and the displacement of the healthy tissues. These approaches are closely coupled to image registration and segmentation tasks. Major difficulties are in finding image descriptors that are consistent with the modeling framework – or, vice versa, a modeling framework that is consistent with the available image information – and in overcoming difficulties arising when approaches that showed to be useful in one or two-dimensional examples are generalized to real clinical image data in 3D.

Further directions may be in developing more complex models of tumor growth, modeling nutrient, oxygen, and metabolite levels in the tumor, considering further structural model components of brain anatomy, or phenomena at the microscopic scale. Imaging modalities providing richer information than tumor outlines, such as positron emission tomography (PET), magnetic resonance spectroscopic imaging (MRSI) [Menze et al., 2006], diffusion contrast-enhanced MRI [Kelm et al., 2009], functional-MRI (fMRI) [Langs et al., 2010], or other, even more specific molecular imaging modalities may serve as the basis for such model extensions. A large body of studies on personalized management of tumor therapy, potentially to be used for such model extensions, is available from the field of theoretical biology. Further work will be required to find straightforward approaches for assimilating 3D image information into the bio-physical framework of those models.

In the coming years, clinicians are expecting reliable tumor models and segmentation algorithms at any scale. The macro scale would be of great benefit to radiologists, oncologists, and neurosurgeons and if these models were image-based they would integrate well into these physicians current workflow. In order for these physicians to adopt these tools, they need to be confident that the models can produce accurate and repeatable results. This thesis is aimed at looking into some of the questions that are currently blocking tumor-based models from being used in treatment planning for glioma patients in clinics.

Chapter 3

Importance of Patient-Specific DTI to Modeling Glioma Growth using the Fisher Kolmogorov Traveling Time Formulation

Contents

Based on a conference paper with full proceedings published and orally presented at the 2013 ISBI conference [Stretton et al., 2013].

3.1 Context

Tumor growth models based on the Fisher Kolmogorov (FK) reaction-diffusion equation have shown convincing results in reproducing and predicting the invasion patterns of glioma brain tumors. Diffusion tensor images (DTIs) were suggested to model the anisotropic diffusion of tumor cells in the brain white matter. However, clinical patient-DTIs are expensive and often acquired with low resolution, which compromises the accuracy of the tumor growth models. In this work, we used the traveling time FK model formulation to describe the evolution of the visible boundary of the tumor and investigate the impact of replacing a patient-specific DTI by i) an isotropic diffusion map or ii) an anisotropic high-resolution DTI atlas formed by averaging multiple patient DTIs. We quantify the impact of replacing the patient-specific DTI using synthetic tumor growth simulations and tumor evolution predictions on a clinical case.

3.2 Introduction

Gliomas are a type of malignant brain tumor with fast infiltration along white matter fiber tracts. Modeling glioma growth is a complex task due to the infiltrative nature of this disease, which makes low concentrations of tumors unobservable in magnetic resonance images (MRIs). Several bio-physical computational models have been proposed for describing the diffusive growth of these tumors that cannot be completely seen in MRIs. Swanson et al. [Swanson et al., 2007] proposed the use of tissue-based tumor cell motility, where their model included different diffusivities in white and grey matter, but isotropic and homogeneous within each. To improve the realism of the model, Clatz et al. [Clatz et al., 2005], Jbabdi et al. [Jbabdi et al., 2005] constructed anisotropic non-homogeneous models within white matter based on patients DTIs. Unfortunately, patient specific DTIs are not widely available because of the added cost and time for acquisition. Patient DTIs are difficult to acquire in a clinical routine since acquiring them increases the total time a patient needs to stay inside a MRI machine, which is difficult for elderly persons. Therefore, if a patient DTI is acquired, it is usually of low quality (low-resolution and low signal-to-noise ratio) due to the limited number of diffusion gradients and repetitions acquired. Although there exist several sequences to accelerate DTI acquisitions, e.g., SENSE [Jaermann et al., 2004], they are not systematically used in a clinical setting. In addition, the white matter tracts on the patient DTIs are often disturbed inside the region of the tumor and close to the boundary causing the image to be incomplete. It is for this reason that Unkelbach et al. [2012] proposed to use Swanson's model without a DTI for radiotherapy planning. Alternatively, instead of relying on a patient-specific DTI ("Patient-DTI"), one may rely on an "Atlas-DTI", which is an average of 75 subject DTIs [Prastawa et al., 2009], or refrain from using a DTI at all ("No-DTI").

To date, there has been no analysis carried out to quantify whether the patient specific information on anisotropic tumor growth directions in Patient-DTIs gives invaluable information in terms of tumor growth prediction. Thus, in this work we provide a comparison among three modeling options to describe tumor diffusivity: using a Patient-DTI, Atlas-DTI, and No-DTI. We compare these three options and evaluate which method aids the traveling time FK model formulation (described by equations 2.14, 2.15, and 2.16) in providing the most accurate description of the tumor growth dynamics. This study also gives insight into whether the tumor growth has directional preference (anisotropic growth) as formulated in [Clatz et al., 2005; Jbabdi et al., 2005] or only obeys tissue based differential motility as proposed in [Swanson et al., 2007]. This question is crucial since most of the available patient data does not have patient specific DTIs. We quantify the impact of replacing the patient DTI using synthetic tumor growth simulations and tumor evolution predictions on a clinical case.

This chapter is organized as follows. In Section 3.3, we present three tumor diffusivity construction options (Patient-DTI, Atlas-DTI, and No-DTI) that we use within the traveling time FK model formulation to simulate tumor growth. In Section 3.4, we present the results of synthetic data experiments to determine the different simulated tumor contour shapes for the three diffusivity construction options. In Section 3.5, we show the results of an experiment on a clinical case to quantify which of the three diffusivity construction options provides the best tumor growth predictions. The discussion and conclusions are presented in Section 3.6.

3.3 Diffusivity Tensor Constructions

Different diffusivity tensor ($D(\mathbf{x})$ in Equation 2.3) constructions have been proposed in the past. Some researchers [Swanson et al., 2007; Unkelbach et al., 2012] have considered isotropic diffusivity and defined $D(\mathbf{x})$ as $d_g I$ if $\mathbf{x}$ is in gray matter and $d_w I$ if $\mathbf{x}$ is in white matter, where d_g and d_w are scalars ($d_g < d_w$) and I is a three by three identity matrix. This representation is used in this chapter for the No-DTI case, where the isotropic and homogeneous growth in white matter is guided by a white matter segmentation (obtained by non-linearly registering the MNI 152 atlas white matter segmentation to the patient images), see Figure 3.1(a). Other researchers [Clatz et al., 2005; Jbabdi et al., 2005; Menze et al., 2011b; Konukoglu et al., 2009; Stretton et al., 2012] have examined anisotropic diffusivity where $D(\mathbf{x})$ is $d_g I$ if $\mathbf{x}$ is in gray matter and $d_w D_{water}$ if $\mathbf{x}$ is in white matter, where D_{water} is the water diffusivity tensor obtained from a DTI normalized using the maximum eigenvalue in white matter [Clatz et al., 2005]. These D_{water} based DTIs are used for the Patient-DTI and Atlas-DTI cases. Even though Patient-DTIs represent better the patient's white matter structure, they also have the drawbacks of having less resolution and more noise. On the other hand, Atlas-DTIs are less noisy as a result of the averaging caused by using multiple patients [Prastawa et al., 2009]. Figure 3.1 shows a comparison between a Patient-DTI and an Atlas-DTI.

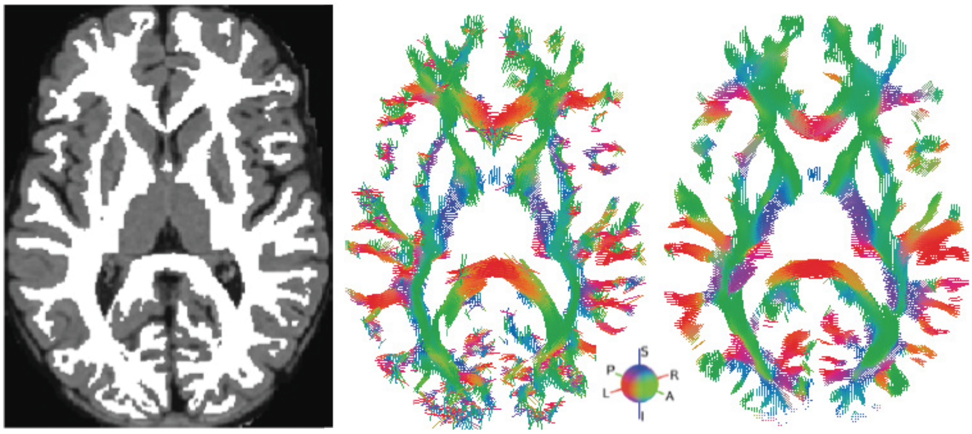

(a) White Matter Seg (b) Patient-DTI (c) Atlas-DTI

Figure 3.1: Diffusivity tensor constructions. The MNI 152 white matter segmentation, depicted overlaid on a FLAIR MRI, is used to model regions where a tumor grows isotropically for the No-DTI case (a). The Patient-DTI (b) and Atlas-DTI (c) show the water diffusion tensor directions that are used to model anisotropic tumor growth in white matter.

3.4 Synthetic Case

In this section we present the results of using the three diffusivity tensor options presented in Section 3.3 within the traveling time FK model formulation on synthetic data.

3.4.1 Data

Our synthetic dataset consisted of three images from a healthy subject: a $T1$ MRI, a FLAIR MRI, and a Patient-DTI. In addition, we used an anisotropic high-resolution DTI atlas formed by averaging DTIs of multiple patients, taken from [Prastawa et al., 2009]. We rigidly registered all the subject images to the Apparent Diffusion Coefficient (ADC) map of the Patient-DTI. To account for brain shape differences, the Atlas-DTI and the MNI 152 $T1$ were non-linearly registered to the Patient-DTI and to the registered patient $T1$ MRI respectively. The transformation of the registration of the MNI 152 $T1$ to the registered patient $T1$ MRI was applied on the MNI 152 white matter mask, which was de facto registered to the MNI 152 $T1$ [Fonov et al., 2009]. The FSL's FAST [Zhang et al., 2001] was used on the registered $T1$ image to find the brain parenchyma mask (BM).

3.4.2 Method

The traveling time FK model formulation (equations 2.14, 2.15, and 2.16) with the three different diffusivity tensors (Patient-DTI, Atlas-DTI, and No-DTI) was used to simulate 120 synthetically grown tumor evolutions from single voxels at randomly chosen locations. The method followed for each of these 120 simulations is shown graphically in Figure 3.2, where the inputs to the simulation are a white matter mask (WM), a brain parenchyma mask (BM), three types of diffusion tensor images (Patient-DTI, Atlas-DTI, and No-DTI), and the proliferation rate parameter ρ; the outputs include tumor delineations for the Patient-DTI (Γ_P), the Atlas-DTI (Γ_A), and the No-DTI (Γ_N) options. Notice that the speeds related to the three diffusivity tensors were not directly comparable since the Atlas- and Patient-DTIs had much lower diffusion values in areas that were anisotropic, but not the main directions of growth. Therefore, to provide a meaningful comparison, tumor growths were stopped when the tumor volumes for the Atlas-DTI and No-DTI options were the same as the ones obtained after a fixed day count for the Patient-DTI. Furthermore, out of the 120 synthetically grown tumor evolutions half were done using low resolution images ($1mm \times 1mm \times 3mm$) and the other half using high resolution images ($0.5mm \times 0.5mm \times 1.5mm$). Note that the low resolution images were still within American College of Radiology (ACR) guidelines [American College of Radiology, 2013], which states that the maximum slice thickness should be no greater than $5mm$ and an interslice gap should be no greater than $2.5mm$. In addition, for 120 tumor evolutions the FK model parameters ρ, d_w, and d_g were varied to account for different glioma grades (high grade glioma [HGG], low grade glioma [LGG], and very LGG). Table 3.1 shows the values employed, which were the same values used in the work of Konukoglu [2009].

3.4.3 Results

The results of the 120 synthetically grown tumor evolutions show that the shape of the tumor for LGG and very LGG is not too sensitive to the type of diffusivity tensor used; however, for HGG it was observed in some locations of the brain

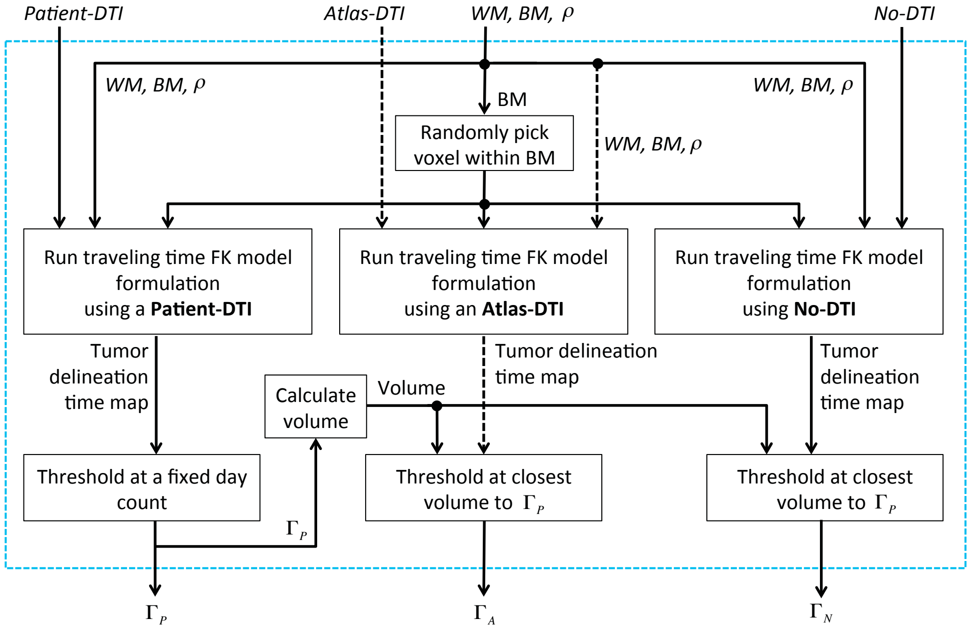

Figure 3.2: Synthetic experiments method. The inputs to the simulations are a white matter mask WM, a brain parenchyma mask BM, three types of diffusion tensor images (Patient-DTI, Atlas-DTI, and No-DTI), and the proliferation rate parameter ρ, while the outputs include tumor delineations for the Patient-DTI (Γ_P), the Atlas-DTI (Γ_A), and the No-DTI (Γ_N) options.

Table 3.1: Various Glioma Grades Parameters

Glioma Grade	d_w mm^2/day	d_g mm^2/day	ρ $1/day$
HGG	0.5	0.25	0.009
LGG	0.25	0.01	0.012
Very LGG	0.1	0.005	0.024

that the Patient- and Atlas-DTI had good agreement between them, but did not match the No-DTI case. Moreover, the resolution of the images seemed not to affect the result of the simulations significantly.

Figure 3.3 displays two synthetically grown tumors developed in the occipital lobes showing the differences in tumor growth patterns when the tumor contours were thresholded at similar volumes. We chose to display HGG simulation results since they show the most dramatic contour differences. Notice that similar tumor shapes for the three diffusivity tensor constructions resulted for either high- or low-resolution images.

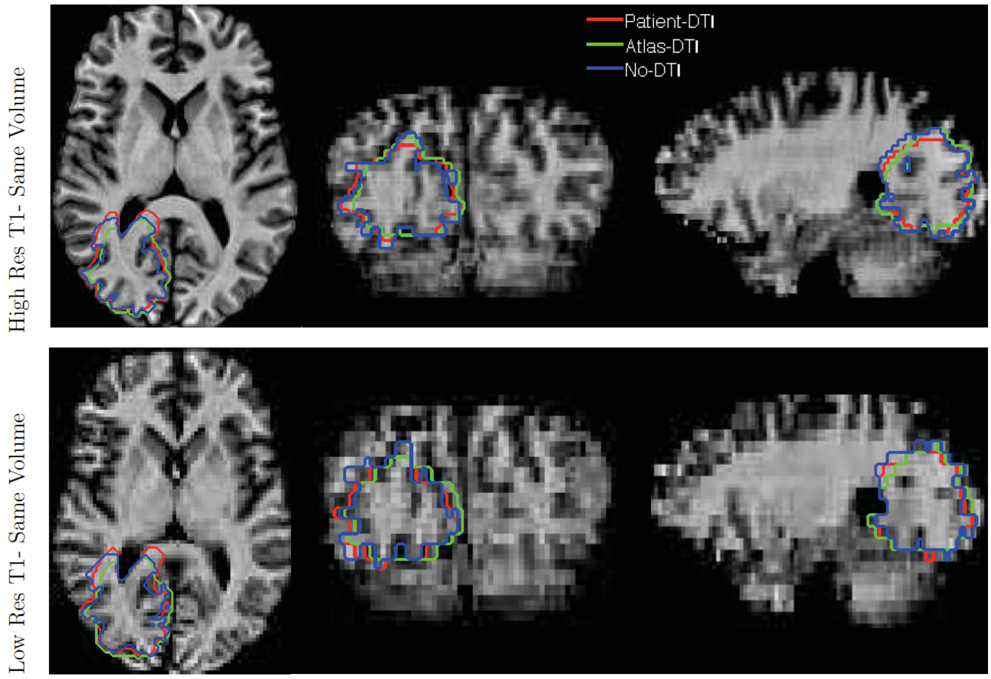

HGG in the right occipital lobe

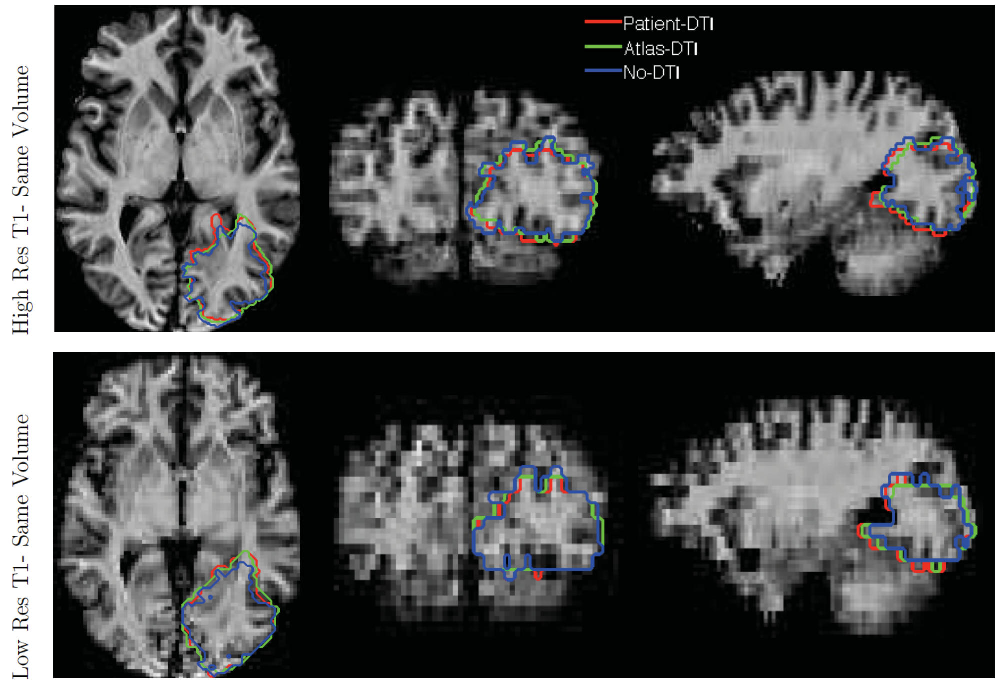

HGG in the left occipital lobe

Figure 3.3: High-resolution synthetically grown tumors overlaid on a registered T1 MRI. Displays the differences in tumor growth patterns when the tumor results are thresholded at similar volumes. Notice that similar tumor shapes between the high and low resolution images.

Figure 3.4 shows another two synthetic tumor cases: in the frontal lobe and in the corpus callosum. The shapes of the synthetic tumors look visibly similar for the results of the Patient- and Atlas-DTI cases due to the fact that both simulate anisotropic tumor growth in white matter where the speed of growth in each area is dictated by the non-homogeneity of the DTI. As expected, the directional non-homogeneity of the DTIs is slightly different between the Patient- and Atlas-DTIs in very anisotropic regions, e.g., the area indicated by the white circle in the LGG image. This difference is more significant in very anisotropic areas of the brain like the corpus callosum when the tumor growth speed is high. Furthermore, there is not too much visible difference between the tumor contour from No-DTI option and the options that used a DTI in the tumor growth simulation.

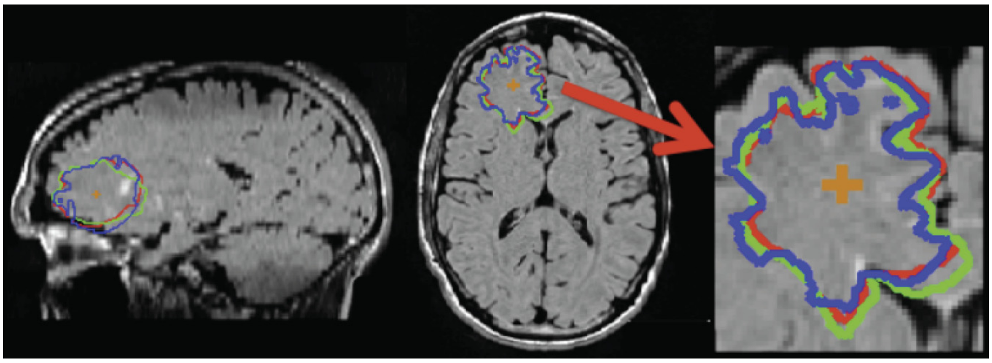

LGG in the frontal lobe

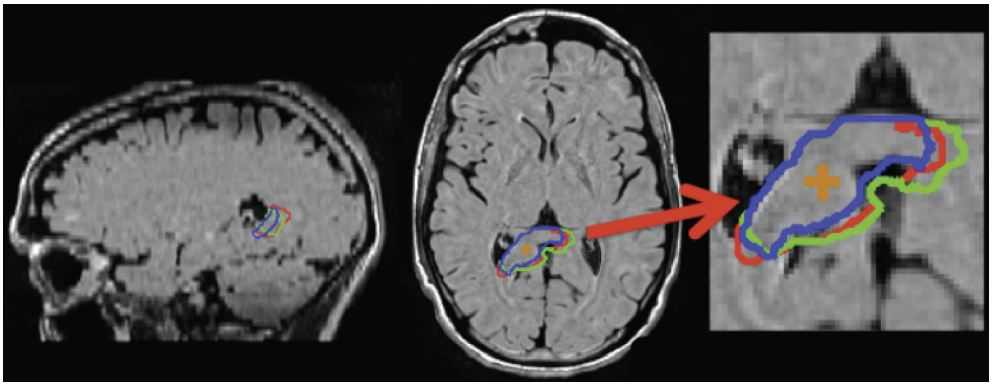

HGG in the corpus callosum

Figure 3.4: High-resolution synthetically grown tumors overlaid on a registered FLAIR MRI. Atlas-DTI and No-DTI contours are compared to Patient-DTI. The start seeds are the orange cross-hairs. Notice that the directional non-homogeneity of the Patient- and Atlas-DTI are slightly different in very anisotropic regions (pointed out by the white circle in the LGG image).

3.5 Clinical Case

In this section we present the results of comparing the three diffusivity tensor constructions within the traveling time FK formulation using a clinical case. These results include the estimation of the tumor growth speed, and the tumor contours at future time points.

3.5.1 Data

We used a clinical data set of a LGG patient with five acquisition data points, where the tumor was located in the supratentorial region of the brain. The Patient-DTI, T1, and FLAIR MRIs were affinely registered to the resampled baseline image of the patient (first FLAIR MRI acquisition), where the baseline was resampled to $1 \times 1 \times 1mm^3$. The original baseline image resolution was $0.5 \times 0.5 \times 6.5mm^3$, where it had a $5mm$ slice thickness and a $1.5mm$ interslice gap in the z-direction. The Atlas-DTI was non-linearly registered to the registered Patient-DTI, using a mask over the tumor to exclude the tumor area from the registration since it could not be matched between the images. The tumor was manually segmented in the original FLAIR MRI resolution and then the transformations of the registrations of the FLAIR MRIs to the FLAIR baseline image were applied on the tumor segmentations using shape based interpolation. The MNI 152 $T1$ was also registered to the registered patient $T1$ MRI and the transformation of the registration of the MNI 152 $T1$ to the patient $T1$ MRI was applied on the MNI 152 WM, which was de facto registered to the MNI 152 $T1$ [Fonov et al., 2009]. FSL's FAST [Zhang et al., 2001] was used on the registered patient $T1$ MRI to find the patient's BM.

In Stretton et al. [2013], two additional patients were studied; however, the data of those patients were lost and for that reason, they are no longer included in this manuscript.

3.5.2 Method

The method consists of two main steps: personalization and prediction. Personalization consists of solving the parameter estimation problem in Equation 2.19 using tumor delineations at two different time points. The outputs of the personalization step are the tumor growth parameters (ρ, d_w, d_g, and the time from the time of appearance of the tumor) and the simulated delineation at the second time point. The notation Personalize(T_1,T_2), used in the remainder of this chapter, signifies for a given patient that the personalization was done between delineations at the time points T_1 and T_2. Prediction consists of running the traveling time FK formulation (equations 2.14, 2.15, and 2.16) for given tumor growth parameters between two time points, where the tumor delineation at the first time point is given as an input. The output is the simulated delineation at the second time point. The notation Predict(T_3,T_4) represents the application of this prediction step between the time points T_3 and T_4. To calculate the accuracy of each simulation (for either personalization or prediction), we compute the root mean squared error (RMSE), defined as

$$RMSE = \sqrt{\text{dist}(\Gamma, \overline{\Gamma})^2}, \tag{3.1}$$

where Γ is the surface encompassing the tumor in the image taken at the second acquisition date, and $\overline{\Gamma}$ is the tumor delineation simulated by the traveling time approximation of the FK model at the second acquisition date, and dist( ) is the symmetric distance between them, normalized by their surface area.

3.5.3 Results

In this section, we present the results of the personalization and prediction for one patient using five image acquisition points and the three diffusivity tensor construction options, i.e., Patient-DTI, Atlas-DTI, and No-DTI. Thus, we perform for each of these tensors ten personalizations: Personalize(T_1,T_2), Personalize (T_1,T_3), Personalize(T_1,T_4), Personalize(T_1,T_5), Personalize(T_2,T_3), Personalize (T_2,T_4), Personalize(T_3,T_5), Personalize(T_3,T_4), Personalize(T_3,T_5), and Personalize(T_4,T_5). From each one of these personalizations we perform nine predictions, e.g., for Personalize(T_1,T_2), we did Predict(T_1,T_3), Predict(T_1,T_4), Predict(T_1,T_5), Predict(T_2,T_3), Predict(T_2,T_4), Predict(T_2,T_5), Predict(T_3,T_4), Predict(T_3,T_5), and Predict(T_4,T_5). This resulted in a total of ninety predictions for each one of the diffusivity tensors. Figure 3.5 shows the acquisition timeline of our patient, where T_i stands for the *ith* image acquisition time point, and the numbers in between the acquisition times are the time intervals between images. This figure depicts an example where the orange delineation shows the output of Personalize(T_1,T_2) and the purple delineations depict different prediction results at time points T_3, T_4, and T_5.

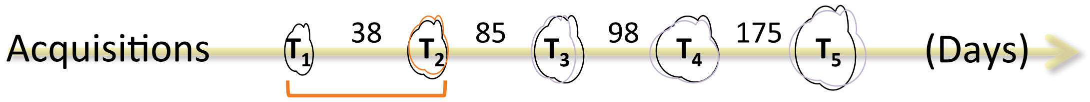

Figure 3.5: Patient acquisition timeline with personalization and predictions.

Figure 3.6 shows the estimated tumor growth speed in white and gray matter resulting from the ten personalizations, where on the horizontal axis are displayed the ten time intervals used in the personalization. This plot shows that the estimated tumor growth speed in both white and gray matter did not change much between the personalizations estimated using the Patient- and Atlas-DTI options. However, for the No-DTI option, the white matter speed was slower and showed more run-to-run variability than for the other two options. Table 3.2 shows the mean and the standard deviation of the estimated tumor growth speeds for each of the DTI options in both white and gray matter. Notice that on average the personalization runs using the No-DTI estimated slower growth speed in white matter and a faster growth speed in gray matter than the personalization runs using a DTI. Most importantly, notice that on average there was about $1mm/year$ difference between the white matter speed estimated using a DTI and not using a DTI, and the worst case scenario was $3mm/year$ difference (see Figure 3.6). Also, notice that the speed estimate standard deviations were all under $1mm/year$, where the No-DTI option had the highest standard deviation in white matter and slowest in gray matter.

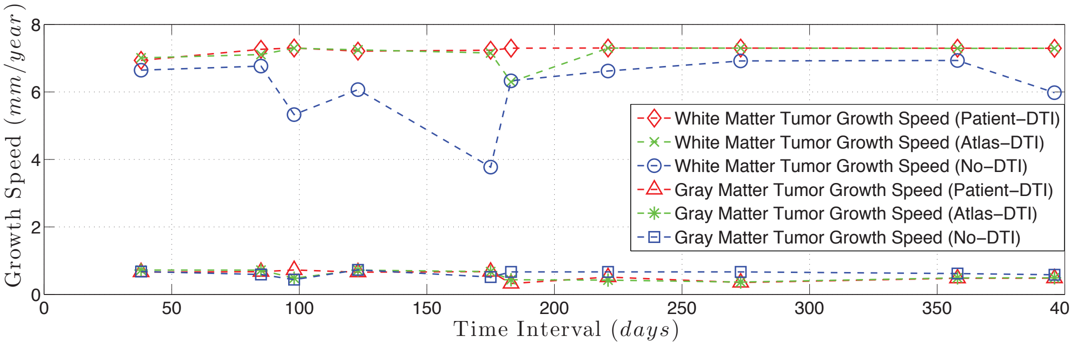

Figure 3.6: Tumor growth speed estimated for white matter (diamond, cross, circle) and gray matter (triangle, star, square) using the traveling time FK model formulation with three different diffusivity tensor constructions (Patient-DTI, Atlas-DTI, and No-DTI).

Table 3.2: Patient Tumor Growth Speed Estimation Statistics

DTI Options used within Equation 2.19	*White Matter* Mean $(mm/year)$	*White Matter* Std. Dev. $(mm/year)$	*Gray Matter* Mean $(mm/year)$	*Gray Matter* Std. Dev. $(mm/year)$
Patient-DTI	7.23	0.11	0.55	0.14
Atlas-DTI	7.12	0.31	0.55	0.14
No-DTI	6.13	0.99	0.62	0.09

Figure 3.7 shows the RMSE obtained in the personalization runs against the time interval between the two time points being personalized. Notice in this plot the upward RMSE value trend for personalization runs with larger time intervals. This is an expected result for each of the DTI options independently because the tumor of this patient had a finger-like pattern. However, it was interesting to see no improvement in RMSE for the Patient-DTI case in comparison to the other two DTI cases as the time interval became larger.

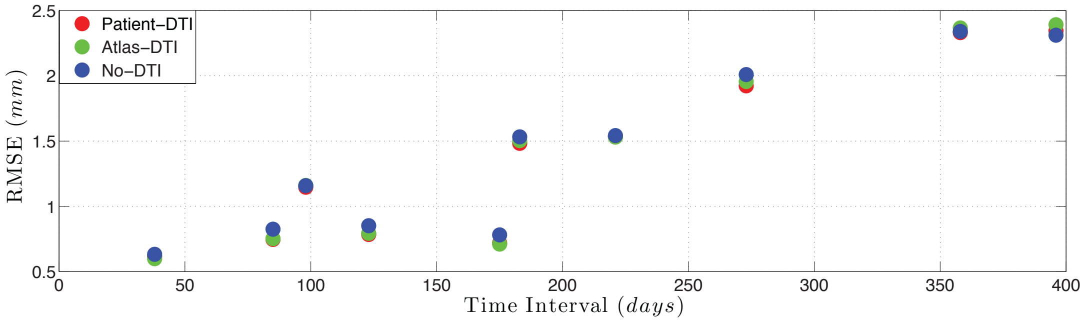

Figure 3.7: RMSE of the personalization runs.

Figure 3.8 shows the RMSE differences of the personalization runs between the Patient-DTI case and the Atlas- and No-DTI cases. Notice that most of the personalization runs for the Patient-DTI case were more accurate, i.e., most of data points in the plot are negative. However, the RMSE differences between the different DTI options were less than $0.1mm$. Table 3.3 shows the mean and standard deviation of the points plotted in Figure 3.8, where the No-DTI case had slightly worse performance than the Atlas-DTI case.

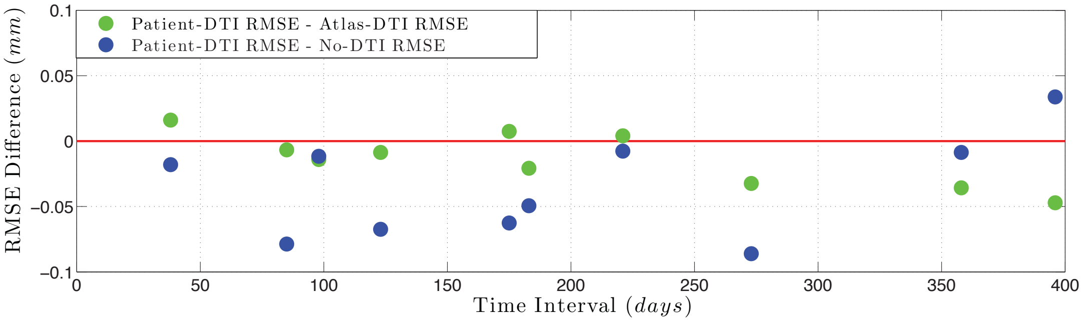

Figure 3.8: RMSE differences of the personalization runs.

Table 3.3: Patient Personalization RMSE Difference Statistics

RMSE Difference Cases	Mean (mm)	Std. Dev. (mm)
Patient-DTI RMSE - Atlas-DTI RMSE	-0.014	0.020
Patient-DTI RMSE - No-DTI RMSE	-0.036	0.039

Figure 3.9 shows the RMSE obtained in the prediction runs against the time interval of the prediction. As in the personalization case, notice in this plot the upward RMSE value trend for prediction runs with larger time intervals. Notice that there was also no improvement in RMSE for the Patient-DTI case in comparison to the other two DTI cases as the time interval became larger.

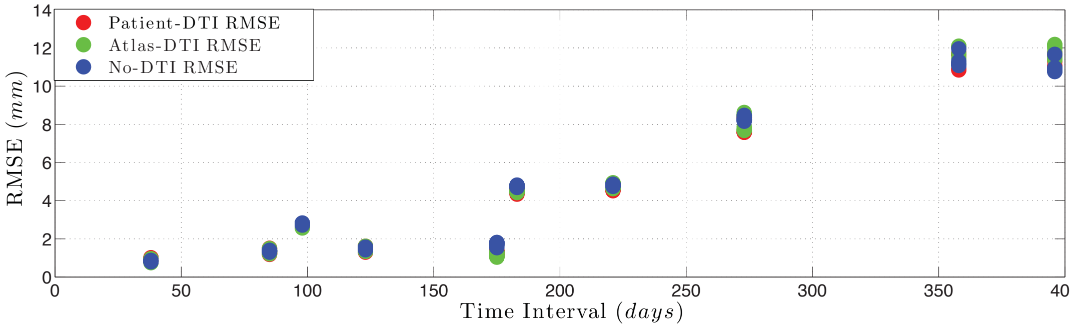

Figure 3.9: RMSE of the prediction runs.

Figure 3.10 shows the RMSE differences of the prediction runs between the Patient-DTI case and the Atlas- and No-DTI cases. Notice that most of the prediction runs for the Patient-DTI case were more accurate, i.e., most of data points in the plot are negative. However, we can also observed that for larger time intervals the No-DTI case had lower RMSE values than the Patient-DTI case. In addition, we can observe that the RMSE differences were larger for larger time intervals. Table 3.4 shows the mean and standard deviation of the points plotted in Figure 3.10, where the No-DTI case showed more run-to-run variability than the Atlas-DTI case, but a mean value closer to zero. However, we can conclude that there is no significant difference among the DTI options in the tumor growth predictions since the values of the mean and standard deviation in Table 3.4 are relatively small with respect to the patient's images resolution.

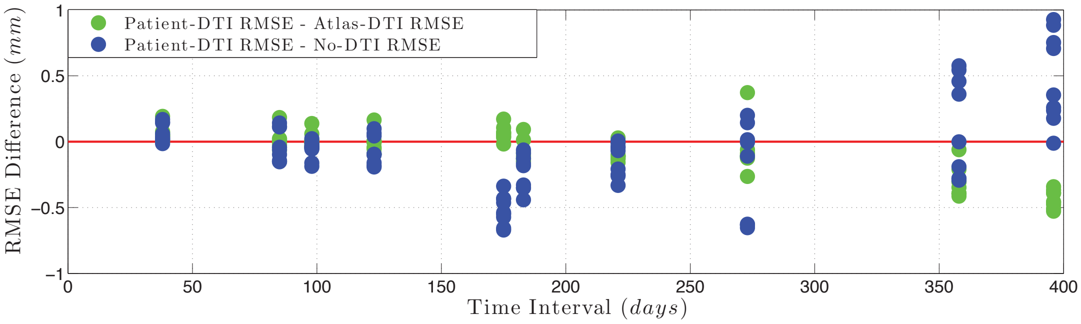

Figure 3.10: RMSE differences of the prediction runs.

Table 3.4: Patient Prediction RMSE Difference Statistics

RMSE Difference Cases	Mean (mm)	Std. Dev. (mm)
Patient-DTI RMSE - Atlas-DTI RMSE	-0.086	0.178
Patient-DTI RMSE - No-DTI RMSE	-0.066	0.325

Figure 3.11 shows prediction results for three time intervals of different duration. Notice that for the time intervals of 85 days and 175 days, the Patient- and Atlas-DTI prediction results were practically identical to the actual tumor segmentation, i.e., the contour lines are sitting on top of each other, and the No-DTI prediction was also very close, deviating only in a couple of regions, e.g., inside the red circle. For the time interval of 396 days we can observe from the image that the three DTI options struggle to match the tumor segmentation in a region where the tumor has a spiky finger-like shape. This result explains the high RMSE values in Figure 3.9 for large time intervals. The image at 396 days in Figure 3.11 also shows that the lower RMSE values for the No-DTI case observed in Figure 3.10 for large time intervals were caused by having the No-DTI delineation (blue line) closer to the finger-like pattern segmentation (yellow line) than the Patient- and Atlas-DTI delineations. However, the shape of the tumor was better matched in terms of shape by the Patient- and Atlas-DTI delineations (blue and red lines). Therefore, even thought the RMSE values for the No-DTI case were lower, the tumor segmentation was matched better by the Patient- and Atlas-DTI delineations.

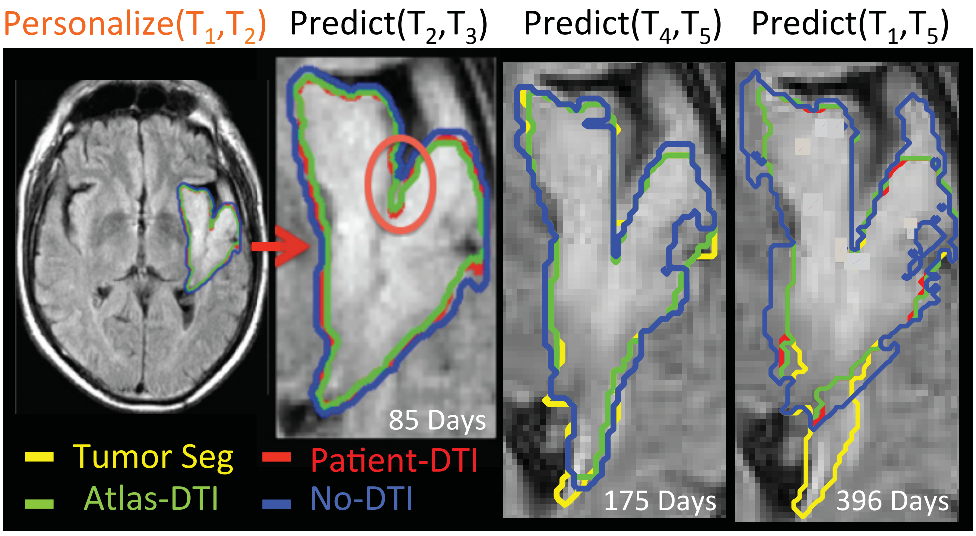

Figure 3.11: Prediction results for three time intervals of different durations.

3.6 Discussion and Conclusions

Three options to model tumor diffusion in white matter within the traveling time FK formulation were compared using both synthetic and clinical data. A future study including the data of additional patients would improve the significance of the study. The results of the preliminary study, published in [Stretton et al., 2013], led to the same conclusions as were reached in this study even though the preliminary study included the data of two additional patients. In this study, consisting of one patient, it was found that the traveling time FK model formulation is most accurate for each of the three DTI options when the prediction interval is under 175 days. The resulting delineations of the Atlas- and Patient-DTI matched the actual tumor contours slightly better, but not significantly, than the No-DTI option. However, the prediction results of the No-DTI option for under 175 days time interval were also close to the actual tumor. Therefore, this chapter suggests that a Patient-DTI (when available) is the best option to model tumor cell diffusion in white matter within the FK framework since the results show that tumor growth has directional preference (anisotropic growth) as formulated in [Clatz et al., 2005; Jbabdi et al., 2005]. It was also found that not very much accuracy is lost with the use of an Atlas-DTI, even though the Atlas-DTI has a slightly different directional non-homogeneity than a Patient-DTI. This study suggests that modeling glioma growth with tissue based differential motility (using the No-DTI option) as proposed in [Swanson et al., 2007] yields slightly less precise results. However, refraining from using a DTI would be sufficient when modeling LGGs.

Chapter 4

Tumor Growth Modeling of Glioma Reoccurrence after Surgical Resection

Contents

Based on an extended version of the published conference paper [Stretton et al., 2012], which was orally presented at the Spatio-temporal Image Analysis for Longitudinal and Time-Series Image Data - Second International Workshop that was held in conjunction with MICCAI 2012. This work was submitted to the Journal of Frontiers in Oncology.

4.1 Context

As a result of medical protocols, most glioma patients are subject to resections within a short period of time after tumor detection. Then, medical professionals want to know what the best type of follow-up treatment would be for a particular patient, i.e., chemotherapy for diffuse tumors or a second resection after a given amount of time for bulky tumors. Recent mathematical models to simulate brain tumors, especially gliomas, have shown promising results in predicting tumor growth and tumor cell infiltration. In this chapter, we proposed a thorough method to leverage glioma growth models on post-operative cases showing brain distortions to estimate the tumor infiltration maps after surgery. Our method builds on a reaction-diffusion formulation of the tumor growth process to estimate tumor cell infiltration beyond its visible boundaries in MRIs after a surgical resection. There are two main challenges involved with estimating glioma infiltration directly after surgery. First, there is substantial brain parenchyma and CSF movement after surgery causing simulation post surgery to be very challenging (no brain parenchyma alignment). Second, it is difficult to obtain quality tumor segmentations because the tumor segmentations after surgery may not be complete since there is a potential for blood and scar tissue to be confused with tumor. It is only after several scans that a neurosurgeon can tell the difference between these hyper-intense signals on MRIs and therefore a neurosurgeon will generally under-segment a tumor in scans taken within a few months after surgery. We tried to address the first challenge in our method with the use of a non-linear registration algorithm that compensates for the brain parenchyma and CSF movement. Our method addresses the second challenge by combining two infiltration maps, where one was simulated from a pre-operative image and one estimated from a post-operative image. We use two patients' data to demonstrate the effectiveness of the proposed method. For one patient, we successfully apply the method at four time points after surgery (from 172 to 458 days) that when thresholded at 20% cell density match neurosurgeon's tumor segmentations (Dice coefficient > 0.7). For the other patient, severe mass effects cause lower effectiveness of the method soon after surgery; however, the method is able to find an infiltration map at 344 days after surgery that when thresholded at 20% cell density matches a neurosurgeon's tumor segmentation (Dice coefficient $= 0.9$). We believe that our proposed method could potentially help clinicians anticipate tumor regrowth and better characterize the radiological non-visible infiltrative extent of a tumor to plan therapy.

4.2 Introduction

Glioma surgical resection has shown to be a critical therapeutic modality and is usually the first type of therapy given to patients soon after diagnosis. Brain resections are not only used to control symptoms, e.g., seizures, and relieve cranial pressure that causes neurological defect, but also to refine the diagnosis. Analyzing a resected lesion allows an oncologist to define the tumor grade and to identify the genetic profile. Resections are part of a standard treatment that has demonstrated increased patient survival time [Sanai and Berger, 2008]. However, gliomas are a diffuse, infiltrative, and resilient form of brain cancer. That is why most low-grade glioma patients have a tumor reoccurrence after the first tumor resection. Indeed, low tumor cell density regions, invisible in MRIs, proliferate and cause reoccurrence [Gerin et al., 2013; Pallud et al., 2010] (see Figure 4.1). Treatment then includes a second surgery or chemotherapy depending on the diffusivity of the tumor: surgery should be preferred for a tumor without a large non-visible extent (referred to as a “bulky” tumor), whereas, chemotherapy is applied to highly diffuse and invasive tumors.

The Fisher Kolmogorov (FK) model (Equation 2.3) is a well-acknowledged standard for modeling glioma growth. There have been many scientists who have incrementally improved this model since the pioneering 2-D work of Murray and Alvord in the nineties, leading to more realistic brain tumor growth simulations [Burgess et al., 1997; Tracqui et al., 1995b; Woodward et al., 1996]. Swanson et al. [2000] extended the model to include the heterogeneity of brain tissue on synthetic data modeling isotropic spatial diffusion. Then, Clatz et al. [2005] and Jbabdi et al. [2005] proposed treating the 3-D spatial diffusion coefficient as a tensor using DTI construction methods that estimated the tumor cell diffusion in white matter. Later, in a post mortem study, Swanson et al. [2007] investigated the effectiveness of using different types of brain resections, where their simulations were run on virtual controls (not patient data). Their model was limited to personalization using patient T1 Gad and T2 MRIs, without taking into account the anisotropy in white matter fiber tracts visible in DTIs. Additionally, their model did not estimate tumors’ infiltrative extents before and after a resection. Konukoglu et al. [2010a] and Cobzas et al. [2009] created methods to calculate infiltration maps to approximate tumor invasion margins for radiotherapy treatment from a single MRI of any given patient; however, these methods require the FK model parameters: diffusion in white matter (d_w) and proliferation rate (ρ). Konukoglu et al. [2009] defined a method to find the tumor growth velocity ($v = 2\sqrt{d_w \rho}$) from a MRI, where d_w and ρ appear as a product. In this chapter we address the problem of separating the parameters ρ and d_w from the tumor growth velocity estimate v of Konukoglu et al. [2009] by estimating the quotient d_w/ρ. Then, we used these parameters with the method of Konukoglu et al.

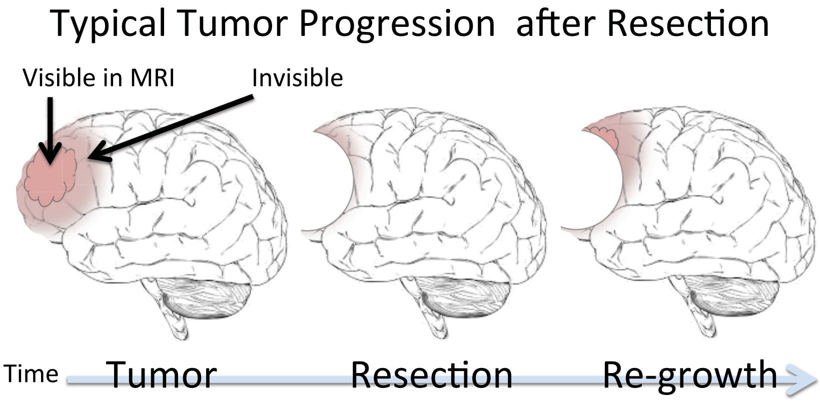

Figure 4.1: Cartoon of the tumor re-growth process after resection.

[2010a] to find the infiltration maps from pre- and post-operative MRIs.

The two challenges in estimating tumor infiltration maps using pre- and post-operative images, which this chapter addresses, are: i) brain parenchyma and CSF movement after surgery, and ii) the difficulty in obtaining quality tumor segmentations. To the best of our knowledge, estimating tumor infiltration after a brain tumor resection, using patient data and a DTI, has not been tackled before. Preliminary results were published in [Stretton et al., 2012], which we extend in this chapter with an improved non-linear registration technique and a more refined methodology.

This chapter is organized as follows. In Section 4.3 we detail a novel methodology to predict glioma reoccurrence after surgical resection. In Section 4.4, we describe the patient data that were used to illustrate how the proposed method works. In Section 4.5, we present the results of our experiments to validate our method, which shows that this method is feasible. The discussion is presented in Section 4.6. Conclusions and perspectives are presented in Section 4.7.

4.3 Method

In this section, we present a method to estimate glioma reoccurrence development after a brain resection. Figure 4.2 shows the main steps of this method, which requires as inputs patient and atlas images. The output of the method is a predicted tumor infiltration map at a future time after surgery, which tells us if a tumor is bulky or diffuse. In Figure 4.2 and in the rest of this chapter the variable T represents the time from the origin of the tumor, where the negative subindices indicate time points before surgery and the positive subindices indicate time points after surgery.

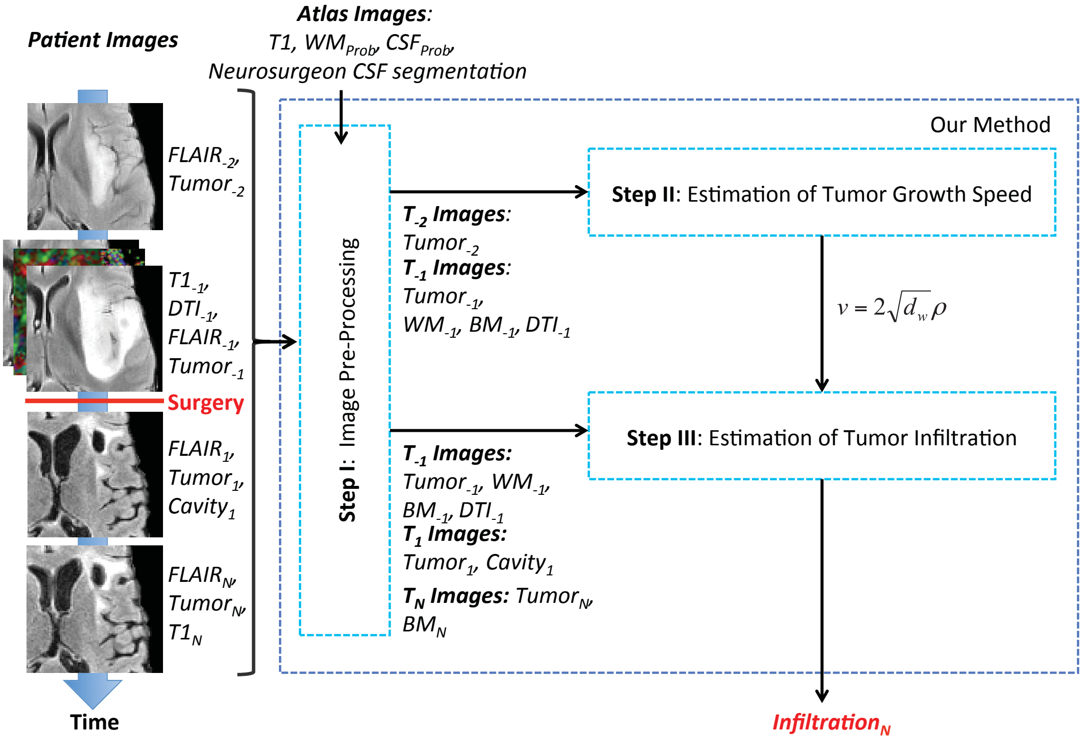

Figure 4.2: Graphical representation of a method to estimate glioma infiltration after a brain resection. This method requires as inputs patient and atlas images, and produces as output a tumor infiltration map at a future time after surgery. There are three steps in the method: image pre-processing, estimation of tumor growth speed, and estimation of tumor infiltration. The variable T represents the time from the initial appearance of the tumor, where the negative subindices indicate time points before surgery and the positive subindices indicate time points after surgery.

Assumptions: We make the following assumptions in this work, which are deemed reasonable by our collaborating neurosurgeon:

- We chose the tumor cell density threshold of visibility value as 20% because it is an intermediate value in literature for T2 MRIs, which includes FLAIR (the imaging modality that shows the most glioma tumor cell density threshold of visibility extents). Tracqui et al. [1995a] proposed 40% maximal tumor cell density to be visible in T2 MRIs, Konukoglu et al. [2009] used Tracqui's value, and Swanson et al. [2007] used a 18% value. Menze et al. [2011b] suggested the minimal tumor cell density that is visible in FLAIR MRIs to be 9.5%.

- Gliomas, scar tissue, and edema appear as hyper-intense voxels in FLAIR MRIs making difficult to distinguish one from the other, especially in images soon after surgery. When a neurosurgeon segments a tumor, he/ she segments conservatively and includes only what is known to be tumor in his/ her segmentation. We assume that the neurosurgeon would not over segment a tumor.
- Sometimes, before surgery, patients suffer from generalized seizures. This makes the enhanced region, which we assume is tumor, to swell with edema that makes the tumor look larger than it is. Therefore, if we know a patient has had a generalized seizure close to the date of an MRI acquisition, we choose not to include this MRI time point in our study.
- Tumor cells diffuse in the same way after surgery as before surgery. In our method, we use a before surgery DTI.
- A low-grade glioma grows with the same velocity before and after surgery [Mandonnet et al., 2010].
- Tumors diffuse in gray matter isotropically [Clatz et al., 2005; Jbabdi et al., 2005; Swanson et al., 2007; Konukoglu et al., 2009; Stretton et al., 2012; Menze et al., 2011a].
- In Step III of our method (see Figure 4.2), the ratio d_w/d_g is assumed to be 10 because it is an intermediate value of the ones encountered in the literature. Konukoglu [2009] chose values for d_w/d_g to be between $4 - 375$. Swanson et al. [2000] fixed $d_w/d_g = 5$ and later said that d_w/d_g could range from $2 - 100$ [Swanson et al., 2003; Swanson, 1999].

In the following sections, the three steps of our method depicted in Figure 4.2 are described in detail.

4.3.1 Step I: Image Pre-processing

The first step of our method, Image Pre-processing, consists of several intricate segmentation and registration operations (see Figure 4.3). Inputs are images from an atlas (MNI 152 [Fonov et al., 2009]) and from a patient at different time points before and after surgery (T_{-2}, T_{-1}, T_1, and T_N). After surgery, the brain parenchyma shifts position and continues shifting even a year after. Therefore, in order to compare the MRIs of a resection patient, both between pre- and post-operative images and between consecutive post-operative images, we decided to register all patient MRIs and segmentations to the baseline MRI $FLAIR_{-1}$. The registered outputs of Step I include a white matter mask before surgery

(WM_{-1}), a brain parenchyma mask before and after surgery (BM_{-1} and BM_N), a diffusion tensor image before surgery (DTI_{-1}), two tumor segmentations before surgery ($Tumor_{-2}$ and $Tumor_{-1}$), two tumor segmentation after surgery ($Tumor_1$ and $Tumor_N$), and a resection cavity mask after surgery ($Cavity_1$). We will first present the non-linear registration algorithm used and then describe how we achieved the registrations of the WM_{-1}, BM_{-1} & BM_N segmentations, the DTI, and the tumor & cavity segmentations.

Non-linear Registration: The most important part of our registration pipeline is the method used for non-linear registration of the images, where there exists no one-to-one correspondence between both images due to the tumor resection. The non-linear deformation between the pre-operative images and the post-operative images can be seen with the ventricles swelling and brain tissue shifting position after surgery. The idea of the non-linear registration algorithm employed is to model pathological regions with zero confidence using local deformations instead of global ones. We employed the framework proposed by Lorenzi [2012], which extends the diffeomorphic demons algorithm [Vercauteren et al., 2009] by implementing the local correlation coefficient as a similarity measure, to robustly register the images with respect to bias fields and differences in image histograms. The algorithm was adapted in order to account for the areas that cannot be matched between the images, i.e., resection cavity, by excluding the mask volume from the registration. However, this algorithm cannot account for shifting under the resection cavity mask. This method is symmetric and therefore, we can recover the original image with the transformation found in this step and apply this transformation on the infiltration map estimated in Step III.

Brain Parenchyma and White Matter Masks: The BM_{-1} and BM_N are used to define the no flux boundary conditions of the brain for modeling, i.e., tumor cells cannot leave this mask. The WM_{-1} marks out the inhomogeneous tissue boundaries used in tumor growth model simulations at later steps in our method. These binary masks were segmented using a series of steps shown graphically in Figure 4.3 and explained further in order of occurrence as follows:

- Resample the baseline image $FLAIR_{-1}$ and $Tumor_{-1}$ to a voxel size of $1 \times 1 \times 1mm^3$.
- Skull-strip the patient $T1_{-1}$ and $FLAIR_{-1}$ images using the method described in [Smith, 2002]. Then, register the skull-stripped $T1_{-1}$ to the skull-stripped $FLAIR_{-1}$ using a rigid [8] registration algorithm.

---

[8] Rigid registration has 6 degrees of freedom: 3 parameters for the rotation and 3 parameters for the translation.

- Affinely and non-linear register the patient $T1_{-1}$ image to the baseline MRI $FLAIR_{-1}$ (see Tumor and Cavity Segmentations) and then skull-strip it. Its new name is $NL\ Registered\ T1_N$.
- Non-linear register the patient $Tumor_N$ and $Cavity_1$ to the baseline MRI (see Tumor and Cavity Segmentations).
- Affinely [9] register the skull-stripped atlas $T1$ [Fonov et al., 2009] to the Registered Patient $T1_{-1}$ and NL Registered $T1_N$ images. Apply the re-

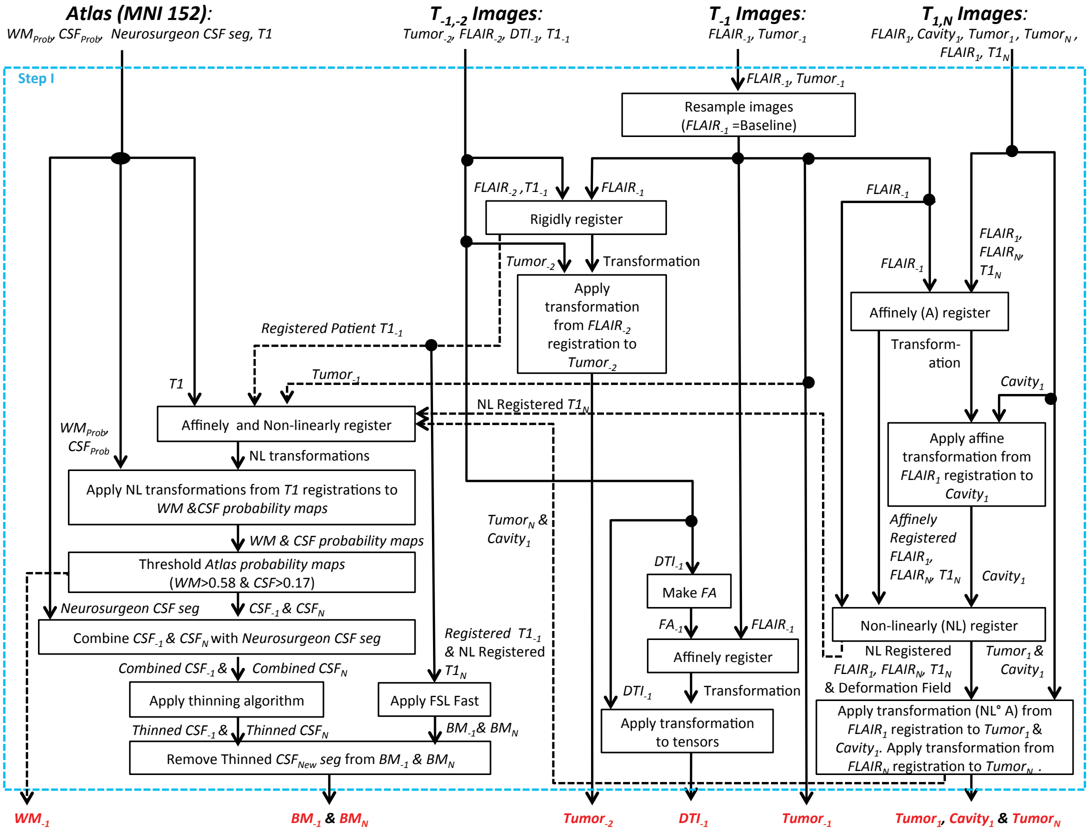

Figure 4.3: Step I: Image Pre-processing. The objective of this step is to register all images to a common baseline image ($FLAIR_{-1}$). Inputs are images from an atlas (MNI 152), a neurosurgeon's CSF segmentation, and from a patient at different time points before and after surgery (T_{-2}, T_{-1}, T_1, and T_N). The registered outputs of Step I include a white matter mask before surgery (WM_{-1}), a brain parenchyma mask before and after surgery (BM_{-1} and BM_N), a diffusion tensor image before surgery (DTI_{-1}), two tumor segmentations before surgery ($Tumor_{-2}$ and $Tumor_{-1}$), two tumor segmentations after surgery ($Tumor_1$ and $Tumor_N$), and a resection cavity mask after surgery ($Cavity_1$).

sulting transformations to the original atlas $T1$ to obtain registered images with skulls present in the images. Then, using the resampled $Tumor_{-1}$ as a mask, non-linearly register the atlas $T1$ [Fonov et al., 2009] (with skull) to the Registered Patient $T1_{-1}$ (with skull) to obtain a non-linear transformation. In the same way, non-linear register the atlas $T1$ to the NL Registered $T1_N$, using a mask ($Tumor_N$ and $Cavity_1$), to obtain another non-linear transformation.

- Apply the non-linear transformations found from registering the $T1$s on the atlas WM and CSF probability maps that are de facto registered to the atlas $T1$ [Fonov et al., 2009].
- Threshold the probability maps ($WM > 0.58$ & $CSF > 0.17$) according to the values specified by our collaborating neurosurgeon. In this step, the WM mask (WM_{-1}) is found.
- Combine each of the atlas registered CSF segmentations with a very accurate neurosurgeon segmented CSF segmentation (see Appendix B).
- Apply a thinning algorithm [Pudney, 1998; Bertrand and Malandain, 1994] to these CSF segmentations so that they will not be too thick.
- Use FSL's FAST [Zhang et al., 2001] on the registered patient $T1_{-1}$ and $T1_N$ images to find the patient's brain parenchyma segmentations, which do not have all of the sulci patterns distinguished, and then subtract out the registered thinned CSF segmentations to obtain patient registered brain parenchyma masks (BM_{-1} and BM_N) with correct representations of the patient's sulci patterns.

Another method of obtaining a WM is by thresholding the fractional anisotropy (FA) map of a DTI. The WM segmentation method proposed in this section is superior to thresholding a FA map, as was done in[Konukoglu et al., 2010b], for two reasons. First, our method can be part of a streamline standard procedure that can be executed in the same way for every patient. Second, our method, which produces similar results to what the WM would look like before the tumor started growing, can show white matter fiber tracts surrounding the tumor since it is based on a registered atlas. In contrast, the FA map is based on a DTI where the white matter fiber tracts that are visible in DTIs are often disturbed or destroyed with tumor growth. Finally, another method that could have been used for performing a brain parenchyma segmentation was proposed by Baillard

---

[9] Affine registration has 12 degrees of freedom: 3 for the rotation, 3 for the translation, 3 for the scaling, and 3 for the shearing.

et al. [2001], who suggested a method for segmenting the brain from volumetric MRIs, which integrates 3D segmentation and registration processes. However, there is no mention of the method being able to define sulci patters or separate brain lobes.

DTI: For the registration of the DTI, our method requires several steps. First, the fractional anisotropy (FA) map is created from the DTI_{-1}. Second, affinely register the FA_{-1} to the $FLAIR_{-1}$ to obtain the registration transformation. Then, this transformation is applied on the unregistered DTI_{-1}.

Tumor and Cavity Segmentations: There were three pipelines for registering the tumor segmentations: i) $Tumor_{-2}$, ii) $Tumor_{-1}$, iii) $Tumor_1$, $Cavity_1$, and $Tumor_N$. For the registration of $Tumor_{-2}$, the $FLAIR_{-2}$ is rigidly registered to the resampled baseline $FLAIR_{-1}$, where both images are first skull-stripped using the method described in Smith [2002]. The transformation found in this registration is applied to the tumor segmentation $Tumor_{-2}$ that the neurosurgeon segmented from the unregistered $FLAIR_{-2}$. The image resampling method used to apply the transformation is shape-based interpolation, which accounts for the large anisotropy in the voxels. For the registration of $Tumor_{-1}$, the original $Tumor_{-1}$ image is resampled in the same way as the baseline $FLAIR_{-1}$. For the registration of $Tumor_1$, $Cavity_1$, and $Tumor_N$, the skull-stripped $FLAIR_1$ and $FLAIR_N$ are affinely registered to the skull-stripped resampled baseline $FLAIR_{-1}$. The resulting transformations are applied to the original $FLAIR_1$ and $FLAIR_N$ to obtain registered images with skull present in the images. Then, the affine transformation (from the affine registration of $FLAIR_1$) is applied to the $Cavity_1$. There was no need for a neurosurgeon to segment $Cavity_N$, which would have been time consuming, since the BM_N was made with the cavity excluded. Then, the affinely registered $FLAIR_1$ and $FLAIR_N$ (with skulls) are non-linearly registered to the resampled $FLAIR_{-1}$ using the $Cavity_1$ as a mask. Finally, the transformations (deformation fields and transformation matrices) are applied to register $Tumor_1$, $Cavity_1$, and $Tumor_N$, which the neurosurgeon segmented from the unregistered $FLAIR_1$ and $FLAIR_N$.

4.3.2 Step II: Estimation of Tumor Growth Speed

Step II of our method in Figure 4.2 uses the registered images of Step I at times T_{-2} and T_{-1} ($Tumor_{-2}$, $Tumor_{-1}$, WM_{-1}, and BM_{-1}, and DTI_{-1}), since we are more confident in the tumor segmentations before surgery than just after surgery, to find the tumor growth parameters d_w and ρ using a Simplex minimization algorithm [Lagarias et al., 1998; Nelder and Mead, 1965] that solves an extension of the parameter estimation problem in Equation 2.19. Konukoglu [2009] performed the parameter estimation in Equation 2.19 for relatively small tumors; however, when applied to larger tumors we observed that the resulted simulated tumors had toroidal shapes. To overcome this problem, we modified the cost function in Equation 2.19 to take into account the volumetric mismatch between the segmented tumor and the simulated tumor. Thus, in our method we extended the parameter estimation problem definition as follows:

$$\arg \min_{d_w, d_g, \rho, T_{-2}} C = \operatorname{dist}(Tumor_{-1}, \overline{Tumor_{-1}})^2 + (v_{min}|T_{min} - T_{-2}|)^2 \\ + \zeta \left(1 - \frac{2(V_{-1} \cap \overline{V_{-1}})}{V_{-1} + \overline{V_{-1}}}\right)^2, \quad (4.1)$$

where V_{-1} is the volume of the real tumor extracted from the MRI before surgery, $\overline{V_{-1}}$ is the volume of the simulated tumor using the traveling time formulation in equations 2.14, 2.15, and 2.16 at time T_{-1}. The term $\frac{2(V_{-1} \cap \overline{V_{-1}})}{V_{-1} + \overline{V_{-1}}}$ is known as the Dice coefficient (see Figure 4.4) and ζ is a scalar weighting factor. The Dice coefficient is used together with Specificity and Sensitivity (see Figure 4.4) to evaluate the matching quality between simulated and segmented tumor volumes. Specificity is a metric of false positive tumor estimations, i.e., it measures how much of the simulated tumor does not belong to the segmented tumor. On the contrary, sensitivity is a metric of false negative tumor estimations , i.e., it measures how much of the segmented tumor was not estimated by the simulated tumor. The Dice coefficient accounts for both scenarios and that is the reason for choosing it for the cost function of Equation 4.1. We chose to use the Simplex method instead of the Powell method [Nelder and Mead, 1965], which was used in [Konukoglu, 2009], because the Simplex method is more robust to noise and it does not rely on smooth functionals. Consequently, the Simplex method can work on functions that are not locally smooth such as experimental data points, as long as they show a large-scale bell-shape behavior. An important property of the Simplex method is that it converges even when the initial simplex straddles two or more valleys, a property that is not shared by the Powell method.

The procedure within Step II is graphically shown in Figure 4.5 and goes as follows:

- The traveling time formulation of the FK model, described in equations 2.14, 2.15, and 2.16, is used to simulate the tumor growing from T_{-2} to T_{-1}.
- The cost function C is calculated (see Equation 4.1).

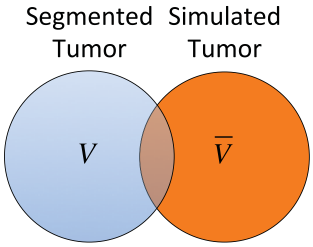

$$
\begin{aligned}
\text{Dice coefficient} &= \tfrac{2(V \cap \overline{V})}{V+\overline{V}} \\
\text{Sensitivity} &= \tfrac{V \cap \overline{V}}{V} \\
\text{Specificity} &= \tfrac{(V \cup \overline{V})^c}{V^c}
\end{aligned}
$$

Figure 4.4: Dice coefficient, Sensitivity, and Specificity definitions between segmented and simulated tumor volumes, represented by V and $\overline{V}$ respectively. The Dice coefficient ranges from zero to one, where one means that the simulated and segmented tumors match volumetrically.

- The Simplex algorithm checks if the algorithm has converged. If it has, the program exits.
- If the algorithm has not converged, the Simplex algorithm chooses a new set of parameters to evaluate and the procedure runs again.

In [Konukoglu, 2009], it was found that d_w and ρ cannot be estimated separately with the minimization method described in Section 2.3.3, but the product $d_w \rho$ can be estimated. This product is essentially the asymptotic tumor growth speed $v = 2\sqrt{d_w \rho}$. Therefore, we consider the tumor growth speed v as the output of the Step II of our method and not d_w and ρ individually.

4.3.3 Step III: Estimation of Tumor Infiltration

In order to estimate an infiltration map at a future time after surgery (T_N) it is important for Step III of our method in Figure 4.2 to determine which invisibility index (d_w/ρ) matches each particular patient's data using the T_{-1}, T_1, and T_N FLAIR MRIs. Separating these parameters is important because different values of d_w and ρ, for the same tumor growth velocity $v = 2\sqrt{d_w \rho}$, produce different tumor shapes [Konukoglu et al., 2009]. If the value of d_w/ρ is low, the tumor is said to be bulky; whereas if the value of d_w/ρ is high, the tumor is said to be diffuse (see Figure 2.9). Figure 4.6 depicts the relationship between v and d_w/ρ. Then, to find d_w/ρ we created an algorithm that sweeps through the physically feasible values of d_w/ρ while keeping the tumor growth speed v, found in Step II, constant, where the range of values were proposed by Harpold et al. [Harpold et al., 2007]. In other words, once v is estimated from the parameters d_w and ρ obtained from Step II, we move down the dotted red line of Figure 4.6 trying different values of d_w/ρ to find the best result in terms of Dice coefficient between simulation and real tumor delineation. Figure 4.7 illustrates how the internal

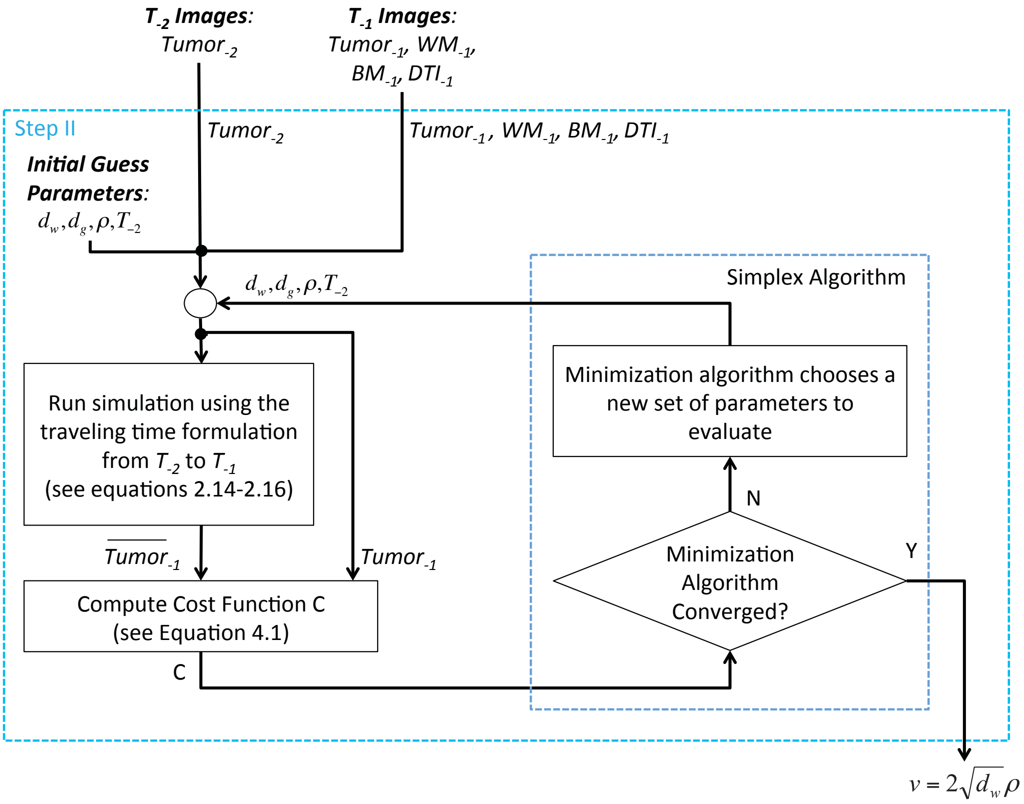

Figure 4.5: Step II: Estimation of Tumor Growth Speed. The objective of this step is to estimate the asymptotic tumor growth speed ($v = 2\sqrt{d_w \rho}$) based on the FK model parameters: diffusivity in white matter (d_w) and proliferation rate (ρ). The inputs are the registered patient images from Step I at the pre-operative times T_{-2} and T_{-1}.

steps of Step III were iteratively executed. The inputs to Step III are the tumor growth speed $v = 2\sqrt{d_w \rho}$ estimated in Step II, and the images at times T_{-1}, T_1, and T_N that were registered in Step I. The output of Step III is the infiltration map at T_N ($Infiltration_N$). The internal steps of Step III are further detailed in order of occurrence as follows:

- Calculate the $Tensor_{-1}$ by using the Clatz tensor construction method proposed in [Clatz et al., 2005] (Equation 2.4). The inputs to this operation are d_w, d_g, WM_{-1}, and DTI_{-1}.

- Calculate the infiltration maps at times T_{-1} and T_1 ($Infiltration_{-1}$ and $Infiltration_1$), which are approximations of the initial tumor densities at times T_{-1} and T_1, using the "Infiltration Map Calculation" approach,

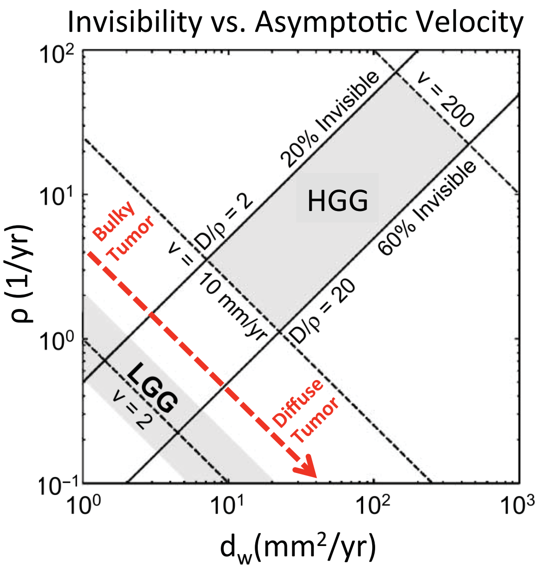

Figure 4.6: Relationship between the invisibility index (d_w/ρ) and the asymptotic tumor growth speed ($v = 2\sqrt{d_w\rho}$) using log-log coordinates. The red dotted line is a visual representation of our sweeping method, where we cycle through different values of d_w/ρ while keeping the speed v constant. [10]

described in Section 2.3.3. The inputs are $Tensor_{-1}$, the segmentations $Tumor_{-1}$ and $Tumor_1$, the brain parenchymas BM_{-1} and BM_1, and the parameter ρ. Notice in Figure 4.7 that there are two different blocks for the $Infiltration_{-1}$ and $Infiltration_1$ calculations.

- Use the resection cavity segmentation ($Cavity_1$) that was segmented from the $FLAIR_1$ MRI to remove the voxels from $Infiltration_{-1}$ map and the BM_{-1} that were removed in the resection.
- Run the FK model simulation [McCorquodale et al., 2001] (equations 2.3 and 2.4), from T_{-1} to T_1, where the inputs are $Infiltration_{-1}$ and BM_{-1} without $Cavity_1$, $Tensors_{-1}$, and ρ. The output of this operation is the simulated tumor infiltration at time T_1 ($\overline{Infiltration_1}$).
- Combine the infiltration maps $\overline{Infiltration_1}$ and the $Infiltration_1$, where the highest values for each voxel in either map are chosen to create the combined map ($Combined\ Infiltration_1$).
- Run the FK model simulation from T_1 to T_N using $Combined\ Infiltration_1$, $Tensor-1$, BM_N, and ρ. This produces a simulated tumor infiltration at

---

[10] This annotated plot was taken from [Harpold et al., 2007].

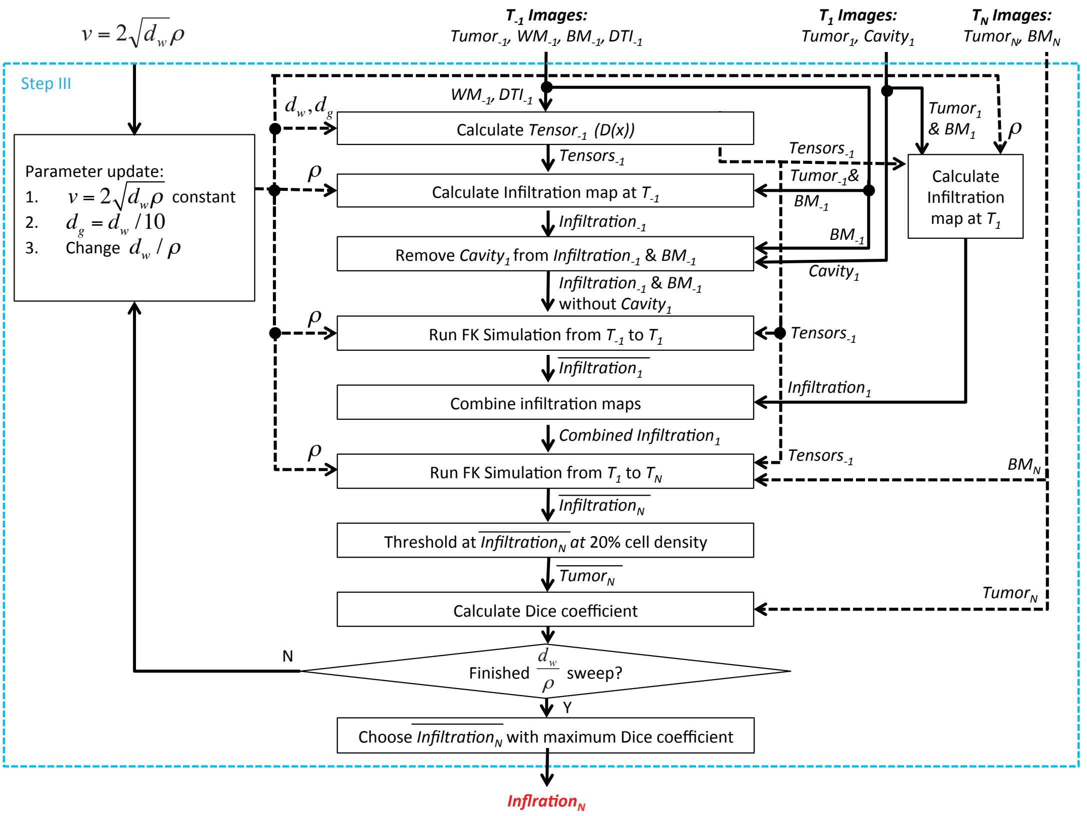

Figure 4.7: Step III: Estimation of Tumor Infiltration. This step takes the tumor growth speed $v = \sqrt{d_w \rho}$ found in Step II, and the images at times T_{-1}, T_1, and T_N as inputs. It sweeps through the physically feasible d_w/ρ range (changing them at each iteration) and outputs a tumor infiltration map at time T_N.

time T_N ($\overline{Infiltration_N}$).

- Threshold $\overline{Infiltration_N}$ at 20% cell density to produce the tumor delineation $\overline{Tumor_N}$.
- Calculate the Dice coefficient between the simulated delineation $\overline{Tumor_N}$ and the neurosurgeon segmentation $Tumor_N$.
- Check if the sweep is complete. If it is, exit loop and chose the $\overline{Infiltration_N}$ that produced the max Dice coefficient.
- If the sweep is not complete, update parameters and run the sweep algorithm again.

4.4 Data

We applied the method described in Section 4.3 to two World Health Organization grade II glioma patient data sets treated at Hôpital Lariboisière in Paris, where both patients experienced brain tumor resections. The first patient (Patient 1) had a tumor that was located in the frontal lobe only. This patient presented a generalized seizure the day before the first MRI, causing the tumor to possibly have appeared larger than it really was in the first image. A complete resection was performed and a reoccurrence of the tumor was observed 74 days later. This patient's tumor progress was followed for a little over a year before a second resection was performed. The second patient (Patient 2) had a tumor located in the insular, temporal, and frontal lobes. This patient's tumor was progressing and under observation for a year after the first brain resection. Both patients gave informed consent to use their data sets and for the first time these data sets are being used in a research study. These patients' MRI acquisition dates, tumor volumes, type of MRIs, and orientations of segmentation are recorded in Table 4.1. Notice that there were more time points than required for the proposed method. We included these time points for analysis and validation purposes. The voxel size of the MRIs in our case study ranged from $0.9 \times 0.46 \times 0.46mm^3$ to $0.5 \times 0.5 \times 5.0mm^3$. Our collaborating neurosurgeon manually segmented all patient tumors and Patient 1 cavity in the axial orientation from the original MRI resolution using the OsiriX tool [Rosset et al., 2004]. These segmentations were converted into a nifty file format (which can be read by Matlab) using the method described in [Angelini et al., 2012; Schmitt et al., 2013]. For Patient 2, the first follow-up image after surgery was discounted (85 days after surgery) because it was right on the border of adherence to the American College of Radiology (ACR) guidelines [American College of Radiology, 2013], which states that the maximum slice thickness should be no greater than $5mm$ and an interslice gap should be no greater than $2.5mm$. For this $FLAIR$, the voxel size was $0.9 \times 0.9 \times 5.0mm^3$ with interslice gap of $1mm$. Figure 4.8 shows the patients' tumor volume evolution and the mean tumor diameter (MTD) calculated using the segmentations of our collaborating neurosurgeon, where the zero days date corresponds to the date of the tumor resection. MTD is used by the medical community [Mandonnet et al., 2013] to evaluate the size of a tumor based on its volume V and it is defined as

$$MTD = (2V)^{1/3}. \tag{4.2}$$

Data Challenges: There were four main challenges encountered with these patient's data. Two of the challenges can only be highlighted, but not solved. For the other two we created rules to foster coherency between the tumor seg-

Patients’ Data Sets

	Patient 1				***Patient 2***			
Time	*Date (days)*	*Volume (mm^3)*	*Image Type*	*Orien-tation*	*Date (days)*	*Volume (mm^3)*	*Image Type*	*Orien-tation*
T_{-3}					-643	55681	FLAIR	Coronal
T_{-2}	~~-49~~	~~17961~~	~~FLAIR~~	~~Axial~~	-468	67968	FLAIR	Axial
T_{-1}	-1	17961	FLAIR	Axial	-11	94370	FLAIR	Axial
				Surgery (Day 0)				
T_1	+74	1422	FLAIR	Axial	+221	22586	FLAIR	Coronal
T_2	+172	4317	FLAIR	Axial	+344	30564	FLAIR	Coronal
T_3	+211	8705	FLAIR	Axial				
T_4	+267	11537	FLAIR	Axial				
T_5	+348	15374	FLAIR	Axial				

Table 4.1: Patient MRI acquisition dates (in days from the surgery), tumor volumes (segmented by neurosurgeon), type of MRI, and orientations of acquisitions. The red font highlights the MRI that was used as the baseline image for the registrations. The blue strike-through displays the MRI that could not be used in our study because the patient had a generalized seizure the day before imaging.

mentations throughout the patients’ sequential imaging timelines. First, many of the FLAIRs were interlaced together when acquired causing a one to two voxel toggle shift between each z-slice. This introduced extra error into the tumor segmentations. Second, in clinical practice there is not a standard way of collecting or reviewing data because a clinician will segment a tumor’s progress in the orientation that best shows the tumor and the type of MRI sequence can change from one study to another. For example, at some time points axial FLAIR MRIs, where the original MRI z-slices were sparsely sampled, were acquired and a tumor was segmented in the axial orientation. At other time points, sagittal FLAIR MRIs, where the original MRI x-slices were sparsely sampled, were ordered and segmented in the coronal direction. This registration challenge, along with no standard naming convention for the MRIs, creates a difficulty for automating the registration process with clinical data in the future. Third, manual tumor segmentation is subjective and has inter- and intra-expert segmentation variability. If a tumor is chronologically segmented at several time points, the follow-up registered segmentations may or may not include the same voxels that were included in the segmentation of the first time point. To account for this, since our method is not able to account for tumors that decrease in size and with

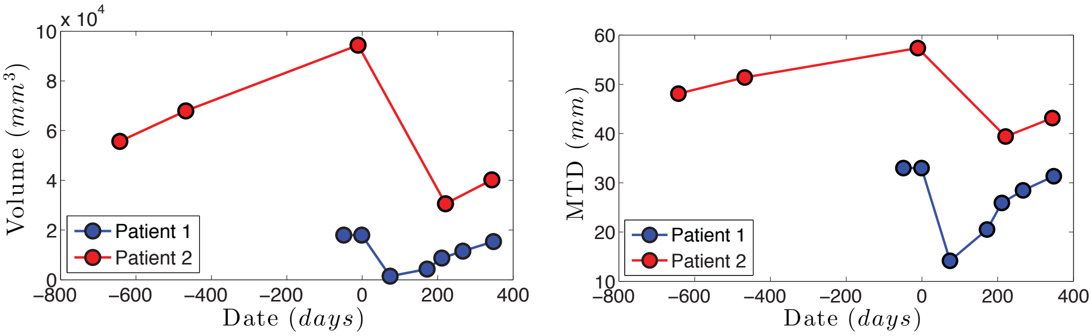

Figure 4.8: Patients' tumor volume evolution (left) and mean tumor diameter (MTD) (right) calculated using the segmentations of our collaborating neurosurgeon. The zero days date corresponds to the date of the surgery.

agreement from our collaborating neurosurgeon, we made *Rule* #1: Once a voxel has been marked as tumor, it will remain as tumor in follow-up segmentations as long as the updated segmentations agree with the hyper-intense voxels of the corresponding FLAIR MRIs. If this step is not taken, the minimization in Step II will not converge, in which case it will not be possible to find the tumor growth speed. This requirement held true for all of the segmentations in this study. Fourth, since the post-operative tumor and resection cavity segmentations in our method were done manually, the borders between the two will not always touch in the areas that they should have and overlapped in areas that they should not. We propose to account for when they overlap by making *Rule* #2: If a voxel is marked as both a tumor segmentation at T_1 and a resection cavity at T_1, the resection cavity voxel is relabeled as a tumor segmentation at T_1. The overlap between resection cavity and tumor were never more than two voxels for Patient 1 and not relevant for Patient 2 (see Section 4.5.1). Therefore, for these patient cases *Rule* #2 could have been omitted.

4.5 Results

In this section, we show the results of using the data of the two patients presented in the previous section to evaluate the proposed method in Figure 4.2 to obtain an infiltration map at a future time after the tumor resection.

4.5.1 Image Pre-processing Results

In Figure 4.9 we show, for each patient, the quality of the registrations performed in Step I of our method (see Figure 4.3). To demonstrate that the non-linear registration after surgery was successful on the FLAIR MRIs, meaning that the brain

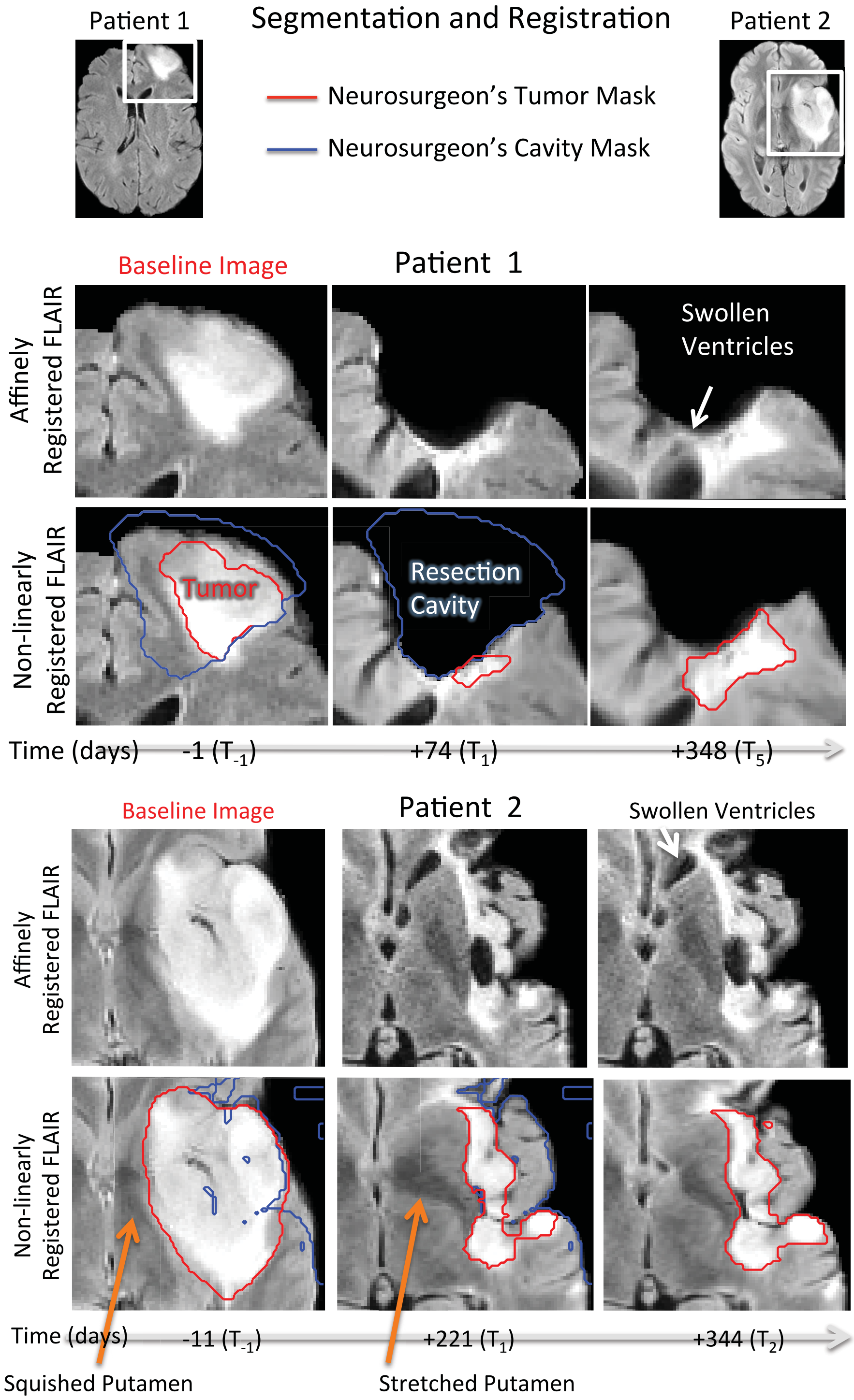

Figure 4.9: Image pre-processing results, where the top images (per patient) were affinely registered and the bottom images were non-linear registered. Notice that after surgery the non-linearly registered tissue was in the same orientation as the before surgery, this includes the ventricles going from swollen to not swollen. The orange arrows indicate the change in the size of the putamen.

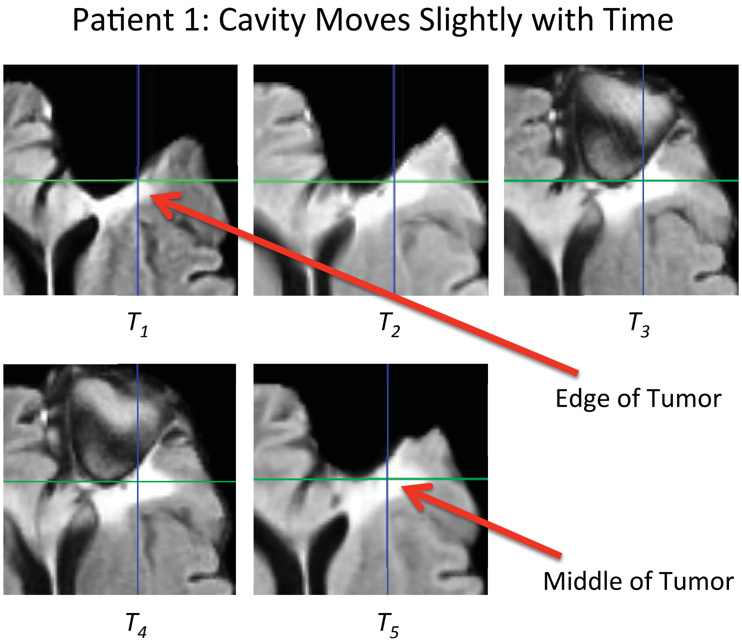

Figure 4.10: Patient 1 resection cavity movement shown by five post-operative non-linearly registered FLAIR MRIs. The cross hairs show the same coordinates in each image. $FLAIR_3$ and $FLAIR_4$ have some CSF artifacts in the resection cavity that can be ignored according to our collaborating neurosurgeon.

parenchyma was aligned after surgery to the images before surgery, we compared, for both patients, the non-linear registrations against their respective affine registrations. For Patient 1, notice that in the post-operative affine registrations the ventricles are swollen, while in the non-linear registrations the brain parenchyma before and after surgery is well aligned with the FLAIR images (see the red and blue delineations in Figure 4.9). This alignment outside the mask of the resection cavity confirms the success of the registration and makes modeling tumor progression after a brain resection possible. For Patient 2, the images after surgery are also successfully registered to the baseline image at T_{-1}; however, the tumor at T_{-1} does not seem to match the tumor, CSF, and brain parenchyma at time T_1. This was caused by a very large mass effect before surgery and brain shift after surgery. Thus, Figure 4.9 shows that even though the non-linear registrations accounted for brain shifts inside the brain parenchyma mask, it could not account for brain shifts inside the resection cavity. This issue is shown for Patient 1 in Figure 4.10 and for Patient 2 in Figure 4.11. Notice for Patient 1 in Figure 4.10 that the cavity moved from the first FLAIR image taken at T_1 to the last one at T_5, shown with the cross-hairs. Since this shift was not large and $Tumor_{-1}$ did not overlap $Tumor_1$ (see Figure 4.9), this brain shift did not effect the results for

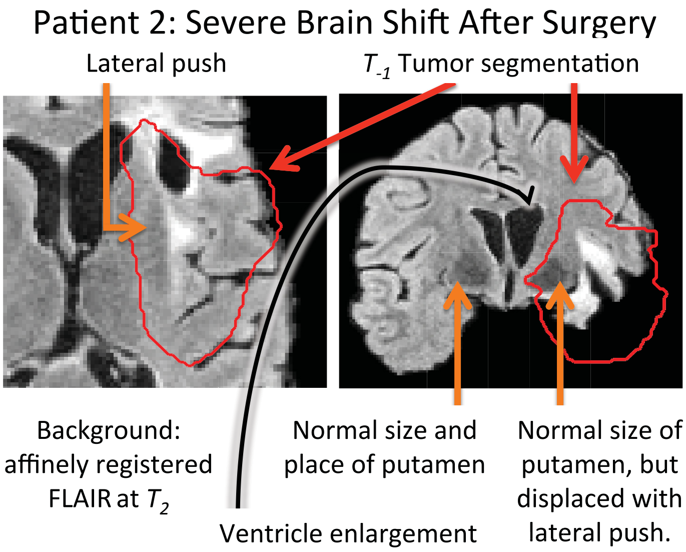

Figure 4.11: Patient 2 severe brain shift after surgery. The before surgery tumor segmentation is much larger than the after surgery tumor cavity and leftover tumor. This is an artifact of the significantly displaced tissue before surgery. After surgery, the squished tissue tried to return to its normal position and applied a lateral push towards the cavity.

Patient 1. For Patient 2, we observed in Figure 4.11 that the brain shift inside the resection cavity was very large. The tumor caused large mass effects in other parts of the brain, which moved when the tumor was removed. In Figure 4.9, the orange arrows show the mass effect in the depth of the insula. The putamen was significantly displaced (towards the midline) and squished before surgery, as can be seen with the image at T_{-1}. After surgery, it returned to its normal size; however, because of ventricular enlargement, it was pushed a little bit more laterally than the healthy normal position. Figure 4.11 shows this lateral push with an orange arrow. The non-linear registration was not able to displace the CSF of the resection from the ventricle enlargement to the outside of the brain. Instead, the non-linear registration stretched the putamen, seen Figure 4.9. Therefore, we are not able to model tumor growth between the before surgery images and the after surgery images, which means that we are not able to combine the infiltration maps of before and after surgery in Step III of our method on Patient 2. In conclusion, we found from this image pre-processing results that our method is applicable when the brain mass effect is not too severe before surgery and the brain parenchyma shift is small after surgery.

4.5.2 Estimation of Tumor Growth Speed Results

In this section we present the results of applying Step II of our method (Figure 4.5) to the registered images of both patients, obtained in Step I (Figure 4.3). For Patient 1, Step II was applied to images after surgery (time points T_1 and T_2) instead of images before surgery as the method indicates. The reason for this was that it was not possible to obtain a good tumor segmentation from the FLAIR images at T_{-2} since Patient 1 had suffered from seizures just before this image was taken. For Patient 2, we were able to use pre-operative images from three time points (T_{-1}, T_{-2}, and T_{-3}). For both patients the Simplex algorithm was able to converge to a solution of the parameter estimation problem in Equation 4.1. In Figure 4.12 we show the minimization results for Patient 2 using the tumor segmentations at time points T_{-2} and T_{-1}. To compare the asymptotic tumor growth speed ($v = 2\sqrt{d_w \rho}$), resulting from the time-dependent parameter estimation optimization, to manual calculations of speed we define, based on Equation 2.8, the average growth rate between two time points T_i (time from origin of the tumor to i^{th} tumor segmentation) and T_j (time from origin of the tumor to j^{th} tumor segmentation) as

$$\overline{v} = \frac{1}{2}\left(\sqrt{d_w}\frac{4T_i\rho - 3}{2T_i\sqrt{\rho}} + \sqrt{d_w}\frac{4T_j\rho - 3}{2T_j\sqrt{\rho}}\right). \tag{4.3}$$

To compare our results with those found by the medical community, we define the tumor growth rate (GR) based on MTD (see Equation 4.2) between two images at times T_i and T_j ($T_j > T_i$) as

$$GR = \frac{MTD_j - MTD_i}{T_j - T_i}. \tag{4.4}$$

Table 4.2 displays the comparison among the tumor growth speeds v, $\bar{v}$, and GR. Notice that the GR and $\overline{v}$ were similar in value for Patient 1; however, for Patient 2, there was a big difference between them. We attribute this to the fact that the tumor shape of Patient 2 was very irregular making the spherical assumption the cause of the errors in the calculation of GR. We can also see from Table 4.2 that the Dice coefficient found for Patient 1 was lower than the ones from Patent 2. This was expected due to the use of post-operative images for Patient 1, which were very difficult to segment because of the presence of scar tissue in the images. It is worth noticing the agreement of the tumor growth speed estimates of Patient 2 between the time intervals [T_{-3}-T_{-2}] and [T_{-2}-T_{-1}], which gives more confidence to our speed estimates.

Algorithm Runtime: The runtime of the minimization algorithm is about twenty minutes, which is similar to the runtime of minimization proposed by

[Konukoglu, 2009]. The tests were performed on a Mac Desktop with a 2 x 3.2GHz Quad-Core Intel Xeon processor with 16GB of memory.

Estimated Tumor Growth Speed

Patient #	*Time Interval*	*GR (mm/yr)*	$\overline{v}$ *(mm/yr)*	v *(mm/yr)*	*Dice coeff.*
1	$[T_1\text{-}T_2]$	24	23	25	0.7
2	$[T_{-3}\text{-}T_{-2}]$	5	15	16	0.9
2	$[T_{-2}\text{-}T_{-1}]$	5	15	16	0.9

Table 4.2: Comparison of the tumor growth speed estimates for Patient 1 and Patient 2 using different time intervals.

4.5.3 Estimation of Tumor Infiltration Results

In this section we present the results of performing Step III of the method, graphically described in Figure 4.7. First, we present the results by patient, and then

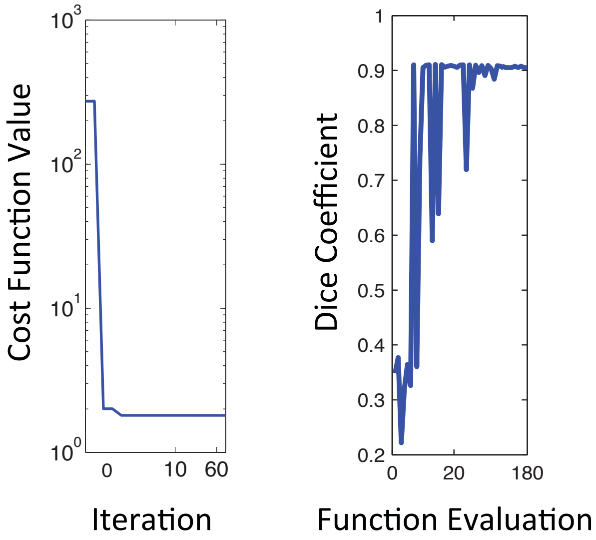

Figure 4.12: Minimization results of the parameter estimation problem in Equation 4.1 for Patient 2 using tumor segmentations at T_{-1} and T_{-2} time points. The plot on the left shows the minimization of the cost function value (C in Equation 4.1) as the iterations of the Simplex algorithm progress. The plot on the right shows how the Dice coefficient increases as the number of evaluations increases. In the Simplex algorithm there are several evaluations per iteration.

report the algorithm runtime.

Patient 1: Step III was successfully performed on Patient 1. Figure 4.13 shows the sweeping results for the time interval [T_1-T_2]. The red boxes show the invisibility index d_w/ρ that resulted in the maximum Dice coefficient at T_2, i.e., $d_w/\rho = 4mm^2$ achieved the maximum Dice coefficient of 0.7. Figure 4.13 also shows how the Dice coefficient resolved the trade-off between Specificity and Sensitivity. In Table 4.3 we can see that the sweep between the time intervals [T_1-T_5] had a higher Dice coefficient than the sweep between [T_1-T_2]. This accuracy difference can be attributed to the possible segmentation inaccuracies in $FLAIR_2$. Due to our method of combining the infiltration maps at T_{-1} and T_1, the tumor segmentation at T_1 does not have as much uncertainty as the one at T_2. In $FLAIR_5$, the neurosurgeon was able to distinguish between other hyper-intense artifacts and delineate the tumor. Notice that the optimal value of d_w/ρ was only $1mm^2$ different between the two time intervals. Therefore, we can say that the tumor of Patient 1 was bulky according to our method. To further validate Step III, we used the $d_w/\rho = 4mm^2$ with the combined infiltration map and ran the FK reaction diffusion equation for the time intervals [T_1-T_2], [T_1-T_3], [T_1-T_4], and [T_1-T_5]. Table 4.4 shows these recorded Dice coefficient values after thresholding the found infiltration maps at 20% cell density. Notice that from time T_3 on, the neurosurgeon was able to easily identify in the $FLAIR$ images what was tumor and what was not. Finally, Figure 4.14 shows three sequential tumor infiltrations maps, which used $d_w/\rho = 4mm^2$ invisibility index. The top images show the unannotated non-linearly registered MRI $FLAIR$s for the same time points as the bottom images. The annotated image at T_{-1} includes the infiltration map from time T_{-1}, while the image at T_1 includes the combined infiltration map (see Figure 4.7). The image at T_5 is the result of using the combined infiltration map and running the FK reaction diffusion model simulation from T_1 to T_5. The estimated visible tumor (20% infiltration mark shown with light blue line in Figure 4.14) matched the neurosurgeon's tumor segmentation (red line) for the T_5 time point reasonably well (Dice coefficient was 0.9, see Table 4.4). The black arrows show the directions of the tensors, which will be the fastest direction of growth. The tumor was very bulky so we showed the estimated infiltration until 0.001%.

Patient 2: Step III could not be successfully performed on Patient 2 due to the large amount of brain shifting after surgery and the large mass effect that this patient was burdened with before surgery. Therefore, it was not possible to use a combined infiltration map at time T_1. Thus, the infiltration was calculated using only post-operative images. However, to get good infiltration maps, the images needed to be from much later time points than in the case of Patient 1

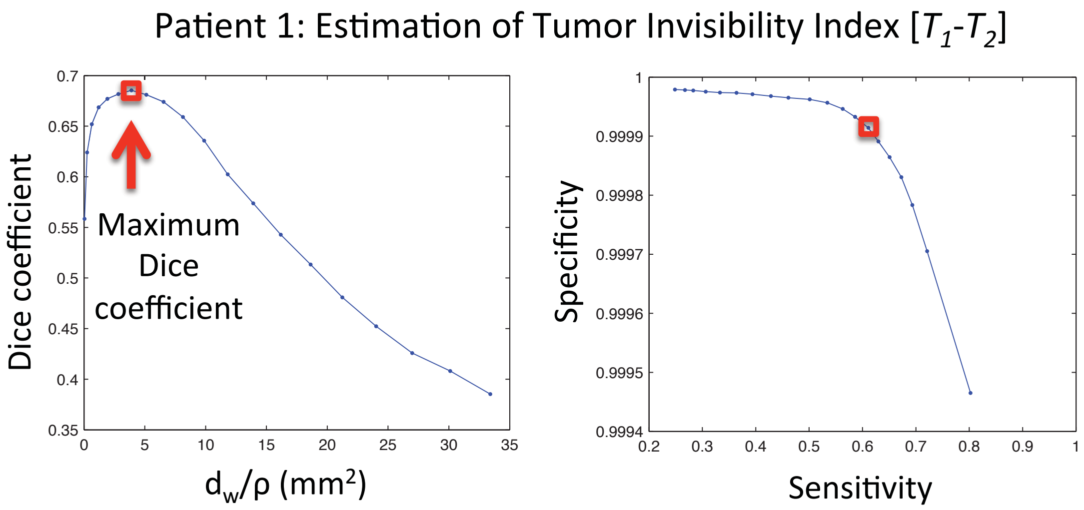

Figure 4.13: Results of sweeping through the physically feasible ranges of d_w/ρ while keeping v constant for Patient 1 between T_1 and T_2, where the infiltration map used was a combination of the simulated map from T_{-1} to T_1 with the infiltration map of T_1. Notice the maximum Dice coefficient highlighted in each plot with red boxes. It can be seen that the Dice coefficient resolved the trade-off between Specificity and Sensitivity.

Patient 1: Sweep Through d_w/ρ, v constant

Time Interval	d_w/ρ *range (mm^2)*	d_w/ρ *optimal (mm^2)*	*Dice coefficient*
T_1-T_2	[0-34]	4	0.7
T_1-T_5	[0-34]	5	0.9

Table 4.3: Results of sweeping through the feasible range of d_w/ρ, while keeping v constant, for Patient 1 with different time intervals.

(+221 days vs +74 days after surgery). The rest of the operations of Step III were followed as outlined in Figure 4.7. Figure 4.15 shows the sweeping results for the time interval $[T_1 - T_2]$. The red boxes show the invisibility index d_w/ρ that resulted in the maximum Dice coefficient at T_2, i.e., $d_w/\rho = 22mm^2$ achieved the maximum Dice coefficient of 0.9. Figure 4.15 also shows how the Dice coefficient resolved the trade-off between Specificity and Sensitivity. Figure 4.16 shows the infiltrations maps, which used $d_w/\rho = 22mm^2$ invisibility index. The top images show the un-annotated non-linearly registered MRI FLAIRs for the same time

Patient 1: Tumor Development After Resection

Time Intervals	$[T_1\text{-}T_2]$	$[T_1\text{-}T_3]$	$[T_1\text{-}T_4]$	$[T_1\text{-}T_5]$
Dice coefficient	0.7	0.9	0.9	0.9

Table 4.4: Tumor development after resection of Patient 1 for different time intervals. Displayed are the Dice coefficients, between the threshold of the simulated tumor, which used $d_w/\rho = 4mm^2$, and the neurosurgeon's tumor segmentations.

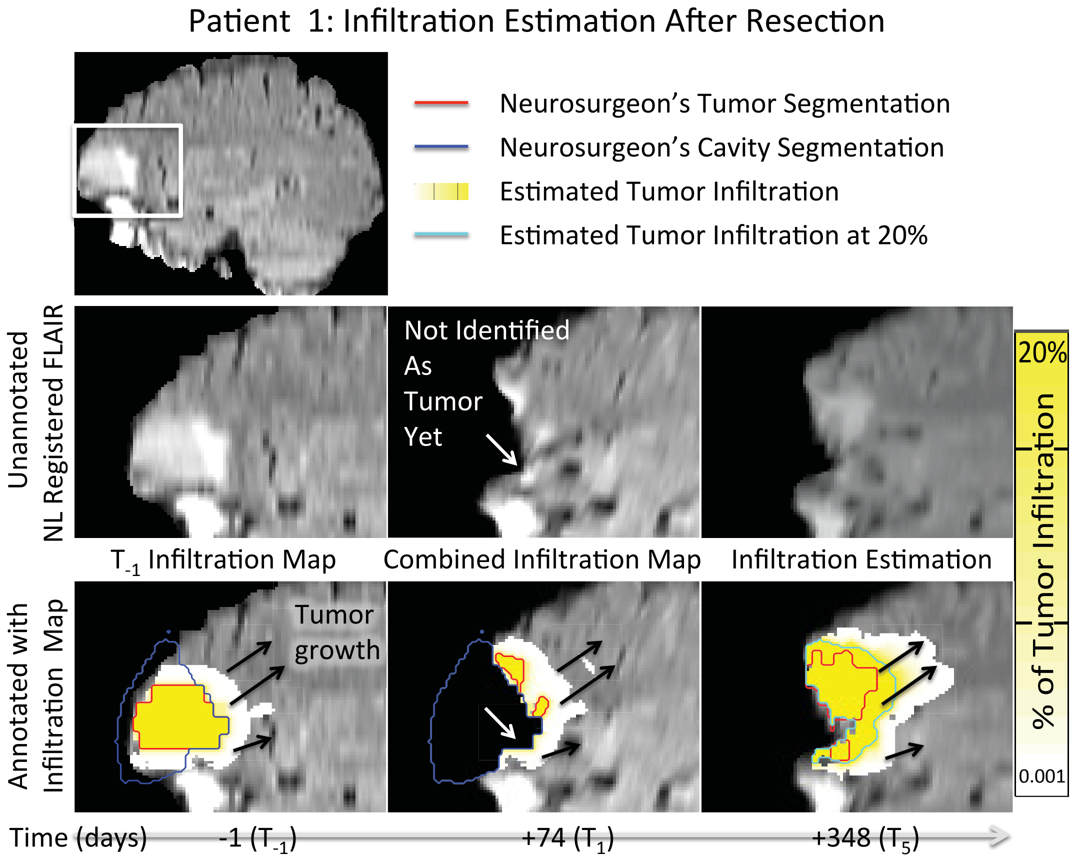

Figure 4.14: Infiltration maps for Patient 1 overlaid on the non-linearly registered FLAIR MRIs. From left to right: the infiltration map for T_{-1}, the combined infiltration map for T_1, and the tumor infiltration estimation at T_5. The black arrows represent the registered diffusion tensor directions. The white arrows indicate the hyper-intense voxels that were not identified as tumor by the neurosurgeon at time T_1, but that the combined infiltration map included.

points as the bottom images. The annotated image at T_{-1} includes the infiltration map from time T_{-1}, and the image at T_1 includes only the infiltration map from time T_1. The image at T_2 is the result of using the infiltration map at T_1 and running the FK reaction diffusion model simulation from T_1 to T_2. The estimated visible tumor (20% infiltration mark) shown with light blue line in Figure 4.16 matched the neurosurgeon's tumor segmentation (red line) for the T_2 time point reasonably well (Dice coefficient = 0.9). The tumor was diffuse so we showed the estimated infiltration until 5%.

Algorithm Runtime: This entire process took on average 24 minutes per d_w/ρ combination (19 images printed out per test). The tests were performed on a MacBook Pro with a 2.2 GHz Intel Core i7 processor with 8 GB of memory.

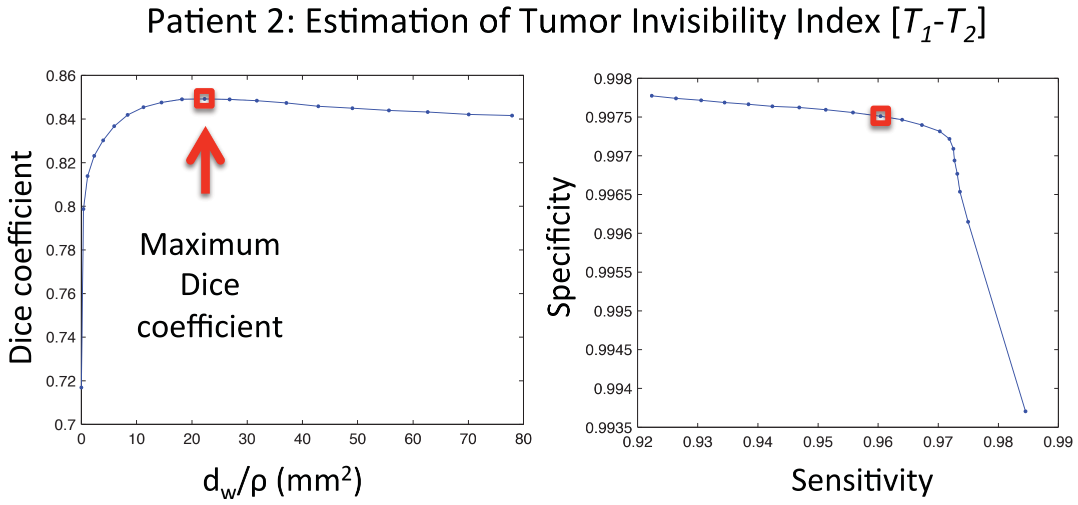

Figure 4.15: Results of sweeping through the physically feasible ranges of d_w/ρ while keeping v constant for Patient 2 between T_1 and T_2, where the infiltration map used was from time T_1. Notice the maximum Dice coefficient highlighted in each plot with red boxes. It can be seen that the Dice coefficient resolved the trade-off between Specificity and Sensitivity.

4.6 Discussion

There are two main challenges to estimate infiltration maps after tumor resections that our proposed method was able to address: i) brain parenchyma and CSF shifts after surgery, and ii) the quality of the tumor segmentations.

For the brain parenchyma and CSF shifts after surgery, the non-linear registration was able to put all images into the orientation before surgery, but the

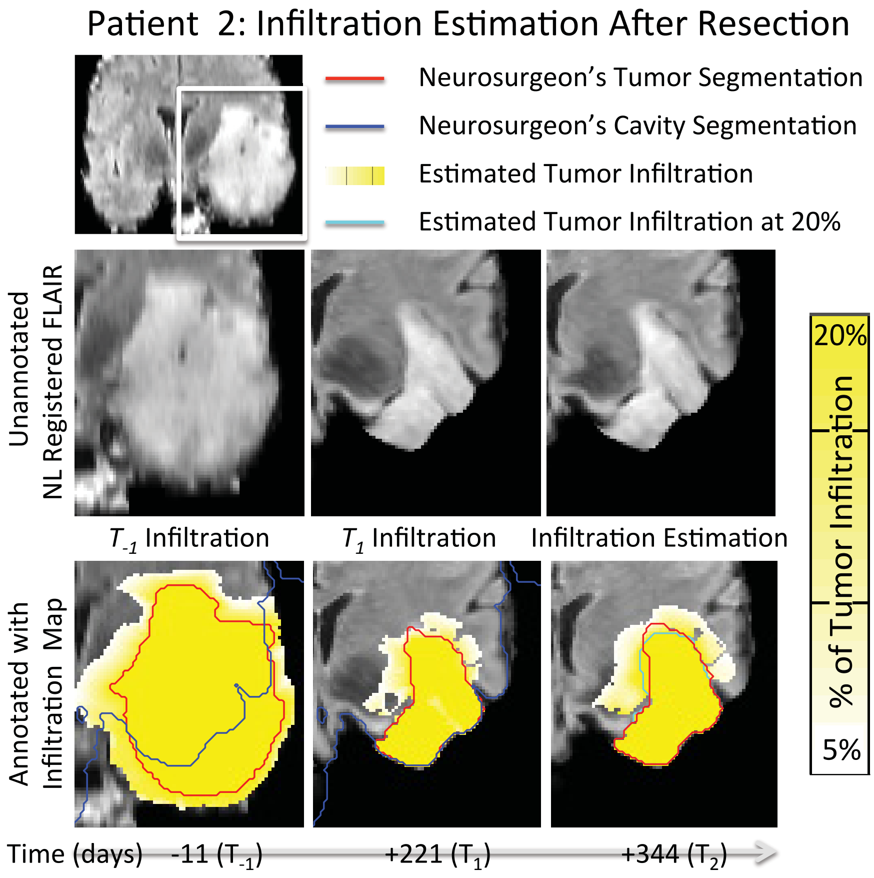

Figure 4.16: Infiltration maps for Patient 2 overlaid on the non-linearly registered FLAIR MRIs. From left to right: the infiltration map for T_{-1}, the infiltration map for T_1, and the tumor infiltration estimation at T_2.

non-linear registration algorithm could not totally account for the brain shifts under the cavity mask and could not rearrange the position of CSF in the brain. However, the use of a brain parenchyma mask at T_N instead of T_1 in our method made these effects less severe. For instance, for Patient 1, when we used the brain mask at T_5 in Step III, we were able to model the evolution of the tumor quite well (Dice coefficient between simulation and segmented tumor equal to 0.9, see Table 4.3). Yet, if we use the brain mask at T_1 we could only achieve a Dice coefficient of 0.5 (see Figure 4.17) since we could not account for 22% of the tumor that was under the brain mask at T_1. For Patient 2, there was a very large mass effect in the pre-operative images that caused a large redistribution of CSF and brain matter in the post-operative images. The non-linear registration was able to put the post-operative images into the pre-operative orientation, allowing us to model tumor evolution; however, it could not redistribute the locations of the

CSF after surgery. Therefore, after the non-linear registration, the structures in the post-operative images did not correspond to the exact same locations in the pre-operative images, preventing us from combining the infiltration maps at times T_{-1} and T_1 in Step III. To overcome this problem, instead of using a combined infiltration map in Step III we used the infiltration map at T_1 that corresponded to 221 days after surgery. With this infiltration map we were able to successfully estimate the infiltration map at T_2 (344 days after surgery). This result showed that large mass effects have an impact on how early the method can estimate infiltration maps after surgery. Notice, that for Patient 1 we were able to estimate infiltration maps 172 days after surgery while for Patient 2 we did it for 344 days after surgery.

Regarding the quality of the segmentations, when a glioma is diffuse it is very hard to segment and it is unclear in FLAIR MRIs whether a hyper-intense voxel is tumor, scar tissue, or blood after surgery. It is only after several scans that a neurosurgeon can tell the difference between these hyper-intense signals on MRIs and therefore a neurosurgeon will generally under-segment a tumor in scans taken within a few months after surgery. In Figure 4.14, we show a white arrow pointing to a hyper-intense set of voxels that a neurosurgeon was unsure if they were tumor or not, so he did not include them in his tumor segmentation at T_1 (red delineations). Notice that the combined infiltration map (yellow map) includes this area at time T_1 and that the neurosurgeon includes this area in his tumor segmentation at time T_5; this shows that the combined infiltration map was able to account for the non-segmented regions at T_1.

4.7 Conclusion and Perspectives

In the cancer-modeling field, estimating glioma infiltration after surgery is of great importance since as a result of medical protocols, most glioma patients are subject to resections within a short period of time after tumor detection. Then, medical professionals want to know what the best type of follow-up treatment would be for a particular patient, i.e., chemotherapy for diffuse tumors or resection for bulky tumors. There are two main challenges involved in estimating glioma infiltration directly after surgery: i) there is substantial brain parenchyma and CSF movement after surgery, and ii) the tumor segmentations after surgery may not be complete since there is a potential for blood and scar tissue to be confused with tumor. We addressed the first challenge with the use of a non-linear registration algorithm, and our method resolved the second challenge by using a combined infiltration map, i.e., combination of tumor infiltration maps from before and after surgery. We used two patients' data, with different tumor locations and invasiveness to demonstrate the effectiveness of the proposed

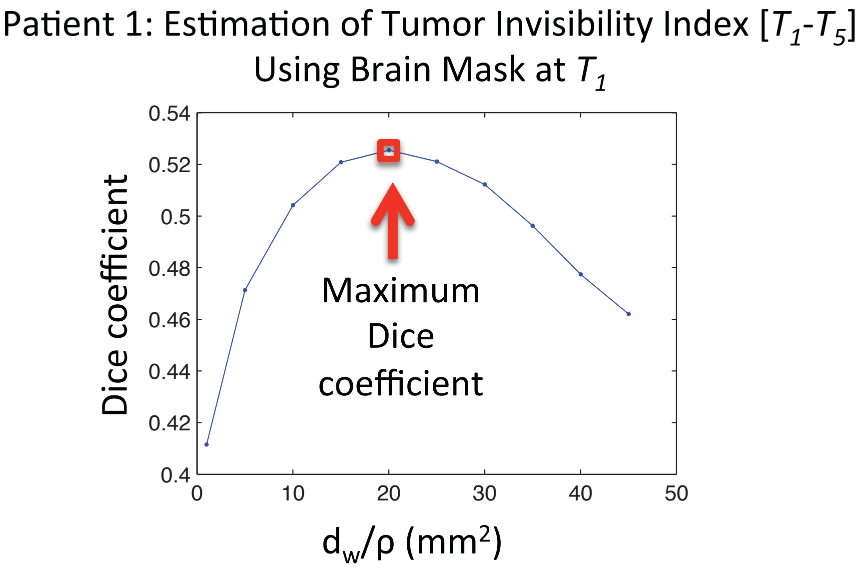

Figure 4.17: Sweeping through the values of d_w/ρ using the brain mask of time T_1. A combined infiltration map was used to grow the tumor simulation forward to the last time point T_5, using the brain parenchyma segmentation of T_1. However, we could not account for 22% of the tumor that was under the brain mask at T_1.

method. For one patient, we successfully applied the method at four time points after surgery (from 172 to 458 days) that when thresholded at 20% cell density match neurosurgeon's tumor segmentations (Dice coefficient > 0.7). For the other patient, severe mass effects caused a lower effectiveness of the method soon after surgery; however, the method was able to find an infiltration map at 344 days after surgery that when thresholded at 20% cell density matched a neurosurgeon's tumor segmentation (Dice coefficient $= 0.9$). We think that in subsequent studies data of more patients shall be used to improve the proposed method and increase the confidence on its effectiveness. In addition, we believe that the post-operative brain and CSF shifts could be further compensated in future works by using mechanical models, such as the one proposed by Clatz et al. [2005]. Finally, we would like to highlight in the following list the novel contributions attained during the development of the proposed method to estimate tumor infiltration after surgery resection:

- We developed a novel registration framework to register post-operative MR images following tumor resection and segmentations to pre-operative MR images and segmentations (Step I).
- We defined a novel registration framework to register a reference brain mask

to a patient T1 image while preserving the CSF sulci barriers (Step I).

- We applied a combination of a non-linear registration algorithm (Step I), a FK model traveling time formulation (Step II), an infiltration map calculation (Step III), and a FK model reaction-diffusion simulation (Step III).
- We added the Dice coefficient into the cost function used to find the FK model parameters (see Equation 4.1 in Step II).
- We utilized a Simplex optimization algorithm to find the FK model parameters (Step II).
- We combined pre- and post-operative infiltration maps to compensate for incomplete segmentations soon after surgery (Step III).
- We swept through d_w/ρ to identify the infiltration characteristics of a glioma, i.e., bulky or diffuse (Step III).

In summary, we hope that this work can be used by the medical and image processing community and that this topic continues to receive attention so that in the near future a tool will become available for clinicians to estimate tumor infiltration after brain resection to aid them in their therapy planning.

Chapter 5

Assessing LGG Progressive Disease using Growth Speed Estimates from a Fisher Kolmogorov Model Formulation

Contents

Based on a paper that was submitted to the Journal of Computerized Medical Imaging and Graphics.

5.1 Context

Progressive disease (PD) for low-grade glimoas (LGG) is reached when radiological evidence of malignant transformation of a lesion or clinical deterioration not attributed to other causes apart from the tumor occurs. There have been many studies in the literature to correlate PD of brain tumors to different metrics of tumor size change, based either in tumor diameters (one-dimensional), tumor areas (two-dimensional), or tumor volumes (three-dimensional). However,

for LGG captured on FLAIR/T2 MRIs, there is substantial amount of debate on selecting a definite threshold on these size-based metrics to determine PD and it is still an open item for the Response Assessment in Neuro-Oncology (RANO) Working Group. In this chapter we propose to use model-based tumor growth speed estimates as an alternative metric to determine PD since one can anticipate future growth based on growth speed. Manual tumor growth speed methods have already been used by physicians to determine the aggressiveness of tumors. However, these manual calculations suffer from large inter-rater variability and inaccuracies. To address this we introduce a tumor growth speed formulation based on the Fisher Kolmogorov (FK) model, which promises to be more accurate since it takes into consideration irregularities in tumor shape, differences in growth speed between gray matter and white matter, and volumetric changes. Thus, in this chapter we propose an approach to assess PD of LGG using tumor growth speed estimates from a FK formulation. Using FLAIR MRIs of nine patients we compare the PD estimates of the proposed approach to i) the ones calculated using manual tumor growth speed estimates and ii) the ones calculated using a set of well established size-based criteria (RECIST, Macdonald, and RANO). We conclude from our comparison results that our proposed approach is promising for assessing PD of LGG from a limited number of MRI scans and worthy of further research.

5.2 Introduction

Low-grade gliomas (LGG) are a type of malignant and very diffuse brain tumor that invades the fastest along white matter fiber tracts with dynamic and spatial features that vary widely between patients. For decades, a mainstay of treatment for diffuse LGG patients has been radiotherapy [Buzdar and Freedman, 2007]. However, there is a controversy as to when to give radiotherapy since it is *unknown* if immediate or delayed radiotherapy offers any advantage. Some radiation oncologists follow the approach of "watchful waiting" for the well-differentiated grade II astrocytomas (not anaplastic) and reserve radiotherapy for tumors that progress to a higher-grade malignancy, which are undifferentiated or anaplastic, to allow the patient to have a higher quality of life for a longer time. The main argument in favor of this approach is that radiation is more effective in proliferative cells [Buzdar and Freedman, 2007] and it is not possible to repeat radiation indefinitely since there is a maximum cumulative dose a patient can tolerate. Other radiation oncologists prefer to immediately initiate radiotherapy on the hypothesis that early intervention eradicates the most proliferative and aggressive cells at the earliest stages, thereby reducing the population of cells most likely to progress to a higher grade. In the end, both groups of radiation

Table 5.1: Comparison of Measurement Methods for Progressive Disease (PD).

Imaging Modality	*RECIST* (1D)	*Macdonald* (2D)	*RANO* (2D)	*Volumetric* (3D)
T1-gad	$\geq$ 20% increase in sum of maximal diameters; confirm at 4 weeks	$\geq$ 25% increase in product of orthogonal diameters; confirm at 4 weeks	$\geq$ 25% increase in product of orthogonal diameters; confirm at 4 weeks	$\geq$ 40% increase in volume
T2/FLAIR	$\geq$ 20% increase in sum of maximal diameters; confirm at 4 weeks	N/A	Significant increase	$\geq$ 40% increase in volume

oncologists want to know the best time to start radiotherapy.

There have been several proposed types of criteria to help oncologists distinguish the progression status of gliomas and decide when therapy should be given. Table 5.1 compares, in terms of progressive disease (PD), four of these criteria: the Response Evaluation Criteria in Solid Tumors (RECIST) [Eisenhauer et al., 2009], the Macdonald [Henson et al., 2008], the Response Assessment in Neuro-Oncology (RANO) [Wen et al., 2010], and a volumetric-based criterion [Galanis et al., 2006].

For the RECIST, PD is measured in one-dimension (1D) and requires either i) an increase of 20% or more in the longest diameter (d in Figure 5.1) of a solid tumor, which must be confirmed four weeks later, or ii) the appearance of new lesions. If there are multiple lesions, the longest diameter measurements of the lesions are summed. The minimal measurable lesion diameter is either $10mm$ or two times the imaging section thickness in order to reduce the variability in section selection and volume averaging between clinical studies. This criterion accepts different types of MRIs in which the tumor growth is measured. In addition, the RECIST has not been validated as a method for assessing time-to-progression (TTP) in brain tumors [Warren et al., 2001], which is defined as the time from a patient's first set of MRI scans to the time a patient reaches PD. It has also not been widely used in brain tumor clinical trials due to the historic use of 2D measurements.

The Macdonald criterion uses a two-dimensional (2D) metric that is applied

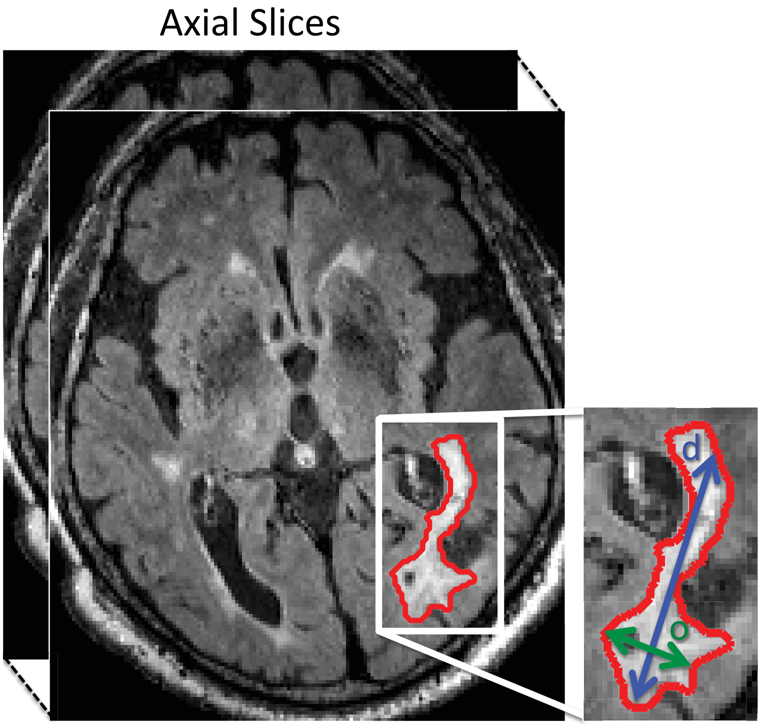

Figure 5.1: Diameter-based measurements on a single-axial section used for the evaluation of tumor size on serial MR image studies. d is the maximum tumor diameter among all the axial slices of a lesion and o is the maximum diameter orthogonal to d within the same axial slice. The RECIST criterion uses d to determine the progressive state of the lesion (1D-based) while the Macdonald and RANO criterions use the product $d * o$ (2D-based).

in many high-grade glioma clinical trials to determine disease progression. This metric is defined as the maximal enhancing tumor diameter on a single axial gadolinium-enhanced T1-weighted slice (d in Figure 5.1) multiplied by the largest perpendicular diameter on that same slice (o in Figure 5.1). For multiple lesions, this product is summed. For each patient scan this metric is re-calculated and PD is defined when its value increases more than 25% from a patient's first scan or smallest measurement.

The RANO is a 2D criterion that measures tumors size in the same way as the Macdonald criterion except that T2 and FLAIR imaging can also be used to determine PD. This is important since FLAIR MRIs produce the clearest and most reproducible definition of World Health Organization (WHO) grade II glioma (LGG) margins [Bynevelt et al., 2001; Pallud et al., 2010]. The down side of using FLAIR and T2 imaging is that it can be difficult to differentiate increased T2 or FLAIR signal from radiation effects, decreased corticosteroid dosing, demyelination, ischemic injury, infection, seizures, postoperative changes, and other treatment effects. Therefore, the RANO Working Group believes that it is not possible at present, given the limitations of current technology, to put a precise percentage of tumor increase to define PD when using T2 or FLAIR MRIs.

The volumetric criterion is a three-dimensional (3D) measurement that simply includes all voxels inside of a 3D tumor segmentation. This metric has been compared to the current 1D and 2D measurements [Galanis et al., 2006; Shah et al., 2006; Warren et al., 2001]. For each patient scan this metric is re-calculated and PD is defined when its value increases more than 40% from a patient's first scan or smallest measurement. The added value of using a volumetric criterion is yet to be determined and is a current area of investigation [Galanis et al., 2006].

The RECIST, Macdonald, and RANO criteria are based on measuring diameters and as a result have the down side to not taking into account i) irregularities in tumor shape, ii) differences in growth speed in white and gray matter, iii) interobserver variability, and iv) tumor volume. The volumetric criterion has only the first three weaknesses. In [Therasse et al., 2006] it was reported that four separate studies, with a total of 204 patients, had a high concordance between manual 1D (RECIST), 2D (WHO: 25% increase in product) and 3D (volumetric) measurements for detecting responses in brain tumors. However, in [Therasse et al., 2006] it was also indicated that the results of assessing disease progression were less uniform among the different dimensional criteria. It is foreseen, in the near future by the RANO Working Group that volumetric measures, new physiologic imaging techniques (perfusion imaging, permeability imaging, diffusion imaging, magnetic resonance spectroscopy), metabolic imaging, and other end points such as quality-of-life measures will be further developed, validated, and incorporated into the RANO response criterion.

Biophysical models have been proposed to model glioma growth speed and predict future tumor expansion, taking into account the irregularities in tumor shape, volume, and tissue growth speed differences [Tracqui, 2009]. The Fisher Kolmogorov (FK) model is a well accepted standard for modeling glioma growth [Murray, 2002; Konukoglu et al., 2009; Menze et al., 2011a; Gooya et al., 2011a; Hogea et al., 2008; Stretton et al., 2013]. This model was first proposed in 2D [Burgess et al., 1997; Tracqui et al., 1995b; Woodward et al., 1996], and then evolved to 3D [Clatz et al., 2005; Jbabdi et al., 2005]. Swanson et al. [Swanson et al., 2000] extended the 2D model to include the heterogeneity of brain tissue on synthetic data modeling isotropic spatial diffusion. Then, Konukoglu et al. [Konukoglu et al., 2009] proposed a method to estimate the tumor growth parameters for specific patients (personalization) and estimate the tumor's growth speed using both time-dependent and asymptotic growth speed formulations.

A future goal would be to use these biophysical models in a clinical setting to help radiation oncologists decide when to start therapy on LGG patients. However, we need to take incremental steps in order to have these mathematical tools adopted by clinicians. To the best of our knowledge, this chapter acts as a first step towards this goal by comparing various manual measures of glioma tumor growth speed with a biophysical model, proposing a weighted tumor growth speed based on the white matter segmentation of a patient, and proposing to use speed as an additional new parameter to indicate the aggressiveness of a tumor and to predict TTP, which could be helpful in determining when to treat a patient.

This chapter is organized as follows. In Section 5.3, the methods used for this comparison are presented. In Section 5.4, the data and pre-processing techniques are examined. In Section 5.5, the results are presented and in Section 5.6, the results are discussed. Finally, in Section 5.7 we conclude about our findings from this study.

5.3 Methods

In this section we present three manual methods for calculating tumor growth speed, use the results from the FK model parameter estimation to calculate tumor growth speeds, present an inter-expert tumor segmentation variability measure, and propose a novel Time-To-Progression calculation based on tumor growth speed.

Manual Tumor Growth Speed Calculations: Three methods for calculating radial tumor growth speed from MRI scans at two different time points are presented: a 1D-based, a 2D-based, and a 3D-based. For the 1D-based calculation, the radial tumor growth speed is defined as

$$v_{1D} = \frac{d_2 - d_1}{2\delta t}, \tag{5.1}$$

where d is the maximum tumor diameter among all the axial slices of a lesion (see Figure 5.1), the sub-indices indicate the MRI scan time points, and δt denotes the time in between the two MRI scans. For the 2D-based calculation, the maximum tumor diameter and the orthogonal diameter (d and o in Figure 5.1 respectively) are considered. To get a radial distance measurement, the area of an ellipse, calculated using d and o, is equated to the area of a circle, and then the radii of the correspondent circles at the two different MRI scan time points is used to calculate the 2D-based tumor growth speed (v_{2D}). Thus, it follows that

$$v_{2D} = \frac{\sqrt{d_2 o_2} - \sqrt{d_1 o_1}}{2\delta t}. \tag{5.2}$$

The 3D-based tumor radial growth speed calculation is given by

$$v_{3D} = \frac{\sqrt[3]{V_2 \frac{3}{4\pi}} - \sqrt[3]{V_1 \frac{3}{4\pi}}}{\delta t}, \tag{5.3}$$

where V_1 and V_2 represent the volumes at the first an second MRI acquisition time points respectively. Notice that it is assumed that the tumor is formed in homogeneous and isotropic tissue in all of these manual speed calculations.

Tumor Growth Speed Calculations based on the FK Model: From the results of the parameter estimation problem of the FK Model in Equation 2.19 we calculated the average growth rate, in white matter, between two time points (T_1 and T_2) by using the time-dependent speed formulation of Equation 2.8 as follows:

$$v_{w\_TD} = \frac{1}{2}\left(\sqrt{d_w}\frac{4T_1\rho - 3}{2T_1\sqrt{\rho}} + \sqrt{d_w}\frac{4T_2\rho - 3}{2T_2\sqrt{\rho}}\right), \tag{5.4}$$

and in gray matter by

$$v_{g\_TD} = \frac{1}{2}\left(\sqrt{d_g}\frac{4T_1\rho - 3}{2T_1\sqrt{\rho}} + \sqrt{d_g}\frac{4T_2\rho - 3}{2T_2\sqrt{\rho}}\right). \tag{5.5}$$

Since the white matter segmentation mask is available in our model, then it is also possible to calculate a weighted tumor growth speed based on the percentage of the tumor in either white matter or gray matter, i.e.,

$$v_{weighted\_TD} = (v_{w\_TD})^{\alpha}(v_{g\_TD})^{1-\alpha}, \tag{5.6}$$

where α is the percentage of the tumor in white matter. To the best of our knowledge using a weighted average to estimate tumor growth speed has not been proposed before.

Using the same estimated parameters we calculate the asymptotic speed of growth, which is not unique for ρ and $d_{w,g}$ separately [Konukoglu et al., 2009; Stretton et al., 2012], in white matter by

$$v_{w\_A} = 2\sqrt{d_w\rho}, \tag{5.7}$$

and in gray matter by

$$v_{g\_A} = 2\sqrt{d_g\rho}, \tag{5.8}$$

and weighted in both white and gray matter by

$$v_{weighted\_A} = (v_{w\_A})^{\alpha}(v_{g\_A})^{1-\alpha}. \tag{5.9}$$

To calculate the simulation error of our model, we compute the root mean squared error (RMSE), defined as

$$RMSE = \sqrt{\text{dist}(\Gamma_2, \overline{\Gamma_2})^2}, \tag{5.10}$$

where dist() is the symmetric distance separating the simulated and segmented surfaces normalized by the surface area of the surfaces. Γ_2 is the surface encompassing the tumor in the image taken at the second acquisition date (T_2), and $\overline{\Gamma_2}$ is the tumor delineation simulated by the traveling-time approximation of the FK model at acquisition time T_2 (equations 2.14, 2.15, and 2.16). To account for the size of a tumor in the error calculation, we scaled the error using the tumor volume at T_2 as follows

$$\epsilon = \frac{RMSE}{\sqrt[3]{V_2}}, \tag{5.11}$$

where V_2 is the volume of the tumor segmentation at the second time point.

For comparing manual speed calculations with model-based speeds one should consider that the confidence on the computation depends on the scaled minimization error ϵ in Equation 5.11 and the time in between images for manual speed calculations (δt in equations 5.1, 5.2, and 5.3). Table 5.2 shows the roles of these elements in our confidence of the speed comparison. Notice that if the time differences between the images of the manual speed calculations are high and the scaled error of our model is low, a good confidence on our speed comparison (manual vs. model) can be concluded. When both the time in between the manual calculations are high and our model's scaled error calculation is high, or both the time in between the manual calculations is low and our model's scaled error calculation is low, we cannot conclude whether the speed comparison would be good since $\epsilon/\delta t$ is a relative measurement. However, if the time in between the manual calculations is low and our model's scaled error calculation is high, our confidence in a good comparison is low.

Table 5.2: Speed Comparison Confidence Criteria

Manual δt	ϵ	$\epsilon/\delta t$	*Speed Comparison Confidence*
↑	↓	↓	↑
↑	↑	?	?
↓	↓	?	?
↓	↑	↑	↓

Inter-Expert Segmentation Error: A radiologist and an expert performed the segmentations used for the speed estimations in this chapter. The radiologist's manual segmentations included all imaging acquisitions for each patient. The expert's segmentations included only two time points and were used with the time-dependent FK speed formulation to find v_{w_TD} and v_{g_TD}.

The expert segmented the patients' tumors using a level-set segmenter implemented in ITK-SNAP [Yushkevich et al., 2006], where two of the patients' segmentations needed to be manually corrected. For all patient tumor segmentations, we removed any voxels that went outside of the brain parenchyma segmentation to ensure that the boundary conditions of the time-dependent model were respected and visually inspected the tumor segmentations to ensure accuracy.

We calculated the relative differences in volume and maximum diameter between the two specialists' segmentations to document the segmentation variability and to validate if the level-set segmenter produced reasonable segmentations. For the volume, we have

$$\delta V_{seg} = \left| \frac{(V_E - V_R)}{V_R} \right|, \tag{5.12}$$

where V_E is the tumor volume segmented by the expert and V_R is the tumor volume segmented by the radiologist. For the maximum diameter, we have

$$\delta d_{seg} = \left| \frac{(d_E - d_R)}{d_R} \right|, \tag{5.13}$$

where the d_E is the maximum diameter of a tumor on an axial slice measured by the expert and d_R is the maximum diameter of a tumor on an axial slice measured by the radiologist.

Time-To-Progression Calculations: The TTP calculations based on the 1D RECIST, the 2D RANO, and the 3D volumetric criteria considered in this chapter are given by

$$TTP_{1D} = T_2 - T_1 \quad \text{when} \quad d_2 - d_1 \geq 0.2 d_1, \tag{5.14}$$

$$TTP_{2D} = T_2 - T_1 \quad \text{when} \quad d_2 o_2 - d_1 o_1 \geq 0.25 d_1 o_1, \quad \text{and} \tag{5.15}$$

$$TTP_{3D} = T_2 - T_1 \quad \text{when} \quad V_2 - V_1 \geq 0.4 V_1, \tag{5.16}$$

where T, d, o, and V represent, for two different FLAIR scans indicated by the sub-indices, the time points, maximum tumor diameter, orthogonal maximum tumor diameter, and the tumor volume respectively. Our collaborating radiologist choose to set the 2D RANO threshold at 0.25, consistent with the threshold given for the T1-gad MRIs, since the RANO criteria does not state an exact signal percentage increase to define PD using FLAIR MRI.

In order to use tumor growth speed estimates (either manual or model-based) to predict TTP we consider the tumor growth speed when the 1D RECIST criteria is satisfied ($d_2 - d_1 = 0.2d_1$) to be

$$v = \frac{d_2 - d_1}{2TTP} = \frac{0.2d_1}{2TTP} = \frac{0.2r_1}{TTP}, \tag{5.17}$$

where the radius of the tumor at the first scan (r_1) is extracted from the tumor volume also at the first scan (V_1) assuming a spherical tumor shape, i.e., $r_1 = \sqrt[3]{\frac{3V_1}{4\pi}}$. Then we have that TTP based on a tumor growth speed v is given by

$$TTP_v = \frac{0.2\sqrt[3]{\frac{3V_1}{4\pi}}}{v}. \tag{5.18}$$

If we consider from the model white matter speed (v_w), then an earlier TTP will be found than if we consider the gray matter speed (v_g). The “true” TTP shall be within the white matter speed estimate (TTP_{v_w}) and the gray matter speed estimate (TTP_{v_g}), i.e., “true” $TTP \in [TTP_{v_w}\ TTP_{v_g}]$. Having this interval in the prediction of TTP could be beneficial to the radiologist when deciding between a “watchful waiting” approach or a more aggressive approach. In addition, a TTP based on a weighted speed, i.e., $v_{weighted_A}$, could be calculated to get a more precise prediction. Furthermore, the scaled model error ϵ in Equation 5.11 could also be regarded as a confidence indicator for these TTP predictions. Thus, we considered that this novel proposed TTP calculation based on a biophysical model where heterogeneous tissue is accounted for and volumetric changes are considered will bring better predictions of PD to the radiation oncologist because these predictions will contain not only a TTP value, but also a worse-case-best-case interval of TTP values with a confidence indicator.

5.4 Data

The data was acquired as part of an unpublished study from the Heidelberg German Cancer Research Center (DKFZ) on the radiological follow-up of patients with astrocytoma grade II, approved by the local ethics board. All nine patients had given informed consent to participate in this study.

Description of Patient Data: The grade of the tumors were determined by surgical biopsies for all, but one patient (Patient 9). MRI sequences FLAIR and T1 after applications of gadolinium contrast agents were used to monitor the patients; however, only FLAIRs were used to calculate tumor growth speed. We had anywhere from 4 to 16 scan dates for each patient who only had one glioma each. There were no resections or records of therapy applied among these patients during the observation time captured in this study, except for patients 3 and 6, who had partial resections and completed radiation therapy before entering the study.

Pre-Processing: In order for the simulations to be run using the mathematical model, the patients images needed to be pre-processed. The MRIs of each patient were rigidly registered (using FSL FAST [Jenkinson and Smith, 2001; Jenkinson et al., 2002]) to the highest resolution MRI in their longitudinal sequence and interpolated to $1 \times 1 \times 1mm^3$. Note that none of these patients suffered from a tumor mass-effect. The white matter and brain parenchyma were registered and segmented the same way as described in Section 4.4. Some patients did not reach TTP using one or all of the metrics (equations 5.14, 5.15, and/or 5.16) because they switched hospitals for care or passed away.

5.5 Results

In this section we present the results of using the patients data of Section 5.4 in combination with the FK formulation to estimate tumor growth speeds and predict TTP. The results of the nine patients studied are compared to manual calculations of tumor growth speeds and to PD estimates using 1D, 2D, and 3D size-based criteria. Before presenting these comparisons we first discuss three items that have an effect on the FK formulation speed estimates accuracy: i) algorithm repeatability, ii) segmentation variability, and iii) error correlation on tumor volume.

To assess the algorithm repeatability, we ran the FK formulation for Patient 6 eight times with input parameters varied by the standard deviations listed in Table 5.3. The algorithm produced speed estimates with a standard deviation of less than 0.5mm/year. Thus, in the rest of this chapter 0.5mm/year will be considered as the accuracy level of the FK formulation estimates.

For the segmentations variability, we use equations 5.12 and 5.13 to compare the segmentations of both specialists. It was found that the expert and radiologist segmentations agreed in volume on every patient except Patient 2. The average δV_{seg} of all patients, but Patient 2, was 30% for both time points. The segmentation of the radiologist for Patient 2 was 5.5 times smaller than the one

Table 5.3: Repeatability of the FK formulation speed estimates (Patient 6 data)

Parameter Inputs	*Standard Deviation*
d_w	$1.36\ mm^2/year$
d_g	$0.73\ mm^2/year$
ρ	$2.73E^{-06}\ 1/year$
T_0	$1278\ days$
Output	*Standard Deviation*
v_{w_A}	$0.4\ mm/year$
v_{g_A}	$0.5\ mm/year$
$v_{weighted_A}$	$0.5\ mm/year$

from the expert for the first time point and 22 times smaller for the second one. The reason for this difference was that the expert included some microangiopathy hyper-intense areas around the tumor, which could not be distinguished from the tumor without significant medical knowledge. However, the average δd_{seg} of all patients (including Patient 2) for both time points was 17%. Therefore, with the exception of Patient 2, the segmentations made by the expert using ITK-Snap were similar to the segmentations made by the radiologist.

For the FK formulation error correlation to the tumor volume we plot in Figure 5.2 the cubic root of the patients tumor volumes at the second image against their RMSE (see Equation 5.10). It is not surprising that as the tumor volume increased, so did the error since the larger a tumor is, the more difficult it is to match the entire tumor shape using the minimization algorithm. The two patients with the largest error (patients 2 and 4) also had difficult images to segment, where Patient 2 had a white matter lesion (microangiopathy) and Patient 4 had a poor quality second image.

For the comparison of the tumor growth estimates between the model and the manual calculations we considered two cases: i) time-dependent speed calculations and ii) asymptotic speed calculations.

For the time-dependent speed calculations, two early time points MRI scans were used by the model (equations 5.4, 5.5, and 5.6) and the manual calculations (equations 5.1, 5.2, and 5.3) to estimate the tumor growth speed between these two time points. In Figure 5.3, the model speed estimations are compared with the manual speed calculations by stacking four different plots on top of each other to give a complete picture of this complex comparison. The top plot compares the radial tumor speed by patient, where the plot is blown up in the right-hand corner to display more clearly the tumor speed estimates of the patients with slower growing tumors (patients 5-9). Notice that v_{w_TD} was always larger than

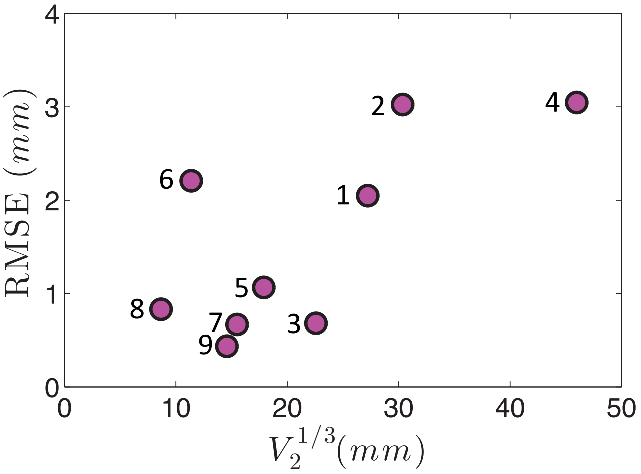

Figure 5.2: RMSE compared with cube-root of the volume (second time point of speed comparison segmented by expert). The numbers in the plot indicate the patient numbers.

v_{g_TD} as suggested in literature. The values that we found for d_w/d_g were between 1-131, where the average value was 33. The second plot from the top displays the time interval (δt) between the baseline image and the second image that the speed was calculated from, where the time differences of the manual calculations made by the radiologist are in blue and the model and experts' ones are in pink. For patients 1 and 5, different baseline images were used for the segmentations made by the expert and the radiologist, but the same second image was used. The third plot shows the model error scaled by volume (ϵ in Equation 5.11). The fourth plot is a combination of the second and third plot that can be used to indicate the confidence of our comparison between the model and the manual calculations (see Table 5.2). Patients 3, 4, 5, 7, and 9 had lower values of $\epsilon/\delta t$ than patients 1, 2, 6, and 8. This would imply that for the former group of patients the match between the model and the manual speed estimates was better than for the later. This is actually the case for most of them. The only exceptions are patients 1 and 3. For Patient 1 the matching between model and manual calculations was good even thought the value of $\epsilon/\delta t$ was larger. This is explained by the fact that the tumor growth speed for Patient 1 was much larger than the other patients making the manual speed calculations less sensitive to a small value of δt. For Patient 3, two out of the six manual calculations did not match with the model estimates. Since these two manual calculations had a very large negative value, which was not physically possible, we concluded that their segmentations were erroneous. The main result of the comparisons in Figure 5.3 is that the speeds of the biophysical model compare well with the manual speed calculations for small

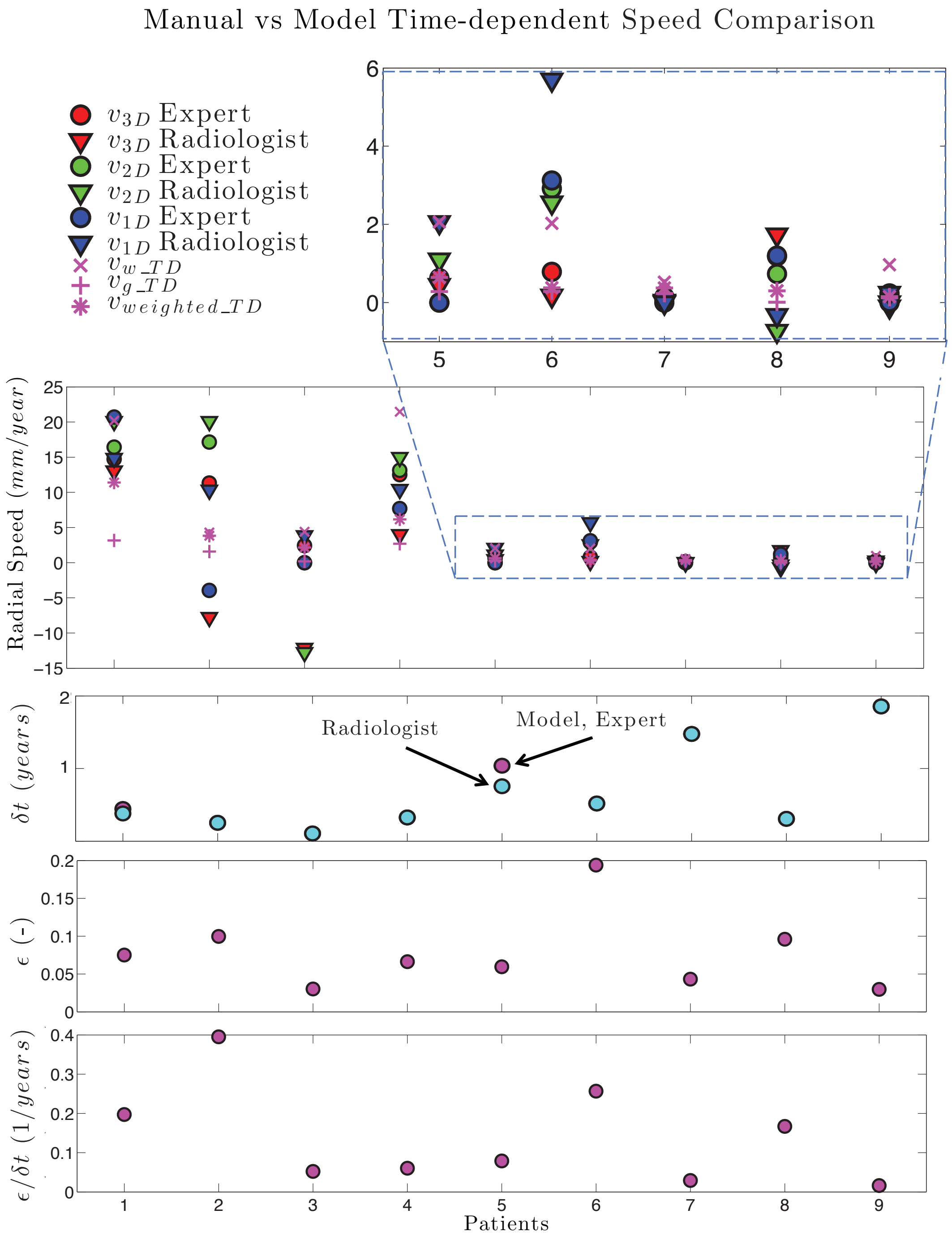

Figure 5.3: Comparison of the time-dependent model speed estimations with the manual speed calculations between the first and second image acquisition dates. The top plot compares the radial tumor growth speed by patient. The second plot displays the time in between speed measurements δt. The third plot shows the scaled model error ϵ, and the fourth plot of $\epsilon/\delta t$ exhibits our confidence on the comparison between the model and the manual speed estimations.

values of $\epsilon/\delta t$.

For the asymptotic speed calculations the model used two early time point MRI scans in combination with equations 5.7, 5.8, and 5.9 while the manual calculations used the first and the last possible time point MRIs with equations 5.1, 5.2, and 5.3. In Figure 5.4 the manual and the model asymptotic speed estimates are compared. The second plot from the top displays the time in between the asymptotic speed calculations for the manual methods (blue) and the model (pink). The third and fourth plots are calculated in the same way as in Figure 5.3. Notice that, as expected, there is a tighter match between the model and the manual calculations for patients 3, 5, 7, and 9, resulting from a lower $\epsilon/\delta t$. Patient 1 also have a good match between the manual and the model regardless of the lower $\epsilon/\delta t$ value, which was caused by a larger tumor growth speed (explained already in the time-dependent case). Thus, we can conclude from Figure 5.4 that the FK formulation was good at predicting asymptotic tumor growth speed from two early MRI scans.

In Figure 5.5 we display the speed changes over time for patients 2, 3, and 4. These patients were chosen for plotting since they had quite substantial amount of variability in the manual measurements displayed in Figure 5.3. Still using equations 5.1, 5.2, and 5.3 for the manual calculations, we estimated the speed for each time point using the baseline image and images at follow-up time points, which allowed us to see the speed progression in time of the tumors. Observe that $v_{weighted\_TD}$ was in between the range of manual speed calculations for patients 2 and 4 for the tumor speed between the first two time points. Patient 3 had to two miss-calculations (1D & 2D) for the speed between the first two time points since they were negative and the rest of the time points showed positive tumor growth speed. In addition, notice that $v_{weighted\_A}$ better predicted these patients' tumor growth speeds for larger time points and that the standard deviation between the three different manual calculations was larger for short time periods and became smaller for longer time periods.

Figure 5.6 presents the white matter tumor growth speeds of these nine patients on a loglog plot for the purpose of comparing with Harpold et al. [Harpold et al., 2007]. Notice that the speed in white matter represents the upper boundary of our model's speed estimates. In the research of Harpold et al., they said that a velocity of more than 10 $mm/year$ indicates a high-grade glioma. The patients in this study have been surgically assessed as harboring low-grade gliomas, yet some of their radial growth speeds are above $10 mm/year$. The model that we used (Equation 2.19 from [Konukoglu et al., 2010b]) cannot find d_w and ρ separately such that d_w/ρ can be calculated. The method of Chapter 4 was not repeated in this chapter; therefore, in this chapter the problem of separating the product $d_w\rho$ is not addressed. Hence, the invisibility measurements are not valid from this plot, since only speed can be calculated from Equation 2.19. Notice

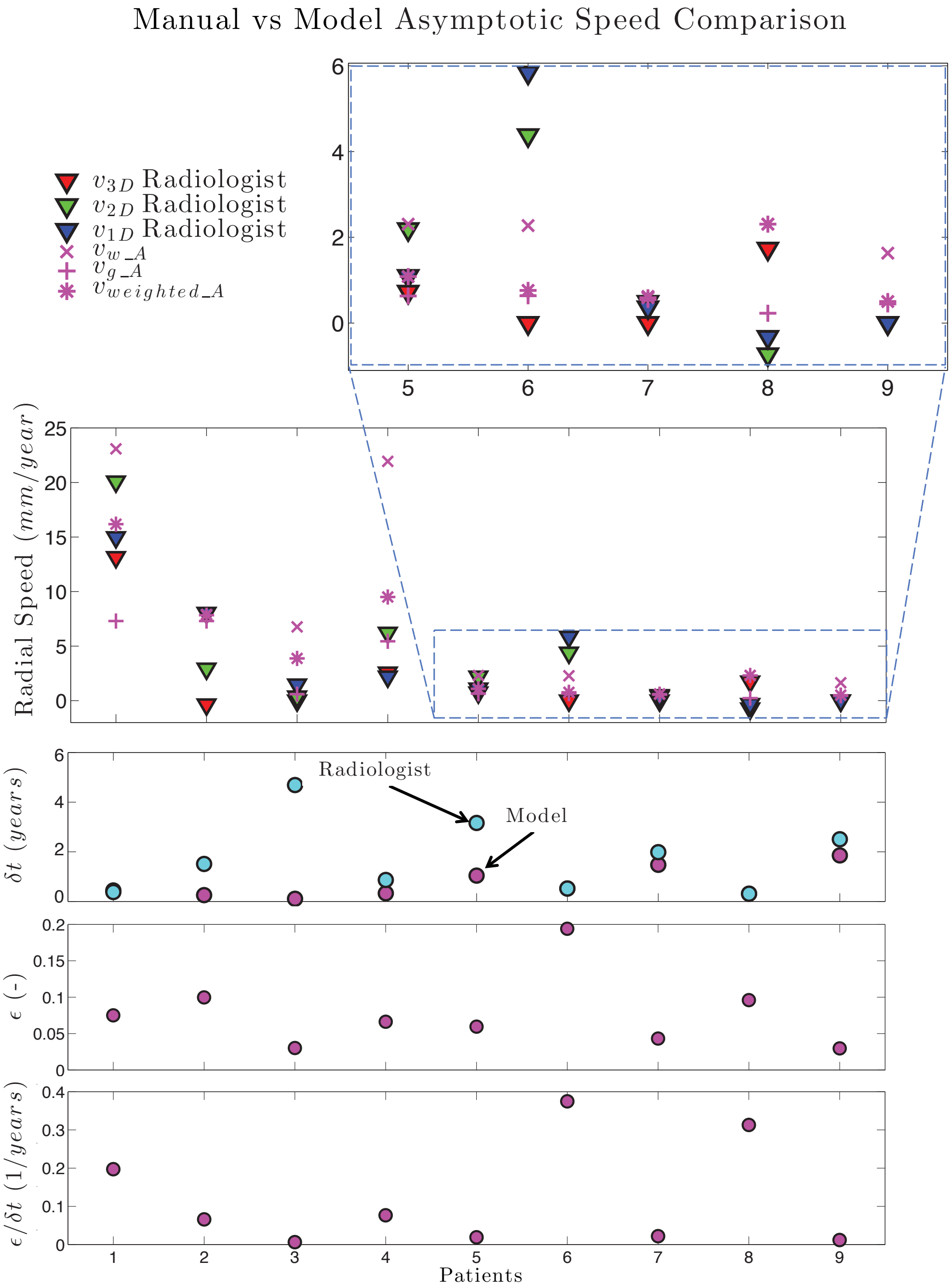

Figure 5.4: Comparison of manual vs. model asymptotic speed calculations to visualize the predictive nature of the biophysical model, where the manual calculations used the baseline and the tumor segmentation (by the radiologist) of the last possible sequential image for each patient before therapy was applied. The model's asymptotic speed estimates used only the first two images. The top plot compares the radial tumor growth speed by patient. The second plot displays the time in between speed measurements δt. The third plot shows the scaled model error ϵ, and the fourth plot exhibits our confidence of the comparison between the model and the manual speed estimates ($\epsilon/\delta t$).

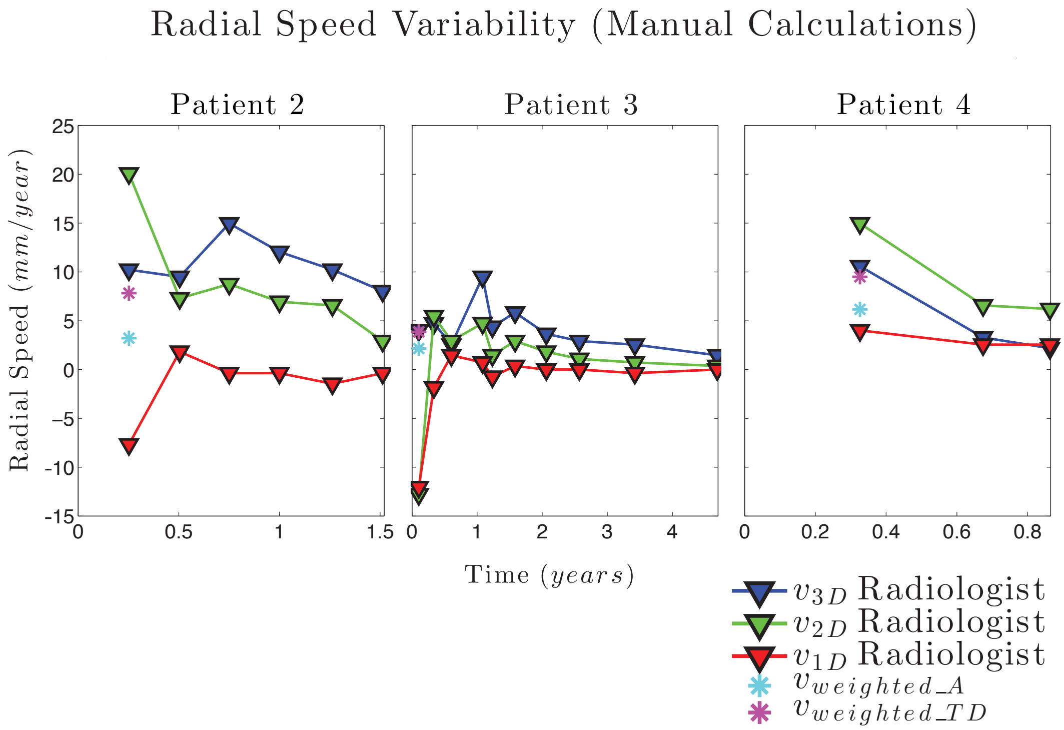

Figure 5.5: Comparison of speed measurements between manual and model-based estimates. The manual calculations of speed were calculated using the baseline image and later longitudinal images for each scan date. The model calculations used only the first two images (Asymptotic and Time-Dependent).

also that there are essentially two ρ values in this plot which remain basically consistent from simulation initialization.

From the asymptotic speed estimates of the model (v_{w_A}, v_{g_A}, and $v_{weighted\_A}$) we predict TTP using Equation 5.18. In Figure 5.7 we show the comparison of the TTP model predictions (pink markers) with the retrospective calculations of TTP (black lines) for 1D RECIST, 2D RANO, and 3D Volumetric (equations 5.14, 5.15, and 5.16). The solid lines in Figure 5.7 indicate that TTP was reached for that metric while the dotted lines indicate the last time point without reaching TTP. Therefore, we expect, for a good match, to have the model TTP predictions (pink markers) below the solid lines and above the dotted lines or at least to have the solid and dotted lines within the interval $[TTP_{v_{w\_A}}\ TTP_{v_{g\_A}}]$. Notice that three out of nine patients reached TTP with the 1D RECIST metric, six out of nine with the 2D RANO metric, and one out of nine with the 3D Volumetric metric. This result agrees with the results of Galanis et al. [2006], where the 2D RANO metric was the most sensitive to estimate progressive disease and the 3D

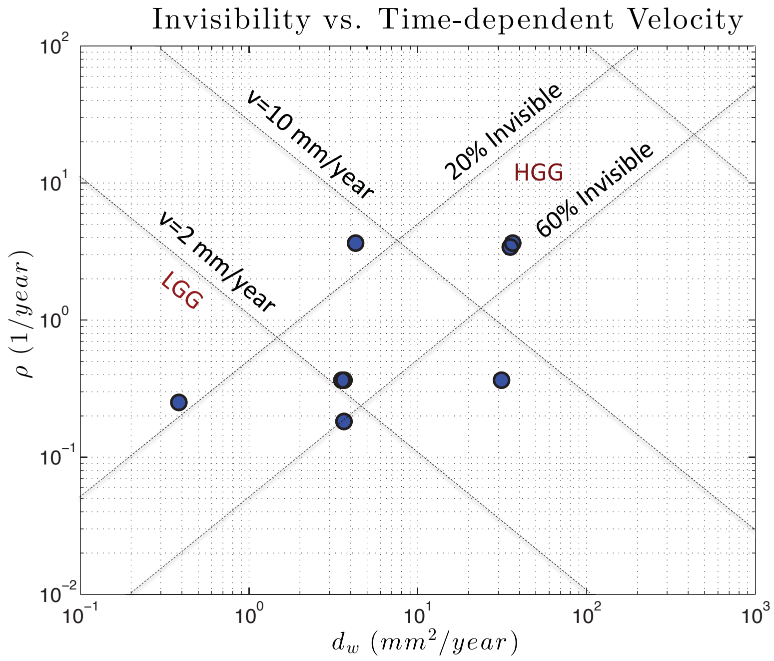

Figure 5.6: Log-log plot of white matter speed estimates. These speed estimates represent the white matter tumor growth speed for these patients. Average speed of a LGG is $2mm/year$ radially. This model, which did not use the method from Chapter 4, could not solve for $d_w\rho$ separately (in the speed formulation); therefore, only the v can be trusted from this plot and not the invisibility amount.

Volumetric metric was the least sensitive. The tumor shape is the main reason for these discrepancies among the 1D, 2D and 3D TTP metrics. For instance, Patient 3 in our study had a finger-like tumor cross section (see Figure 5.8) that resulted in reaching TTP_{1D} and TTP_{2D} before TTP_{3D}. For Patient 5, the rounded shape of the tumor cross section (see Figure 5.9) caused reaching TTP_{2D} earlier than TTP_{1D} and TTP_{3D}. Regarding the TTP model predications in Figure 5.7, we have that for Patient 1, the TTP measures matched with the same date ($TTP_{1D} = TTP_{2D} = TTP_{1D}$), and the predictions of the model were under the solid lines, which means that the model had an accurate prediction of TTP. For Patient 2, the model TTP prediction only matched the 1D RECIST (TTP_{1D}) measure but showed to be closed to the 2D RANO (TTP_{2D}) measure. The mismatch of Patient 2 for the 3D case is explained as the result of large δV_{seg}, discussed previously in the segmentations variability analysis. For patients 3, 4, 5, and 6, at least two out of the three retrospective measures agreed with the TTP model predictions. For patients 7, 8, and 9, the predicted $TTP_{v_{weighted}}$ were above the dotted lines for the three measures. Thus, the main result is that the

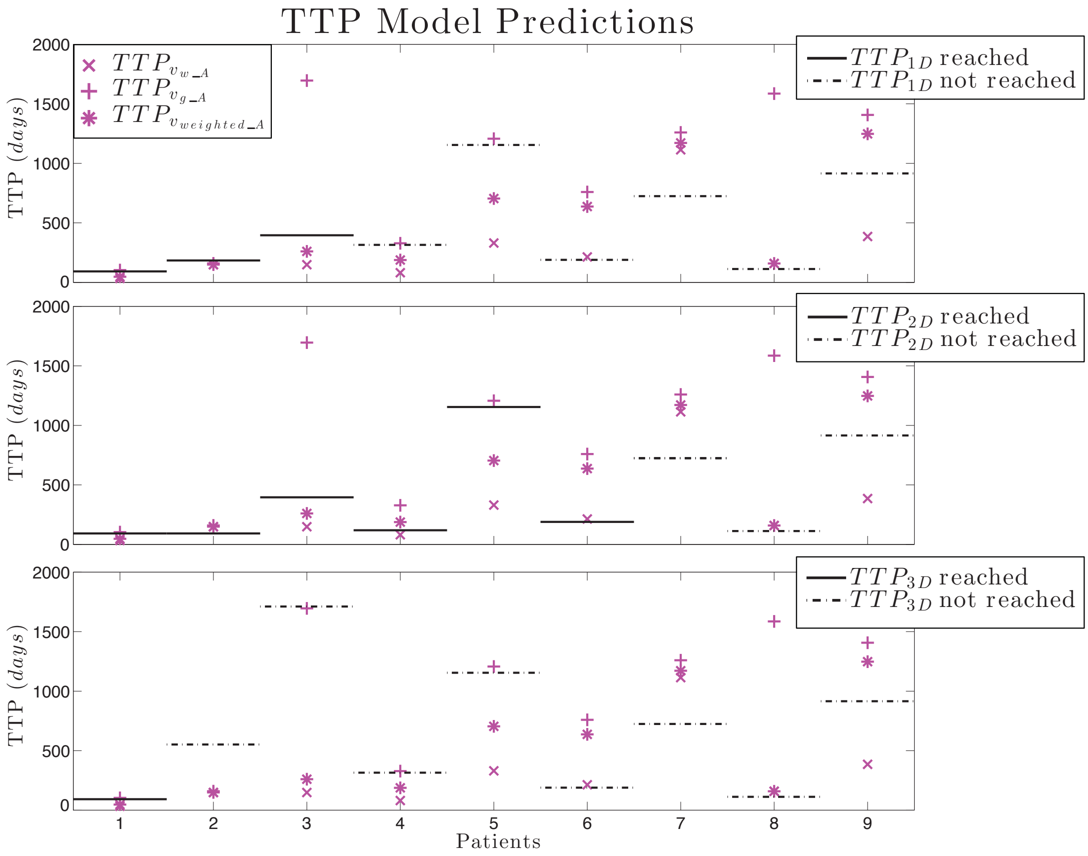

Figure 5.7: Comparison of the TTP model predictions (pink markers) with the retrospective calculations of TTP (black lines) for 1D RECIST, 2D RANO, and 3D Volumetric (equations 5.14, 5.15, and 5.16). The solid lines indicate that TTP was reached for that metric while the dotted lines indicate the last time point without reaching TTP. For a good match, the model TTP predictions (pink markers) should be below the solid lines and above the dotted lines or at least the solid and dotted lines should be within the interval $[TTP_{v_{w\_A}}\ TTP_{v_{g\_A}}]$.

predictive model estimates of TTP, which used only two patient scans, compared well with the manual retrospective calculations, especially for the 1D RECIST and 2D RANO criteria.

Finally, in Table 5.4 we compare the model predicted $TTP_{v_{weighted\_A}}$ from Figure 5.7 with a predicted TTP using manually calculated tumor growth speeds from the radiologist segmentations in 1D (v_{1D} in Equation 5.1) and Equation 5.18, i.e., $TTP_{v_{1D}}$. Notice that the second column in Table 5.4 contains either the interval within which TTP was reached or a single value indicating the last time point when TTP was evaluated. Only the first two acquisition images of each patient were used to estimate both $TTP_{v_{1D}}$ and $TTP_{v_{weighted\_A}}$. The red strikeouts

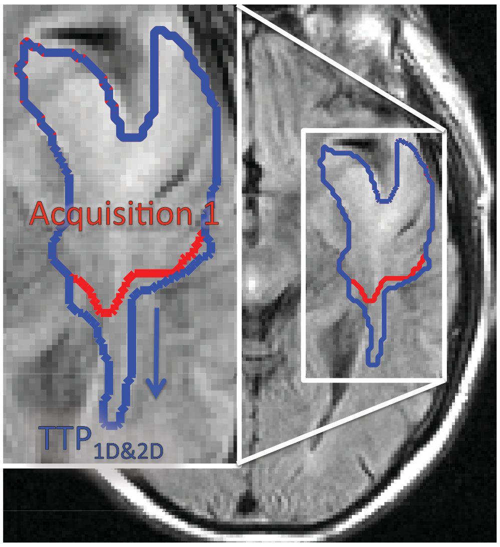

Figure 5.8: Patient 3 reached TTP_{1D} and TTP_{2D} at 396 days but did not reach TTP_{3D}. The red delineation is the first MRI scan and the blue delineation is the scan when TTP_{1D} and TTP_{2D} were reached. The large finger-like pattern resulted in the 1D RECIST and 2D RANO metrics being more sensitive than the 3D Volumetric metric.

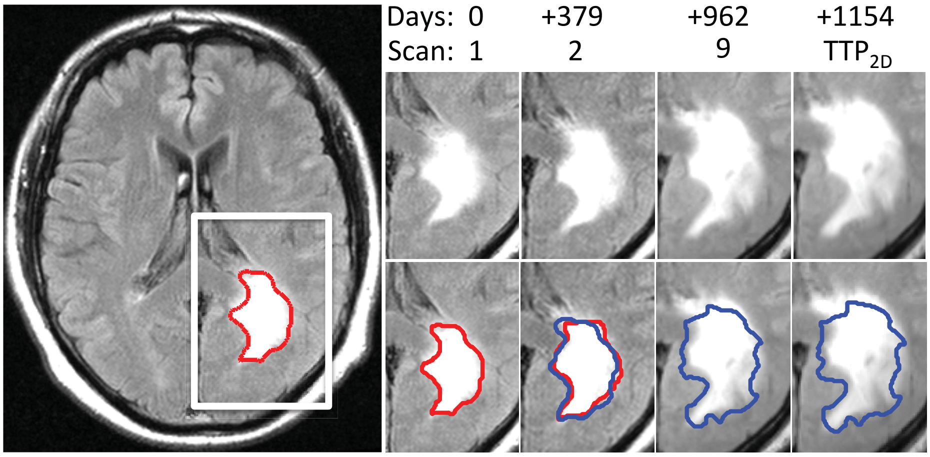

Figure 5.9: Patient 5 reached $TTP_{2D} = 1154$ days, but did not reach TTP_{1D} or TTP_{3D}. The rounded shape of the tumor cross section resulted on the 2D RANO metric being more sensitive than the 1D RECIST and 3D Volumetric metrics.

Manual and Model TTP Predictions in 1D

Patient No.	Retrospectively Calculated TTP Interval in 1D *(days)*	Radiologist Predicted $TTP_{v_{1D}}$ *(days)*	Model Predicted $TTP_{v_{weighted\_A}}$ *(days)*
1	[1 92]	58	47
2	[92 184]	~~60~~	149
3	[221 396]	328	260
4	[315)	~~174~~	~~188~~
5	[1154)	~~961~~	~~704~~
6	[189)	~~78~~	637
7	[724)	~~undefined~~	1171
8	[112)	~~-1046~~	159
9	[915)	2428	1248

Table 5.4: Manual and model predictions of TTP in 1D using Equation 5.18. The manual predictions used manual tumor growth estimates in 1D (v_{1D}) from the radiologist segmentations (Equation 5.1). The model predictions used $v_{weighted\_A}$. Both $TTP_{v_{1D}}$ and $TTP_{v_{weighted\_A}}$ were estimated using only the first two acquisition images of each patient. The red strikeouts represent the patients where the predicted TTP did not fall within the interval of column two. Notice that the $TTP_{v_{1D}}$ was correct for only three of the patients while $TTP_{v_{weighted\_A}}$ produced reasonable results for seven of the patients.

represent the patients where the predicted TTP did not fall within the interval of column two. Notice that the $TTP_{v_{1D}}$ was correct for only three of the patients while $TTP_{v_{weighted\_A}}$ produced reasonable results for seven of the patients. Therefore, the model was more accurate at predicting PD than the manual predictions from the radiologist segmentations.

5.6 Discussion

There are three main points of discussion: i) image quality, ii) model limitations, and iii) usefulness of the heterogonous tissue time-dependent speed model.

Image quality was a challenge in this study since the quality of the images and/or tumor segmentations had a direct impact on the quality of the estimated tumor speeds. The voxel size of the original MRIs were $5-6mm$ in z-direction, which led to i) inaccuracies in tumor measurements and segmentations, and ii) a substantial amount of interpolation when making the voxels isotropic ($1 \times 1 \times$

$1mm^3$). This led to tumor segmentation variability, on top of the inherent inter- and intra-expert variability since tumor segmentation is quite a subjective task. Negative radial speed on Figures 5.3, 5.4, and 5.5 point to either i) difficultly in deciphering what is tumor for tumor segmentations, since the patients were not undergoing therapy, or ii) that there was a loss in tumor cells, or iii) a false remission [Galanis et al., 2006].

In terms of model limitations we have that the model accuracy is contingent on the quality of the tumor segmentations, which depend mainly on the imaging modality used, e.g., in FLAIR, hyper-intense signals do not necessarily represent tumor. In addition, it is time consuming to segment tumors and there is inter- and intra-expert segmentation variability. Thus, we believe that automatic tumor segmentation tools that consistently measure tumors in an objective way can overcome these limitations. In 2012, there was a Multimodal Brain Tumor Segmentation Challenge (BRATS) [Menze et al., 2014] where several promising methods were proposed that will hopefully develop into reliable clinical solutions in the upcoming years.

In this chapter we show that our heterogonous tissue time-dependent speed model i) estimates tumor growth speed that matches well with manual calculations between two images (Figure 5.3), and ii) predicts future tumor speed which also match well with manual estimations (figures 5.4, and 5.5). We presented $\epsilon/\delta t$ that is a measure to exhibit our confidence of the radial speed model rage $[v_{g_{TD}}\ v_{w_{TD}}]$ and $[v_{g_A}\ v_{w_A}]$ with manual calculation range matching. Our study shows that when $\epsilon/\delta t$ is low, the manual calculation range and the model speed calculation range are similar. The combined speed estimate $v_{weighted_{TD}}$ and $v_{weighted_A}$ produced the model's best speed estimate since it takes into account both white and gray brain matter. Results demonstrated that this speed estimates generally rested in the middle of the manual estimations. Then, we showed that using the asymptotic speed estimates, we could i) predict TTP dates that match the retrospectively calculated TTP(Figure 5.7), and ii) predict TTP better than manual TTP predictions (Table 5.4). It is evident from Figure 5.7 that TTP can be different depending on which measurement is used (1D, 2D, 3D, or another type of measurement) since all of these measurements show a different trait of a tumor. In contrast to using TTP as a retrospective measure in LGG PD analysis, our approach predicts TTP which could be used proactively by physicians in treatment planning. Since the speed estimates also produce an error measurement ϵ, if the segmentation was not good, this error measure would be high and therefore one should not trust the model's results. When a patient reaches progressive disease, the "watchful waiting" is over and the tumor has to be surgically resected if possible by any means. Therefore, it is important to know when a patient reaches or will reach TTP. The fact that radiologists use different metrics for calculating TTP highlights the challenges facing clinical radiologists in determining progression and the need for more robust tools.

5.7 Conclusion and Perspectives

In this chapter we proposed an approach to assess PD of LGG using tumor growth speed estimates from an asymptotic FK formulation. We compared the PD estimates of nine patients of the proposed approach to i) the ones computed using 1D, 2D, and 3D manual tumor growth speed estimates and ii) the ones calculated using a set of well established size-based criteria (RECIST, Macdonald, and RANO). We showed with the data of nine patients that our heterogonous tissue time-dependent speed model, which used only two patient scans, i) estimates tumor growth speed that matches well with 1D, 2D, and 3D manual calculations between two images, and ii) predicts future tumor speed which also match well with manual calculations. Then, we showed that using the asymptotic speed estimates we could i) predict TTP dates that match the retrospectively calculated TTP, and ii) predict TTP better than manual TTP predictions. In addition, we proposed i) a way of calculating confidence in the speed estimations of the model and ii) a weighted average of the speed in white matter and gray matter. Finally, the predictive model estimates of TTP compared well with the manual retrospective calculations, especially for the 1D RECIST and 2D RANO criteria. We conclude from the results of this comparison, although we did not have a statistically significant number of patients in our study, that the heterogeneous tissue time-dependent speed model may better assess PD of LGG when a limited number of MRI scans are available than the manual calculations. With these results, we can deduce that using a heterogeneous tissue tumor growth model on serial patient MRIs can generate useful speed estimates that radiation oncologists could use in the future for individual patients' therapy planning.

There are several possible extensions of this study that should be carried out in the future. First, a statistically significant number of patients should be studied to confirm the results of this study. Second, it should be studied the root-causes of LGG tumor growth speed changes in time that could be attributed to i) segmentation variation, ii) image quality, iii) LLG to HGG transition, and iv) effects of treatment (if used). It would also be interesting to see how these speed changes affect a patient's predicted TTP.

Chapter 6

Contributions and Perspectives

Contents

6.1 Contributions

Cette thèse se concentre sur la proposition de nouveaux outils de traitement et d'évaluation pour améliorer l'élaboration de la stratégie thérapeutique en utilisant différentes formulations du modèle Fisher Kolmogorov (FK) en combinaison avec de l'imagerie médicale.

6.1.1 Importance de l'IDT du patient dans la modélisation de la croissance du gliome

L'imagerie du tenseur de diffusion (IDT) a été suggérée afin de modéliser la diffusion anisotrope de cellules de la tumeur dans la matière blanche du cerveau. Cependant, les IDT spécifiques au patient sont chères et souvent prises basse résolution, ce qui compromet la précision les résultats du modèle de croissance de la tumeur. Nous avons utilisé une formulation FK pour décrire l'évolution du contour visible de la tumeur afin d'investiguer l'impact du remplacement de l'IDT spécifique au patient (option patient-IDT) par i) une carte de diffusion isotrope (option sans-IDT) ou bien ii) un IDT atlas anisotrope haute résolution formé par la moyenne des IDT de plusieurs patients (option atlas-IDT). Nous avons comparé des trois options d'IDTs en utilisant d'un côté des données synthétisées, et de l'autre – des données cliniques. Une étude future incluant des données de patients additionnels permettrait d'améliorer la portée de l'étude. Dans cette étude qui consiste d'un patient, il a été trouvé que la formulation du modèle FK en temps de déplacement est la plus précise pour chacune des trois options d'IDT lorsque l'intervalle de prédiction est inférieur 175 jours. Les délimitations résultantes de l'IDT atlas et patient ont correspondu avec les contours de la tumeur réelle légèrement mieux que celles de l'option sans-IDT. Cependant, les résultats des prédictions de l'option sans-IDT pour un intervalle temporel inférieur 175 jours étaient également proches de la tumeur réelle. Par conséquent, le chapitre 3 suggère que l'IDT patient (lorsque celui-ci est disponible) est la meilleure option pour modéliser la diffusion de cellules tumorales dans la matière blanche dans la plateforme du modèle FK puisque les résultats montrent que la croissance de la tumeur possède une préférence directionnelle (croissance anisotrope), comme il a été formulé dans [Clatz et al., 2005; Jbabdi et al., 2005]. Il a également été trouvé que seulement peu de précision est perdue en utilisant un IDT atlas, bien que l'IDT atlas ait une non-homogénéité directionnelle légèrement différente de celle de l'IDT du patient. Cette étude suggère que la modélisation de la croissance du gliome motilité différentielle basée sur le tissu (avec l'option sans-IDT), comme proposé dans [Swanson et al., 2007] produit des résultats légèrement moins précis. Cependant, s'abstenir d'utiliser une IDT serait suffisant dans la modélisation de gliomes bien différenciés. Par conséquent, chacune des trois options peut être utilisée avec une formalisation FK pour modéliser la croissance du gliome dans le but de la planification de thérapies.

Le chapitre 3 est une version étendue de l'article de conférence publié et présenté oralement [Stretton et al., 2013].

6.1.2 Estimation de l'infiltration après une résection

Le chapitre 4, notre connaissance, est un premier essai pour estimer l'infiltration de la tumeur après une résection. Dans le domaine de la modélisation de cancers, estimer la croissance du gliome après une intervention chirurgicale est d'une grande importance puisque, suite au protocoles médicaux, la plupart des patients atteints de gliome sont sujets des résections dans une courte période après la détection de la tumeur. Ensuite, les médecins ont besoin de savoir quel est le type de traitement de suivi le mieux adapté chaque patient, c'est--dire la chimiothérapie pour les tumeurs diffuses, ou bien la résection pour les tumeurs agglomérées. Il y a deux défis principaux impliqués dans l'estimation de l'infiltration du gliome immédiatement après une intervention chirurgicale : i) le cerveau présente d'importants parenchymes et un mouvement du liquide céphalo-rachidien après la chirurgie, et ii) la segmentation de la tumeur après la chirurgie pourrait être incomplète puisqu'il peut être difficile de distinguer la tumeur du sang et du tissu cicatriciel. Nous avons appréhendé le premier défi en utilisant un algorithme de recalage non linéaire, et nous avons résolu le deuxième défi par l'utilisation, faisant partie d'une nouvelle méthodologie, d'une carte d'infiltration combinée, c'est--dire une combinaison des cartes d'infiltration de la tumeur avant et après l'intervention chirurgicale. Par conséquent, la contribution principale du chapitre 4 était une méthodologie inédite pour estimer les régions de densité de cellules tumorales invisibles après une résection.

En outre, nous voudrions souligner dans la liste suivante les contributions novatrices atteintes lors du développement de la méthode proposée pour estimer l'infiltration de la tumeur après une résection chirurgicale :

- Nous avons développé une plateforme d'enregistrement novatrice pour enregistrer les IRM post-opératoires suivant une résection de la tumeur et les segmentations pré-opératoires d'IRMs.
- Nous avons développé une plateforme d'enregistrement novatrice pour enregistrer un masque de référence du cerveau pour une image T1 d'un patient tout en préservant les sillons du liquide céphalo-rachidien.
- Nous avons appliqué une combinaison d'un algorithme recalage non linéaire, d'une formulation du modèle FK temps de déplacement, d'un calcul de carte d'infiltration, et d'une simulation d'un modèle FK réaction-diffusion.

- Nous avons ajouté le coefficient Dice la fonction de cot utilisée pour déterminer les paramètres du modèle FK.
- Nous avons utilisé un algorithme d'optimisation Simplexe pour déterminer les paramètres du modèle FK.
- Nous avons combiné des cartes d'infiltration pré- et post-opératoires pour compenser la segmentation incomplète suivant la chirurgie.
- Nous avons balayé d_w/ρ pour identifier les caractéristiques d'infiltration d'un gliome, c'est--dire aggloméré ou diffus.

En résumé, ce travail a proposé une nouvelle manière pour les cliniciens d'estimer l'infiltration de la tumeur après une résection cérébrale afin de les aider dans la planification thérapeutique.

Le chapitre 4 est la version longue de l'article [Stretton et al., 2012] publié et oralement présenté une conférence. Ce travail a été soumis au Journal of Frontiers in Oncology.

6.1.3 Constatation de la maladie évolutive du gliome bien différencié en utilisant les estimation de la vitesse de croissance

Dans le chapitre 5 nous avons proposé une approche afin de constater la maladie évolutive (ME) du gliome bien différencié (GBD) en utilisant les estimations de la vitesse de croissance obtenues d'une formulation FK asymptotique. Nous avons comparé les estimations des ME de neuf patients obtenues en utilisant l'approche proposée i) celles calculées en utilisant les estimations de vitesse de croissance manuelles 1D, 2D et 3D et ii) celles calculées en utilisant un ensemble de critères basés sur la taille bien établis (RECIST, Macdonald et RANO). Nous avons montré sur les données de neuf patients que notre modèle de vitesse tissu hétérogène lié au temps, basé seulement sur deux scanners de patients, i) produit une estimation de la vitesse de croissance qui correspond bien aux vitesses 1D, 2D et 3D de croissance de tumeurs calculées manuellement entre deux images, et ii) prédit des vitesses de croissance futures qui correspondent également aux calculs manuels. Ensuite, nous avons montré qu'en utilisant les estimations de vitesse asymptotiques, nous pouvions i) prévoir les dates du temps jusqu' progression (TTP) qui on correspondu en rétrospective aux TTP calculés, et ii) prévoir le TTP mieux que les prédictions du TTP manuelles. En outre, nous avons proposé

i) une manière d'estimer la confidence en les estimations de vitesse du modèle et ii) une moyenne pondérée de la vitesse dans la matière blanche et grise. Enfin, les estimations de TTP prédictives du modèle ont bien correspondu avec les calculs rétrospectifs manuels, surtout pour les critères 1D RECIST et 2D RANO. Les résultats de cette comparaison nous permettent de conclure, bien que nous n'ayons pas eu dans cette étude un nombre de patients statistiquement significatif, que le modèle de vitesse tissu hétérogène et dépendant du temps permet de constater la ME du GBD mieux lorsqu'un nombre limité de scanners sont disponibles que le calcul manuel. Avec ces résultats, nous pouvons déduire qu'utiliser le modèle de vitesse de croissance tissu hétérogène et dépendant du temps sur des IRM en série du patient peut générer des estimations de vitesse utiles que les oncologues pourraient utiliser dans le futur pour la planification de thérapies individuelles.

Cette contribution a été soumise au Journal of Computerized Medical Imaging and Graphics.

6.1.4 Revue sur le gliomes et la modélisation de tumeurs

Nous avons fourni une présentation de fond sur la maladie du gliome, les protocoles d'IRM pour cette maladie, les indices basés sur images pour ces multi-protocoles, les défis du traitement des gliomes, et les atlas d'IRM cérébrales pour ces modalités. Puis, nous décrivons différentes stratégies de modélisation de tumeurs (in vivo, in vitro et in silico), différents types de modèles de tumeurs (continus, discrets, hybrides et basés agent) et différentes échelles de modèles de tumeurs (atomiques, moléculaires, microscopiques et macroscopiques). Ensuite, nous avec passé en revue les travaux réalisés dans les modèles de vitesse de croissance de tumeurs de l'état de l'art, en commenant par les modèles généraux réaction-diffusion pour l'invasion cellulaire, puis le modèle de réaction-diffusion plus spécifique FK. Par la suite, nous avons discuté sur les modèles de déplacement Eikonal, et enfin, les rles de ces modèles dans la modélisation de la réponse de gliomes aux traitements. Enfin, nous avons revu les modèles de tumeur génératifs dans la segmentation d'images et l'enregistrement qui ont été proposés. Ce travail contribue aux connaissances générales pour la communauté de modélisation de tumeurs.

Le chapitre 2 est une version étendue de l'article en co-auteur qui a été publié dans [Menze et al., 2011a].

6.1.5 Estimation de paramètres et localisation de la source

Cet travail est le résultat d'une collaboration avec Rekik et al. [Rekik et al., 2012] et suit le sujet principal de cette thèse. Dans ce travail, une méthode est décrite qui fournit deux principales caractéristiques spécifiques au patient d'une tumeur en utilisant une IRM un seul point temporel donné : la localisation de sa source et un indice quantifiant l'irrégularité de sa forme. L'approche proposée est macro-échelle et a été évaluée en utilisant des données synthétiques, ainsi que les données GBD de quatre patients. Ce modèle a produit des prédictions prometteuses du comportement spatial des tumeurs en partant de l'estimation des deux paramètres.

Ce travail se trouve dans l'annexe A et a été publié dans le journal Computer Vision and Image Understanding *[Rekik et al., 2012].*

6.1.6 Segmentation validée par un expert de liquide céphalo-rachidien dans un atlas MNI

Ce travail est le résultat d'une collaboration avec Aymeric Amelot et Emmanuel Mondonnet. Il est reconnu dans la communauté de modélisation d'imagerie médicale qu'une segmentation précise de parenchyme cérébral est essentielle pour une modélisation réaliste de croissance de gliome. Nous montrons une précisions accrue dans notre segmentation de parenchyme cérébral dans les résultats de simulation FK, o les tumeurs synthétiques n'ont pas cr entre les lobes. Ce travail est extrêmement important pour la modélisation de croissance de tumeurs avec le but d'aider la planification thérapeutique.

Ce travail peut être trouvé dans l'appendice B et a été accepté dans le Journal of Neuro-Oncology*.*

6.2 Perspectives

L'utilisation de modèles mathématiques dans la planification de thérapies dans la malade du gliome présente un futur tout fait prometteur. Cependant, les modèles actuels de croissance de gliomes et la qualité de leur données d'entrées doivent être améliorés pour que ces modèles aient une réelle valeur dans la pratique clinique. Après avoir apporté ces améliorations, ces modèles ont besoin d'être validés et chaque composant de leur processus doit être automatisé. Une fois ces modèles et les méthodes de génération de données entrée matures, ces modèles ont besoin d'être intégrés dans un module d'aide la décision pour l'oncologie qui puisse être largement utilisé dans les cliniques. Les résultats de ce module doivent être faciles et rapides interpréter. Ce module devrait être configurable afin de répondre aux besoins spécifiques de différentes spécialités : la radiologie, la radio oncologie, l'oncologie et la neuro-chirurgie.

6.2.1 Les modèles de croissance de gliomes

Dans cette thèse, deux modèles différents ont été utilisés pour modéliser la croissance des gliomes : la formulation de réaction-diffusion FK et le modèle déplacement temporel FK. Ces deux approches présentent des améliorations potentielles qui pourraient être apportées par de futures recherches. La formulation FK modélise des densités de cellules tumorales invisibles dans les IRM. La validation des résultats du modèle pourrait être comparée la densité de cellules du gliome obtenue par une biopsie du gliome ou bien une résection. En alternative, le seuil de visibilité du gliome pourrait être quantifié en utilisant des échantillons de tissu et des IRM d'un cerveau animal. Au mieux de nos connaissances, ceci n'a pas été poursuivi. L'effet de masse n'a pas non plus été pris en compte avec les modèles FK déplacement temporel, et pourrait l'être dans le futur.

L'un des aspects les plus importants des formulations actuelles des modèles réaction-diffusion FK est que les paramètres du modèles peuvent être personnalisés pour chaque patient (équation 2.19). Cependant, des personalisations plus robustes pourraient être appliquées pour améliorer la précision. Dans le chapitre 4, nous avons proposé l'utilisation de la méthode du simplexe afin d'ajouter un nouveau terme de personalisation (équation 4.1) qui empêche une tumeur simulée de se transformer en tore. Ce nouveau terme implique le coefficient de Dice, cependant, dans le futur, les médecins pourraient vouloir contrôler le compromis entre les fausses positives et les fausses négatives. Pour aborder ce problème, une possibilité est de modifier le nouveau terme en un facteur pondéré par la sensibilité et la spécificité au lieu d'utiliser un coefficient de Dice. De cette manière, il serait possible pour un médecin de pénaliser lourdement les fausses positives, qui posent un risque plus grand dans la planification de thérapies que les fausses négatives.

Ni le modèle réaction-diffusion FK, ni le modèle FK déplacements temporels ont été testés sur un grand nombre de patients et, au mieux de notre connaissance, aucune analyse détaillée de la sensibilité aux paramètres (basée sur des données patient) n'a été menée. Il est envisageable que la forme, la taille, l'aire dans le cerveau et la vitesse de croissance d'une tumeur peuvent influencer les résultats de la simulation. Par conséquent, ceci est une autre direction de recherche logique.

L'un des sujets principaux du chapitre 4 était d'estimer la diffusivité d'un gliome bien différencié pour des patients individuels. Après avoir trouvé qu'une approche itérative fournit des résultats prometteurs, l'étape suivante serait d'essayer d'améliorer ces résultats, en particulier la vitesse et l'incertitude des paramètres d'entrée, et d'incorporer de nouvelles technologies d'imagerie qui deviendront disponibles dans les prochaines années. Nous allons évoquer quelques manières d'améliorer l'estimation de la diffusivité d'un gliome bien différencié pour des patients individuels. D'abord, une chane de Markov Monte Carlo pourrait améliorer la vitesse des modèles FK avec des distributions de probabilités sur la confidence des résultats. Cette méthode utilise des distributions pour les paramètres sur lesquels il existe une incertitude (segmentation de la matière blanche due l'enregistrement, segmentations tumorales, etc.). En utilisant un modèle probabiliste au lieu d'un modèle déterministe, une partie de l'incertitude due l'enregistrement pourrait être prise en compte. Ceci serait une prochaine étape logique essayer puisque tous les paramètres d'entrée ont des limitations de précision. Deuxièmement, l'on pourrait également aborder le problème de l'estimation de la diffusivité d'un gliome en utilisant un modèle multi-échelle, o les données de la biopsie détermineraient les valeurs de ρ, qui pourraient être différentes dans différentes zones de la tumeur une micro échelle, et la macro échelle pourrait utiliser le modèle FK déplacements temporels. Il y a trois principaux défis utiliser des données de biopsies pour la modélisation : i) l'étiquetage du site dont la biopsie est issue, ii) la consistence du parenchyme cérébral et iii) les biopsies qui fournissent des informations locales sur la densité de cellules tumorales. Premièrement, le défi dans l'utilisation de données de biopsies est qu'actuellement les neuro-chirurgiens et pathologistes ne connaissent pas la localisation exacte d'o a été prélevée la biopsie. Ce n'est pas actuellement inclus dans la procédure pour les neuro-chirurgiens d'étiqueter les biopsies avec la zone de la tumeur d'o elles ont été prélevées (même sans parler de coordonnées exactes). Par conséquent, si quatre biopsies sont prélevées sur un même individu, le pathologiste ne saura pas de quelle zone de la tumeur chaque biopsie provient. Deuxièmement, la consistence du tissu cérébral n'est pas rigide par nature. Le Dr Lyons, président de la division de chirurgie neurologique de la clinique Mayo en Arizona (USA), a décrit le tissu cérébral comme ayant la même flexibilité qu'un yaourt ; par conséquent, il est très difficile de savoir précisément d'o une biopsie a été prélevée, moins de laisser un marqueur métallique sur le site de la biopsie. Troisièmement, les biopsies fournissent de l'information locale, et non globale. Dans le futur, ceci pourrait changer avec l'introduction de nouvelles technologies. Une fois la localisation des sites de biopsies connue, un modèle multi-échelle pourrait utiliser cette information. Enfin, des méthodes double seuil pourrait être utilisées pour déterminer la diffusivité d'un gliome. Pour les gliomes mal différenciés, les contours d'images T1-gadolinium et FLAIR pourraient être utilisés en tant que les deux seuils. Cependant, pour les gliomes bien différenciés, seuls les FLAIRs sont utilisés pour déterminer l'ampleur de la tumeur. Des cartes P et Q, qui sont deux seuils qui pourraient être obtenus d'une IDT, affichent des niveaux d'infiltration différents de la tumeur. Cette méthode a été proposée dans [Price et al., 2006, 2007]. Malheureusement, nous n'avons pas pu reproduire ces résultats sur nos données patient. Par conséquent, la méthode des cartes P et Q ne fonctionne pas chez tous les patients, mais parait être une idée prometteuse ; ainsi elle devrait donc être explorée dans de futures recherches. Dans le futur de la modélisation de gliomes bien différenciés, les images PET pourraient également fournir le second seuil, là où le FLAIR fournit le premier seuil.

6.2.2 Entrées du modèle

Les entrées du modèles qui ont eu un impact crucial sur l'exactitude des résultats du modèle sont les suivants : i) les segmentations tumorales et ii) le masque du parenchyme cérébral.

Les segmentations de tumeurs présentent plusieurs grands défis. Premièrement, les segmentations tumorales présentent une variabilité inter- et intra-expert puisque la plupart des bords de tumeurs sont flous / estompés sur les IRM. Deuxièmement, ceci n'aide pas que voxels IRM hyper-intenses ne représentent pas nécessairement la tumeur, en particulier pour les IRM FLAIR, qui sont la norme pour constater la progression de gliomes bien différenciés. Les voxels hyper-intenses pourraient également représenter un œdème supplémentaire provenant de crises, du sang, de la cicatrisation, ou bien des lésions de la matière blanche. Par conséquent, la taille réelle de la tumeur est très difficile à déterminer de manière certaine. Troisièmement, les protocoles d'image ne sont pas standard, ce qui affecte la qualité des enregistrements. Parfois, un patient commence par avoir acquisitions axiales, puis il passe au sagittal. Souvent, le z-espacement des IRM change d'un scan à l'autre. En outre, chaque scanner produit des images légèrement différentes, et les patients n'ont pas nécessairement leurs images séquentielles prises avec le même scanner. Un autre point à prendre en compte avec les protocoles d'imagerie est qu'un technicien a la liberté de nommer les IRM. Il n'existe actuellement aucune convention de nommage, ce qui pose des problèmes pour l'enregistrement d'un grand ensemble de données patient. Quatrièmement, parfois l'imagerie présente des traînées dues à des mouvements du patient.

Voici quelques façons de faire face aux défis de la segmentation de tumeurs. Tout d'abord, l'utilisation d'un outil de segmentation automatique de tumeurs qui exécuterait la segmentation de la même manière à chaque fois permettrait d'améliorer la vitesse et la précision de la segmentation de tumeurs. Dans le workshop BRATS [Menze et al., 2014], plusieurs segmentations tumorales automatisés ont été présentés et avaient l'air prometteur. Espérons que la précision de ces méthodes va augmenter dans les années à venir. Le vrai défi dans la segmentation automatique de tumeurs sera de distinguer les tumeurs des lésions de la matière blanche, qui se ressemblent dans les IRM FLAIR. Deuxièmement, la technologie IRM pourrait également s'améliorer dans les années à venir, comme l'a envisagé le groupe de travail RANO. Troisièmement, rigidifier les protocoles par des paramétrages systématiques des scanners IRM pourrait être une solution viable. Quatrièmement, améliorer la relaxation des patients pourrait réduire leurs mouvements et accroître leur coopération. Ceci a déjà été proposé par Philips (*Philips Ambient Lighting MR*) [Philips, 2010] en utilisant la lumière ambiante et pourra être vu dans de nombreux hôpitaux dans les années à venir.

En ce qui concerne l'acquisition d'un masque du parenchyme cérébral correct, c'est-à-dire qui a les lobes séparés et les modèles de sillons définis, c'est également un grand défi [Unkelbach et al., 2014]. Il ne suffit pas de simplement utiliser des algorithmes de segmentation, comme Bet2 du FLS, ou d'utiliser un atlas enregistré, tel que le MNI 152, pour estimer un masque du parenchyme cérébral à utiliser dans la modélisation de la croissance de gliome puisque ces masques ne séparent pas complètement les lobes du cerveau et les motifs des sillons, ce qui est crucial pour la modélisation précise de la croissance tumorale. Dans l'annexe B, nous avons créé un masque du cerveau en combinant des cartes de matière grise et blanche seuillées de l'atlas MNI 152. Dr Amelot, un neurochirurgien qui a collaboré sur ce travail, a segmenté les motifs du LCR de ce masque et ensuite nous avons soustrait cette segmentation du LCR au masque du cerveau. Pour créer un masque du cerveau enregistré d'un patient qui a les lobes séparés, on pourrait soit i) enregistrer les images du patient dans l'espace de l'atlas MNI 152 et utiliser ce masque amélioré du cerveau pour faire tourner les simulations, ou bien ii) enregistrer le masque du cerveau (de la manière proposée dans le chapitre 4) à l'espace patient. L'inconvénient du premier procédé est qu'il pourrait y avoir des déformations de la tumeur du patient lorsque la transformation inverse est appliquée aux résultats de simulation. L'inconvénient de la dernière méthode est que les motifs de sillons pourraient ne pas être à l'endroit exact du patient puisque le masque atlas a été enregistré à un patient, mais décalés de quelques voxels, ce qui aura une incidence sur les conditions aux limites de la simulation et, finalement, sur les résultats de simulation. Une étude devrait être réalisée dans les travaux futurs afin d'analyser l'approche qui pourrait être la mieux pour résoudre ce problème.

6.2.3 Validation et automation

Une orientation future serait de valider la formulation FK sur plus de patients en utilisant les processus que nous avons proposé. Pour qu'un modèle biophysique soit adopté dans la pratique médicale, il doit être: i) fiable, ii) répondre à des questions médicales spécifiques, iii) rapide, et iv) de préférence ne pas ajouter des étapes supplémentaires dans le flux de travail des cliniciens. Pour atteindre ce but, on aurait besoin de travailler en étroite collaboration avec les cliniciens afin d'examiner les résultats du modèle et de trouver des lacunes. De ces résultats et de l'affinage continu des exigences de l'outil avec des cliniciens, le modèle peut être amélioré de manière itérative et, en fin de compte, validé. Ensuite, il serait important pour une équipe de développement logiciel d'automatiser toutes les étapes de pré- et post-traitement. Lorsque ceci sera réalisé, il sera possible pour ce modèle un jour de devenir un produit de d'être utilisé dans un environnement clinique.

6.2.4 Planification de thérapie

La formulation FK réaction-diffusion du modèle pourrait être améliorée pour gérer la planification de la chirurgie. Si la formulation du modèle FK réaction-diffusion était inscrite sur un atlas fonctionnel, le modèle pourrait marquer certaines régions fonctionnelles que la tumeur atteindrait et donnerait une estimation quant la date laquelle la tumeur atteindrait ces régions fonctionnelles. Par exemple, les gliomes qui sont situés dans la région motrice du pied du cerveau sont difficiles et dangereux opérer. Par conséquent, il serait utile d'avoir un modèle de marqueur du moment o une tumeur atteindrait la zone du cerveau régissant les pieds.

Il serait également intéressant de combiner le modèle avec des fIRMs pour voir quelles régions fonctionnelles sont touchées par la progression tumorale un moment précis dans le temps. Cette information serait importante pour la planification de la thérapie et pour décider quel moment appliquer le traitement si l'attente vigilante est appliquée.

Dans l'avenir, la technologie d'IRM va s'améliorer, permettant l'amélioration de l'exactitude de toutes les étapes de notre processus. En outre, un meilleur enregistrement non-linéaire, des méthodes de segmentation automatique améliorées, et un modèle mécanique sera élaboré, qui pourra également améliorer la précision de nos méthodes proposées dans les chapitres 4 et 5 de cette thèse, et amener les formulations du modèle FK réaction-diffusion plus près d'être utilisées dans la planification de la thérapie de gliome.

6.2.5 Conclusion

Dans ce travail de thèse, nous avons détaillé d'importants progrès dans la modélisation des gliomes bio-médicale spécifique au patient. Les résultats obtenus sont prometteurs et nous espérons que, après de futurs développements, les formulations de modèles de réaction-diffusion Fisher Kolmogorov avec personnalisations pourraient être utilisés dans la pratique médicale. Pourtant, d'avantage de recherche est nécessaire pour faire face aux problèmes qui sont présents chaque étape dans le processus de modélisation, par exemple, la segmentation, l'enregistrement, la modélisation, etc., avant que ce modèle ne soit prêt être validé grande échelle et, plus tard ,adopté dans les hpitaux.

Contributions and Perspectives

⋆ English translation

Contributions

This thesis focuses on proposing novel processing and evaluation tools to aid in therapy planning using different Fisher Kolmogorov (FK) model formulations in combination with medical images.

Importance of Patient DTI to Model Glioma Growth

Diffusion tensor images (DTIs) have been suggested to model the anisotropic diffusion of tumor cells in brain white matter. However, patient specific DTIs are expensive and often acquired with low resolution, which compromises the accuracy of the tumor growth models' results. We used a FK formulation to describe the evolution of the visible boundary of the tumor to investigate the impact of replacing a patient specific DTI (Patient-DTI option) by i) an isotropic diffusion map (No-DTI option) or ii) an anisotropic high-resolution DTI atlas formed by averaging the DTIs of multiple patients (Atlas-DTI option). We compared these three DTI options using both synthetic and clinical data. A future study including the data of additional patients would improve the significance of the study. In this study, consisting of one patient, it was found that the traveling time FK model formulation is most accurate for each of the three DTI options when the prediction interval is under 175 days. The resulting delineations of the Atlas- and Patient-DTI matched the actual tumor contours slightly better than the No-DTI option. However, the prediction results of the No-DTI option for under 175 days time interval were also close to the actual tumor. Therefore, Chapter 3 hints that a Patient-DTI (when available) is the best option to model tumor cell diffusion in white matter within the FK framework since the results show that tumor growth has directional preference (anisotropic growth) as formulated in [Clatz et al., 2005; Jbabdi et al., 2005]. It was also found that not very much accuracy is lost with the use of an Atlas-DTI, even though the Atlas-DTI has a slightly different directional non-homogeneity than a Patient-DTI. This study suggests that modeling glioma growth with tissue based differential motility (using the No-DTI option) as proposed in [Swanson et al., 2007] yields slightly less precise results. However, refraining from using a DTI would be sufficient when modeling LGGs. Therefore, any of the DTI options can be used with a FK formalization to model glioma growth for the purpose of therapy planning.

Chapter 3 is the extended version of the published and orally presented conference paper [Stretton et al., 2013].

Infiltration Estimation after a Resection

Chapter 4, to the best of our knowledge, acts as a first attempt to estimate tumor infiltration after a brain resection. In the cancer-modeling field, estimating glioma growth after surgery is of great importance since, as a result of medical protocols, most glioma patients are subject to resections within a short period of time after tumor detection. Then, medical professionals want to know what the best type of follow-up treatment would be for a particular patient, i.e., chemotherapy for diffuse tumors or resection for bulky tumors. There are two main challenges involved in estimating glioma infiltration directly after surgery: i) there is substantial brain parenchyma and CSF movement after surgery, and ii) the tumor segmentations after surgery may not be complete since there is a potential for blood and scar tissue to be confused with tumor. We addressed the first challenge with the use of a non-linear registration algorithm, and resolved the second challenge by using, as part of a new methodology, a combined infiltration map, i.e., combination of tumor infiltration maps from before and after surgery. Therefore, the main contribution of Chapter 4 was a novel methodology to estimate the invisible tumor cell density regions after a resection.

In addition, we would like to highlight in the following list the novel contributions attained during the development of the proposed method to estimate tumor infiltration after surgical resection:

- We developed a novel registration framework to register post-operative MR images following tumor resection and segmentations to pre-operative MR images and segmentations.
- We defined a novel registration framework to register a reference brain mask to a patient T1 image while preserving the CSF sulci barriers.
- We applied a combination of a non-linear registration algorithm, a FK model traveling time formulation, an infiltration map calculation, and a FK model reaction-diffusion simulation.
- We added the Dice coefficient into the cost function used to find the FK model parameters.
- We utilized a Simplex optimization algorithm to find the FK model parameters.

- We combined pre- and post-operative infiltration maps to compensate for incomplete segmentations soon after surgery.
- We swept through d_w/ρ to identify the infiltration characteristics of a glioma, i.e., bulky or diffuse.

In summary, this work proposed a new way for clinicians to estimate tumor infiltration after brain resection to aid them in their therapy planning.

Chapter 4 is the extended version of the published and orally presented conference paper [Stretton et al., 2012]. This work was submitted to the Journal of Frontiers in Oncology.

Assessing LGG PD using Growth Speed Estimates

In Chapter 5 we proposed an approach to assess progressive disease (PD) of LGGs using tumor growth speed estimates from an asymptotic FK formulation. We compared the PD estimates of nine patients using the proposed approach to i) the ones computed using 1D, 2D, and 3D manual tumor growth speed estimates and ii) the ones calculated using a set of well established size-based criteria (RECIST, Macdonald, and RANO). We showed with the data of nine patients that our heterogonous tissue time-dependent speed model, which used only two patient scans, i) estimates tumor growth speed that matches well with 1D, 2D, and 3D manual tumor growth speeds between two images, and ii) predicts future tumor speed which also match well with manual calculations. Then, we showed that using the asymptotic speed estimates we could i) predict TTP dates that match the retrospectively calculated TTP, and ii) predict TTP better than manual TTP predictions. In addition, we proposed i) a way of estimating the confidence in the speed estimations of the model and ii) a weighted average of the speed in white matter and gray matter. Finally, the predictive model estimates of TTP compared well with the manual retrospective calculations, especially for the 1D RECIST and 2D RANO criteria. We conclude from the results of this comparison, although we did not have a statistically significant number of patients in our study, that the heterogeneous tissue time-dependent speed model may better assess PD of LGG when a limited number of MRI scans are available than the manual calculations. With these results, we can deduce that using a heterogeneous tissue tumor growth model on serial patient MRIs can generate useful speed estimates that radiation oncologists could use in the future for individual patients' therapy planning.

This contribution was submitted to the Journal of Computerized Medical Imaging and Graphics.

Review on Gliomas and Tumor Modeling

We presented background information on the glioma disease, MRI multi-protocols for gliomas, image-based indices for the multi-protocols, glioma treatment challenges, and population brain atlases of MRI modalities. Then, we describe different tumor modeling strategies (in vivo, in vitro, and in silico), tumor modeling types (continuous, discrete, hybrid, and agent-based), and tumor modeling scales (atomic, molecular, microscopic, macroscopic). Next, we reviewed work done on the state-of-the-art tumor growth models starting with the general reaction-diffusion model of cell invasion and then the more specific FK reaction-diffusion model. Following, we discussed the Eikonal approximation of the FK reaction-diffusion model, the parameter estimation problem for the FK model, then, the infiltration map calculation. Next, we describe coupled bio-mechanical models of tissue displacement, joint invasion and displacement models, and lastly, these models role in modeling glioma response to therapy. Finally, we review generative tumor models in image segmentation and registration that have been proposed. This work contributes to the general knowledge of the tumor modeling community.

Chapter 2 is an extended version of a coauthored paper that was published in [Menze et al., 2011a].

Parameters Estimation and Source Localization

This work came from a collaboration with Rekik et al. [Rekik et al., 2012] and follows the main focus of this thesis. In this work, a method is described that provides two main patient-specific spatial characteristics of a tumor using one MRI at a single time point: its source location and an index quantifying the irregularity of its shape. The proposed macro-scale approach was evaluated using synthetic data and four LGG patients. This model produced promising predictions of tumor spatial behavior from the estimation of both parameters.

This work can be found in Appendix A and was published in the journal of Computer Vision and Image Understanding [Rekik et al., 2012].

Expert-validated CSF segmentation of MNI Atlas

This work came from a collaboration with Aymeric Amelot and Emmanuel Mondonnet. It is well known throughout the medical image modeling community that an accurate brain parenchyma segmentation is essential for realistic glioma growth modeling. We created and show improved accuracy with our brain parenchyma segmentation in FK formulation simulation results, where the synthetic tumors grown did not grow between lobes. This work is extremely important for modeling tumor growth with the purpose to aid in therapy planning.

This work can be found in Appendix B and was accepted the Journal of Neuro-Oncology.

Perspectives

Using mathematical models in glioma therapy planning has a very promising future. However, the current glioma growth models and the quality of their inputs need to be improved for these models to add value in clinical practice. After these improvements have been made, the models need to be validated and every component of their process needs to be automated. Once these models and the methods to generate inputs are mature, the model needs to be integrated into an oncology clinical decision support module to be used widely in clinics, where the module results would be fast and easily interpretable. The module would need to be configurable to answer the specific questions in the areas of progression and therapy planning of several different specialties: radiology, radio oncology, oncology, and neurosurgery.

Glioma Growth Models

In this thesis, two different models were used to model glioma growth: the reaction-diffusion FK model formulation and the traveling time FK model formulation. Both of these models have possible improvements that could be addressed in future research. The FK formulation models tumor cell densities that cannot be seen in MRIs. Validation of the model's results could be compared with a glioma's tumor cell density quantified using a glioma biopsy or resection. Or, the glioma threshold of visibility could be quantified with an animal's brain using both tissue samples and MR images. To the best of our knowledge, this has not been pursued. Mass-effect has also not been taken into account with the traveling time FK model formulation and could be in future models.

One of the most important aspects of the current reaction-diffusion FK model formulations is that the model parameters can be personalized to a specific patient (Equation 2.19). However, more robust personalizations could be used to improve the accuracy of the personalizations. In Chapter 4, we proposed to use the Simplex method and add a new term to the personalization (Equation 4.1), which prevents a simulated tumor from becoming a toroid. The new term involves the Dice coefficient, however, in the future, physicians might want more control over the trade-off between false positives and false negatives being considered in the personalization. To address this, one possibility is to change the new term to be a weighting factor on sensitivity and specificity instead of using the Dice coefficient. In this way, it would be possible for a physician to penalize heavily for false positives, which pose more risk to the patient in therapy planning then false negatives do.

Neither the reaction-diffusion FK nor the traveling time FK model formulations have been tested on a large number of patients and to the best of our knowledge a detailed sensitivity analysis on the parameters (using patient data) has not been done. One could imagine that tumor shape, size, area of the brain, and speed could have effects on the simulation results. Therefore, this is another logical next step.

One of the main focuses of Chapter 4 was to estimate the diffusivity of a low-grade glioma for individual patients. After finding that an iterative approach yields promising results, the next step would be to try to improve these results, mainly speed, uncertainty of input parameters, and incorporating new imaging technologies that will become available in the upcoming years. We will mention a few ways of improving the estimate of diffusivity of a low-grade glioma for individual patients. First, a Markov Chain Monte Carlo formulation would provide speed improvements to the FK model with probability distributions on the confidence of the results. This method uses distributions for the parameters we are unsure about (white matter segmentation due to registration, tumor segmentations, etc.). By using a probabilistic model instead of a deterministic one, some of the uncertainty due to registration can be taken into account. This would be a logical next method to try since all of the input parameters of the model have accuracy limitations. Second, one could also address the problem of estimating the diffusivity of a glioma by using a multi-scale model, where biopsy data determines the values of ρ, which would be different in different areas of the tumor at the micro-scale, and the macro-scale could use the traveling time FK model formulation. There are three main challenges associated with using biopsy data in modeling: i) labeling from which site a biopsy is from, ii) consistency of the brain parenchyma, and iii) biopsies providing local tumor cell density information. First, the challenge with using biopsy data is that currently neurosurgeons and pathologists do not know the exact location of where a biopsy was taken from. It is not currently in the procedure for neurosurgeons to label the biopsies with which area of the tumor they took the biopsy from (even if it is not an exact coordinate). Therefore, if four biopsies are taken from the same individual, a pathologist will not know from which area of the tumor the biopsies were sampled. Second, the consistency of the brain tissue is not rigid in nature. Dr. Lyons, Chair of Neurological Surgery at Mayo Clinic in Arizona, described brain tissue as having the same flexibility as yogurt; therefore, it is very difficult to precisely know where a biopsy was taken from unless one leaves a metal clip where the biopsy site was. Third, biopsies provide local and not global information. In the future, this could change with the introduction of new technology. Once we know the location of the biopsy sites, a multi-scale model could utilize this information. Lastly, two-threshold methods could be used to find the diffusivity of a glioma. For high-grade gliomas T1-gadolinium and FLAIR image contours can be used as the two-thresholds. However, for low-grades only FLAIRs are used to determine the tumor extent. P and Q maps, which are two thresholds that can be obtained from a DTI display different levels of tumor infiltration. This method was proposed in [Price et al., 2006, 2007]. Unfortunately, we were not able to reproduce these results using our patient data. Therefore, the P and Q map method does not work with all patient data cases, but sounds like a promising idea and therefore should be explored in future research. In the future of low-grade glioma modeling, PET imaging could also provide the second threshold, where FLAIR provides the first threshold.

Model Inputs

The model inputs that had a crucial effect on the accuracy of the model results were: i) the tumor segmentations and ii) the brain parenchyma mask.

Tumor segmentations had several large challenges. First, tumor segmentations have inter- and intra-expert segmentation variability since most tumor boundaries are fuzzy/blurred in MRIs. Second, it also does not help that MRI hyper-intense voxels do not necessarily represent tumor, especially for FLAIR MRIs, which are standard for assessing low-grade glioma progression. Hyper-intense voxels could also represent extra edema from seizures, blood, scaring, or white matter lesions. Therefore, the actual tumor size is very difficult to actually determine. Third, image protocols are not standard which affects the quality of the registrations. Sometimes a patient starts off by having axial acquisitions, and then this changes to sagittal. Often times the z-spacing of the MRIs changes from scan to scan. In addition, each scanner produces slightly different images, and patients do not necessarily have their sequential images taken with the same scanner. Another point to make with imaging protocols is that a technician has the freedom of naming MRIs. There is currently no naming convention in place, which poses challenges for registering a large set of patient data. Fourth, sometimes imaging has streaks from the patient moving.

Some ways to cope with the tumor segmentation challenges could be the following. First, the use of an automatic tumor segmentation tool that would segment a tumor the same way each time would improve the speed and accuracy of tumor segmenting. In the BRATS [Menze et al., 2014] workshop several automated tumor segmentations were presented that looked promising. Hopefully these methods will increase in accuracy in the upcoming years. The true challenge in automatic tumor segmentation will be to separate tumors from white matter lesions, which look the same in FLAIR MRIs. Second, hopefully MRI technology also improves in the upcoming years as the RANO Working Group has envisioned. Third, influencing protocols through MRI scanner settings could be a viable solution. Fourth, relaxing patients, which will hopefully cut down on patient movement and increase patient cooperation, through ambient light has already been proposed by Philips (Philips Ambient Lighting MR) [Philips, 2010] and may be seen in many hospitals in the upcoming years.

Regarding having a correct brain parenchyma mask, which has the lobes separated and the sulci patterns defined, is also a large challenge [Unkelbach et al., 2014]. It is not enough to simply use segmentation algorithms, such as Bet2 from FLS, or use a registered atlas, such as the MNI 152, to estimate a brain parenchyma mask to use in glioma growth modeling since these masks do not completely separate brain lobes and sulci patterns, which is crucial for accurate tumor growth modeling. In Appendix B, we created a brain mask from combining the thresholded white and gray matter maps from the MNI 152 Atlas. Dr. Amelot, a collaborating neurosurgeon, segmented the CSF patterns from this mask and then we subtracted this CSF segmentation from the brain mask. To create a registered brain mask of a patient case that has the lobes separated, one could either i) register the patient images to the MNI 152 Atlas space and use this improved brain mask to run their simulations, or ii) register the brain mask (in the way proposed in Chapter 4) to the patient space. The drawback of the former method is that there might be deformations to the tumor of the patient when the inverse transformation is applied to the simulation results. The drawback to the latter method is that the sulci patterns might not be in the exact location of the patient since the atlas mask was registered to a patient, but a couple voxels off, which will affect the simulation boundary conditions and ultimately the simulation results. There should be a study done in future work to analyze which approach might be better to address this problem.

Validation and Automation

A future direction would be to validate the FK formulation on more patients using the processes that we proposed. In order for a biophysical model to be adopted in medical practice, it has to be: i) reliable, ii) answer specific medical questions, iii) fast, and iv) preferably not add extra steps to clinicians workflow. To accomplish this end, one would need to work closely with clinicians to scrutinize the results of the model and find shortcomings. From these findings and continuously refining tool requirements with clinicians, the model can iteratively be improved and ultimately validated. Next, it would be important for a software team to automate all of the pre- and post-processing steps. When this is accomplished, it will be possible for this model to be productized and one day be used within a clinical environment.

Therapy Planning

A reaction-diffusion FK model formulation could be improved to handle surgery planning. If reaction-diffusion FK model formulation would be registered with a functionality atlas, the model could flag certain functional areas that the tumor would reach and would give an estimate as to when the tumor would reach these functional areas. For example, gliomas that are located in the foot motor region of the brain are difficult and risky to operate on. Therefore, it would be helpful to have a model to flag when a tumor would reach the foot area of the brain.

It would also be interesting to combine the model with fMRIs to see what functional areas are being affected with tumor progression at a particular moment in time. This information would be important for therapy planning and deciding when to apply therapy if the watchful waiting approach is being applied.

In the future, MRI technology will improve, allowing the accuracy of all of the steps in our process to improve as well. In addition, better non-linear registration, improved automatic segmentation methods, and a mechanical model will be developed, which will also ameliorate the accuracy of our proposed methods in chapters 4 and 5 of this thesis, and bring reaction-diffusion FK model formulations closer to being used in glioma therapy planning.

Conclusion

In this PhD work, we have detailed important advancements in patient-specific bio-medical modeling of gliomas. The obtained results are promising and we hope that, after future development, reaction-diffusion Fisher Kolmogorov model formulations with personalizations could be used in medical practice. Still, more research is needed to face the issues that are present at every step in the modeling process, e.g., segmentation, registration, modeling, etc., before this model is ready to be validated on a large scale and later adopted in hospitals.

List of Publications

The presented work led to several published and ready to submit publications as a first author and a co-author.

Book Chapters

- *This book chapter reviews the state-of-the-art models for tumor modeling.* Bjoern H Menze, **Erin Stretton**, Ender Konukoglu, and Nicholas Ayache. Image-based modeling of tumor growth in patients with glioma. In C S Garbe, R Rannacher, U Platt, and T Wagner, editors, *Optimal control in image processing.* Springer, Heidelberg,Germany, 2011.

Journal Papers

- *This journal article presents a new method to find tumor growth parameters and source location from only one MRI.*
  Islem Rekik, Stéphanie Allassonnière, Olivier Clatz, Ezequiel Geremia, **Erin Stretton**, Hervé Delingette, and Nicholas Ayache. Tumor Growth Parameters Estimation and Source Localization From a Unique Time Point: Application to Low-grade Gliomas. *Computer Vision and Image Understanding*, 117(3):238-249, 2013.

- *This paper was submitted to the Journal of Frontiers in Oncology and proposes a way to estimate the tumor infiltration after a surgical brain resection.*

Erin Stretton, Emmanuel Mandonnet, Hervé Delingette, and Nicholas Ayache. Tumor Growth Modeling of Glioma Reoccurrence after Surgical Resection. In *Journal of Frontiers in Oncology*, submitted, 2014.

- *This paper was submitted to the Journal of Computerized Medical Imaging and Graphics. In this paper we propose an approach to assess progressive disease of LGGs using tumor growth speed estimates from a Fisher Kolmogorov formulation.*
  Erin Stretton, Lars Gerigk, M. Weber, Bjoern H. Menze, Hervé Delingette, and Nicholas Ayache. Assessing LGG Progressive Disease using Growth Speed Estimates from a Fisher Kolmogorov Model Formulation. In *Journal of Computerized Medical Imaging and Graphics*, submitted, 2014.

- *This paper was accepted in the Journal of Neuro-Oncology and proposes a brain segmentation that has all of the sulci patterns and lobes separated.*
  AymericAmelot (co-first author), **Erin Stretton** (co-first author), Hervé Delingette, Nicholas Ayache, Sebastien Froelich, and Emmanuel Mandonnet. Expert-validated CSF segmentation of MNI atlas enhances accuracy of virtual glioma growth patterns. In *Journal of NeuroOncology*, accepted, 2014.

Conference Papers

- *This conference paper was orally presented and covers the topic of trade-offs for using three different DTI options within a Fisher Kolmogorov tumor growth formulation.*
  Erin Stretton, Ezequiel Geremia, Bjoern H. Menze, Hervé Delingette, and Nicholas Ayache. Importance of patient DTI's to accurately model glioma growth using the reaction diffusion equation. In *Proceedings of the IEEE 10th International Symposium on Biomedical Imaging: From Nano to Macro (ISBI)*, San Francisco, CA, USA, pages 1130-32, 2013. IEEE.

- *This conference paper was orally presented and describes a proposed method for predicting the volume of glioma growth after a resection.*
  Erin Stretton, Emmanuel Mandonnet, Ezequiel Geremia, Bjoern H. Menze, Hervé Delingette, and Nicholas Ayache. Predicting the Location of Glioma Recurrence After a Resection Surgery. In *Proceedings of 2nd International MICCAI Workshop on Spatiotemporal Image Analysis for Longitudinal and Time-Series Image Data (STIA)*, Nice, France, pages 113-123, 2012. Springer.

Appendix A

Tumor Parameters Estimation and Source Localization

Based on a fruitful collaboration carried out during the time of the PhD, which ties in with the main goal of this thesis. This chapter was published in the Journal of Computer Vision and Image Understanding [Rekik et al., 2012].

A.1 Context

Coupling time series of MR Images with reaction-diffusion-based models has provided interesting ways to better understand the proliferative-invasive aspect of glial cells in tumors. In this paper, we address a different formulation of the inverse problem: from a single time point image of a non-swollen brain tumor, estimate the tumor source location and the diffusivity ratio between white and grey matter, while exploring the possibility to predict the further extent of the observed tumor at later time points in low-grade gliomas. The synthetic and clinical results show the stability of the located source and its varying distance from the tumor barycenter and how the estimated ratio controls the spikiness of the tumor.

A.2 Introduction

Brain gliomas represent about 50% of all primary brain tumors [Tovi, 1993] and can be classified according to their grade of malignancy. Low grade gliomas (LGG) are slow invaders of brain tissue as they keep growing for many years, presenting one of the most controversial decision treatment areas. High grade gliomas (HGG) remain unfortunately incurable with an average life expectancy of one year after its discovery, eventually creating symptoms due to an increase of the intracranial pressure or swelling around the tumor. The diagnosis of brain gliomas includes the analysis of various MRI sequences of the brain which partially reveal the tumor invasion. Based on those images and other clinical information, neurologists try to determine the grade of the gliomas and to estimate their current and further spatial extent and if possible their source location.

For more than a decade, mathematical models of brain tumors have been devised to help clinicians answer these questions. Microscopic models study the cellular mechanisms [Bearer et al., 2009; Frieboes et al., 2007; Sanga et al., 2007; Wang et al., 2009] that explain the growth dynamics of gliomas at a microscopic scale. On the other hand, macroscopic models pioneered by Murray [Murray, 2002] describe the evolution of tumor cell density. However, those quantities cannot be directly observed in clinical medical images, but it is commonly assumed that visible tumor boundaries correspond to an isovalue of this density. More realistic reaction-diffusion models have been proposed by Swanson et al. [Swanson et al., 2000] based on the fact that tumor cells migrate faster on white matter fibre tracts myelin sheaths [Giese et al., 1996]. They have been further refined by Jbabdi *et al.* [Jbabdi et al., 2005] and Clatz *et al.* [Clatz et al., 2005] by considering an anisotropic diffusion in the white matter whose diffusion tensor is estimated from those acquired in DT-MRI.

A key issue for those models to answer clinical questions is their personalization, *i.e.* the estimation of some patient-specific parameters from medical images. The main parameters to be identified based on reaction-diffusion models were pointed out in [Angelini et al., 2007] as a combination of tumor diffusion tensors in white and grey matter, its proliferation rate, its initial point and its initial time. Several authors have estimated patient-specific parameters manually [Clatz et al., 2005] or through major model simplifications [Swanson et al., 2003]. Colin *et al.* in [Colin et al., 2012] used a reduced model based on Proper Orthogonal Decomposition (POD) in order to identify growth parameters of pulmonary nodules in CT images. Konukoglu *et al.* [Konukoglu et al., 2007b,a, 2009] have proposed an approach to automatically and accurately personalize brain tumor models. They first remarked that given time series of brain MR images, only the motion of a tumor front can be observed and therefore only the three following parameters can be recovered : diffusivity in the white d_w and grey matter d_g as well as the initial time T_0. Furthermore, since the tumor cell density are only observed in MR images through visible tumor boundaries corresponding to an isovalue, the reaction-diffusion equations can be advantageously replaced by an Anisotropic Eikonal Equation (AEE) [Konukoglu et al., 2009] which models the time at which a tumor front reaches a given point. By minimizing the distance between the segmented tumor and the simulated one, they were able to estimate uniquely those three parameters and test the prediction of future tumor evolution from at least a pair of images.

In this paper, we tackle a slightly different problem than the one approached by previous authors. Instead of estimating the speed of tumor growth from a time series of images, we aim at characterizing the nature of the glioma, more precisely LGG, from a single MR image. Indeed, we hypothesized that the tumor shape is dependent on the proliferating or infiltrating nature of the tumor. Contrary to HGG where the presence of brain edema is common and usually associated with tumor malignancy, LGG are slowly growing tumors with a minimal surrounding edema [Deangelis, 2001; Kaal and Vecht, 2004; Whittle, 2004]. Since our methodology main focus is on LGG, we will not consider the edema-induced mass effect in our further formulation of the tumor growth model. Therefore, the anatomical boundaries such as the ventricles' will remain static as the tumor grows.

Given a segmented brain glioma from an MR image, we solve an inverse problem in order to estimate the diffusivity ratio d_w/d_g and the tumor source position. By localizing the tumor source and estimating the invaded tissue characteristic using this ratio d_w/d_g our objective is to provide clinicians with new indices that can be used for diagnosis from the first acquired MR images, combined with a subsequent prediction of tumor invasive margins as it grows from the initially observed boundary. This additional information may help in surgical and/or radio-therapeutic treatment planning especially when it comes to determining the margins for applying the therapy. The problem of tumor seed localization was recently raised in [Gooya et al., 2011a], where a reaction-diffusion based joint estimation of tumor evolution parameters was addressed within a multimodal deformable registration framework. This approach focuses on the MR image registration with an atlas providing the estimation of the initial seed location as a by-product. Later on, this approach was extended into a joint segmentation and deformable registration as multi-channel tumor images were implanted in a healthy atlas to reconstruct a statistical atlas of gliomas [Gooya et al., 2012, 2011b]. These recent publications targeting a localization of tumor seed and a quantification of the strength of its mass effect and its white matter diffusion coefficient required the us.epse of a normal atlas. In this paper, we investigate a different problem from registration or segmentation in low-grade gliomas. Our approach addresses a spatio-temporal tumor evolution with the estimation of the diffusivity ratio and the position of its source. Moreover, thanks to our personalized model, we have the opportunity to produce a predictive sequence of images showing the tumor potential evolution.

Additionally, after solving the inverse problem, we analyze the location of tumor sources, and their stability over time. Also, the relationship between the tumor source and tumor barycenter is evaluated since both locations have been assumed to match in past studies [Laigle-Donadey et al., 2004; Drabycz et al., 2010; Anderson, 2005; Sottoriva et al., 2010; Kansal et al., 2000]. Finally, knowing the diffusivity ratio d_w/d_g and the tumor source from a single image, we evaluate whether this information gives insights into predicting further tumor shape evolution in two distinct cases of low-grade gliomas.

A.3 Material and Method

A.3.1 MR Glioma images

In this work, we assume that for a given patient, one MR FLAIR image of the brain has been acquired, showing visible boundaries of glioma cells. We also assume that a Diffusion Tensor MR Image (DT-MRI) is also available and acquired at the same time as the FLAIR image. While FLAIR images are acquired in routine on patients with brain tumors, this is unfortunately not the case for DT-MRI. The extent of the tumor has been manually segmented in FLAIR images. Similarly, brain masks have been manually delineated on those images from which brain ventricles have been removed by a simple thresholding of the signal. Also white matter regions have been isolated by thresholding the voxels with the largest eigenvalue in the DT-MRI.

Objective: From the segmented tumor in the FLAIR image, our objective is to provide a quantitative analysis of the tumor shape which is not simply based on geometry (spheroid vs star-shaped) but based on simple biophysics growth principles. Indeed, two quantities are estimated in this analysis: the tumor source position and the diffusivity ratio between white matter and grey matter. This information may provide additional hints about the nature and the future progression of the tumor.

Data issues: Collecting LGG data with DT-MRIs is not a very straightforward task since diffusion MR is a quite recent technology [Young, 2007], rarely used in the common clinical practice and furthermore acquired DT-MRI may have various anomalies like black holes, low resolution and signal distortion. This is particularly true around any tumor lesion. This lack of information may be compensated by assuming the symmetry of the brain. For this, we perform a symmetrization process to “reinitialize” the region where the tumor grew and induced a diffusion signal distortion. Hence, for a proper simulation of tumor growth, we have corrected the tensor field by making the hypothesis that the DT MRI was originally symmetric with respect to the mid-sagittal plane. Thus the DT-MRI voxels corresponding to the largest extent of the tumor have been modified by symmetrizing and copying the voxels from the healthy brain hemisphere. However, this *symmetrization process* is prone to the following difficulties:

a- the DT MRI is asymmetric especially in white matter where about 50% of the contralateral tumor volume has zero Fractional Anisotropy (FA) values, while in the corresponding affected region where the tumor grew, the diffusion signal exists with a remarkable distortion (see Fig A.1-a where the FA tumor map is darker than the contralateral part with a significant absence of symmetry).

b- even with a reliable DT-MRI symmetry, about 50% of the contralateral non-pathological symmetric volume to the tumor volume has no DT (*i.e* FA) signal. In Fig A.2-a, the presence of large black hole in the FA signal in the contralateral part to the tumor invasion area presents a major barrier to diffusion tensor-guided glioma evolution simulation. To cope with this DT signal-missing problem, an interpolation algorithm based on isotropic diffusion (solving the heat equation) was applied to estimate the missing tensors from neighboring regions. This is done by applying a Gaussian convolution separately on the six components of the diffusion tensors.

Dataset: By excluding LGG cases with completely distorted or missing DTI, we succeeded to include four LGG patients. The first case, *a.k.a* patient A, has developed a second grade astrocytoma classified as a low-grade glioma. Four successive time points of T2 flair MR images with a resolution of $0.99 \times 1 \times 2.16\ mm^3$ were acquired and visible tumor boundaries were manually delineated by an expert. A DT-MRI image was also acquired at the first acquisition time point. As expected, the white matter fiber tracts are perturbed by the tumor growth and the DT-MRI signal near the tumor does not capture the original diffusion tensors of the brain at the onset of the disease. Therefore, we used the symmetrization process to reset the affected area to non-pathologically spatially deviated tensors (see Fig A.3 where the white matter diffusion tracts were beautifully recovered).

The second case, *a.k.a* patient B, suffers from a low-grade glioma and four MR images were acquired at distinct time points with a resolution of $0.89 \times 0.97 \times 0.97\ mm^3$. Only one DT-MRI was acquired during the initial scanning process and the tumor region of the DT-MRI has been symmetrized similarly to patient A. In addition, the DT-MRI includes small holes in the opposite region to the tumor that were successfully interpolated.

The third case, *a.k.a* patient C, with LGG has three acquisition timepoints with a resolution of $2 \times 2 \times 2\ mm^3$. In this particular case, displayed in Fig A.1, we encountered difficulty (-a-) where the DT-MRI is not fully symmetric.

The fourth case, *a.k.a* patient D, with a resolution of $2 \times 2 \times 2\ mm^3$ was not symmetrized due to the large holes in the symmetric region to the tumor as show in Fig A.2-a. Therefore, we interpolated the holes in the affected tissue without the symmetrization process.

A.3.2 Tumor Growth Modeling : from reaction-diffusion to Eikonal equations

Glial cells dynamics are essentially governed by two biological phenomena : proliferation and invasion. They can be jointly modeled by a reaction-diffusion equation which describes the change over time of the normalized tumor cell density u:

$$\begin{cases} \frac{\partial u}{\partial t} = \nabla.\ (\mathbf{D}(\mathbf{x})\nabla u) + \rho u(1-u) \\ \mathbf{D}\ \nabla u.\ n_{\partial\Omega} = 0 \end{cases} \tag{A.1}$$

where ρ is the proliferation rate, $\mathbf{D}$ the local diffusion tensor, and $n_{\partial\Omega}$ is the normal vector at the domain boundary surface $\partial\Omega$. In the first equation, the proliferation of tumor cells follows a logistic growth parameterized by ρ whereas the tumor infiltration into neighboring neural fibers is captured by an anisotropic diffusion parameterized by $\mathbf{D}$. The second equation indicates that there is no flux of tumor cells outside the domain Ω.

The diffusion tensor is a definite positive and symmetric 3×3 matrix whose value may be linked to Diffusion Tensor MRI (DT-MRI) [Jbabdi et al., 2005]. Indeed, it characterizes the motility of tumor cells that is considered to be isotropic in grey matter but anisotropic in white matter. More precisely, the tumor diffusion tensor (TDT) may be written as $\mathbf{D}(\mathbf{x}) = d_g\mathbf{I}_3$ in grey matter, where d_g is the diffusivity coefficient.

In white matter, there are several approaches to link the TDT $\mathbf{D}(\mathbf{x})$ with the DT-MRI signal $\mathbf{D}_{water}(\mathbf{x})$. Clatz *et al.* [Clatz et al., 2005] proposed to have $\mathbf{D}(\mathbf{x})$ proportional to $\mathbf{D}_{water}(\mathbf{x})$ whereas Jbabdi *et al.* [Jbabdi et al., 2005] have introduced a formulation which takes into account the possible equality of the two largest eigenvalues corresponding to a possible fiber crossing. Due to high anisotropies of $\mathbf{D}_{water}(\mathbf{x})$ in most parts of the white matter, these two approaches lead however to diffusivities that are much lower than d_g in the directions orthogonal to the fibers, which is questionable. Furthermore, the high ratios of anisotropy encountered in those two expressions also lead to large computational times.

In this paper, we propose to use the following white matter tumor diffusion tensor:

$$\mathbf{D}(\mathbf{x}) = \mathbf{V}(\mathbf{x})[diag(e_1(\mathbf{x})d_w, d_g, d_g)]\mathbf{V}(\mathbf{x})^T \tag{A.2}$$

where d_w is the white matter diffusivity coefficient, $\mathbf{V}(\mathbf{x})$ represents the matrix of sorted eigenvectors of $\mathbf{D}_{water}(\mathbf{x})$ and $e_1(\mathbf{x})$, is the normalized largest eigenvalue (between 0 and 1) of $\mathbf{D}_{water}(\mathbf{x})$. With this choice, tensors have a non-homogeneous anisotropy ratio which is always less than d_w/d_g but is maximized at the center of the white matter fibers and continuously decreases towards their boundaries. By simply dividing the duration of tumor evolution simulation of its propagating front using our adopted diffusion tensor A.2 by the simulation duration as we used the diffusion tensor formulas presented in [Jbabdi et al., 2005] (we precisely refer the reader to formulas A11 and A12), we have noticed that our choice speeds-up the computational time by a factor of 200 without any significant differences in performance. In fact, the use of a more nonlinear (more anisotropic) diffusion tensor field increases the computational time of the solution as the characteristic direction of the recursive anisotropic fast marching algorithm used to solve the AEE A.5 becomes harder to find. This also may be explained by the fact that below a certain anisotropy ratio, the difference in tumor growth simulation is hardly noticeable.

The reaction-diffusion equation (A.1) is not practical when dealing with clinical images. Indeed, in MR images tumor cell density u cannot be observed but the visible tumor boundary can. Hence, a front motion approximation for the reaction-diffusion equation was introduced by Konukoglu *et al.* [Konukoglu et al., 2009] assuming that the visible contour is associated with iso-density contour $u = 0.4$ [Tracqui et al., 1995b]. They introduced an Anisotropic Eikonal Equation (AEE) describing the time $T(\mathbf{x})$ at which the evolving tumor front passes through the location $\mathbf{x}$. In its simplest form, the AEE writes as:

$$F\sqrt{\nabla T^T \mathbf{D} \nabla T} = 1 \text{ with } \; F = 2\sqrt{\rho} \tag{A.3}$$

where T stands for the transposition operator.

However, they noticed that such approximation of equation A.1 was too simplistic and then proposed to account for the fact that the tumor front speed increases over time to reach an asymptotic value equal to $2\sqrt{\rho \ \mathbf{n}^T\mathbf{D}\mathbf{n}}$ where $\mathbf{n}$ is the normal direction of the front. Here, the definition of an “asymptotic behavior” implies that we look at tumors way of growing, regardless of their size, at larger times. In our case, in both LGG patients, the last acquired timepoint represents our scale of “larger times”, around which we can assume an asymptotic behavior of the tumor front speed. In other words, at the asymptotic stage, the behavior of the tumor that we are interested in understanding and potentially predicting is at later times and not during the initial growth stage where the tumor is presumably small and sphere-like. Therefore, the asymptotic speed hypothesis doesn't apply as small tumors proliferation-invasion kicks off. Before reaching the asymptotic stage, a dynamic formula of the time-evolving speed of the propagating tumor front was introduced in [Konukoglu et al., 2009] as the tumor growth simulation modelling became more realistic and less simplistic:

$$F = \frac{4\rho T - 3}{2\sqrt{\rho T}} \tag{A.4}$$

Furthermore, the front curvature $\kappa_{eff}(\mathbf{x})$ also plays a role in the front speed as the front slows at high curvature points. This is especially important at the early stage of the tumor growth when the front is similar to a small sphere. In this setting, the speed term is :

$$F = \frac{4\rho T - 3}{2\sqrt{\rho T}} - 0.3\sqrt{\rho}\left(1 - e^{-|\kappa_{eff}|/0.3\sqrt{\rho}}\right) \tag{A.5}$$

This last formulation is no longer a Hamilton-Jacobi equation due to the second-order curvature term and therefore cannot be solved by fast sweeping methods such as the Anisotropic Fast Marching (AFM) [Konukoglu et al., 2007b]. However, a multi-pass approach was proposed [Konukoglu et al., 2009] to solve efficiently this equation by applying several times the AFM method while estimating the curvature front from previous iterations. The AFM method is recursive and the larger the tensor anisotropy the more iterations are needed to compute the characteristic direction of equation (A.5). Our white matter TDT of equation (A.2) limits the anisotropy ratio and therefore leads to reasonable computational times (typically few minutes for a tumor growth from a seed point).

A.3.3 Parameter estimation problem from a unique MR image

Based on the previously exposed mathematical model, we can simulate the growth of a glioma given its initial source $S(\mathbf{x})$ for which we assume that $T(S(\mathbf{x})) = 0$. From this boundary condition and the knowledge of diffusivity d_w, d_g and proliferation rate ρ we can compute the time $T(\mathbf{x})$ at which the visible tumor front reaches a given point. The isocontours of the field $T(\mathbf{x})$ correspond to the successive shapes of the visible tumor boundary over time as shown in Fig A.4.

The speed on the front is not constant but its asymptotic value is $2\sqrt{\rho d_g}$ in grey matter and $2\sqrt{\rho d_w}$ in white matter.

In this paper, we are interested in solving the following inverse problem: given a visible tumor boundary S_{Seg} in an MR image, can we extract the growth parameters $S(\mathbf{x}), d_w, d_g, \rho, T_{\text{Obs}}$ that best explain the observed tumor boundary. The duration T_{Obs} between the onset of the tumor and the MR image acquisition is indeed also unknown.

Based on [Konukoglu et al., 2009], it has been already established that several combinations of ρ, d_w, d_g lead to the same front speed and therefore the same tumor growth simulations. Therefore, it is sufficient in this inverse problem to consider a fixed value of the proliferation rate ρ corresponding to the tumor grade and to estimate the remaining parameters. However, unlike [Konukoglu et al., 2007a, 2009] this problem can be further simplified by realizing that the front speed cannot be estimated since T_{Obs} is unknown. If one multiplies the diffusivities by a scale factor α then one obtains the same isocontours for a propagation time divided by $\sqrt{\alpha}$[1]. This means that the simulated tumor isocontours do not depend on that absolute value of d_g and d_w but on the *diffusivity ratio*:

$$r = \frac{d_w}{d_g}$$

In the remainder, we will show that this ratio is related to the spikiness of the tumor.

Therefore a simple sensitivity analysis has led to conclusion that solving the inverse tumor growth problem only depends on the following 2 parameters: the source location $S(\mathbf{x})$ and the *spikiness index* r. Here, the "spikiness index" represents a biology-driven estimated measure which quantifies the tortuousness of the boundary of the tumor as displayed on MR axial slices (see Figure A.4-A), an index related to the frequency at which the tumor shape bends and twists. We consider that $\{S(\mathbf{x}), r\}$ appropriately characterize well a tumor extent if its visible boundary in MRI, S_{Seg}, is an isocontour of the simulated tumor growth initiated at $S(\mathbf{x})$ with diffusivity ratios equal to r. Therefore, we propose to estimate the patient specific parameters by minimizing the following criterion:

$$C_\rho(S(x,y,z),r) = \frac{1}{N\overline{T}}\sqrt{\sum_{x\in S_{\text{Seg}}}(T(x)-\overline{T})^2} \tag{A.6}$$

---

[1] This is not strictly true if one uses the speed term F taking into account the transient speed as in Equation A.4 or A.5. However, the difference in simulations due to the absolute value of the diffusivities was found to be negligeable.

with

$$\overline{T} = \frac{1}{N} \sum_{x \in S_{\mathrm{Seg}}} T(x) \tag{A.7}$$

where N is the number of points belonging to the manually delineated tumor boundary S_{Seg}. In these equations, $\overline{T}$ and C_ρ are respectively the mean time value and time standard deviation computed over the tumor boundary. Our motivation to use this criterion to get good estimates of our unknowns $(S(x, y, z), r)$ derives from the fact that a tumor boundary (propagating front) is simultaneously defined as an isotime and an isosurface. Thus, to quantify how good is the estimation of the parameters guiding the spatio-temporal evolution of the tumor shape, we need to quantify how closely the simulated isosurface matches the observed one (manually delineated boundary). From a time perspective, this also implies that when measuring the time T at every point x of the manually delineated tumor isotime boundary, its value $T(x)$ will be constant in the best case scenario where the simulated tumor front exactly matches the observed tumor boundary. Therefore, minimizing the time standard variation criterion C_ρ over the delineated tumor boundary S_{Seg} will guide the algorithm towards a better estimation of the two key parameters driving the invasive tumor front into fitting the successive MR observed boundaries. Note that C_ρ is normalized by $\overline{T}$ because the criterion should be made independent of the tumor front speed and therefore the mean time $\overline{T}$.

In order to efficiently minimize the previously outlined criterion, we use the multidimensional unconstrained minimization algorithm without gradient introduced by Powell in [Powell, 2009]. This algorithm suits our case since our parameters are bounded in both biological and geometrical spaces. Moreover, the derivative of minimization criterion C_ρ is not easy to compute. To better study the convergence of this algorithm and evaluate its outcome, 15 tests were performed using synthetic tumors. Further evaluation of this method was then studied using real data: two patients with LGG.

A.3.4 Synthetic Data: synthetic tumor generation process

In order to validate our parameter estimation, we propose to produce synthetic tumor MR images, where the initial tumor location and diffusivity ratio are known. The procedure of generating synthetic tumors relies on choosing a seed point S_0 in either white or grey matter and the proliferation rate ρ to one of the following values $0.008, 0.012, 0.024$/day. The tumor front propagation is simulated with a white matter diffusion rate d_w and grey matter diffusion rate d_g whose ratio varies between 1 and 100 (considered to be a biologically valid range) using equation (A.5). The growth simulation is stopped at a specified time T_{Obs} thus leading to a time distance map as seen in Fig A.4. Different synthetic tumors were created at different anatomical locations with different sizes and asymptotic speeds of growth in both white and grey matter.

A.4 Results

A.4.1 Convexity of the minimization function: a convergence study

To check the convergence of the Powell minimization algorithm to the initially set parameters, we study the convexity of the minimization criterion C (see Equation (A.6)) for the four scalar parameters $[S_x, S_y, S_z, r]$, writing separately the coordinates of the tumor source location. We proceed by alternatively fixing some parameters to their ground truth values and optimizing the remaining ones with the proposed minimization process. In Fig A.5, we can clearly see the convexity of the minimization surface plotted after setting the diffusivity ratio r and one of the source coordinates to their right values.

The convexity of the minimization criterion C_ρ was successfully checked also when optimizing three parameters and setting the fourth one at its true value. The fact that the minimization criterion appears to be convex at the vicinity of the ground truth parameters is reassuring about the observability of the four parameters. However, the functional may still have local minima and practical optimization results will be discussed in the next sections.

A.4.2 Synthetic data

We evaluated our method on 15 synthetically generated tumors with a diffusivity ratio ranging from 1 to 100. The algorithm succeeded to identify the original tumor source with a mean error of 0.42mm and a standard deviation of 0.36mm. Moreover, it always converges to the real diffusivity ratio $d_w/d_g$with a mean error equal to 0.18 and a standard deviation of 0.06.

Furthermore, we use this synthetic data to provide a better understanding of the diffusivity ratio r. The first row of Fig A.6 shows how the shape of the tumor boundary can switch from “sphere-like”to “star-like”as the diffusivity ratio value jumps from 1 to 50. Although the displayed tumors in the third row are of different sizes, the correlation between tumors' shape spikiness and the value of the diffusivity ratio $r \in [1 - 100]$ is clear.

Besides, we also notice from the second row of Fig A.6 similar tumor contours in terms of spikiness and irregularity when fixing the diffusivity ratio at the same value and varying the location of the initial tumor seed. This confirms that the diffusivity ratio value r controls the spikiness of tumor shape.

A.4.3 Clinical data

A.4.3.1 Evaluation criteria

In clinical data, no ground truth values of the parameters are available and therefore additional criteria must be introduced in order to assess the quality of the parameter estimation.

After the optimization of criterion A.6, we extract the simulated isocontour which is closest from the visible tumor boundary in MRI. Computing symmetric distances between the two surfaces provides a quantitative information about how well the tumor shape can be explained by the proposed tumor growth model. We detail below the proposed approach.

We extract the closest isocontour defined by time $\hat{T_{Obs}}$ by optimizing $C_{isoTime}(50\%)(T)$:

$$\hat{T_{Obs}} = \min_{T} \ C_{isoTime}(50\%)(T) \tag{A.8}$$

The criterion $C_{isoTime}(50\%)(T)$ is defined as the median symmetric distance between the visible tumour boundary S_{Seg} and the isosurface $\hat{S}_{isoTime}$ at time T. More precisely, for each voxel of $\hat{S}_{isoTime}$ (resp. S_{Seg}) its closest distance from S_{Seg} (resp. $\hat{S}_{isoTime}$) is computed through a distance map and added to a list. The median value of that list is then taken as $C_{isoTime}(50\%)(T)$. The optimization of the functional is done with the Powell algorithm [Powell, 2009] already used for solving the general inverse problem and requiring few estimations of the functional. The range of time value for the optimization is constrained to be in the range $[\overline{T} - \delta; \overline{T} - \delta]$ where δ is the standard deviation:

$$\delta = \sqrt{\frac{\sum\limits_{x \in S_{\text{Seg}}} (T(x) - \overline{T})^2}{N}}$$

We also compute other robust distance criteria $C_{isoTime}(y\%)(T)$ by taking the $y\%$

quantile of the symmetric distances.

Once the closest isochrone surface $\hat{S}_{isoTime}$ is estimated, we define the symmetric distance between (S, $\hat{S}_{isoTime}$) as the first evaluation criterion:

$$C_{symDist}(S_{\mathrm{Seg}}, \hat{S}_{isoTime}) = \frac{1}{|S_{\mathrm{Seg}}| + |\hat{S}_{isoTime}|} \left[\sum_{\mathbf{x} \in S_{\mathrm{Seg}}} min\ d(\mathbf{x}, \hat{S}_{isoTime}) + \sum_{\mathbf{x} \in \hat{S}_{isoTime}} min\ d(\mathbf{x}, S_{\mathrm{Seg}}) \right] \quad \text{(A.9)}$$

where d denotes the closest Euclidean distance between a point and a surface.

We can also measure the similarity between the visible tumor volume V_{seg} and the simulated tumor volume $V_{isoTime}$:

$$C_{overlap}(V_{seg}, V_{isoTime}) = \frac{V_{seg} \cap V_{isoTime}}{0.5\ (V_{seg} + V_{isoTime})} \quad \text{(A.10)}$$

A.4.3.2 Study of Patient A

For patient studies, we take advantage of the fact that several FLAIR MR images are available for different time points. We first check the stability of source locations for the M time points per patient and correlate the spikiness index with the observed tumor evolution. To estimate the two target parameters $[S(\mathbf{x}), r]$, the proliferation rate was fixed to $0.012/day$. Table A.1 represents the outcome of the estimation method for the four time points (t_1, t_2, t_3, t_4) of Patient A.

	t_1	t_2	t_3	t_4
$S(\mathbf{x})$	(120, 111, 31)	(120, 111, 31)	(122, 115, 30)	(121, 116, 30)
$d(G, S)$ in mm	2.00	1.73	1.42	5.38
r	41.98	40.47	40.58	41.38

Table A.1: Outcome of the minimization algorithm of Patient A which was separately computed at four time points. The distance d denotes the Euclidean distance between the tumor barycenter G and its estimated source S.

We can clearly observe in Table A.1 the stability of the tumor source location and the fact that for the first 3 time points this location is very close to the tumor barycenter since the Euclidean distance between them $d(G, S)$ ranges from

	$C_{symDist}$ in mm	$C_{overlap}$ in %
$(PatientA, t_2)$	1.97	85.63
$(PatientA, t_3)$	1.79	87.76
$(PatientA, t_4)$	1.74	88.04
$(PatientB, t_2)$	1.53	82.20
$(PatientB, t_3)$	1.48	84.79
$(PatientB, t_4)$	1.13	88.02

Table A.2: Prediction evaluation based on the error measures $C_{symDist}$ and $C_{overlap}$ computed for Patient A and B to predict the evolution of the tumor at specific time points t_i using the minimization outcome of the previous time t_{i-1}.

$1.42mm$ to $2mm$. Nonetheless, for the fourth time point, the estimated tumor source distance from its barycenter is $5.38mm$. Moreover, the diffusion rate r is mainly constant. In fact, patient A showed a very slow and quasi-static evolution of the tumor boundary between the second and the third acquisition timepoints. Our simulation model depicts this static evolution behavior as the corresponding estimated spikiness index r shown in Table A.1 remains quasi-static ($r = 40.47$ at t_2 and 40.58 at t_3), which is in line with the identical appearance of the estimated tumor red boundaries shown in the first and second rows of Figure A.7. However, it is worth noting that the algorithm failed to catch the tiny bump that appeared in the tumor boundary at t_3 (see first column, row 1 and 2 in Figure A.7). This can be explained by the fact that the algorithm is based on a mean error minimization process, which therefore accounts for a mean morphological change in tumor shape over all the axial slices included in the tumor volume.

Second, we study the possibility to predict further spatial tumor boundaries evolution based on parameter evaluation. More precisely, after estimating patient specific parameters at time t_i, we run a forward simulation using those estimated parameters trying to predict the tumor invasion process as time evolves. We then proceed by estimating the closest predicted isocontour from the observed tumor boundary at time t_{i+k} as described in sectionA.4.3.1. Fig A.8 and Table A.2 display the outcomes of the evaluation criteria for every time point.

We notice a limited discrepancy between the observed contour at time point t_i and the predicted one at t_{i+1} since the symmetric distance between these contours $C_{symDist}$ ranges from 1.74 mm to 1.97 mm. Moreover the median distance error $C_{isoTime}(50\%)$ ranges from 1.44 mm to 1.68 mm and the volume overlap $C_{overlap}$ between the real tumor volume and the extracted one ranges from 85.63% to 88.04%. It is remarkable that the estimated parameters at a specific time point t_i captures the tumor spatial evolution at the successive time point t_{i+1}. As high-

	t_1	t_2	t_3	t_4
$S(\mathbf{x})$	(34, 145, 117)	(35, 141, 117)	(34, 141, 118)	(34, 140, 119)
$d(G,S)$ in mm	5.09	5.47	5.09	4.24
r	6.45	37.15	30.12	47.70

Table A.3: Outcome of the minimization algorithm of Patient B separately computed at four time points.

lighted in Fig A.8, the estimated-parameters based prediction shows promising results.

A.4.3.3 Study of Patient B

The parameter estimation outcome for Patient B at its four time points is summarized in Table A.3. The obtained results confirm the stability of the tumor source location. At every time point, the distance between the tumor barycenter and the located source exceeds 4 mm, meaning that the tumor source may not be close to its barycenter. Unlike Patient A, the spikiness index value r increases as time evolves as it can also assessed visually in Fig A.9.

Despite the poor signal quality of the DT-MRI, the evaluation criteria confirm that the estimated parameters were adequate to spatially predict the tumor front propagation. In fact, the symmetric distance $C_{symDist}$ between the real front observed at t_i and the extracted one at t_{i+1} ranges from 1.13 mm to 1.53 mm. The volume overlap $C_{overlap}$ ranges from 82.20% to 88.02% (Table A.2). The median distance error $C_{isoTime}(50\%)$ ranges from 0.92 mm to 1.16 mm (Fig A.8). Fig A.10 shows that the algorithm succeeded to spatially capture the geometric behavior of the evolving tumor. However, the maximum distance error $C_{isoTime}(100\%)$ reaches high values ranging from 7.10 mm to 11.97 mm. These outliers are related to the interpolated holes in the DT-MRI where the simulated propagating front fails to capture the real tumor invasion process.

A.4.3.4 Study of Patients C and D

In both patient C and D, the estimated source remained stable from the first timepoint to the third one as the distance between the successively estimated sources $d(S_{t_1}, S_{t_2})$ and $d(S_{t_1}, S_{t_3})$ did not reach a value over $1.42mm$. The estimated diffusivity ratio for Patient C remained constant as time evolves ($r = 7.92$), a spikiness value in concordance with the round shape of the tumor boundary and its very slow evolution between t_1 and t_3 as shown in Fig A.11. The spatial disparity between the estimated source and the barycenter did not exceed $1.8mm$. For Patient D, the estimated diffusivity ratio varied from $r_{t_1} = 20$ to $r_{t_2} = 16.2$ then increased to $r_{t_3} = 23.8$. The successively estimated high diffusivity ratios are in line with the tumor boundary spikiness shown in Fig A.2-b. The computed distance between the estimated source and the tumor barycenter varied from $1.42mm$ at t_1 to $3mm$ at both t_2 and t_3.

A.5 Discussion

The patient-specific parameter estimation method presented in this paper uses two main ingredients: the traveling front approximation presented by Konukoglu et al. [Konukoglu et al., 2009] transformed into the AEE and the Powell minimization algorithm. We have shown using a limited number of LGG cases that our approach could provide clinicians with two fundamental tumor dynamics characteristics: the spatial position of tumor seed point and its diffusivity ratio. Our optimization approach has been successfully evaluated on synthetic data where ground truth is available.

At this point, we have noticed the quasi-stability of the located source in both clinical cases, which is reassuring. Another key finding is related to the distance between the located source point and tumor barycenter. For Patient B, this distance ranges from $4.24mm$ to $5.47mm$ and for the 15 synthetically generated tumors, computed distance ranges from $1.42mm$ to over $13mm$. The disparity between the computed source and its barycenter maybe explained by the spikiness index. Indeed, it is intuitive that "sphere-like" tumors have a source which might be very close to its barycenter but "star-like" tumors or spiky tumors are prone to greater disparities. In the latter case, the barycenter may even end-up outside the tumor shape. This outcome contradicts the assumption that the tumor source is its barycenter as assumed in some studies as in [Laigle-Donadey et al., 2004] (tumor classification process based on the correlation between its located barycenter and molecular profile), in [Drabycz et al., 2010] (MGMT gene methylation status prediction study in glioblastomas) and in [Anderson, 2005; Sottoriva et al., 2010; Kansal et al., 2000] (tumor growth simulation using cancerous cell concentration gradient computed from the center of tumor mass). Therefore, tumor barycenter-derived conclusions may not seem fully reliable and could cloud the true biological phenomena influencing tumor growth patterns. Furthermore, as noticed in Table A.1, the source-to-barycenter distance ranging from 1 to $5mm$ in a tumor of $10mm$-size demonstrates that choosing the barycenter as a source estimator leads to a large bias.

In Patient A, there is a jump of the source-barycenter distance value from

$1.42mm$ to $5.38mm$. This may be explained by a recent study from Bohman *et al.* [Bohman et al., 2010] aiming at a better understanding of glioma ontogeny (development from earlier stage) within the complexity of brain anatomy. In fact, Bohman et al. concluded that as the tumor grows, its boundary approaches the ventricles and the closer its "seed position " is to the ventricles, the larger the tumor would be. This conclusion agrees with our observation in Fig A.7 where the tumor boundary becomes more distorted as it seems to be more "pulled" towards the left lateral ventricle. Note that while Bohman *et al.* use a basic geometric method to estimate the tumor barycenter, it mentions a discrepancy between barycenter and tumor source ranging between 1.25 mm and 15 mm. This is in agreement with our synthetic study and we hope that this work could provide a better understanding of tumor ontogeny.

According to our study, the tumor shape irregularities seems to be well correlated with the diffusivity ratio r. Setting the spikiness index leads to similar irregular tumor contours up to the geometry of their neighboring brain structures (presence of the ventricles for instance). As a matter of fact, the quasi-stability of this ratio for Patient A is justified by the quasi-stability of its shape over time. Its high values ranging from 40.5 to 42 agrees with its "V-like" irregularity (Fig A.7). On the other hand, for Patient B, this ratio raises from 6.45 to 47.70 as its shape evolves from a "sphere-like" to a "star-like" (Fig A.9). Interestingly, in a recent paper [Stretton et al., 2012], a different ratio (d_w/ρ) was used to quantify the diffusivity of the tumor boundary where a low white matter diffusivity rate over proliferation ratio indicates a not very infiltrative glioma (bulky), whereas high ratio defines diffuse tumor. The main objective was to determine whether the tumor recurrence is a bulky or diffuse-type recurring tumor. We believe that a comparison between both of these ratios (d_w/dg and d_w/ρ) in future research works will be a valuable step in determining the patient-specific factors guiding tumor growth.

For patients C and D, which had DT-MRI anomalies as shown in (Fig A.1 and A.2), our method proved its robustness as the estimated tumor source remained stable as time evolved. The symmetrization process induced a tremendous loss in white matter anisotropy as most of the fibers along which the tumor originally grew disappeared as demonstrated in (Fig A.1) through FA histograms comparison. Nevertheless, the algorithm converged to a low diffusivity ratio value ($r = 7.92$). That was visually proven to be in concordance with the tumor "roundness" (Fig A.11) and also remained constant throughout time, a fact in correlation with the very slow and slightly unchanged tumor boundary from t_1 to t_3. The Euclidean distance between the estimated tumor source and its barycenter did not go over $2mm$, which was quite expected when noticing the roundness of the tumor shape.

Patient D did not undergo the symmetrization process because of the large holes in the symmetric region to tumor segmented tissue (Fig A.2-a) and the original diffusion fibers distorted by tumor growth were used. Depite this, the estimated source remained stable with $1mm$ spatial variation along z-axis. Its spatial disparity to the barycenter reaching a value of $3mm$ highlights that the increase of the tortuosity of the tumor quantified by the estimated diffusivity ratio implies an increase in the distance between the tumor barycenter and its original source (as in Patient B where it reached $5.47mm$). Since a good estimation of the spikiness index is tied to the good quality of the acquired DT-MRI, the unexpected drop in r value from $r_{t_1} = 20$ to $r_{t_2} = 16.2$ can be explained by the major tumor-infiltration derived anomalies of the reconstructed diffusion tensors and also the interpolation of the small holes therein.Both of these cases, who had various DTI anomalies as previously pointed out in Section 2.1, demonstrated a good performance when estimating a stable tumor source and also capturing the spikiness of its shape through the estimated diffusivity ratio. However, the prediction step was overlooked since it strongly requires a very good quality of the symmetric DTI to the affected invaded tissue.

Relying on key biological tissue characteristic (diffusivity in white and grey matters), our estimation of the tumor source location and diffusivity rate (or spikiness index) also showed a promising prediction of the further spatial propagation of the glioma boundary as time evolves. The good prediction in both LGG cases presented in Table A.2 and Fig A.7 gives confidence to the estimated tumor source and its diffusivity ratio. However, this spatial prediction was not based on a simulation from the tumor origin but from the tumor boundary at a previous time point using the estimated spikiness index. This is to avoid error accumulation leading to a weak prediction. Although, the diffusion ratio reflects a “snapshot-in-time”, it remarkably reflected the rate-of progression of glioma and specified a quantifying measure of the spikiness of its shape.

DT-MRI serves as the basis for several reaction-diffusion based models to extrapolate glioma invasion margins for radiation [Konukoglu et al., 2010a] and after resection [Stretton et al., 2012] using at least two acquired time points. Although validated using two LGG cases, the predictive power of our model based on a single time point is worth investigating to give some hints to neurosurgeons about the brain tissue to-be-invaded by the tumor as time evolves. Furthermore, being successively evaluated on one healthy patient and one LGG patient, both of these studies confirm that the use of DT-MRI based methodologies is constrained to a good quality of the diffusion signal and limited as the number of recruited patients remarkably drops due to this constraint. Including DT-MRI acquisitions in a standardized brain tumor imaging protocol will increase the number of the recruited patients and allow a thorough validation of these models.

A.6 Conclusion

Going beyond the initial tumor radial expansion model without taking into account the tumor boundary irregularities ([Bohman et al., 2010], [Mandonnet et al., 2003], [Harpold et al., 2007]), we have introduced a new method to estimate tumor growth parameter within a traveling front propagation framework. The described method provides two main patient-specific spatial characteristics of a tumor using one clinical image at a single time point: its source location and an index quantifying the irregularity of its shape. The proposed macro-scale approach was evaluated using synthetic data and four patients with LGG. As a consequence of the estimation of both parameters, a promising prediction of tumor spatial behavior was pointed out.

Some aspects of this work may be subject to improvements. For instance, a sensitivity analysis of the proposed method to the choice of tumor diffusion tensor in white matter is needed. Our proposed formulation leads to efficient computations, but a quantitative evaluation from experimental datasets should help refining the approach. Also, the white matter and brain mask segmentations could be improved by using state-of-the-art image classification tools on high resolution T1 MRI for instance.

Future steps include the application of the proposed method on high-grade gliomas and on a large database of glioma patients advancing a better validation of the predictive power previously highlighted. This could also lead to a statistical study of the correlation between the tumor source location, its grade and its diffusivity ratio. Thus, we could check whether lower spikiness index values are obtained for HGG since they appear to have less spiky and irregular shapes than LGG. Including the mass effect when addressing HGG growth will be a necessary step to include in the presented methodology. Hopefully, the coupling of mathematical models with clinical images should lead to a better understanding of tumor growth and to useful computational tools for diagnosis and therapy planning.

A.7 Acknowledgments

We thank Ender Konukoglu for his assistance in understanding his recent research work previously referenced and for providing us with his source code.

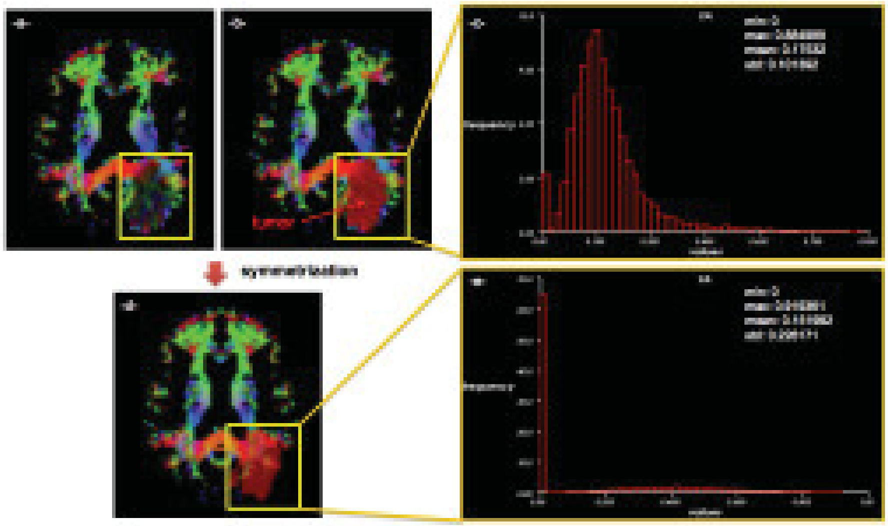

Figure A.1: *Data encountered problems (Patient C): fractional anisotropy (FA) asymmetry.* (a): Non-symmetrized FA color map shows the dramatic diffusion signal distortion as the region where the tumor grew seems darker than the unaffected brain tissue. (b): Non-symmetrized FA color map overlayed on glioma segmentation. (d) Symmetrized FA color map overlayed on glioma segmentation. A preliminary visual comparison between (b) and (d) clearly shows that when symmetrizing the diffusion tensor image and therefore the driven FA map, there is a tremendous loss in white matter anisotropy as most of the fibers along which the tumor originally grew disappear. The comparison of FA histograms only computed in the segmented tumor region (c) and (d) successively corresponding to (b) and (d) tumor figures demonstrates the anisotropy bias introduced by symmetrization process in this case.

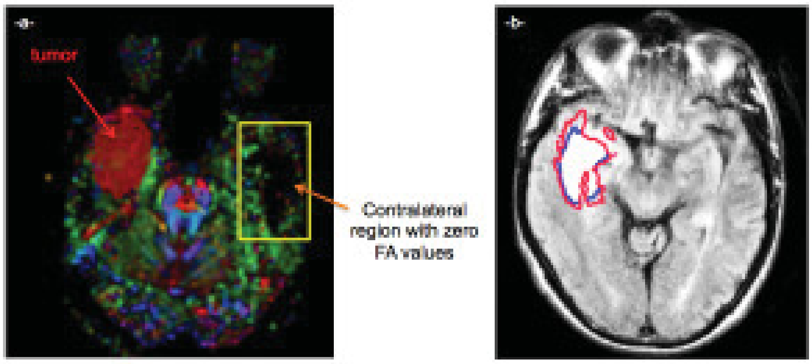

Figure A.2: *Data encountered problems (Patient D): large black holes in the DTI.* (a) Tumor segmentation in red is overlayed on the fractional anisotropy map, a measure derived from Diffusion Tensor Imaging. The significantly missing diffusion signal in the contralateral region to tumor segmented tissue prohibited our proceeding to the symmetrization process and therefore we used for our estimation the affected tissue tensors by tumor infiltration. (b) The tumor boundary is drawn on the FLAIR image at the first and second time points in light and dark blue (in this slice they are identical) and at the third time point in red.

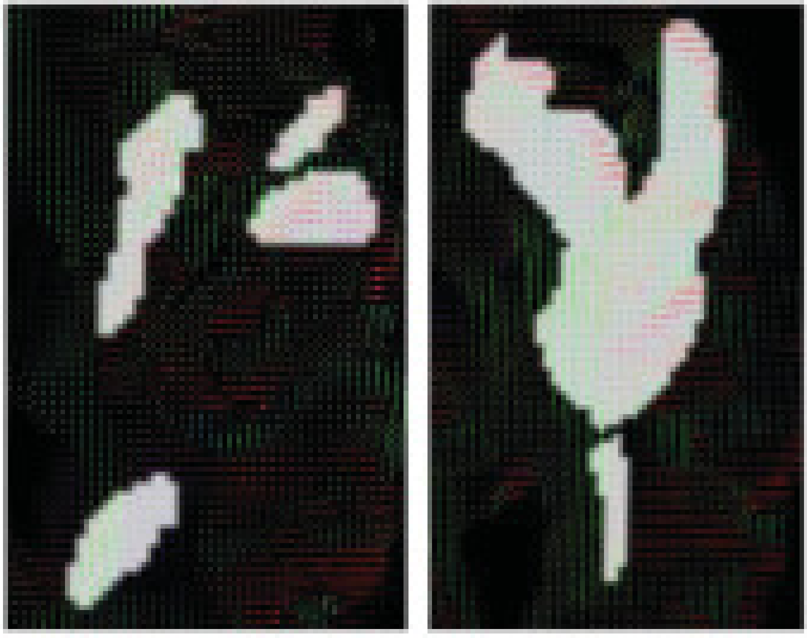

Figure A.3: Two axial slices of the first included patient (Patient A) where the manually segmented glioma (in white) is visualized on the diffusion tensor MR image. The symmetrization process in this case led to reliably recovered infiltration fiber tracts where the simulation of tumor growth starting from a seed point is legitimate.

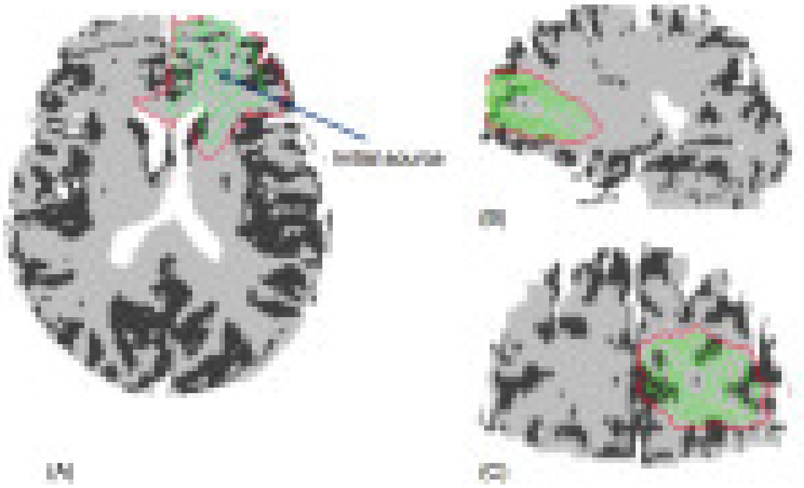

Figure A.4: Simulation from a source point of the iso-time contours representing the tumor invasion process with a diffusivity ratio d_w/d_g equal to 25. The synthetic tumor displayed in red is created by thresholding the time distance map at $T = T_{Obs}$. (A) represents the axial slice, (B) coronal slice and (C) sagittal slice.

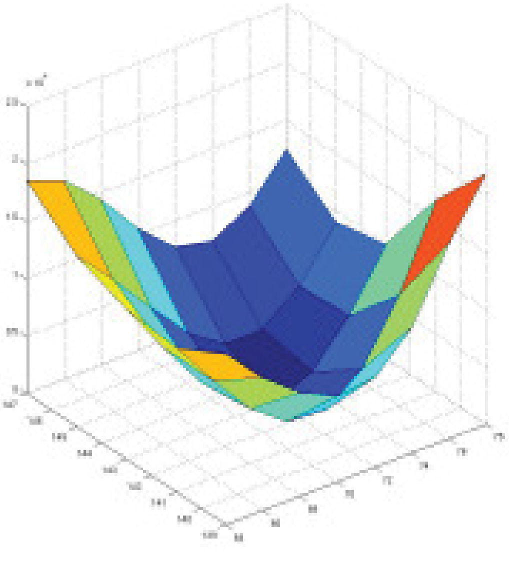

Figure A.5: The minimization surface after fixing r and S_z. The x axis of this 3D plot represents x coordinate of tumor source and the y axis represents its y coordinate.

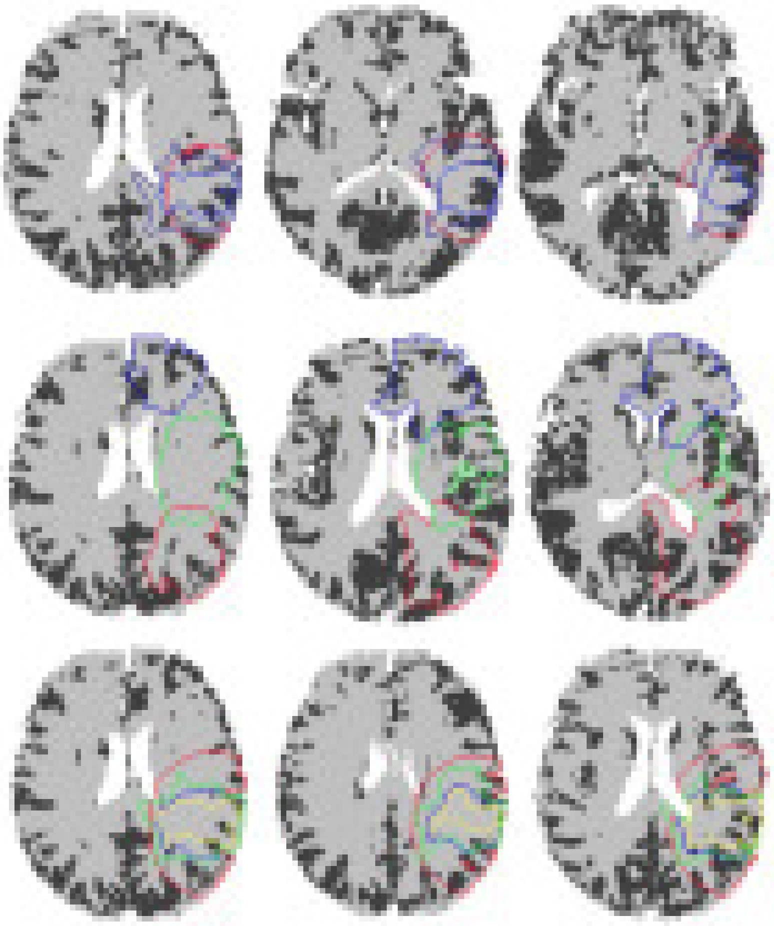

Figure A.6: Synthetic tumors generated at different locations with different diffusivity ratios and observation times. First row: At a fixed source location, two iso-time contours with the same observation time ($T_{Obs} = 900 days$) are respectively colored in red for a diffusivity ratio ($r = 1$) and in light blue ($r = 50$). The darker blue contour represents the tumor further spatial invasion with ($r = 50$) and ($T_f = 1200 days$). Second row: 3 synthetic tumors are generated using the same observation time value T_{Obs} and the same diffusivity ratio ($r = 25$) for 3 different source locations. Third row: At the same fixed location, five iso-time contours with the same observation time are colored in red ($r = 1$), in blue ($r = 10$), in green ($r = 50$) and in yellow ($r = 100$).

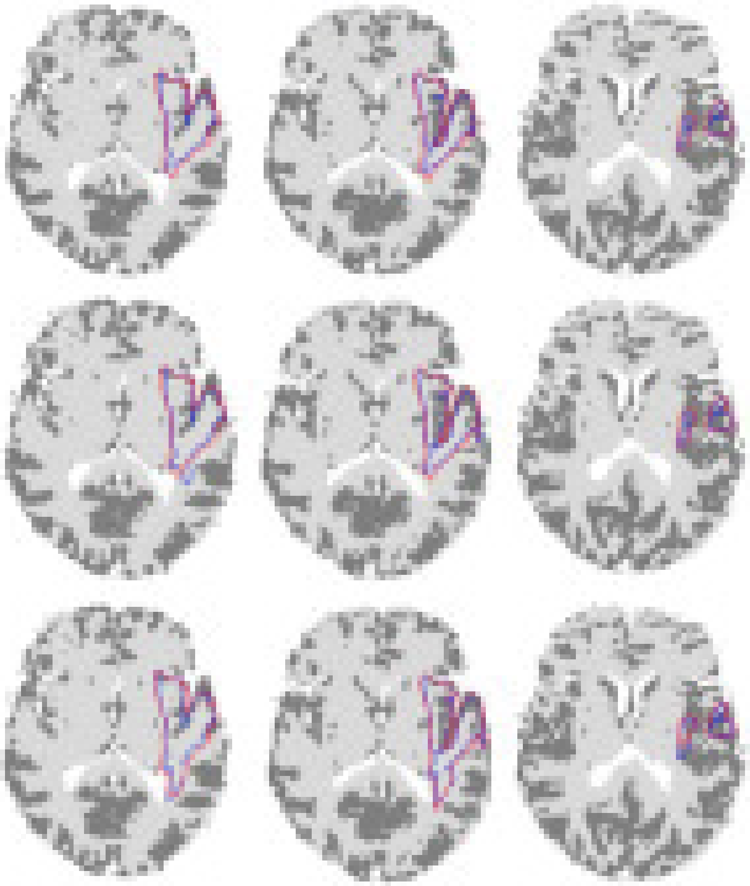

Figure A.7: Different axial slices of Patient A showing the discrepancy between the real boundary and the estimated one at 3 different successive time points. First row: using the algorithm outcome at t_1, we spatially determine the tumor evolution at t_2. The blue contour represents the manually delineated tumor at the second time point and the red one is the extracted iso-time surface $\hat{S}_{isoTime}$. Second row: using the algorithm outcome at t_2, we predict the tumor evolution at t_3. Tumor boundary at t_3 is colored in blue and the estimated one in red. Third row: using the algorithm outcome at t_3, we predict the tumor evolution at t_4. Same colors are used to show the similarity between the estimated and the ground-truth tumor contours.

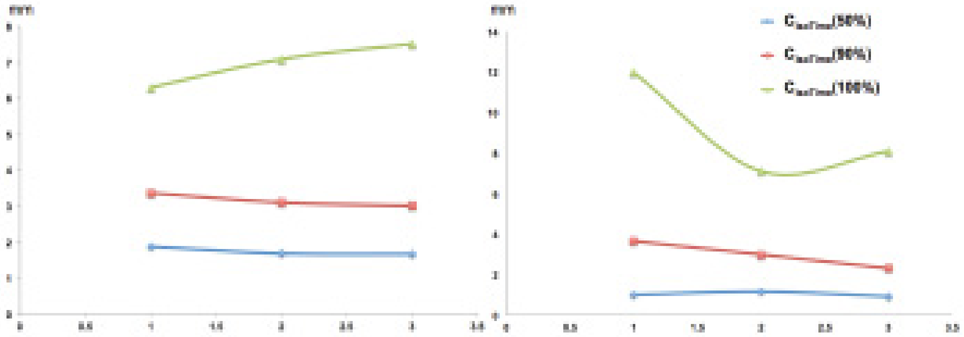

Figure A.8: Evaluation curves plotted using the distance error measure $C_{isoTime}(y\%)$ for $y \in (50, 90, 100)$. For each patient (A or B), we try the predict the evolution at a successive time point $(A/B, t_i)$ based on the estimated parameters at the previous one.

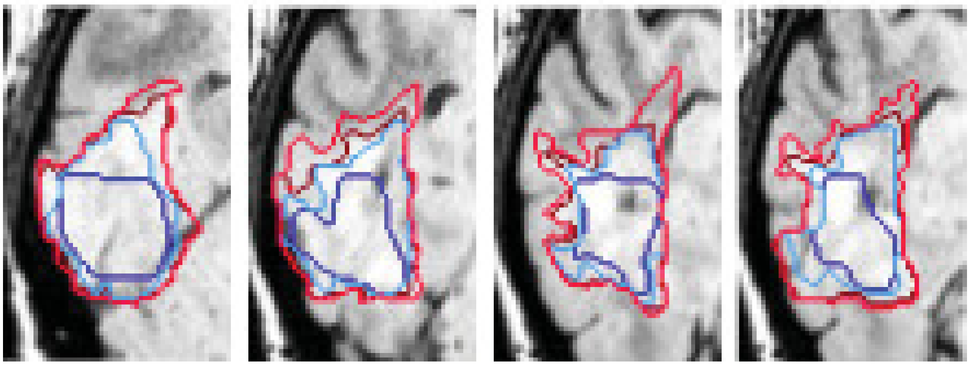

Figure A.9: Four different axial slices of Patient B showing the remarkable tumor boundary spikiness evolution from the initial time point t_1 to the final one t_4. Tumor contours at successive time points are respectively colored in: dark blue for t_1, light blue for t_2, dark red for t_3 and light red for t_4.

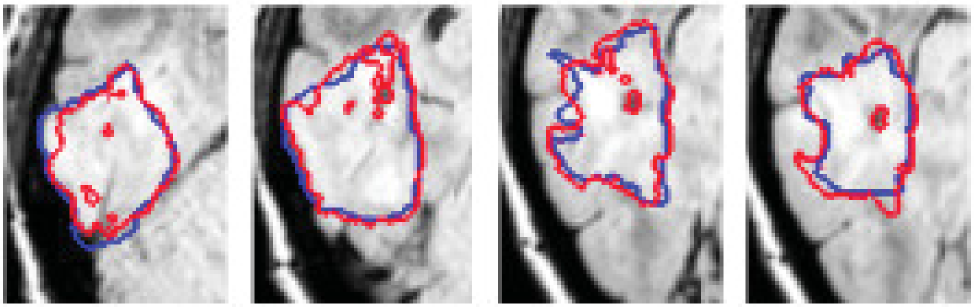

Figure A.10: Four different axial slices of Patient B illustrating the prediction of the tumor evolution based on two different time points. Using the algorithm outcome at t_2, the tumor front is predicted at the next time point t_3. The red contour represent the predicted tumor boundary and the blue one represents the ground truth or the real tumor boundary.

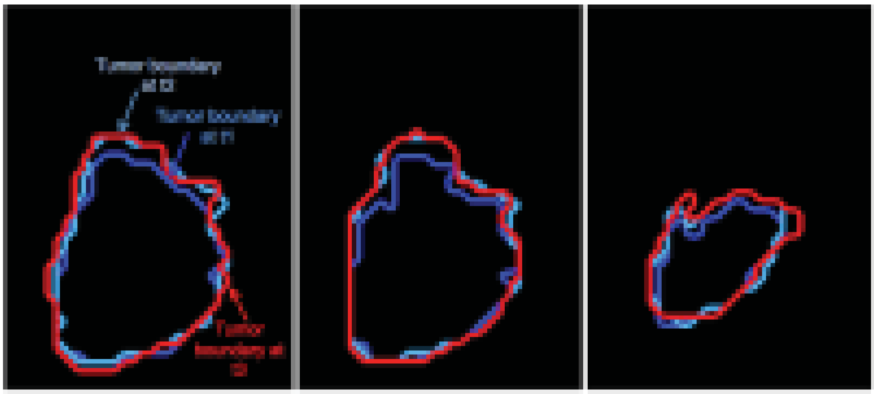

Figure A.11: Patient C: three different axial slices of the manually segmented tumor boundary at t_1 in dark blue, at $t2$ in dark blue and at t_3 in red.

Appendix B

Expert-validated CSF segmentation of MNI atlas enhances accuracy of virtual glioma growth patterns

Based on a clinically oriented collaboration carried out during the time of the PhD, which ties in with the main goal of this thesis. This chapter accepted in the Journal of Neuro-Oncology.

B.1 Context

Biomathematical modeling of glioma growth has been developed to optimize treatments delivery and to evaluate their efficacy. Simulations currently make use of anatomical knowledge from standard MRI atlases. For example, cerebrospinal fluid (CSF) spaces are obtained by automatic thresholding of the MNI probability atlas, leading to an approximate representation of real anatomy. To correct such inaccuracies, an expert-revised CSF segmentation map of the MNI atlas was built. Several virtual glioma growth patterns of different locations were generated, with and without using the expert-revised version of the MNI atlas. The adequacy between virtual and radiologically observed growth patterns was clearly higher when simulations were based on the expert-revised atlas. This work emphasizes the need for close collaboration between clinicians and researchers in the field of brain tumor modeling.

B.2 Introduction

Gliomas are brain tumors that remain incurable despite recent advances in treatments that combine surgery, chemotherapy and radiation therapy. Their diffuse behavior, resulting in an invasion of normal appearing parenchyma peripheral to the bulk lesion, is a major cause of treatment failure.

Biomathematical modeling of these tumors has been developed over the past two decades. The hope is that in silico tumor growth models could help to optimize treatments delivery [Bondiau et al., 2011; Corwin et al., 2013; Ribba et al., 2012; Rockne et al., 2009] and to evaluate their efficacy [Wang et al., 2009; Mandonnet, 2011; Neal et al., 2013]. Such clinical applications require patient-specific inputs, obtained for example from pre-treatment sequential MRIs. Simulations are either performed in the patient MRI space [Stretton et al., 2012] onto which anatomical knowledge of atlases can be matched (to obtain brain parenchyma segmentation and create white and gray matter segmentations), or in a reference space - usually the MNI atlas [Fonov et al., 2009] - onto which all patient images are registered. Hence accurate anatomical atlases are needed in both cases.

Advances have been made in integrating a more precise anatomy in the atlas. Whereas the very first templates in the nineties were built from a 2D CT scan [Woodward et al., 1996; Cruywagen et al., 1995; Tracqui et al., 1995b], just outlining the brain surface and the ventricles, more recent works are based on 3D-MRI atlases of CSF, grey matter and white matter [Swanson et al., 2000], and eventually including detailed white matter architecture via DTI sequences [Jbabdi et al., 2005; Clatz et al., 2005; Stretton et al., 2012, 2013]. CSF spaces are of utmost importance for achieving realistic glioma growth patterns, as they constitute anatomical barriers that cannot be crossed by tumor cells (a statement that is implemented in the model by no flux boundary conditions). The segmentation of CSF delineation is commonly obtained by an automated thresholding of the atlas, without any expert validation of its anatomical accuracy. For example, it has been previously shown that current templates contain unphysiological bridges of brain matter between frontal and temporal operculum, which should normally be separated by the subarachnoid spaces of the sylvian fissure [Jbabdi et al., 2005].

As a consequence, the virtual tumor can grow directly from one operculum to the other, resulting in unrealistic growth patterns as compared to clinically reported ones [Mandonnet et al., 2006].

In this paper, we build an expert-revised CSF segmentation map of the MNI reference brain. We then propose to analyze how these corrections influence tumor growth patterns, by comparing simulations obtained using the native and corrected templates.

B.3 Data

The MNI 152 T1 MRI, gray matter probability map, and white matter probability map are de facto registered [Fonov et al., 2009] and are all downloadable from the MNI website. The MNI 152 brain segmentation was created from the threshold gray and white matter MNI 152 probability maps (process described in following section). A neurosurgeon (A. Amelot) segmented the missing sulci patterns from the T1 image to refine this baseline brain parenchyma mask (BM), creating an improved BM. For the simulations in the Experiment section, the data inputs were the white matter segmentation (WM), which was segmented from the white matter probability map, and either the MNI 152 original brain segmentation or the improved brain segmentation (see below).

B.4 Method

In this section, we describe the preprocessing of the data and the model used to simulate tumor growth.

Preprocessing of Data: The WM, gray matter segmentation (GM), original MNI 152 BM and improved BM were created with the following steps.

The WM and GM mark out the inhomogeneous tissue boundaries of the brain and the CSF segmentation marks out where brain tissue is not. The WM was achieved by thresholding the MNI 152 white matter probability map or a probability > 0.58. The GM was estimated by thresholding the MNI 152 gray matter probability map for a probability > 0.42 and the CSF segmentation was achieved by thresholding the MNI 152 CSF probability map for probability > 0.17. These threshold values depict the most accurate account for where the white and gray matter and CSF are according to a neurosurgeon (E. Mandonnet).

The original MNI 152 BM was created by combining the WM and GM segmentations and removing all voxels that were marked as CSF by the CSF segmentation.

It took several steps to enhance the original MNI 152 BM. First, we determined where the original MNI 152 BM was imperfect by visually inspecting each slice along the three dimensions (axial, coronal, and sagittal). In this scan, we studied all sulci, gyrus, and cerebral lobes. Second, we created an improved CSF segmentation manually by redrawing, using Slicer [Fedorov et al., 2012], all of the subarachnoid spaces physiologically present that were lacking in the original MNI 152 BM (Figure B.1).

Third, we used the improved CSF segmentation to identify additional voxels in the original MNI 152 BM to be marked as CSF instead of brain.

Simulation Model: The traveling time FK model formulation in 3D described in Chapter 2 by equations 2.14, 2.15, and 2.16 was chosen as the simulation model for our experiments.

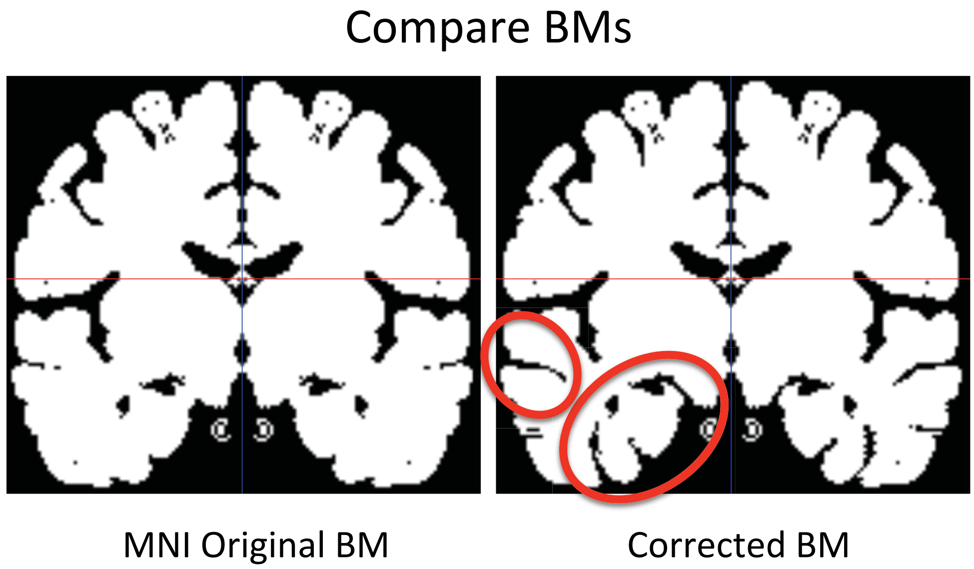

Figure B.1: MNI 152 original BM vs improved BM. Left, the MNI 152 original BM is displayed. Right, the improved BM is shown with the changes highlighted by red circles.

B.5 Experiment

We performed a comparison between MNI original BM and improved BM using synthetic tumor simulations. Using the traveling time formulation in equations 2.14, 2.15, and 2.16, we simulated three synthetic tumor evolutions using both the BMs within the simulations. Each simulation was started from a voxel with a asymptotic tumor growth speed ($v = 2\sqrt{d_w \rho}$) of $v = 24\ mm/year$, $\rho = 6\ 1/year$, $d_w = 24\ mm^2/year$, $T_0 = 1$ day (tumor age), and $d_g = d_w/10\ mm^2/year$ [Konukoglu, 2009; Swanson et al., 2003; Swanson, 1999].

B.6 Results

A total of 111963 voxels have been redefined as CSF by the expert, representing 2% of the total number of brain voxels. Despite that this ratio is very small, we show now the importance of these corrections by comparing the growth patterns obtained with simulations using the baseline BM (original MNI 152) versus the improved BM for 4 different starting points.

We first selected a starting point in the deep white matter of the anterior middle frontal gyrus (see Figure B.2). In this situation, there was no significant difference in the growth patterns between baseline BM and improved BM simulations.

In Figure B.3, the tumor starting point was chosen in the right frontal operculum, pars triangularis of the right inferior frontal gyrus. When using the original MNI 152 BM, the tumor invaded the right insula in the first year of tumor growth, whereas the insula remained free of tumor after two years of growth when using our improved BM. This latter tumor growth pattern better depicts what is observed on a real patient (see Figure B.3). Figure B.4 illustrates tumor growth in the right temporal lobe. The starting point of the simulated tumor was set in the superior temporal gyrus. As seen in the coronal section on the original BM, the virtual tumor started to invade the middle temporal gyrus during the first year of tumor growth, as tumor cells could find a way to go through the superior temporal sulcus. The simulated tumor using the improved BM clearly shows no tumor invasion of the middle temporal gyrus and the growth remained confined to the superior temporal gyrus as observed on a real patient (see Figure B.4).

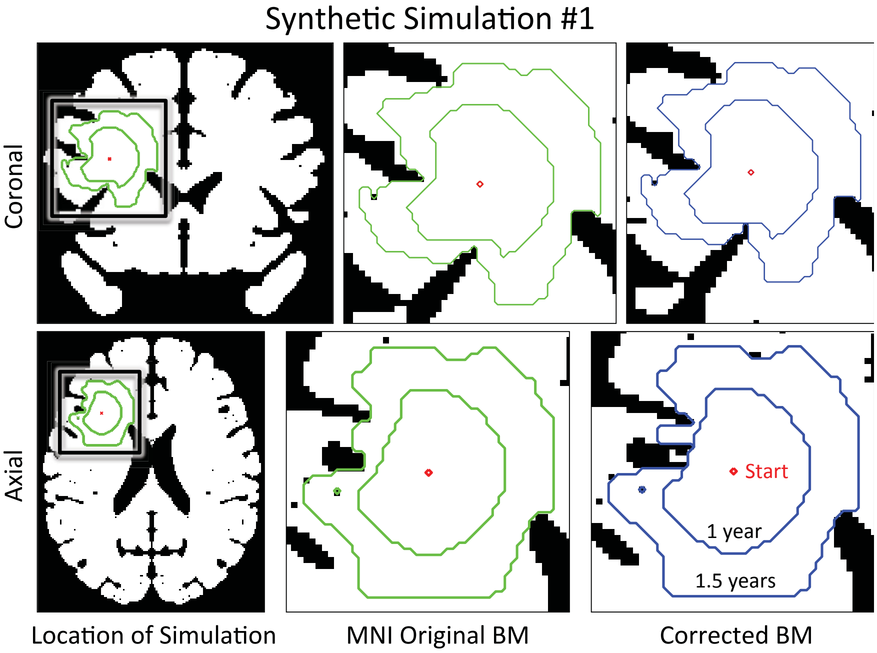

Figure B.2: Comparison between MNI 152 original BM and improved BM using synthetic tumor simulation #1. The BMs are the background of each image. Left images show the location in the BM where this synthetic tumor was simulated. On the right bottom is displayed a time map (shown for 1 and 1.5 years) for this synthetic tumor that was started from a single voxel (red). Notice that the simulations run using the original MNI 152 BM and improved MNI 152 BM are the same for a tumor growing in the white matter of anterior middle frontal gyrus (2 cm lateral to the frontal horn).

B.7 Discussion

Computational modeling of glioma growth has recently emerged as an active field of biomathematics. The aim is to built a patient-specific virtual tumor, whose evolution is as close as possible to the real patient tumor. On this perfect virtual copy, several treatment sequences could be simulated, helping to select the optimal regimen. However, there is currently a huge gap between advances in numerical simulations and their effective use in clinical practice, and actually, very few studies attempted to evalute the veracity of virtual glioma growth patterns [Jbabdi et al., 2005; Konukoglu et al., 2010a].

In this paper, we showed the difference in simulated growth patterns when using two different templates of segmented CSF spaces, obtained from a baseline and an expert-revised version of the MNI 152 atlas. The mismatch between real and simulated tumors was minimal when using the expert-revised template. This

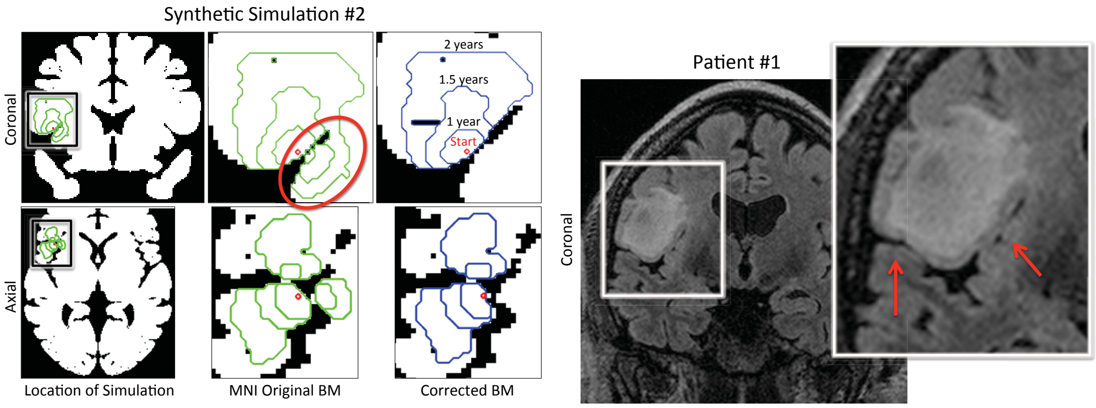

Figure B.3: Left: Comparison between MNI 152 original BM and improved BM using synthetic tumor simulation #2. The BMs are the background of each image. Left images show the location in the BM where this synthetic tumor was simulated. On the right top is displayed a time map (shown for 1, 1.5, and 2 years) for this synthetic tumor that was started from a single voxel (red). A red circle is drawn around an area where the synthetic tumor grew because the MNI 152 original BM (background) was incorrect. Right is displayed the simulation which used the improved BM where this synthetic tumor did not grow across the sylvian fissure incorrectly. Right: Patient #1 had a tumor in the same place as where the synthetic simulation #2 was grown. This demonstrates the importance of the improved BM as there was indeed no tumor growth into the insular and superior temporal gyrus (red arrows).

result emphasizes that detailed anatomy has to be taken into account in computational models. Here, anatomical inaccuracies of sulcal anatomy in the baseline template allow virtual glioma cells to cross a sulcus - that should normally not be crossed by real glioma cells - leading to unrealistic shapes of simulated tumors. Of course, the difference is especially great for tumors with a starting point close to important sulci. Our results reinforce the idea that glioma simulations cannot be purely be based on patient images and require anatomical information from atlases. It is indeed unrealistic to perform manual segmentation of CSF spaces for each patient case. The simplest way to overcome this issue is to register all patient images in the reference space, perform the simulations in the reference space, and project the results back to the patient space. However, this approach might not always produce good results due to a possible non-correspondence between the patient and atlas geometries. The reverse method of registering the atlas onto the patient space is an alternative, but it carriers the risk of recreating artificial bridges of gray matter between the two flanks of sulci. Hence this paper has important consequences regarding the elaboration of an efficient pipeline for

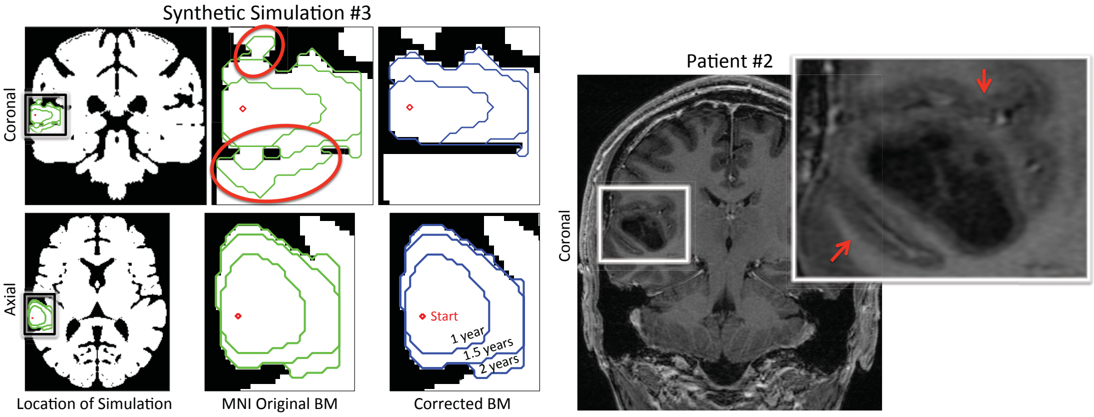

Figure B.4: Left: Comparison between MNI 152 original BM and improved BM using synthetic tumor simulation #3. The BMs are the background of each image. Left images show the location in the BM where this synthetic tumor was simulated. On the right bottom is displayed a time map (shown for 1, 1.5, and 2 years) for this synthetic tumor that was started from a single voxel (red). A red circle is drawn around an area where the synthetic tumor grew because the MNI 152 original BM (background) was incorrect. Right is displayed the simulation which used the improved BM where the synthetic tumor did not grow across the sulci incorrectly. Right: Patient #2 had a tumor in the same place as where the synthetic simulation #3 was grown. This demonstrates the importance of the improved BM in the superior temporal gyrus, as the tumor growth remained confined to the superior temporal gyrus, with no growth across the superior temporal sulcus and sylvan fissure (red arrows).

patient-specific tumor growth simulations. Moreover, previous works that did not make use of an expert-revised segmentation of CSF spaces could be of limited value. For example, it has been proposed to use the proliferation-diffusion model to determine the starting point of a patient glioma [Konukoglu et al., 2010b]. The starting point is indeed key information that can be used to find spatially distinct clusters of glioma [Konukoglu et al., 2010a] arising from different cells of origin, with distinct patterns of recurrence and prognosis [Lim et al., 2007; Bohman et al., 2010]. This paper shows that infering tumor starting points by solving the inverse problem of the proliferation-diffusion equation is meaningless if the CSF template has not been carefully designed to take into account precise sulcal anatomy.

B.8 Conclusion

We have shown the importance of using expert-revised templates when dealing with glioma computational simulations. We invite researchers to make use of the presented map of CSF spaces in their simulations of tumor growth, or to give in the methods section how their CSF segmentation was obtained. Clinicians will not trust biomathematical models predictions unless anatomical knowledge is adequately incorporated in the modeling processes.

References

American College of Radiology (2013). ACR-ASNR-SPR practice guideline for the performance and interpretation of magnetic resonance imaging (MRI) of the brain. `http://www.acr.org/~/media/ACR/Documents/PGTS/guidelines/MRI_Brain.pdf`. [Online; accessed 11-Sept-2013].

Anderson, A. (2005). A hybrid mathematical model of solid tumour invasion: the importance of cell adhesion. *Mathematical Medicine and Biology*, 22(2):163–186.

Angelini, E., Clatz, O., Mandonnet, E., Konukoglu, E., Capelle, L., and Duffau, H. (2007). Glioma dynamics and computational models: a review of segmentation, registration, and in silico growth algorithms and their clinical applications. *Current Medical Imaging Reviews*, 3(4):262–276.

Angelini, E. D., Delon, J., Capelle, L., Mandonnet, E., et al. (2012). Differential MRI analysis for quantification of low grade glioma growth. *Medical Image Analysis*, 16(1):114–126.

Bach Cuadra, B., Pollo, C., Bardera, A., Cuisenaire, O., and Thiran, J. P. (2004). Atlas-based segmentation of pathological brain MR images using a model of lesion growth. *IEEE TMI*, 23:1301–14.

Baillard, C., Hellier, P., and Barillot, C. (2001). Segmentation of brain 3D MR images using level sets and dense registration. *Medical Image Analysis*, 5(3):185–194.

Bangiyev, L., Rossi, E. M., Young, R., Shepherd, T., Knopp, E., Friedman, K., Boada, F., and Fatterpekar, G. M. (2014). Adult brain tumor imaging: state of the art. In *Seminars in Roentgenology*, page 39.

Bauer, S., Nolte, L.-P., and Reyes, M. (2011). Segmentation of brain tumor images based on atlas-registration combined with a Markov-Random-Field lesion growth model. In *Biomedical Imaging: From Nano to Macro, 2011 IEEE International Symposium on*, pages 2018–2021. IEEE.

Bearer, E., Lowengrub, J., Frieboes, H., Chuang, Y., Jin, F., Wise, S., Ferrari, M., Agus, D., and Cristini, V. (2009). Multiparameter computational modeling of tumor invasion. *Cancer research*, 69(10):4493.

Benjamin, R., Thierry, C., and Santiago, S. (2006). A multiscale mathematical model of cancer, and its use in analyzing irradiation therapies. *Theoretical Biology and Medical Modelling*, 3.

Bertrand, G. and Malandain, G. (1994). A new characterization of three-dimensional simple points. *Pattern Recognition Letters*, 15(2):169–175.

Bohman, L.-E., Swanson, K. R., Moore, J. L., Rockne, R., Mandigo, C., Hankinson, T., Assanah, M., Canoll, P., and Bruce, J. N. (2010). Magnetic resonance imaging characteristics of glioblastoma multiforme: implications for understanding glioma ontogeny. *Neurosurgery*, 67(5):1319.

Bondiau, P.-Y., Konukoglu, E., Clatz, O., Delingette, H., Frenay, M., and Paquis, P. (2011). Biocomputing: Numerical simulation of glioblastoma growth and comparison with conventional irradiation margins. *Physica Medica*, 27(2):103–108.

Burgess, P. K., Kulesa, P. M., Murray, J. D., and Alvord Jr, E. C. (1997). The interaction of growth rates and diffusion coefficients in a three-dimensional mathematical model of gliomas. *Journal of Neuropathology & Experimental Neurology*, 56(6):704–713.

Buzdar, A. and Freedman, R. (2007). *M.D. Anderson Cancer Care Series*, volume 2. Springer.

Bynevelt, M., Britton, J., Seymour, H., MacSweeney, E., Thomas, N., and Sandhu, K. (2001). FLAIR imaging in the follow-up of low-grade gliomas: time to dispense with the dual-echo? *Neuroradiology*, 43(2):129–133.

Campbell, N. (1996). Biology.

Chakrabarty, S. and Hanson, F. (2005). Optimal control of drug delivery to brain tumors for a distributed parameters model. In *Proc American Control Conference*.

Chicoine, M. R. and Silbergeld, D. L. (1995). Assessment of brain tumor cell motility in vivo and in vitro. *Journal of Neurosurgery*, 82(4):615–622.

Clatz, O., Sermesant, M., Bondiau, P.-Y., Delingette, H., Warfield, S. K., Malandain, G., and Ayache, N. (2005). Realistic simulation of the 3D growth of brain tumors in MR images coupling diffusion with biomechanical deformation. *IEEE Transactions on Medical Imaging*, 24:1334–1346.

Cobzas, D., Mosayebi, P., Murtha, A., and Jagersand, M. (2009). Tumor invasion margin on the Riemannian space of brain fibers. *MICCAI*, pages 531–539.

Colin, T., Iollo, A., and Lombardi, D. (2012). System identification in tumor growth modeling using semi-empirical eigenfunctions. *Mathematical Models and Methods in Applied Sciences*, 22(06):1250003.

Collins, D. L., Neelin, P., Peters, T. M., and Evans, A. C. (1994). Automatic 3D intersubject registration of MR volumetric data in standardized talairach space. *Journal of computer assisted tomography*, 18(2):192–205.

Corwin, D., Holdsworth, C., Rockne, R. C., Trister, A. D., Mrugala, M. M., Rockhill, J. K., Stewart, R. D., Phillips, M., and Swanson, K. R. (2013). Toward patient-specific, biologically optimized radiation therapy plans for the treatment of glioblastoma. *PloS one*, 8(11):e79115.

Cruywagen, G., Woodward, D., Tracqui, P., Bartoo, G., Murray, J., and Alvord, E. (1995). The modelling of diffusive tumours. *J Biol Systems*, 3:937–45.

Danchaivijitr, N., Waldman, A. D., Tozer, D. J., Benton, C. E., Caseiras, G. B., Tofts, P. S., Rees, J. H., and Jäger, H. R. (2008). Low-grade gliomas: Do changes in rCBV measurements at longitudinal perfusion-weighted MR imaging predict malignant transformation? *Radiology*, 247(1):170–178.

Deangelis, L. (2001). Brain tumors. *New England Journal of Medicine*, 344(2):114–123.

Deisboeck, T., Wang, Z., Macklin, P., and Cristini, V. (2011). Multiscale cancer modeling. *Annu. Rev. Biomed. Eng.*, 13:12755.

Deisboeck, T. S., Zhang, L., Yoon, J., and Costa, J. (2008). In silico cancer modeling: is it ready for prime time? *Nature Clinical Practice Oncology*, 6(1):34–42.

Drabycz, S., Roldán, G., Robles, P. D., Adler, D., Mcintyre, J., Magliocco, A., and Cairncross, J. (2010). An analysis of image texture, tumor location, and

MGMT promoter methylation in glioblastoma using magnetic resonance imaging. *Neuroimage*, 49(2):1398–1405.

Ebert, U. and van Saarloos, W. (2000). Front propagation into unstable states: universal algebraic convergence towards uniformly translating pulled fronts. *Physica D: Nonlinear Phenomena*, 146(1):1–99.

Eisenhauer, E. A., Therasse, P., Bogaerts, J., Schwartz, L. H., Sargent, D., Ford, R., Dancey, J., Arbuck, S., Gwyther, S., Mooney, M., et al. (2009). New response evaluation criteria in solid tumours: revised RECIST guideline. *European J. of Cancer*, 45(2):228–247.

Fedorov, A., Beichel, R., Kalpathy-Cramer, J., Finet, J., Fillion-Robin, J.-C., Pujol, S., Bauer, C., Jennings, D., Fennessy, F., Sonka, M., et al. (2012). 3D slicer as an image computing platform for the quantitative imaging network. *Magnetic Resonance Imaging*.

Ferreira Jr, S., Martins, M., and Vilela, M. (1998). A growth model for primary cancer. *Physica A: Statistical Mechanics and its Applications*, 261:569–580.

Ferreira Jr, S., Martins, M., and Vilela, M. (1999). A growth model for primary cancer (II). new rules, progress curves and morphology transitions. *Physica A: Statistical Mechanics and its Applications*, 272(1-2):245–256.

Fonov, V., Evans, A., McKinstry, R., Almli, C., and Collins, D. (2009). Unbiased nonlinear average age-appropriate brain templates from birth to adulthood. *Neuroimage*, 47:S102–S102.

Fonov, V., Evans, A. C., Botteron, K., Almli, C. R., McKinstry, R. C., and Collins, D. L. (2011). Unbiased average age-appropriate atlases for pediatric studies. *NeuroImage*, 54(1):313–327.

Frieboes, H., Lowengrub, J., Wise, S., Zheng, X., Macklin, P., Bearer, E., and Cristini, V. (2007). Computer simulation of glioma growth and morphology. *Neuroimage*, 37:S59–S70.

Galanis, E., Buckner, J. C., Maurer, M. J., Sykora, R., Castillo, R., Ballman, K. V., Erickson, B. J., et al. (2006). Validation of neuroradiologic response assessment in gliomas: measurement by RECIST, two-dimensional, computer-assisted tumor area, and computer-assisted tumor volume methods. *Neuro-oncology*, 8(2):156–165.

Geremia, E., Menze, B. H., Prastawa, M., Weber, M.-A., Criminisi, A., and Ayache, N. (2013). Brain tumor cell density estimation from multi-modal MR images based on a synthetic tumor growth model. In *Medical Computer Vision. Recognition Techniques and Applications in Medical Imaging*, pages 273–282. Springer.

Gerin, C., Pallud, J., Deroulers, C., Varlet, P., Oppenheim, C., Roux, F.-X., Chrétien, F., Thomas, S. R., Grammaticos, B., and Badoual, M. (2013). Quantitative characterization of the imaging limits of diffuse low-grade oligodendrogliomas. *Neuro-oncology*.

Gevertz, J., Gillies, G., and Torquato, S. (2008). Simulating tumor growth in confined heterogeneous enviorments. *Physical Biology*, 5:036010.

Giese, A., Kluwe, L., Laube, B., Meissner, H., Berens, M., Westphal, M., Laws, E., Edvardsen, K., Rosenblum, M., and Rutka, J. (1996). Migration of human glioma cells on myelin. commentaries. *Neurosurgery*, 38(4):755–764.

Goodenberger, M. L. and Jenkins, R. B. (2012). Genetics of adult glioma. *Cancer Genetics*.

Gooya, A., Biros, G., and Davatzikos, C. (2011a). Deformable registration of glioma images using EM algorithm and diffusion reaction modeling. *Medical Imaging, IEEE Transactions on*, 30(2):375–390.

Gooya, A., Pohl, K., Bilello, M., Biros, G., and Davatzikos, C. (2011b). Joint segmentation and deformable registration of brain scans guided by a tumor growth model. *Medical Image Computing and Computer-Assisted Intervention (MICCAI)*, pages 532–540.

Gooya, A., Pohl, K. M., Bilello, M., Cirillo, L., Biros, G., Melhem, E. R., and Davatzikos, C. (2012). GLISTR: Glioma image segmentation and registration. *Medical Imaging, IEEE Transactions on*, 31(10):1941–1954.

Harpold, H., Alvord, E., and Swanson, J. (2007). The evolution of mathematical modeling of glioma proliferation and invasion. *Journal of Neuropathology & Experimental Neurology*, 66(1):1.

Henson, J., Ulmer, S., and Harris, G. (2008). Brain tumor imaging in clinical trials. *American Journal of Neuroradiology*, 29(3):419–424.

Hogea, C., Davatzikos, C., and Biros, G. (2008). An image-driven parameter estimation problem for a reaction-diffusion glioma growth model with mass effects. *J. of Math. Bio.*, 56(6):793–825.

Hogea, C. S., Murray, B. T., and Sethian, J. A. (2006). Simulating complex tumor dynamics from avascular to vascular growth using a general level-set method. *J Math Biol*, 53:86–134.

Holmes, C. J., Hoge, R., Collins, L., Woods, R., Toga, A. W., and Evans, A. C. (1998). Enhancement of MR images using registration for signal averaging. *Journal of computer assisted tomography*, 22(2):324–333.

Jaermann, T., Crelier, G., Pruessmann, K., Golay, X., Netsch, T., van Muiswinkel, A., Mori, S., van Zijl, P., Valavanis, A., Kollias, S., et al. (2004). SENSE-DTI at 3 T. *Magnetic resonance in medicine*, 51(2):230–236.

Jbabdi, S., Mandonnet, E., Duffau, H., Capelle, L., Swanson, K., Pélégrini-Issac, M., Guillevin, R., and Benali, H. (2005). Simulation of anisotropic growth of low-grade gliomas using diffusion tensor imaging. *Magnetic Resonance in Medicine*, 54(3):616–624.

Jenkinson, M., Bannister, P., Brady, M., and Smith, S. (2002). Improved optimization for the robust and accurate linear registration and motion correction of brain images. *Neuroimage*, 17(2):825–841.

Jenkinson, M. and Smith, S. (2001). A global optimisation method for robust affine registration of brain images. *Medical Image Analysis*, 5(2):143–156.

Jiang, Y., Pjesivac-Grbovic, J., Cantrell, C., and Freyer, J. P. (2005). A multiscale model for avascular tumor growth. *Biophysical journal*, 89(6):3884–3894.

Kaal, E. and Vecht, C. (2004). The management of brain edema in brain tumors. *Current opinion in oncology*, 16(6):593.

Kansal, A., Torquato, S., Chiocca, E., and Deisboeck, T. (2000). Emergence of a subpopulation in a computational model of tumor growth. *Journal of Theoretical Biology*, 207(3):431–441.

Kaster, F. O., Menze, B. H., Weber, M.-A., and Hamprecht, F. A. (2010). Comparative validation of graphical models for learning tumor segmentations from noisy manual annotations. In *Proc MICCAI Workshop on Medical Computer Vision (MCV 2010). LNCS*.

Keener, J. and Sneyd, J. (1998). Mathematical physiology, interdisciplinary applied mathematics 8.

Kelm, B. M., Menze, B. H., Nix, O., Zechmann, C. M., and Hamprecht, F. A. (2009). Estimating kinetic parameter maps from dynamic contrast-enhanced MRI using spatial prior knowledge. *IEEE Trans Med Imaging*, 28:1534–47.

Kikinis, R., Shenton, M. E., Iosifescu, D. V., McCarley, R. W., Saiviroonporn, P., Hokama, H. H., Robatino, A., Metcalf, D., Wible, C. G., Portas, C. M., et al. (1996). A digital brain atlas for surgical planning, model-driven segmentation, and teaching. *Visualization and Computer Graphics, IEEE Transactions on*, 2(3):232–241.

Konukoglu, E. (2009). *Modeling Glioma Growth and Personalizing Growth Models in Medical Images*. PhD thesis, University of Nice-Sophia Antipolis.

Konukoglu, E., Clatz, O., Bondiau, P., Delingette, H., and Ayache, N. (2010a). Extrapolating glioma invasion margin in brain magnetic resonance images: Suggesting new irradiation margins. *Medical image analysis*, 14(2):111–125.

Konukoglu, E., Clatz, O., Bondiau, P., Sermesant, M., Delingette, H., and Ayache, N. (2007a). Towards an identification of tumor growth parameters from time series of images. *Medical Image Computing and Computer-Assisted Intervention, MICCAI 2007*, pages 549–556.

Konukoglu, E., Clatz, O., Menze, B., Stieltjes, B., Weber, M., Mandonnet, E., Delingette, H., and Ayache, N. (2009). Image guided personalization of reaction-diffusion type tumor growth models using modified anisotropic eikonal equations. *Medical Imaging, IEEE Transactions on*, 29(1):77–95.

Konukoglu, E., Clatz, O., Menze, B. H., Weber, M.-A., Stieltjes, B., Mandonnet, E., Delingette, H., and Ayache, N. (2010b). Image guided personalization of reaction-diffusion type tumor growth models using modified anisotropic eikonal equations. *IEEE TMI*, pages 77–95.

Konukoglu, E., Sermesant, M., Clatz, O., Peyrat, J., Delingette, H., and Ayache, N. (2007b). *A recursive anisotropic fast marching approach to reaction diffusion equation: Application to tumor growth modeling*. Springer.

Kyriacou, S. K., Davatzikos, C., Zinreich, S. J., and Bryan, R. N. (1999). Nonlinear elastic registration of brain images with tumor pathology using a biomechanical model. *IEEE T Med Imaging*, 18:580–592.

Lagarias, J. C., Reeds, J. A., Wright, M. H., and Wright, P. E. (1998). Convergence properties of the nelder–mead simplex method in low dimensions. *SIAM Journal on Optimization*, 9(1):112–147.

Laigle-Donadey, F., Martin-Duverneuil, N., Lejeune, J., Criniere, E., Capelle, L., Duffau, H., Cornu, P., Broet, P., Kujas, M., and Mokhtari, K. (2004). Correlations between molecular profile and radiologic pattern in oligodendroglial tumors. *Neurology*, 63(12):2360.

Lancaster, J. L., Woldorff, M. G., Parsons, L. M., Liotti, M., Freitas, C. S., Rainey, L., Kochunov, P. V., Nickerson, D., Mikiten, S. A., and Fox, P. T. (2000). Automated talairach atlas labels for functional brain mapping. *Human brain mapping*, 10(3):120–131.

Langs, G., Tie, Y., Rigolo, L., Golby, A. J., and Golland, P. (2010). Localization of language areas in brain tumor patients by functional geometry alignment. In *Proc MICCAI Workshop on Computational Imaging Biomarkers for Tumors*, page 8.

Lim, D. A., Cha, S., Mayo, M. C., Chen, M.-H., Keles, E., VandenBerg, S., and Berger, M. S. (2007). Relationship of glioblastoma multiforme to neural stem cell regions predicts invasive and multifocal tumor phenotype. *Neuro-oncology*, 9(4):424–429.

Liu, Y., Sadowski, S. M., Weisbrod, A. B., Kebebew, E., Summers, R. M., and Yao, J. (2014). Patient specific tumor growth prediction using multimodal images. *Medical image analysis*, 18(3):555–566.

Lorenzi, M. (2012). *Deformation based morphometry of the brain for the development of surrogate markers in Alzheimer's disease.* PhD thesis, University of Nice-Sophia Antipolis.

Lu, S., Ahn, D., Johnson, G., and Cha, S. (2003). Peritumoral diffusion tensor imaging of high-grade gliomas and metastatic brain tumors. *Am J Neuroradiology.*, 24:937–41.

Mamelak, A. N. and Jacoby, D. B. (2007). Targeted delivery of antitumoral therapy to glioma and other malignancies with synthetic chlorotoxin (TM-601). *Expert Opin Drug Deliv*, 4:175–186.

Mandonnet, E. (2011). Mathematical modeling of glioma on MRI. *Revue neurologique*, 167(10):715–720.

Mandonnet, E., Capelle, L., and Duffau, H. (2006). Extension of paralimbic low grade gliomas: toward an anatomical classification based on white matter invasion patterns. *Journal of neuro-oncology*, 78(2):179–185.

Mandonnet, E., Delattre, J., Tanguy, M., Swanson, K., Carpentier, A., Duffau, H., Cornu, P., Effenterre, R. V., Alvord, E., and Capelle, J. (2003). Continuous growth of mean tumor diameter in a subset of grade II gliomas. *Annals of neurology*, 53(4):524–528.

Mandonnet, E., Wait, S., Choi, L., and Teo, C. (2013). The importance of measuring the velocity of diameter expansion on MRI in upfront management of suspected WHO grade II glioma - case report. *Neurochirurgie.*

Mandonnet, E., Winkler, P. A., and Duffau, H. (2010). Direct electrical stimulation as an input gate into brain functional networks: principles, advantages and limitations. *Acta Neurochirurgica*, 152(2):185–193.

Mazziotta, J., Toga, A., Evans, A., Fox, P., Lancaster, J., Zilles, K., Woods, R., Paus, T., Simpson, G., Pike, B., et al. (2001). A probabilistic atlas and reference system for the human brain: International consortium for brain mapping (ICBM). *Philosophical Transactions of the Royal Society of London. Series B: Biological Sciences*, 356(1412):1293–1322.

McCorquodale, P., Colella, P., and Johansen, H. (2001). A cartesian grid embedded boundary method for the heat equation on irregular domains. *Journal of Computational Physics*, 173(2):620–635.

Menze, B., Jakab, A., Bauer, S., Kalpathy-Cramer, J., Farahani, K., Kirby, J., Burren, Y., Porz, N., Slotboom, J., Wiest, R., Lanczi, L., Gerstner, E., Weber, M.-A., Arbel, T., Avants, B., Ayache, N., Buendia, P., Collins, L., Cordier, N., Corso, J., Criminisi, A., Das, T., Delingette, H., Demiralp, C., Durst, C., Dojat, M., Doyle, S., Festa, J., Forbes, F., Geremia, E., Glocker, B., Golland, P., Guo, X., Hamamci, A., Iftekharuddin, K., Jena, R., John, N., Konukoglu, E., Lashkari, D., Antonio Mariz, J., Meier, R., Pereira, S., Precup, D., Price, S. J., Riklin-Raviv, T., Reza, S., Ryan, M., Schwartz, L., Shin, H.-C., Shotton, J., Silva, C., Sousa, N., Subbanna, N., Szekely, G., Taylor, T., Thomas, O., Tustison, N., Unal, G., Vasseur, F., Wintermark, M., Hye Ye, D., Zhao, L., Zhao, B., Zikic, D., Prastawa, M., Reyes, M., and Van Leemput, K. (2014). The multimodal brain tumor image segmentation benchmark (BRATS).

Menze, B. H., Lichy, M. P., Bachert, P., Kelm, B. M., Schlemmer, H.-P., and Hamprecht, F. A. (2006). Optimal classification of long echo time in vivo magnetic resonance spectra in the detection of recurrent brain tumors. *NMR Biomed*, 19:599–610.

Menze, B. H., Stretton, E., Konukoglu, E., and Ayache, N. (2011a). *Image-based modeling of tumor growth in patients with glioma.* Springer, Heidelberg/Germany.

Menze, B. H., Van Leemput, K., Honkela, A., Konukoglu, E., Weber, M., Ayache, N., and Golland, P. (2011b). A generative approach for image-based modeling of tumor growth. In *IPMI*, pages 735–747. Springer.

Menze, B. H., Van Leemput, K., Lashkari, D., Weber, M.-A., Ayache, N., and Golland, P. (2010). A generative model for brain tumor segmentation in multi-modal images. In *Proc MICCAI, LNCS 6362*, pages 151–159.

Miller, A., Alston, R., and Corsellis, J. (1980). Variation with age in the volumes of grey and white matter in the cerebral hemispheres of man: measurements with an image analyser. *Neuropathology and applied neurobiology*, 6(2):119–132.

Moffat, B. A., Chenevert, T. L., Meyer, C. R., Mckeever, P. E., Hall, D. E., Hoff, B. A., Johnson, T. D., Rehemtulla, A., and Ross, B. D. (2006). The functional diffusion map: an imaging biomarker for the early prediction of cancer treatment outcome. *Neoplasia (New York, NY)*, 8(4):259.

Mohamed, A. and Davatzikos, C. (2005). Finite element modeling of brain tumor mass-effect from 3D medical images. In *Proc MICCAI. LNCS 3749*.

Mohamed, A., Zacharakib, E. I., Shena, D., and Davatzikos, C. (2006). Deformable registration of brain tumor images via a statistical model of tumor-induced deformation. *Medical Image Analysis*, 10:752–763.

Murray, J. (2002). *Mathematical biology*, volume 2. Springer.

Neal, M. L., Trister, A. D., Cloke, T., Sodt, R., Ahn, S., Baldock, A. L., Bridge, C. A., Lai, A., Cloughesy, T. F., Mrugala, M. M., et al. (2013). Discriminating survival outcomes in patients with glioblastoma using a simulation-based, patient-specific response metric. *PloS one*, 8(1):e51951.

Nelder, J. A. and Mead, R. (1965). A simplex method for function minimization. *Computer journal*, 7(4):308–313.

Pallud, J., Varlet, P., Devaux, B., Geha, S., Badoual, M., Deroulers, C., Page, P., Dezamis, E., Daumas-Duport, C., and Roux, F.-X. (2010). Diffuse low-grade oligodendrogliomas extend beyond MRI-defined abnormalities. *Neurology*, 74(21):1724–1731.

Philips (2010). Philips ambient lighting MR opens up a whole new world in patient care. `http://www.healthcare.philips.com/pwc_hc/pk_en/about/Events/RSNA/pdfs/CS_AmbientExp_versaille_E_final_july.pdf`. [Online; accessed 9-July-2014].

Powell, M. (2002). UOBYQA: unconstrained optimization by quadratic approximation. *Mathematical Programming*, 92:555–582.

Powell, M. (2009). The BOBYQA algorithm for bound constrained optimization without derivatives. *Cambridge NA Report NA2009/06, University of Cambridge, Cambridge.*

Prastawa, M., Bullitt, E., and Gerig, G. (2005). Synthetic ground truth for validation of brain tumor MRI segmentation. In *Proc MICCAI. LNCS 3749*.

Prastawa, M., Bullitt, E., and Gerig, G. (2009). Simulation of brain tumors in MR images for evaluation of segmentation efficacy. *Medical image analysis*, 13(2).

Price, S., Jena, R., Burnet, N., Hutchinson, P., Dean, A., Pena, A., Pickard, J., Carpenter, T., and Gillard, J. (2006). Improved delineation of glioma margins and regions of infiltration with the use of diffusion tensor imaging: an image-guided biopsy study. *American journal of neuroradiology*, 27(9):1969–1974.

Price, S. J., Jena, R., Burnet, N. G., Carpenter, T. A., Pickard, J. D., and Gillard, J. H. (2007). Predicting patterns of glioma recurrence using diffusion tensor imaging. *European radiology*, 17(7):1675–1684.

Pudney, C. (1998). Distance-ordered homotopic thinning: A skeletonization algorithm for 3D digital images. *Comput. Vis. Image Underst.*, 72(3):404–413.

Rees, J., Watt, H., Jäger, H. R., Benton, C., Tozer, D., Tofts, P., and Waldman, A. (2009). Volumes and growth rates of untreated adult low-grade gliomas indicate risk of early malignant transformation. *European Journal of Radiology*, 72(1):54–64.

Rekik, I., Allassonnière, S., Clatz, O., Geremia, E., Stretton, E., Delingette, H., and Ayache, N. (2012). Tumor growth parameters estimation and source localization from a unique time point: Application to low-grade gliomas. *Computer Vision and Image Understanding*, 117(3):238–249.

Rexilius, J., Hahn, H., Schluter, M., Kohle, S., Bourquain, H., Bttcher, J., and Peitgen, H. (2004). A framework for the generation of realistic brain tumor phantoms and applications. In *Proc MICCAI, LNCS 3217*.

Ribba, B., Kaloshi, G., Peyre, M., Ricard, D., Calvez, V., Tod, M., Čajavec-Bernard, B., Idbaih, A., Psimaras, D., Dainese, L., et al. (2012). A tumor growth inhibition model for low-grade glioma treated with chemotherapy or radiotherapy. *Clinical Cancer Research*, 18(18):5071–5080.

Riklin-Raviv, T., Menze, B. H., Van Leemput, K., Stieltjes, B., Weber, M. A., Ayache, N., Wells III, W., and Golland, P. (2009). Joint segmentation via patient-specific latent anatomy model. In *Proc MICCAI-PMMIA*.

Riklin-Raviv, T., Van Leemput, K., Menze, B. H., Wells, W. M., and Golland, P. (2010). Segmentation of image ensembles via latent atlases. *Medical Image Analysis*. In press.

Rockne, R., Alvord Jr, E., Rockhill, J., and Swanson, K. (2009). A mathematical model for brain tumor response to radiation therapy. *Journal of mathematical biology*, 58(4-5):561–578.

Rohlfing, T., Zahr, N. M., Sullivan, E. V., and Pfefferbaum, A. (2010). The SRI24 multichannel atlas of normal adult human brain structure. *Human Brain Mapping*, 31(5):798–819.

Roose, T., Chapman, S. J., and Maini, P. K. (2007). Mathematical models of avascular tumor growth. *Siam Review*, 49(2):179–208.

Rosset, A., Spadola, L., and Ratib, O. (2004). OsiriX: an open-source software for navigating in multidimensional DICOM images. *Journal of Digital Imaging*, 17(3):205–216.

Sanai, N. and Berger, M. (2008). Glioma extent of resection and its impact on patient outcome. *Neurosurgery*, 62(4):753.

Sanga, S., Frieboes, H., Zheng, X., Gatenby, R., Bearer, E., and Cristini, V. (2007). Predictive oncology: a review of multidisciplinary, multiscale in silico modeling linking phenotype, morphology and growth. *Neuroimage*, 37:S120–S134.

Schmitt, P., Mandonnet, E., Perdreau, A., and Angelini, E. D. (2013). Effects of slice thickness and head rotation when measuring glioma sizes on MRI: in support of volume segmentation versus two largest diameters methods. *Journal of Neuro-Oncology*, pages 1–8.

Sethian, J. A. (1999). *Level set methods and fast marching methods: evolving interfaces in computational geometry, fluid mechanics, computer vision, and materials science.*, volume 3. Cambridge university press.

Shah, G. D., Kesari, S., Xu, R., Batchelor, T. T., O'Neill, A. M., Hochberg, F. H., Levy, B., Bradshaw, J., and Wen, P. Y. (2006). Comparison of linear and volumetric criteria in assessing tumor response in adult high-grade gliomas. *Neuro-oncology*, 8(1):38–46.

Silbergeld, D. L. and Chicoine, M. R. (1997). Isolation and characterization of human malignant glioma cells from histologically normal brain. *Journal of neurosurgery*, 86(3):525–531.

Smith, S. M. (2002). Fast robust automated brain extraction. *Human brain mapping*, 17(3):143–155.

Soffietti, R., Baumert, B., Bello, L., Von Deimling, A., Duffau, H., Frénay, M., Grisold, W., Grant, R., Graus, F., Hoang-Xuan, K., et al. (2010). Guidelines on management of low-grade gliomas: report of an EFNS–EANO* task force. *European Journal of Neurology*, 17(9):1124–1133.

Sottoriva, A., Verhoeff, J., Borovski, T., Mcweeney, S., Naumov, L., Medema, J., Sloot, P., and Vermeulen, L. (2010). Cancer stem cell tumor model reveals invasive morphology and increased phenotypical heterogeneity. *Cancer research*, 70(1):46.

Stretton, E., Geremia, E., Menze, B., Delingette, H., and Ayache, N. (2013). Importance of patient DTI's to accurately model glioma growth using the reaction diffusion equation. *Proceedings of the IEEE 10th International Symposium on Biomedical Imaging: From Nano to Macro (ISBI)*, pages 1142–1145.

Stretton, E., Mandonnet, E., Geremia, E., Menze, B., Delingette, H., and Ayache, N. (2012). Predicting the location of glioma recurrence after a resection surgery. *Spatio-temporal Image Analysis for Longitudinal and Time-Series Image Data (MICCAI)*, pages 113–123.

Swanson, K. (1999). *Mathematical Modeling of the Growth and Control of Tumors.* PhD thesis, University of Washington.

Swanson, K., Alvord, E., and Murray, J. (2000). A quantitative model for differential motility of gliomas in grey and white matter. *Cell Proliferation*, 33(5):317–330.

Swanson, K., Bridge, C., Murray, J., and Alvord, E. (2003). Virtual and real brain tumors: using mathematical modeling to quantify glioma growth and invasion. *Journal of the neurological sciences*, 216(1):1–10.

Swanson, K., Rostomily, R., and Alvord, E. (2007). A mathematical modelling tool for predicting survival of individual patients following resection of glioblastoma: a proof of principle. *British journal of cancer*, 98(1):113–119.

Swanson, K. R., Alvord, E. C., and Murray, J. D. (2002). Quantifying efficacy of chemotherapy of brain tumors with homogeneous and heterogeneous drug delivery. *Acta Biotheor*, 50:223–237.

Talairach, J. and Tournoux, P. (1988). Co-planar stereotaxic atlas of the human brain. 3-Dimensional proportional system: an approach to cerebral imaging.

Therasse, P., Eisenhauer, E., and Verweij, J. (2006). RECIST revisited: a review of validation studies on tumour assessment. *European journal of cancer*, 42(8):1031–1039.

Tovi, M. (1993). MR imaging in cerebral gliomas analysis of tumour tissue components. *Acta radiologica. Supplementum*, 384:1.

Tracqui, P. (2009). Biophysical models of tumour growth. *Reports on Progress in Physics*, 72(5):056701.

Tracqui, P., Cruywagen, G., Woodward, D., Bartoo, G., and Jr, J. M. A. (1995a). A mathematical model of glioma growth: the effect of chemotherapy on spatio-temporal growth. *Cell Proliferation*, 28(1):17–31.

Tracqui, P., Cruywagen, G. C., Woodward, D. E., Bartoo, G. T., Murray, J. D., and Alvord, E. C. (1995b). A mathematical model of glioma growth: the effect of chemotherapy on spatio-temporal growth. *Cell Proliferation*, 28:17–31.

Unkelbach, J., Menze, B., Motamedi, A., Dittmann, F., Konukoglu, E., Ayache, N., and Shih, H. (2012). Glioblastoma growth modeling for radiotherapy target delineation. In *IGRT MICCAI Workshop*, Nice.

Unkelbach, J., Menze, B. H., Konukoglu, E., Dittmann, F., Le, M., Ayache, N., and Shih, H. A. (2014). Radiotherapy planning for glioblastoma based on a tumor growth model: improving target volume delineation. *Physics in medicine and biology*, 59(3):747.

Van den Bent, M., Wefel, J., Schiff, D., Taphoorn, M., Jaeckle, K., Junck, L., Armstrong, T., Choucair, A., Waldman, A., Gorlia, T., et al. (2011). Response assessment in neuro-oncology (a report of the RANO group): assessment of outcome in trials of diffuse low-grade gliomas. *The lancet oncology*, 12(6):583–593.

Vercauteren, T., Pennec, X., Perchant, A., and Ayache, N. (2009). Diffeomorphic demons: Efficient non-parametric image registration. *NeuroImage*, 45(1):S61–S72.

Wang, C. H., Rockhill, J. K., Mrugala, M., Peacock, D. L., Lai, A., Jusenius, K., Wardlaw, J. M., Cloughesy, T., Spence, A. M., Rockne, R., et al. (2009). Prognostic significance of growth kinetics in newly diagnosed glioblastomas revealed by combining serial imaging with a novel biomathematical model. *Cancer research*, 69(23):9133–9140.

Warfield, S. K., Zou, K. H., and Wells, W. M. (2004). Simultaneous truth and performance level estimation (STAPLE): an algorithm for the validation of image segmentation. *Medical Imaging, IEEE Transactions on*, 23(7):903–921.

Warren, K. E., Patronas, N., Aikin, A. A., Albert, P. S., and Balis, F. M. (2001). Comparison of one-, two-, and three-dimensional measurements of childhood brain tumors. *Journal of the National Cancer Institute*, 93(18):1401–1405.

Wasserman, R. and Acharya, R. (1996). A patient-specific in vivo tumor model. *Math Biosci*, 136:111–140.

Wen, P. Y., Macdonald, D. R., Reardon, D. A., Cloughesy, T. F., Sorensen, A. G., Galanis, E., DeGroot, J., Wick, W., Gilbert, M. R., Lassman, A. B., et al. (2010). Updated response assessment criteria for high-grade gliomas: response assessment in neuro-oncology working group. *J. of Clinical Oncology*, 28(11):1963–1972.

Whittle, I. (2004). The dilemma of low grade glioma. *Journal of Neurology, Neurosurgery & Psychiatry*, 75(suppl 2):ii31–ii36.

Wilson, C. and Berger., M. (1999). *The gliomas.* W.B Saunders Company.

Woodward, D., Cook, J., Tracqui, P., Cruywagen, G., Murray, J., and Alvord, E. (1996). A mathematical model of glioma growth: the effect of extent of surgical resection. *Cell proliferation*, 29(6):269–288.

Wu, J.-S., Zhou, L.-F., Tang, W.-J., Mao, Y., Hu, J., Song, Y.-Y., Hong, X.-N., and Du, G.-H. (2007). Clinical evaluation and follow-up outcome of diffusion tensor imaging-based functional neuronavigation: a prospective, controlled study in patients with gliomas involving pyramidal tracts. *Neurosurgery*, 61(5):935–949.

Young, G. (2007). Advanced MRI of adult brain tumors. *Neurologic clinics*, 25(4):947–973.

Yushkevich, P. A., Piven, J., Cody Hazlett, H., Gimpel Smith, R., Ho, S., Gee, J. C., and Gerig, G. (2006). User-guided 3D active contour segmentation of anatomical structures: Significantly improved efficiency and reliability. *Neuroimage*, 31(3):1116–1128.

Zacharaki, E. I., Shen, D., and Davatzikos, C. (2008). ORBIT: A multiresolution framework for deformable registration of brain tumor images. *IEEE TMI*, 27:1003–17.

Zhang, Y., Brady, M., and Smith, S. (2001). Segmentation of brain MR images through a hidden markov random field model and the expectation-maximization algorithm. *Medical Imaging, IEEE Transactions on*, 20(1):45–57.

Simulation of patient-specific glioma models for therapy planning

ABSTRACT:

Tumor growth models based on the Fisher Kolmogorov (FK) reaction-diffusion equation have shown convincing results in reproducing and predicting the invasion patterns of glioma brain tumors. In this thesis we use different FK model formulations to i) assess the need of patient-specific DTIs when modeling LGGs, ii) study cancer cell infiltration after tumor resections, and iii) define a metric to determine progressive disease for low-grade glimoas (LGG).

Diffusion tensor images (DTIs) have been suggested to model the anisotropic diffusion of tumor cells in brain white matter. However, patient specific DTIs are expensive and often acquired with low resolution, which compromises the accuracy of the tumor growth models' results. We used a FK formulation to describe the evolution of the visible boundary of the tumor to investigate the impact of replacing the patient DTI by i) an isotropic diffusion map or ii) an anisotropic high-resolution DTI atlas formed by averaging the DTIs of multiple patients. We quantify the impact of replacing the patient DTI using synthetic tumor growth simulations and tumor evolution predictions on a clinical case. This study suggests that modeling glioma growth with tissue based differential motility (not using a DTI) yields slightly less accurate results than using a DTI. However, refraining from using a DTI would be sufficient in situations when modeling LGGs. Therefore, any of these DTI options are valid to use in a FK formulation to model LGG growth with the purpose of aiding clinicians in therapy planning.

After a brain resection medical professionals want to know what the best type of follow-up treatment would be for a particular patient, i.e., chemotherapy for diffuse tumors or a second resection after a given amount of time for bulky tumors. We propose a thorough method to leverage FK reaction-diffusion glioma growth models on post-operative cases showing brain distortions to estimate tumor cell infiltration beyond the visible boundaries in FLAIR MRIs. Our method addresses two modeling challenges: i) the challenge of brain parenchyma movement after surgery with a non-linear registration technique and ii) the challenge of incomplete post-operative tumor segmentations by combining two infiltration maps, where one was simulated from a pre-operative image and one estimated from a post-operative image. We used the data of two patients with LGG to demonstrate the effectiveness of the proposed three-step method. We believe that our proposed method could help clinicians anticipate tumor regrowth after a resection and better characterize the radiological non-visible infiltrative extent of a tumor to plan therapy.

For LGGs captured on FLAIR/T2 MRIs, there is a substantial amount debate on selecting a definite threshold for size-based metrics to determine progressive disease (PD) and it is still an open item for the Response Assessment in Neuro-Oncology (RANO) Working Group. We propose an approach to assess PD of LGG using tumor growth speed estimates from a FK formulation that takes into consideration irregularities in tumor shape, differences in growth speed between gray matter and white matter, and volumetric changes. Using the FLAIR MRIs of nine patients we compare the PD estimates of our proposed approach to i) the ones calculated using 1D, 2D, and 3D manual tumor growth speed estimates and ii) the ones calculated using a set of well-established size-based criteria (RECIST, Macdonald, and RANO). We conclude from our comparison results that our proposed approach is promising for assessing PD of LGG from a limited number of MRI scans. It is our hope that this model's tumor growth speed estimates could one day be used as another parameter in clinical therapy planning.

Keywords: Brain Tumor Modeling; Glioma Modeling; Computer Model; Patient-Specific; Medical Imaging; Fisher Kolmogorov Model; Reaction Diffusion Equation; Traveling Wave Equation; Eikonal Equation

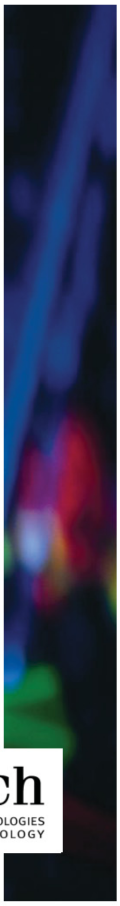

Simulation de modèles personnalisés de gliomes pour la planification de thérapies

Résumé:

Les modèles de croissance tumorale fondés sur l'équation de réaction-diffusion Fisher Kolmogorov (FK) ont montré des résultats probants dans la reproduction et la prédiction de l'invasion de cellules tumorales du cerveau pour les gliomes. Dans cette thèse, nous utilisons différentes formulations du modèle FK pour i) évaluer la nécessité de l'imagerie de diffusion pour construire des modèles spécifiques de gliomes de bas grade ii) l'étude de l'infiltration de cellules tumorales après une résection chirurgicale de la tumeur, et iii) définir une métrique pour quantifier l'évolution de Gliomes de Bas Grade (GBG).

L'imagerie en tenseur de diffusion (ITD) a été suggérée pour modéliser la diffusion anisotrope des cellules tumorales dans la matière blanche du cerveau. Toutefois, les ITD sont coûteuses et souvent acquises en basse résolution, ce qui impacte la précision des résultats des modèles de croissance tumorale. Nous avons utilisé une formulation FK pour décrire l'évolution de la frontière visible de la tumeur pour étudier l'impact du remplacement de l'ITD patient par i) une hypothèse de diffusion isotrope ou ii) une ITD de reférence anisotrope en haute résolution formée par la moyenne des ITD de plusieurs patients. Nous quantifions l'impact du remplacement de l'ITD acquise sur un patient à aide de simulations de croissance tumorales synthétiques et des prévisions d'évolution de la tumeur d'un cas clinique. Cette étude suggère que la modélisation de la croissance du gliome à base de motilité différentielle de tissus (n'utilisant pas d'ITD) donne des résultats un peu moins précis qu'à l'aide d'une ITD. Cependant, s'abstenir d'utiliser une ITD serait suffisant lors de la modélisation de gliomes de bas grade. Par conséquent, toutes ces options d'ITD sont valides à utiliser dans une formulation FK pour modéliser la croissance de gliomes de bas grade dans le but d'aider les cliniciens dans la planification du traitement.

Après la résection d'une tumeur cérébrale, les professionnels de santé veulent savoir quel serait le meilleur traitement de suivi pour chaque patient particulier, c'est à dire, une chimiothérapie pour des tumeurs diffuses ou bien une deuxième résection après un laps de temps donné pour les tumeurs massives. Nous proposons une méthode pour tirer profit de modèles de croissance de gliome FK sur les cas post-opératoires montrant des distorsions du cerveau pour estimer l'infiltration des cellules tumorales au-delà des frontières visibles dans les IRM FLAIR. Notre méthode répond à deux défis de modélisation: i) le défi du mouvement du parenchyme cérébral après la chirurgie avec une technique de recalage non-linéaire et ii) le défi de la segmentation incomplète de la tumeur post-opératoire en combinant deux cartes d'infiltration : une ayant été simulée à partir d'une image pré-opératoire et une estimée à partir d'une image post-opératoire. Nous avons utilisé les données de deux patients ayant des gliomes de bas grade afin de démontrer l'efficacité de la méthode proposée. Nous croyons que notre méthode pourrait aider les cliniciens à anticiper la récurrence de la tumeur après une résection et à mieux caractériser l'étendue de l'infiltration non visible par la radiologie pour planifier la thérapie.

Pour les gliomes de bas grade visibles par une IRM FLAIR/T2, il y a un débat important au sein du groupe de travail RANO (*Response Assessment in Neuro-Oncology*) sur la sélection d'un seuil pertinent des métriques basées sur l'évolution de la taille de la tumeur pour déterminer si la maladie est évolutive (ME). Nous proposons une approche pour évaluer la ME du GBG en utilisant des estimations de la vitesse de croissance de la tumeur à partir d'une formulation FK qui prend en compte les irrégularités de forme de la tumeur, les différences de vitesse de croissance entre la matière grise et la matière blanche, et les changements volumétriques. En utilisant les IRM FLAIR de neuf patients, nous comparons les estimations de ME de notre approche proposée avec i) celles calculées en utilisant les estimations manuel de la vitesse de croissance tumorales 1D, 2D et 3D et ii) celles calculées en utilisant un ensemble bien établi de critères basés sur la taille (critères RECIST, Macdonald et RANO). Nous concluons des résultats de notre comparaison que notre approche est prometteuse pour évaluer la ME du GBG à partir d'un nombre limité d'examens par IRM. On peut espérer que les estimations de vitesse de croissance de la tumeur de ce modèle pourraient un jour être utilisées comme un autre biomarqueur dans la planification de la thérapie clinique.

Mots-clés : Modélisation de Tumeur Cérébrale ; Modélisation de Gliome ; Modèlisation numérique; Patient-Spécifique ; Imagerie Médicale ; Modèle de Fisher Kolmogorov